Advanced optical techniques for laser-interferometric gravitational-wave detectors

Von dem Fachbereich Physik der
Universität Hannover

zur Erlangung des Grades
Doktor der Naturwissenschaften
Dr. rer. nat.

genehmigte Dissertation von

Dipl.-Phys. Gerhard Heinzel,
geboren am 17.11.1964 in Biberach/Riß.

1999

Referent: Prof. Danzmann
Korreferent: Prof. Welling
Tag der Promotion: 12. Februar 1999.
Druckdatum: 20. Februar 1999.

Zusammenfassung

In der Arbeit werden zwei wichtige Techniken für laser-interferometrische Gravitationswellendetektoren behandelt, die beide entscheidende Bedeutung für die gerade im Bau befindlichen großen Detektoren haben, insbesondere für GEO 600. Die Arbeit wurde am Max-Planck-Institut für Quantenoptik in Garching durchgeführt, und insbesondere an dem dort befindlichen Prototyp-Interferometer mit 30 m Armlänge.

Die erste Technik, 'autoalignment', dient zur automatischen Justierung und Regelung der Winkelfreiheitsgrade eines Interferometers. Grundlage sind die früheren Arbeiten von Ward und Morrison, die mit der von ihnen entwickelten Technik 'differential wavefront sensing' ein Fabry-Perot-Interferometer mit insgesamt vier Winkelfreiheitsgraden automatisch justiert haben. In der vorliegenden Arbeit wird diese Technik für allgemeinere Interferometer erweitert, insbesondere für ein Michelson-Interferometer mit 'power recycling'. Es werden die dafür nötige Theorie und der praktische Aufbau eines solchen Systems für den Garchinger Prototypen beschrieben. Das entwickelte System erlaubt es, alle zehn Freiheitsgrade eines Michelson-Interferometers mit 'power recycling' von elektronischen Regelkreisen justieren zu lassen, so daß die Positionen aller Strahlen in einem solchen Interferometer nur noch durch die Positionen des Strahleinkopplers und zweier Detektoren bestimmt sind, und dabei alle miteinander interferierenden Strahlen optimal übereinanderliegen. Für die beiden wichtigsten Freiheitsgrade (diejenigen des Michelson-Interferometers) wird eine verbleibende Regelabweichung von ca. 20 nrad rms (integriert über den Frequenzbereich von 0.1 Hz bis 100 Hz) erreicht. Dies entspricht 0.6 μm auf 30 m, bei einem Strahldurchmesser von 2 mm. Das autoalignment-System funktioniert sehr zufriedenstellend, insbesondere auch noch nach dem Umbau auf Schnupp-Modulation und dual recycling. In einem separaten Abschnitt (2.10) werden Fehlersignale für die automatische Justierung von GEO 600 berechnet.

Die zweite Technik, 'dual recycling', erlaubt es, die Empfindlichkeit eines Michelson-Interferometers für Gravitationswellen zu erhöhen. Durch Hinzufügen eines weiteren Spiegels (des 'signal recycling'-Spiegels M_{SR}) werden die Phasenmodulations-Seitenbänder des Lichtes, die dem zu messenden Signal entsprechen, resonant überhöht und so am Meßausgang verstärkt (die Speicherzeit des Interferometers für diese Signal-Seitenbänder wird optimiert). Signal recycling hat zwei mögliche Betriebszustände, die als 'broadband' und 'detuned' bezeichnet werden. Die maximale Empfindlichkeit liegt im ersten Fall bei DC (0 Hz), und im zweiten Fall bei einer vom Anwender wählbaren höheren Frequenz. In der vorliegenden Arbeit werden zunächst verschiedene mathematische Modelle eingeführt, mit denen das Verhalten eines Interferometers simuliert werden kann. Mit Hilfe dieser Modelle werden dann die Eigenschaften und insbesondere die Regelsignale des Garchinger Prototypen diskutiert. Beide Betriebszustände wurden am Prototypen experimentell demonstriert, und die beschriebenen Experimente stellen die erste Demonstration von signal recycling (bzw. dual recycling) an einem Interferometer mit aufgehängten Spiegeln dar. Die gemessene Signalüberhöhung und deren Frequenzgang sind in guter Übereinstimmung mit der Theorie. Ein weiterer wichtiger Effekt von dual recycling, die Kontrast-Verbesserung des Michelson-Interferometers durch die Unterdrückung von höheren transversalen Moden, wurde ebenfalls beobachtet. Die zur Regelung des Interferometers verwendeten Techniken werden die Grundlage der entsprechenden Systeme von GEO 600 darstellen.

Im Anhang werden verschiedene nützliche elektronische Schaltungen sowie ein ebenfalls im Rahmen dieser Arbeit geschriebenes Programm zur Simulierung und Optimierung von elektronischen Schaltungen beschrieben.

Schlüsselwörter: Gravitationswellendetektor, Autoalignment, Dual Recycling.

Preface

The direct detection of gravitational waves by laser interferometry is expected to be accomplished within the next years and will be one of the most exciting developments in physics and astrophysics. Much has been written about the history and principles of these efforts (see, e.g., [Thorne87, Saulson, Blair]) and that is not repeated here.

Currently there are four projects worldwide that are constructing large laser interferometers. These are LIGO in the US, the French-Italian VIRGO project, TAMA in Japan and the German-British GEO 600. This work was carried out as part of the research for the GEO 600 project, which is being built near Hannover. The Max-Planck-Insitut für Quantenoptik, which is the main German participant in GEO 600, has for many years been operating prototype interferometers in Garching near München. Since 1983 the prototype has 30 m armlength and is known as *the Garching 30 m prototype*. The author has performed two main experiments at the 30 m prototype, which were both carried out in preparation for the construction of GEO 600.

The first was the development of an automatic beam alignment system (short: 'autoalignment') for the 30 m prototype, which is described in Chapter 2. It is based on the *differential wavefront sensing* technique by Ward, Morrison and others [Morrison94], who have used this technique to automatically align a Fabry-Perot cavity with four angular degrees of freedom. In this work the technique is extended to more general interferometers, in particular a Michelson interferometer with power recycling. Both the necessary theory and the practical development of a working system for the 30 m prototype are described. The system allows to have all ten angular degrees of freedom of such an interferometer automatically aligned by electronic control loops, such that the position of all beams is determined only by the lateral position of the beam injector and of two photodetectors, and all interfering beams overlap optimally. For the two most important degrees of freedom, those of the Michelson interferometer, the remaining RMS alignment noise (integrated from 0.1 to 100 Hz) is about 20 nrad, which is equivalent to 0.6 μm over 30 m and which must be compared with the beam diameter (approximately 2 mm). The system in the prototype works well and continued to do so after the change from external modulation to Schnupp modulation and the introduction of dual recycling. The main results are about to be published [Heinzel99]. In Section 2.10 error signals for the autoalignment of GEO 600 are computed.

The second experiment, subject of Chapter 1, was the implementation of *dual recycling* (i.e. the combination of power recycling and signal recycling). As is explained in detail in Section 1.1, the signal storage time in a simple Michelson interferometer intended for gravitational wave detection is too short for the most promising signal frequencies (approximately 100 to 1000 Hz), unless the arms were hundreds of kilometers long.

For armlengths of order kilometer, there are currently two main alternatives considered realistic for optimizing the signal storage time: Fabry-Perot cavities in the arms and signal recycling.

All projects apart from GEO 600 will use Fabry-Perot cavities in the arms and consider signal recycling an option for future stages of their project, whereas GEO 600 has no

arm cavities and needs to implement dual recycling from the beginning.

While the principle of signal recycling was invented more than ten years ago, and a table-top experiment confirmed the most important predictions soon after, dual recycling had never been implemented on a prototype with suspended mirrors, and with a control scheme that resembles the one planned for GEO 600. This gap has been filled by this work.

The most important topic treated in Chapter 1 is the control of a dual recycled interferometer, which includes the generation of error signals, the design of feedback loops and the study of lock acquisition. For this purpose, various mathematical models are presented that are used to simulate an interferometer. These models are then used to analyze the behaviour and the error signals of the 30 m prototype.

There are two main modes of operation in dual recycling, called 'broadband' and 'detuned'. In broadband operation, the maximal sensitivity extends from DC (0 Hz) to some corner frequency, whereas in detuned operation the maximal sensitivity is reached at an arbitrary user-selectable center frequency. Both these modes of operation have been realized in the 30 m prototype. The signal enhancement and its frequency response were in good agreement with theory. Another important effect of dual recycling, the contrast improvement by suppression of higher order transverse modes, was also observed in the experiment. The main results of the broadband experiment have recently been pulished as a letter [Heinzel98].

Inevitably many specialized electronic devices were needed in the experiment. Some were available from earlier experiments, but many were built by the author. A few circuits that might also be useful for other experiments are described in Appendix B. During this work the author has written a program (called 'Liso') that is helpful in designing electronic circuits. While a full description of the program was omitted in this work for space reasons, a short summary of its features and principles is given in Appendix C.

Keywords: Gravitational wave detector, Autoalignment, Dual Recycling.

Contents

Zusammenfassung **iii**

Abstract **v**

Table of Contents **vii**

List of Figures **xiii**

Acknowledgements **xix**

Glossary **xx**

1 Dual Recycling **1**

- 1.1 Introduction to recycling . . . 1
  - 1.1.1 Power recycling . . . 2
  - 1.1.2 Signal recycling and RSE . . . 3
  - 1.1.3 Detection of the signal by modulation methods . . . 6
- 1.2 Common techniques for modelling interferometers . . . 10
  - 1.2.1 Modulated light and sidebands . . . 10
    - 1.2.1.1 Phase modulation . . . 10
    - 1.2.1.2 Amplitude modulation . . . 12
    - 1.2.1.3 Frequency modulation . . . 12
  - 1.2.2 Description of mirrors and beamsplitters . . . 13
  - 1.2.3 Treatment of ‘lengths’ and ‘tunings’ . . . 15
- 1.3 Internal, external and Schnupp modulation . . . 16
  - 1.3.1 Internal modulation in the sideband picture . . . 16

1.3.2 External modulation 19
1.3.3 Schnupp modulation 23
1.4 Simulation tools 26
1.4.1 The interferometer model 26
1.4.2 Static response 28
1.4.3 Frequency response: An introduction 31
1.4.4 Simulating the effects of gravitational waves 33
1.4.5 Computation of the frequency response 34
1.4.6 Demodulation phase χ and reconstruction of the signal 37
1.4.6.1 Two mixers 38
1.4.6.2 One mixer 40
1.4.6.3 Loss in SNR by using only one mixer 42
1.5 Signal recycling: Frequency response 43
1.5.1 ‘Broadband’ and ‘detuned’ 43
1.5.2 Transfer function and signal-to-noise ratio 44
1.5.3 Signal sideband transfer function 45
1.5.4 Schnupp modulation sideband throughput 48
1.6 Control of signal recycling 52
1.6.1 PR cavity loop 53
1.6.1.1 Error signal 53
1.6.1.2 Actuator 57
1.6.1.3 Keeping the PR cavity resonant in the simulation . . . 61
1.6.2 Michelson control 62
1.6.2.1 Error signal without signal recycling 62
1.6.2.2 Error signal with dual recycling 65
1.6.2.3 Actuator and loop filter 68
1.6.3 SR mirror control 72
1.6.3.1 Error signal 72
1.6.3.2 Actuator and loop filter 74
1.6.4 Power recycling gain in dual recycling 76
1.7 Lock acquisition 77

1.7.1 Other stable states 79
1.8 Operation of dual recycling 82
1.8.1 Initial alignment and adjustments 82
1.8.2 Confirmation of dual recycling 84
1.8.3 Noise behaviour of the dual recycled prototype 85
1.9 Contrast improvement and ‘mode healing’ effect 87
1.10 Detuned signal recycling 91
1.10.1 Frequency response of detuned signal recycling 91
1.10.1.1 Signal transfer function 91
1.10.1.2 Schnupp sideband throughput 92
1.10.1.3 Transfer function of the interferometer 94
1.10.2 Control of detuned dual recycling 95
1.10.3 Experimental demonstration of detuned dual recycling 99
1.11 Must PR and SR cavity have different lengths? 106

2 Autoalignment **109**
2.1 Introduction 109
2.2 Misalignments in the mode picture 111
2.3 Detection of misalignments 114
2.3.1 Fabry-Perot cavity 114
2.3.2 Michelson interferometer 115
2.3.2.1 Schnupp modulation 115
2.3.2.2 External modulation 116
2.3.3 Mach-Zehnder alignment 117
2.4 Misalignments caused by individual components 118
2.4.1 PR cavity 118
2.4.2 Michelson interferometer 120
2.4.3 Mach-Zehnder alignment 120
2.5 Computation of lens systems 122
2.6 Experimental setup 124
2.6.1 Quadrant photodetectors 124

2.6.2 Auxiliary beam-steering loops . . . 125

2.7 Automatic alignment loops . . . 126

2.7.1 Actuators . . . 126

2.7.2 Loop filters . . . 127

2.7.3 Auxiliary signals for normalization . . . 129

2.7.4 Alignment loops for Michelson and PR cavity . . . 130

2.7.5 Spot positions on end mirrors . . . 131

2.7.6 Lock acquisition and error checking . . . 132

2.8 Noise spectra . . . 133

2.9 Dark fringe contrast . . . 135

2.10 Alignment error signals for GEO 600 . . . 136

2.10.1 Ray-tracing program . . . 136

2.10.2 The GEO 600 power recycling cavity . . . 136

2.10.3 The GEO 600 modecleaner cavities . . . 141

A The 30 m prototype 147

A.1 Construction . . . 147

A.2 Laser and associated optics . . . 148

A.3 Mirrors, suspensions and local controls . . . 151

A.3.1 Local controls . . . 154

A.4 Optical parameters of the 30 m prototype . . . 157

A.5 Calibration procedures . . . 159

A.5.1 Michelson calibration . . . 159

A.5.2 Frequency noise calibration . . . 164

A.5.3 Calibration of the autoalignment loops . . . 165

A.6 Measurement of the PR cavity length . . . 167

A.7 External modulation . . . 168

A.7.1 External modulation: control of the Mach-Zehnder phase ψ . . . 168

A.7.2 Experimental realization of the Mach-Zehnder control . . . 169

A.7.3 Experimental results of external modulation . . . 171

A.7.4 Conclusions about external modulation . . . 173

B Electronics **175**

B.1 Photodiode preamplifiers . . . 175

B.1.1 Broadband circuit . . . 176

B.1.2 Tuned circuit . . . 179

B.1.3 Combined circuit . . . 182

B.2 Resonant transformers for Pockels cells . . . 182

B.3 The automatic lock acquisition circuit . . . 186

B.4 Analog filter with $f^{+1/2}$ frequency response . . . 190

B.5 Analog filter with $f^{-1/2}$ frequency response . . . 193

C LISO **197**

C.1 Introduction . . . 197

C.2 Features and limitations . . . 198

C.3 Principles of operation . . . 200

C.3.1 Circuit simulation algorithm . . . 200

C.3.2 Noise calculations . . . 202

C.3.3 Op-amp stability calculations . . . 204

C.4 Fitting algorithms . . . 205

C.4.1 Optimizing the dynamic range . . . 206

D Two–mirror cavities **209**

D.1 Impedance–matched cavity . . . 211

D.2 Overcoupled cavity . . . 212

D.3 Approximations of the frequency response . . . 213

D.3.1 Resonant case . . . 213

D.3.2 Detuned case . . . 214

E Mathematica programs **217**

E.1 Simplified interferometer models . . . 217

E.1.1 Auxiliary functions . . . 217

E.1.2 Internal modulation . . . 218

E.1.3 External modulation . . . 219

E.1.4 Schnupp modulation 220

E.1.5 Autoalignment error signals 220

E.2 Full interferometer simulation 221

E.2.1 Static response example 221

E.2.2 Frequency response 222

E.2.3 Resonance of the PR cavity 223

E.2.4 Optimal demodulation phase 223

E.3 Ray-tracing program 224

Bibliography **233**

List of publications **238**

List of Figures

1.1 A Michelson interferometer in the dark fringe condition. 2
1.2 A Michelson interferometer with power recycling. 3
1.3 Phase modulation sidebands generated by a gravitational wave. 4
1.4 A Michelon interferometer with signal recycling. 6
1.5 The power at the output of a Michelson interferometer. 7
1.6 Sinusoidal modulation of the phase difference. 8
1.7 Output power with a sinusoidal modulation of the phase difference. 8
1.8 Resulting signal of the modulation–demodulation technique. 9
1.9 Spectrum of a frequency modulated signal. 13
1.10 Amplitudes at a mirror. 14
1.11 Amplitudes at a beamsplitter. 14
1.12 A Michelson interferometer with internal modulation. 17
1.13 Schematic diagram of external modulation. 20
1.14 External modulation with a recombination plate. 21
1.15 Detailed view of the recombination plate. 21
1.16 A simple Michelson interferometer employing Schnupp modulation. 24
1.17 The dual recyling interferometer simulated by Jun's program. 27
1.18 Simulation of power recycling in the 30 m prototype. 30
1.19 Frequency response of the Michelson error signal. 32
1.20 The nine light frequencies involved in computing the requency response. . . . 34
1.21 The amplitudes used to compute the frequency response. 36
1.22 Amplitude transfer function in broadband signal recycling. 46
1.23 Signal gain obtainable in the 30 m prototype by signal recycling. 47

1.24 A Michelson interferometer with an armlength difference ΔL. 49
1.25 An interferometer with armlength difference ΔL. 50
1.26 Throughput of Schnupp modulation sidebands in the 30 m prototype. 50
1.27 Throughput near the 20th free spectral ranges. 51
1.28 An electrical model of coupled resonators. 52
1.29 Longitudinal control loops for dual recycling in the 30 m prototype. 54
1.30 PR cavity error signal at the normal operating point. 55
1.31 PR cavity error signal at six random operating points. 56
1.32 Frequency response of the AOM. 58
1.33 Estimated frequency noise of the prestabilized laser. 60
1.34 Frequency noise with first and second loop in operation. 60
1.35 The PR cavity tuning φ_{PR} that makes the PR cavity resonant. 62
1.36 Throughput of the upper Schnupp sideband without signal recycling. 63
1.37 Michelson error signal and PR cavity power buildup without signal recycling. . 64
1.38 Throughput of the upper Schnupp sideband with dual recycling. 66
1.39 Michelson error signal as a function of the tunings φ_{MI} and φ_{SR}. 67
1.40 The gain of the Michelson error signal. 69
1.41 The DC (average) light power arriving at the photodetector. 70
1.42 The signal-to-noise ratio of the Michelson error signal. 71
1.43 Open loop gain of the Michelson dark fringe lock. 72
1.44 SR error signal as a function of the tunings φ_{MI} and φ_{SR}. 75
1.45 Frequency response of the SR error signal. 76
1.46 Open-loop gain of the SR mirror control loop. 76
1.47 Power buildup in the PR cavity. 78
1.48 Some lock acquisition transients of the dual-recycled 30 m prototype. 80
1.49 Detail of the lock acquisition transient. 81
1.50 One of the other stable states of the dual recycled 30 m inteferometer. 82
1.51 Noise spectrum of the dual recycled 30 m prototype. 85
1.52 Suppression of higher order transversal modes. 89
1.53 The shape of the beam leaving the interferometer. 90
1.54 Amplitude transfer function in detuned signal recycling. 92

1.55 Schnupp sideband throughput in detuned dual recycling. 93
1.56 Normalized transfer functions for detuned dual recycling. 94
1.57 Error signals for detuned dual recycling. 96
1.58 Error signals for a modulation frequency near 97 MHz. 99
1.59 SR error signals as a function of the demodulation phase χ_{SR}. 100
1.60 Transfer function of the end mirror M_1 driven by coil-magnet actuators. . . . 101
1.61 Experimental results for detuned dual recycling. 102
1.62 Computed error signals for detuned dual recycling. 104
1.63 Further experimental results of detuned dual recycling. 105
1.64 Error signals for equal lengths of PR- and SR-cavity. 107

2.1 A misaligned interferometer. 110
2.2 Two types of misalignments of the PR cavity. 119
2.3 Misalignment of the Michelson interferometer. 121
2.4 Parallel shifts between the two beams in the Mach-Zehnder interferometer. . . 121
2.5 Scheme of the lens system used to introduce additional Guoy phase shift. . . . 122
2.6 RF signal paths in the quadrant detector. 125
2.7 Low frequency signal paths in the quadrant detector. 126
2.8 Mirror transfer function (‘tilt’ input). 127
2.9 Open-loop gain of the Michelson alignment loop. 129
2.10 Open-loop gain curve of the end mirror common mode alignment loop. 130
2.11 Noise spectrum of one channel of the Michelson alignment loop. 133
2.12 Contrast improvement by autoalignment. 135
2.13 Schematic diagram of the GEO 600 PR cavity seen from the side. 137
2.14 Misorientation of M_{PR} in the GEO 600 PR cavity. 138
2.15 Misorientation of M_N in the GEO 600 PR cavity. 139
2.16 Misorientation of M_F in the GEO 600 PR cavity. 139
2.17 Interference structure on the far mirror M_F of the GEO PR cavity. 140
2.18 Schematic diagram of a GEO 600 modecleaner cavity seen from above. 141
2.19 Modecleaner with misoriented input mirror. 142
2.20 Modecleaner with misorientation of α_+. 145

2.21 Modecleaner with misorientation of β_-. 146

A.1 Schematic diagram of the first loop. 150
A.2 Schematic picture of the central tank (in the external modulation setup). . . 152
A.3 Sketch of a double pendulum. 153
A.4 The four degrees of freedom of a single-stage pendulum. 154
A.5 Location of the four sensors/actuators of each local control channel. 155
A.6 Schematic picture of a 'Shadow-sensor'. 156
A.7 Optical parameters of the 30 m prototype 158
A.8 Schematic of the circuit used for the Michelson calibration ('mid-fringe lock'). 161
A.9 Output signal of the 'mid-fringe lock' circuit shown in Figure A.8. 162
A.10 A typical output spectrum of the dual recycled interferometer. 163
A.11 Calibration of the frequency noise measurement. 164
A.12 Frequency noise of the laser light with respect to the power recycling cavity. . 165
A.13 Simple loop model used for the calibration of the autoalignment system. . . . 166
A.14 Resonance of the PR cavity at its first FSR. 168
A.15 Overview of the 30 m prototype with external modulation. 170
A.16 Generation of the Mach-Zehnder error signal ψ. 172
A.17 Sensitivity of the Garching 30 m prototype with external modulation. 173

B.1 Basic circuit of a broadband photodiode preamplifier. 176
B.2 Simplest model of the open-loop gain of an op-amp. 177
B.3 Basic circuit of a tuned photodiode preamplifier. 179
B.4 Impedance of the parallel resonant circuit shown in Figure B.3. 180
B.5 Measurement of the increased output noise of a tuned photodiode preamplifier. 182
B.6 Combined photodiode preamplifier. 183
B.7 Resonant transformer to drive a Pockels cell. 184
B.8 Current through the 1 Ω resistor in Figure B.7. 185
B.9 Alternative resonant transformer circuit with an autotransformer. 185
B.10 Alternative resonant transformer circuit with a capacitive voltage divider. . . . 186
B.11 Input impedance of the alternative resonant transformer circuit. 186
B.12 Sketch of important signals in the automatic lock acquisition circuit. 187

B.13 The main part of the circuit diagram of the automatic lock acquisition circuit. 189
B.14 Straight-line approximation of the frequency response for the $f^{+1/2}$ filter. 190
B.15 Computed exact frequency response of the $f^{+1/2}$ filter. 191
B.16 Frequency response of resonant systems together with the $f^{+1/2}$ filter. 192
B.17 Circuit diagram of the $f^{+1/2}$ filter. 192
B.18 Straight-line approxmation of the frequency response for the $f^{-1/2}$ filter. 193
B.19 Computed exact frequency response of the $f^{-1/2}$ filter 194
B.20 Circuit diagram of the $f^{-1/2}$ filter 194

C.1 Example of a low-pass filter with nodes and currents shown. 201
C.2 Noise model of an op-amp. 203
C.3 How the stability function of an op-amp is computed. 204

D.1 Model of a two–mirrror cavity. 209
D.2 Approximation of the resonance factor d by a two-pole low-pass filter. 215
D.3 The approximation of Figure D.2 in a wider frequency range. 215

Acknowledgements

This work is a combination and continuation of previous works by many people. I would especially like to thank the following people (more or less in chronological order, and far from complete): K. Danzmann for introducing me to the subject and for his continuous unconditional support, and for being the best 'boss' I could ever imagine, H. Lück for introducing me to Garching, J. Mizuno for teaching me many of the things presented in this work and for his program, R. Schilling, A. Rüdiger and W. Winkler for letting me participate in their unique working group (and each of them for many more things too numerous to mention here), H. Klein, H. Emme and A. Weidner for their fantastic technical support, K. Strain for his essential contributions to this work, B. Willke, K. Skeldon, A. Freise and H. Grote for their important contributions to this work.

Clearly computers have played an important role in the preparation of this work. My father Günther Heinzel taught me the essentials of scientific computer usage. I would like to express my gratitude to the international community of programmers who make available free software. In particular, LaTeX, Linux, gcc/egcs and Gnuplot have had an essential role in this work.

I would like to thank A. Rüdiger, R. Schilling, W. Winkler, K. Strain, J. Mizuno, H. Grote and in particular K. Skeldon for proof-reading and improving various parts of the manuscript. Of course, all remaining errors are my own responsibility.

Glossary

Some commonly used terms, abbreviations and symbols are listed here with a short description of their usual meaning in this work.

AM: amplitude modulation.

AOM: an acousto-optic modulator (used to shift the frequency of a light beam).

autoalignment: the automatic beam alignment system of the prototype, subject of Chapter 2.

beam injector: the last component determining the position and angle of the beam hitting the PR mirror.

broadband: the state of a signal recycled interferometer when the the SR cavity is resonant for the carrier frequency (see Section 1.5.1).

BS: a beamsplitter, usually **the** main beamsplitter of a Michelson interferometer.

camera: term used in Garching for a photodiode in an assembly together with preamplifiers etc.

CCD: charge-coupled device, used in a videocamera.

contrast: defined in Section 1.9.

DC: the average of a fluctuating signal; also used to indicate the limit of some function for low frequencies.

detuned: the state of a signal recycled interferometer when the carrier frequency is *not* resonant in the SR cavity (see Section 1.5.1).

DR: dual recycling (i.e. the combination of power and signal recycling).

EOM: an electro-optic modulator (used for modulating or shifting the phase of a light beam); see also ‘Pockels cell’.

first loop: the loop that locks the laser frequency to the reference cavity for frequency prestabilization (see Sections 1.6.1.2 and A.2).

FPZT: the fast piezo in the laser (see Section A.2).

FSR: the Free Spectral Range of a cavity (see Appendix D).

FWHM: the Full Width at Half Maximum of a cavity (see Appendix D).

KDP: ‘Kaliumdihydrogenphosphat’, potassium dihydrogen phosphate (KH_2PO_4), hygroscopic material used for Pockels cell crystals (see, e.g., [Yariv]).

KD*P: KDP with the hydrogen atoms replaced by deuterium (KD_2PO_4), hygroscopic material used for Pockels cell crystals (see, e.g., [Yariv]).

local control: the feedback system installed for each suspended mirror that damps the pendulum resonances and allows to feed in control signals (see Section A.3.1).

longitudinal: in the direction of the beam axis.

LISO: a program for 'Linear Simulation and Optimization' of analog electronic circuits (see Appendix C).

M: a mirror.

$M_1 = M_E$ and

$M_2 = M_N$: the two end mirrors.

$M_{PR} = M_W$: the power recycling mirror.

$M_{SR} = M_S$: the signal recycling mirror.

Michelson: the Michelson interferometer formed by the beamsplitter BS and the two end mirrors M_1 and M_2, often used to specifically indicate this part of a more complex interferometer.

Mix: an electronic mixer (for low frequencies, usually an analog multiplier; for radio frequencies, a double-balanced diode mixer).

N,E,W,S: directions seen from the beamsplitter, see Figure 1.2 (used in this order in Jun's program).

op-amp: an operational amplifier.

PD: a photodetector (usually a photodiode).

Piezo: a piezo-electric transducer, used to control the microscopic position of a mirror; see also 'PZT'.

Pockels cell: used as synonym for EOM.

PR: Power recycling.

PZT: originally 'Lead Zirconate Titanate', $Pb\,(Zr_{0.52}Ti_{0.48})\,O_3$, a piezoelectric material; often 'PZT' is used as a synonym for a piezo-electric transducer.

rotation: a movement of a suspended component that causes a *horizontal* movement of the affected beam (cf. 'translation' and 'tilt').

RF: radio frequency (in the prototype usually around 10 MHz).

rms: root mean square.

second loop: the loop that locks the prestabilized laser frequency to a resonance of the PR cavity (via the first loop, see Section 1.6.1.2).

SNR: signal-to-noise ratio.

SPZT: the slow piezo in the laser (see Section A.2).

SR: Signal recycling.

throughput: the coupling efficiency of the Schnupp modulation sidebands from their place of generation (EOM) to the main output.

tilt: a movement of a suspended component that causes a *vertical* movement of the affected beam (cf. 'rotation' and 'translation').

translation: a longitudinal movement of a suspended component (cf. 'rotation' and 'tilt').

tuning: the microscopic position of a mirror that determines the resonance condition of an interferometer (see Setion 1.2.3).

VCO: a voltage-controlled oscillator (driving the AOM).

$\mathcal{A}$: the total power loss of a mirror or beamsplitter, $\mathcal{A} = 1 - \rho^2 - \tau^2$.

a, b: amplitudes of various light beams in models.

c: the speed of light in vacuum, 299792458 m/s.

C: a capacitor, also used for its capacitance (in Farad).

d: the 'resonance factor' of a cavity (see Equation (D.5)).

E: the electric field.

f: a frequency with the unit Hz.

f_{det}: the frequency of the sensitivity peak in detuned dual recycling (see Section 1.10).

$f_{\mathrm{m}}, \omega_{\mathrm{m}}$: the modulation frequency for Schnupp modulation or external modulation.

$f_{\mathrm{sig}}, \omega_{\mathrm{sig}}$: signal frequency (of gravitational waves or test signals).

$\mathcal{F}$: the finesse of a cavity, $\mathcal{F}$=FSR/FWHM (see Appendix D).

G: the 'frequency response' of the interferometer (see Sections 1.4.3 and 1.4.5).

G_{n}: normalized frequency response (see Equation (1.85)).

H: the 'static response' of the interferometer (see Section 1.4.2).

$H_i(x)$: in Chapter 2, the Hermite polynomials.

h: the strain in space caused by a gravitational wave (see Section 1.4.4).

I: a current, in particular a photocurrent.

i: $\sqrt{-1}$.

$J_0, J_1, \ldots$ the Bessel functions of the first kind (see Section 1.2.1.1).

k: the magnitude of the wave vector of a light beam, $k = \omega/c$, also used for an offset to the carrier wavenumber (see Section 1.2.3).

L: a physical armlength or distance in the interferometer (see also the footnote on page 33); also an inductor or its inductance (in Henry).

m: modulation index (in radians) of a modulation, usually a phase modulation (see Section 1.2.1.1).

N: the number of 'folds' of the beam in a delay-line system ($N = 2$ in GEO 600).

n: the index of a higher order transversal mode (see Section 1.9); also the index of refraction; also the noise amplitude in Section 1.4.6.

p: the microscopic pathlength difference between the two Michelson arms, used in the calibration (see Section A.5.1), $p = \Delta\varphi\,\lambda/(2\pi)$.

Q: the quality factor of a resonant system.

q: a complex parameter describing a Gaussian beam (see Section 2.5).

R: a radius of curvature (of a mirror or wavefront); also a resistor or its resistance (in Ohms).

U: a voltage.

u_0, u_1: modal functions describing the transverse structure of a laser beam (see Section 2.2).

V: longitudinal output signal from a quadrant photodetector (see Section 2.3).

W: alignment output signal from a quadrant photodetector (see Section 2.3).

w: the radius (half-width) of a laser beam (see Section 2.2).

w_0: the radius of a laser beam at its waist.

x, y, z: the three spatial dimensions, with z usually indicating the beam axis or the direction of propagation.

Z: an impedance (usually complex).

z_R: the Rayleigh range of a laser beam ($\lambda z_\mathrm{R} = \pi w_0^2$, see Section 2.2).

α: the angle by which a component is misaligned (see Section 2.2).

β: the angle between the axes of a misaligned beam and its reference in Section 2.2; also used as the angle corresponding to α in the other dimension in section 2.10.3.

γ: the angle between two wavefronts (see Section 2.2).

δ: the angle corresponding to γ in the other dimension in section 2.10.3.

ΔL: the (small) difference between the lengths of the two long arms used in Schnupp modulation.

$\Delta\varphi$: the phase difference between the two interfering beams in a Michelson interferometer.

η: the Guoy phase shift.

θ: an angle describing the ‘character’ of a misalignment (see Section 2.2).

θ^{w}: an angle describing the ‘character’ of a misalignment at the beam waist (see Section 2.2).

θ^{d}: an angle describing the ‘character’ of a misalignment at a detector (see Section 2.2).

κ: the ‘amount’ of a misalignment (see Section 2.2).

λ: the wavelength of the light, 514 nm in the prototype (1064 nm in GEO 600).

ρ: the amplitude reflectivity of a mirror or beamsplitter.

τ: the amplitude transmittance of a mirror or beamsplitter.

Φ: the combined Guoy phase shift of a combination of lenses and sections of free space (see Sections 2.2 and 2.5).

φ: a tuning (i.e. microscopic position of one or several mirrors) of one degree of freedom of the interferometer (see Sections 1.2.3 and 1.4).

φ_{MI}: the Michelson tuning, implemented in the models as $\varphi_{\mathrm{N}} = -\frac{1}{2}\varphi_{\mathrm{MI}}, \varphi_{\mathrm{E}} = \frac{1}{2}\varphi_{\mathrm{MI}}$.

φ_{PR}: the tuning of the power recycling mirror (which determines whether the incoming light is resonant in the interferometer).

φ_{SR}: the tuning of the signal recycling mirror (which has no influence at a perfect dark fringe, but influences the gain and frequency response in dual recycling).

χ: the demodulation phase of a mixer, experimentally implemented with a phase-shifter in the local oscillator line (see Sections 1.4.2 and 1.4.6).

ψ: the phase between signal beam and local oscillator beam in external modulation, also called the ‘Mach-Zehnder phase’.

ω: an angular frequency $\omega = 2\pi f$ with the unit rad/s.

$\Re\{z\}$: the real part of the complex number z.

$\Im\{z\}$: the imaginary part of the complex number z.

$\tilde{x}$: the linear spectral density of x, with the unit of x divided by $\sqrt{\mathrm{Hz}}$.

Chapter 1

Dual Recycling

1.1 Introduction to recycling

In a laser-interferometric gravitational wave detector, the sensitivity fundamentally depends on two parameters of the system: The amount of light energy stored in the arms and the storage time of the gravitational wave-induced optical signal in the arms. These can be changed by implementing the techniques of *power recycling* and *signal recycling*, respectively. The combination of signal recycling and power recycling is called *dual recycling*.

The two recycling techniques will be discussed in the following pages, starting with simple models which will later be refined, as and when necessary.

In all currently operated prototype interferometers and proposed large-scale detectors, the detection system is based on a Michelson interferometer operated in the dark fringe condition. The term 'Michelson interferometer' in this work is intended to represent the combination of a beamsplitter and suspended mirrors at the end of two long orthogonal arms. The directions North, East, West and South, as shown in Figures 1.1 and 1.2 will be used throughout to identify directions as seen from the beamsplitter. 'North' and 'East' represent the long arms; the light from the laser is injected from the 'West', and 'South' represents the detection port.

In the dark fringe condition, all light incident on the beamsplitter will be reflected back to where it came from, as shown in Figure 1.1. This is true for light coming from either the West or the South directions in Figure 1.1. This model is simplified in that it neglects various operational factors, for example:

- The inevitable optical losses in the arms will limit the amount of reflected light to a fraction less than unity.
- Any asymmetry between the arms and in particular, any deviation of the end mirrors from their ideal shape, will limit the contrast of the Michelson. In other words, a certain fraction of the light from each arm will find no component from

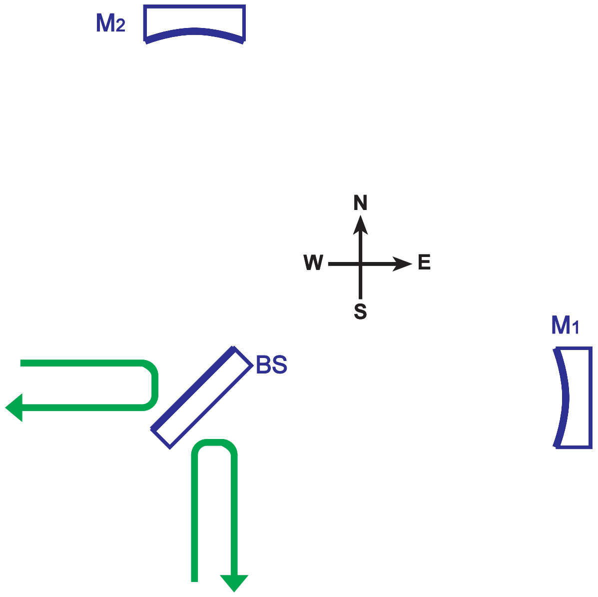

Figure 1.1: A Michelson interferometer in the dark fringe condition will essentially look like a mirror from both ports.

the other arm with which to destructively interfere, and will thus appear at the 'other' port (South or West, if the light was injected from West or South, respectively).

- Finally this simple model does not hold for the Schnupp modulation sidebands (see Section 1.5.4).

In spite of these limitations, the simple model is useful to illustrate the principles of recycling.

1.1.1 Power recycling

If all other parameters remain constant, the shot-noise limited sensitivity of the detector will improve in proportion to the square root of the light power in the arms. All planned detectors will use *power recycling* to increase this power. As seen from the laser, the Michelson in the dark fringe state will look like a highly reflective mirror for the incident light. By placing another mirror, the *power recycling mirror* $\mathrm{M_{PR}}$, between the laser and Michelson, a Fabry–Perot cavity is formed, the *power recycling cavity (PR cavity*, see Figure 1.2). This cavity must be kept resonant with the laser light, usually using the Pound-Drever-Hall scheme [Drever83b].

If the relative power losses of the Michelson interferometer for the light have a given value $\mathcal{A}$ (usually they will be minimized as far as technically possible, e.g. $\mathcal{A} = 1000\,\mathrm{ppm}$

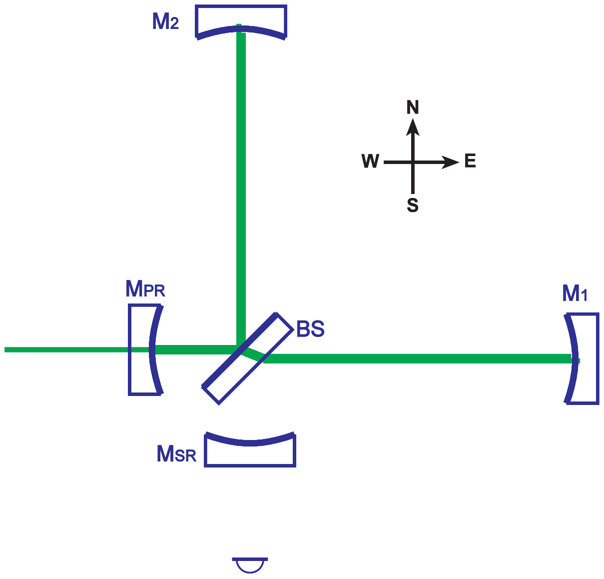

Figure 1.2: Power recycling resonantly enhances the light power circulating in the arms. The directions North, East, West and South, as shown above, will be used throughout this work to identify directions as seen from the beamsplitter.

in power), then the optimal transmission of M_{PR} should also be[1] $\mathcal{A}$; this is the 'impedance-matched' case. The power buildup in the cavity is then given by $1/\mathcal{A}$ (see Appendix D).

In the GEO 600 setup, which has no cavities in the arms, there is an important limitation to the power in the arms: All power must pass through the beamsplitter substrate. Although materials with extremely low absorption loss (a few ppm/cm at 1064 nm) have been developed, there is still a non-negligible amount of power absorbed in the beamsplitter, which will cause a thermal lens effect with various associated problems.

Power recycling is a well-established concept which is discussed in various publications (see, e.g., [Drever83c, Drever83d, Schilling:PR, Schnier97]). This work will concentrate on the experimental realization of this technique in the Garching 30 m prototype.

1.1.2 Signal recycling and RSE

The second fundamental parameter influencing the sensitivity of the detector is the interaction time of the gravitational wave with the light.

One way to describe the effect of a gravitational wave is to say that it induces a phase modulation on light travelling in a given direction in the arms (with respect to the propagation of the gravitational wave, see also Section 1.4.4). The effect is the same as if the index of refraction of the traversed medium were to be modulated. Consequently

---

[1] This is true if the losses of M_{PR} itself are negligible to the losses $\mathcal{A}$ in the rest of the interferometer.

modulation sidebands appear on the light (see Section 1.2.1.1 below), and the light can now be regarded as consisting of a high power carrier with much weaker sidebands imposed by the gravitational wave.

For this simplified discussion, we assume optimal orientation of the Michelson and polarization of the gravitational waves.

Due to the quadrupole nature of the gravitational waves, the modulation sidebands are generated with opposite sign in the two arms, and upon their first encounter with the beamsplitter they interfere constructively towards the South port.

In the absence of any signal recycling, the modulation sidebands produced by the gravitational wave immediately leave the interferometer (see Figure 1.3).

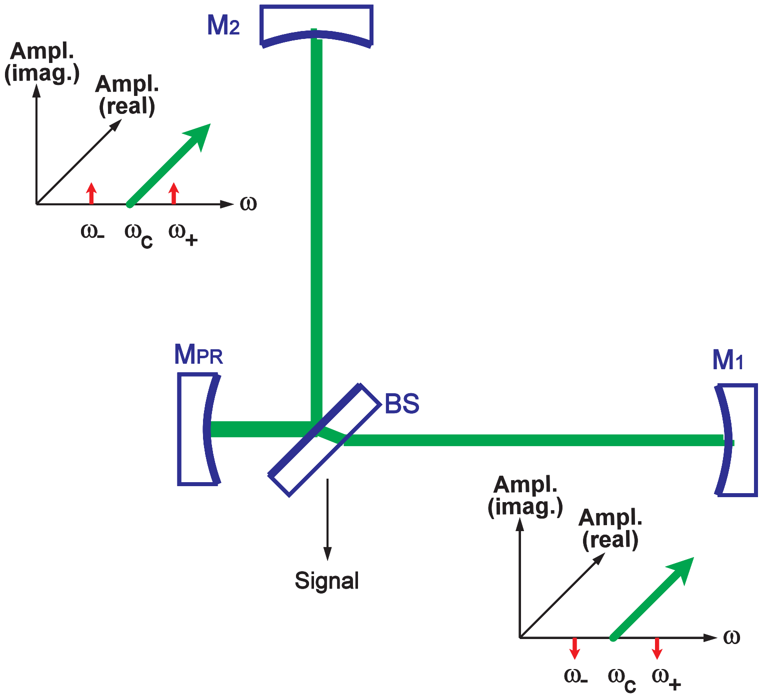

Figure 1.3: A gravitational wave produces phase modulation sidebands of opposite sign in the two arms. They are separated from the carrier by the beamsplitter.

Their interaction time with the gravitational wave is thus given by the round-trip travel time in the arms, $2L/c$. For a signal frequency of 1000 Hz, the optimal armlength would be in the order of 100 km — impossible to realize on Earth.

The interaction time can be increased by the use of (non–resonant) optical multi-reflection delay lines ('Herriot delay lines') in the arms; this was studied in detail at Garching [Winkler]. Two main problems were identified: The mirror size becomes very large (and thus very hard to manufacture with the necessary high quality), and stray light produces spurious signals that can even be resonantly stored in the arm and will cause excess noise. Because of these results, Herriot delay lines are currently not considered a realistic approach for large-scale gravitational wave detectors. However, GEO 600 will use the simplest form of a delay line ('DL4')[2] to double the effective armlength.

At this point there are two ways to increase the signal storage time: By the use of Fabry-Perot cavities in the long arms, or alternatively by implementing signal recycling. Both of these approaches have their merits and problems.

With the exception of GEO 600, all other projects (LIGO, VIRGO, TAMA) have chosen a basic configuration with cavities in the arms. These require a more complex control scheme, since the cavities must also be kept resonant. An advantage is that most of the power appears only inside the arm cavities and never needs to pass through the beamsplitter (or any other substrate), such that the thermal lensing problems in the substrates are reduced. However, thermal lensing can and will also appear due to absorption in the mirror coatings.

The present 'first generation' concepts for LIGO, VIRGO and TAMA do not plan to use any mirror in the south port. Then the signal storage time is given by the length and finesse of the arm cavities and cannot easily be changed. More flexibility can be obtained by placing an additional mirror in the south port. This configuration is called either 'signal recycling' or 'resonant sideband extraction', depending on the microscopic position ('tuning') of the additional mirror. The effect can either be to increase the signal storage time (as in signal recycling) or decrease it (as in resonant sideband extraction, which is useful only with arm cavities). In fact these two cases are only the endpoints of a continuum of possible tunings, with the intermediate points called 'detuned'. These detuned cases may also be useful and cannot easily be classified as either 'resonant sideband extraction' or 'signal recycling'.

Resonant sideband extraction is an interesting configuration for interferometers with arm cavities. It allows the use of high-finesse cavities in the arms, with a bandwidth optimized for maximal light energy stored in the arms. The signal storage time, which is then usually too large, can be reduced independently of the carrier storage time. Resonant sideband extraction was first proposed and demonstrated in a table-top model by the Garching group [Mizuno93, MPQ203, Heinzel95, Heinzel96]. It is now seriously considered for the second generation of the LIGO interferometers.

Interferometers with arm cavities are not considered in the remainder of this work.

In the Michelson without arm cavities, the signal storage time can be increased with a signal recycling mirror (M_{SR} in Figure 1.4). This configuration was chosen for GEO 600 and investigated in the 30 m prototype and is the subject of this work. Signal recycling and dual recycling were first proposed and demonstrated by the Glasgow group around ten years ago [Meers88, Meers89, Strain91].

The partially reflecting signal recycling mirror M_{SR} reflects the signal sidebands back into the interferometer. Again, the Michelson looks like a mirror and reflects the signal sidebands back towards M_{SR} after each roundtrip in the arms. A cavity is formed for the

---

[2] The notation means that the *roundtrip* path length is four times the physical armlength. This is achieved with an extra 'near' mirror and is *not* a Herriot delay line.

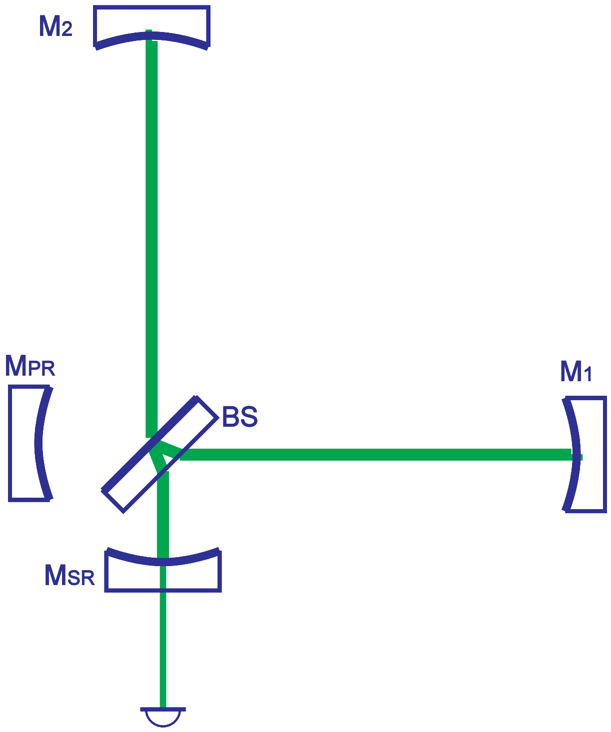

Figure 1.4: The signal sidebands can be resonantly enhanced in the signal recycling cavity, thus increasing the signal storage time.

signal sidebands, the *signal recycling cavity (SR cavity)*. We assume the macroscopic armlength to be fixed by the construction. The finesse of the SR cavity (and hence the signal storage time) can be chosen independently of the carrier storage time, which is determined by the PR cavity finesse. This gives great flexibility in the design of the detector. Of course, M_{SR} must be controlled by appropriate servo loops to reach and maintain its desired position.

The following citation from K. Strain [Strain91] is still applicable to this work: *"Note the rather counterintuitive nature of this system: The signal is enhanced by placing a mirror in front of the photodetector. This is all the more motivation for an experimental demonstration."*

1.1.3 Detection of the signal by modulation methods

Before we can enter a more quantitative discussion of dual recycling, the detection of the signal must be discussed. In a simple Michelson interferometer without any modulation scheme, the power at the output port near the dark fringe depends nearly quadratically[3] upon the phase difference $\Delta\varphi$ between the two interfering beams (see

---

[3] In a perfect Michelson with no recycling, the exact dependence would have the form $\sin^2(\Delta\varphi/2)$.

Figure 1.5). For this discussion, we again assume a Michelson interferometer with perfect contrast.

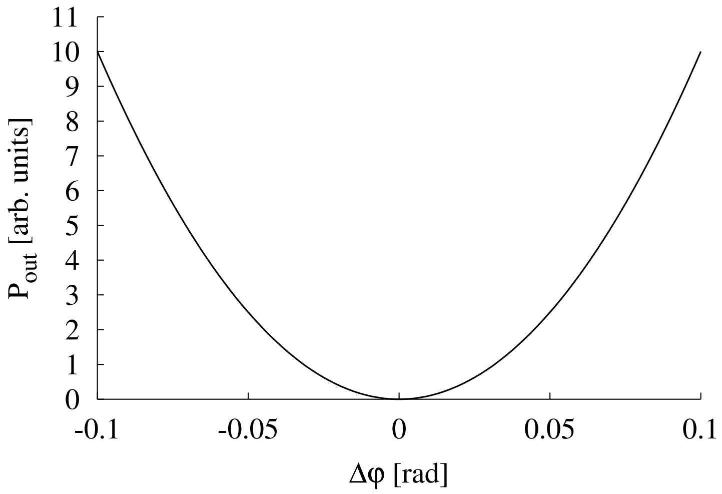

Figure 1.5: Near the dark fringe, the power in the output beam depends nearly quadratically on the phase difference $\Delta\varphi$.

The aim is to extract information about $\Delta\varphi$ from the power at the output port. For various reasons (most importantly, maximal power buildup in the PR cavity), the dark fringe is chosen as operating point. If we try to use the power at the output port to directly measure $\Delta\varphi$ then we lose the sign and have infinitesimally small slope at the precise operating pount.

The problem can be solved by using a modulation scheme for the readout[4]. Because we want to read out optical phase, an optical phase modulation technique is appropriate. It is applied in one of three possible ways discussed below.

Easiest to understand is the 'internal modulation' where the phase difference $\Delta\varphi$ is directly modulated (e.g. by an oscillatory small motion of one or both mirrors or else by an electro-optic modulator in one or both arms). This situation is shown in Figure 1.6. For illustrative purposes, three different operating points a, b and c are shown with phase differences of $\Delta\varphi = -0.06\,\mathrm{rad}$, $0\,\mathrm{rad}$ and $0.04\,\mathrm{rad}$ respectively.

The detected power will in general contain a component at the modulation frequency (see Figure 1.7). The amplitude of this component will be proportional to the phase difference $\Delta\varphi$ which we ultimately want to measure. The detected power also contains components at DC and at twice the modulation frequency, which we ignore for the present discussion.

The signal can finally be extracted by 'coherent demodulation' with the modulation

---

[4] There are also other benefits of a modulation method, in particular the measurement of light power can be 'shifted' from the (low) signal frequencies to the much higher modulation frequency, where there is less technical noise.

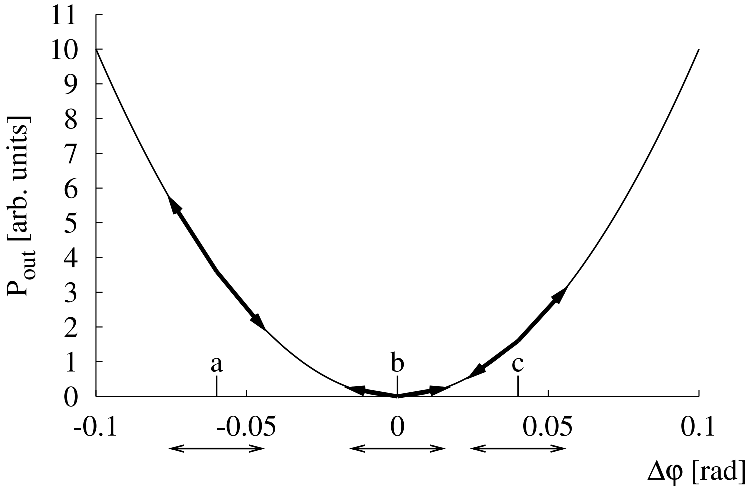

Figure 1.6: When the phase difference is modulated periodically, the output power will change in the rhythm of the modulation. Three different operating points a, b and c are shown.

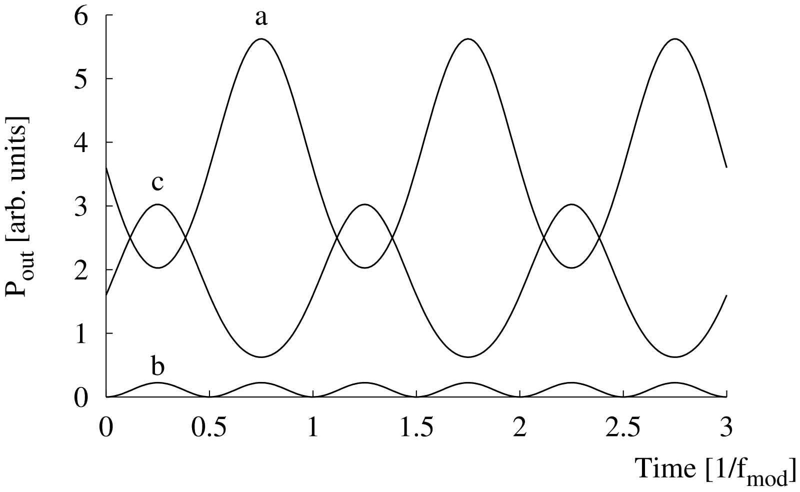

Figure 1.7: The detected power will in general contain a component at the modulation frequency with an amplitude proportional to the phase difference $\Delta\varphi$. The curves labelled a, b and c refer to the three operating points shown in Figure 1.6.

frequency (i.e. multiplication with a copy of the original oscillator signal, usually after removing the DC component from the power signal by band-pass filtering). After the demodulation there will be a DC component, which corresponds to our desired signal (see Figure 1.8). Furthermore there will be some components at the modulation frequency and twice the modulation frequency, which can be removed by low-pass filtering. Finally we obtain the signal as a voltage that is proportional to the phase difference $\Delta\varphi$, and hence preserves the sign of $\Delta\varphi$.

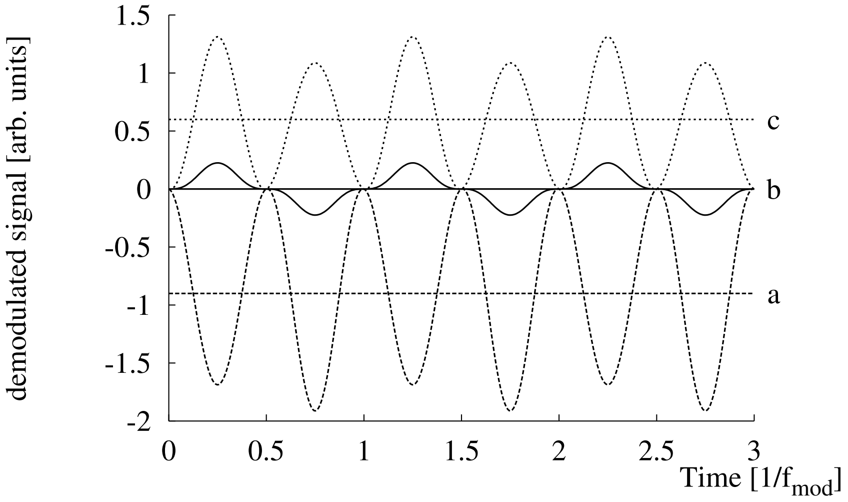

Figure 1.8: The signal is recovered by removing the DC component of the detected power, multiplying with the local oscillator (‘coherent demodulation’) and low-pass filtering. The resulting averaged signal is indicated by the horizontal lines.

It can generally be shown (by Taylor expansion) that this modulation–demodulation technique with small modulation index yields the derivative of the measured parameter with respect to the modulated parameter. In our case, the output signal is the derivative of the power at the detection port with respect to the phase difference $\Delta\varphi$. In this way the quadratic relationship is transformed into a linear relationship.

Related modulation–demodulation techniques are very widespread in experimental physics and are also known as ‘lock-in detection’, for example see [Horowitz–Hill, Chapter 15].

The straightforward application of this modulation–demodulation technique to a Michelson interferometer is called *internal modulation*. In this technique (which was used in the Garching prototype in its first years) the phase difference $\Delta\varphi$ is modulated directly, either by dithering one end mirror or else by placing an electro-optic modulator (EOM) in one or both arms. The detection of the photocurrent now takes place at the modulation frequency instead of at the signal frequency. Because lasers tend to have high levels of technical noise in the region of the gravitational wave signal frequencies, the modulation frequency is usually chosen to be several MHz. This eliminates the possibility of dithering an end mirror and leaves the EOM as the only practical modulator. If power recycling is implemented, all light power would have to pass through the EOM. As we have seen, even the ultra-low loss material of the beamsplitter will already cause problems by absorption, when it is traversed by the high-power beam. This is even more significant for the EOM, which will have much higher absorption. Hence the technique of internal modulation is not suitable for high-power interferometers.

Instead we will consider related but slighty more complicated modulation techniques. Two important alternatives are *external modulation* and *Schnupp modulation*, and these will be described in Sections 1.3.2 and 1.3.3.

1.2 Common techniques for modelling interferometers

In the following Sections mathematical models for interferometers of varying complexity will be used. Some common aspects of these models are treated here.

1.2.1 Modulated light and sidebands

Phase modulation of a light beam will appear in two important contexts in this work: The intentional phase modulation at a radio frequency produced by a Pockels cell, and the tiny phase modulation of the light in the arms caused by a passing gravitational wave. Both these effects can be described by *sidebands*, which are introduced in this section.

1.2.1.1 Phase modulation

We write the electrical field of the unmodulated laser beam at a fixed point in space in the scalar representation

$$E(t) = E_0 \exp(\mathrm{i}\,\omega_0 t)\,. \tag{1.1}$$

Phase modulation with the angular frequency $\omega_{\mathrm{m}} = 2\pi\, f_{\mathrm{m}}$ and the modulation depth (‘modulation index’) m yields

$$\begin{aligned} E_{\mathrm{m}}(t) &= E_0 \exp[\mathrm{i}\,(\omega_0 t + m\cos\omega_{\mathrm{m}} t)] \\ &= E_0 \exp(\mathrm{i}\,\omega_0 t)\exp(\mathrm{i}\,m\cos\omega_{\mathrm{m}} t). \end{aligned} \tag{1.2}$$

Using the identity [Gradstein-Ryshik, Vol. 2, No. 8.511]

$$\exp(\mathrm{i}\;m\cos\alpha) = \sum_{k=-\infty}^{\infty} \mathrm{i}^{\,k} J_k(m)\exp(\mathrm{i}\;k\,\alpha) = J_0(m) + 2\sum_{k=1}^{\infty} \mathrm{i}^{\,k} J_k(m)\cos(k\,\alpha) \tag{1.3}$$

we find for the amplitude of the modulated light

$$E_{\mathrm{m}}(t) = E_0 \exp(\mathrm{i}\,\omega_0 t)\sum_{k=-\infty}^{\infty} \mathrm{i}^{\,k} J_k(m)\exp(\mathrm{i}\;k\omega_{\mathrm{m}} t). \tag{1.4}$$

Here the $J_k(x)$ are the Bessel functions of the first kind of order k. The first terms of their Taylor series are:

$$J_0(x) = 1 - \frac{x^2}{4} + \mathcal{O}(x^4) \tag{1.5}$$

$$J_1(x) = \frac{x}{2} - \frac{x^3}{16} + \mathcal{O}(x^5) \tag{1.6}$$

$$J_2(x) = \frac{x^2}{8} + \mathcal{O}(x^4) \tag{1.7}$$

$$J_k(x) = \frac{1}{k!}\left(\frac{x}{2}\right)^k + \mathcal{O}(x^{k+2}). \tag{1.8}$$

Furthermore we have

$$J_{-k}(x) = (-1)^k J_k(x). \tag{1.9}$$

Sometimes the higher orders are needed (see, e.g., Section 2.3), but often a small modulation index $m < 1$ can be assumed and we need to consider only the first terms:

$$\begin{aligned} E_\mathrm{m}(t) \approx{} & E_0 \exp(\,\mathrm{i}\,\omega_0 t) \\ & \times \Big(J_0(m) + \mathrm{i}\,J_1(m)\exp[\,\mathrm{i}\,\omega_\mathrm{m} t] + \mathrm{i}\,J_1(m)\exp[-\,\mathrm{i}\,\omega_\mathrm{m} t]\Big) \\ \approx{} & E_0 \exp(\,\mathrm{i}\,\omega_0 t)\,(J_0(m) + 2\;\mathrm{i}\;J_1(m)\cos\omega_\mathrm{m} t) \\ \approx{} & E_0 \exp(\,\mathrm{i}\,\omega_0 t)\,(1 + \mathrm{i}\;m\cos\omega_\mathrm{m} t)\,. \end{aligned} \tag{1.10}$$

We see from the first equation that the phase modulation has created two *sidebands* with a frequency offset of $\pm\omega_\mathrm{m}$ against the carrier and with a phase shift of $\mathrm{i} \mathrel{\hat{=}} 90°$ each. Their amplitude is $J_1(m) \approx m/2$, i.e. they contain a fraction $m^2/4$ each of the original (unmodulated) carrier power. The remaining carrier has the amplitude $J_0(m) \approx 1 - m^2/4$, corresponding to $1 - m^2/2$ of the original power.

Note that if we start with an (essentially equivalent) modulation signal given by $\sin\omega_\mathrm{m} t$ instead of $\cos\omega_\mathrm{m} t$, we have to apply a slightly more complicated identity:

$$\begin{aligned} & \exp(\,\mathrm{i}\;m\sin\alpha) = \\ & \qquad J_0(m) + 2\;\mathrm{i}\sum_{k=0}^{\infty} J_{2k+1}(m)\sin((2k+1)\,\alpha) + 2\sum_{k=1}^{\infty} J_{2k}(m)\cos(2k\,\alpha). \end{aligned} \tag{1.11}$$

The modulated field with only the first sidebands now becomes:

$$\begin{aligned} E'_\mathrm{m}(t) \approx{} & E_0 \exp(\,\mathrm{i}\,\omega_0 t) \\ & \times \Big(J_0(m) - J_1(m)\exp[\,\mathrm{i}\,\omega_\mathrm{m} t] + J_1(m)\exp[-\,\mathrm{i}\,\omega_\mathrm{m} t]\Big) \\ \approx{} & E_0 \exp(\,\mathrm{i}\,\omega_0 t)\,(J_0(m) + 2\;\mathrm{i}\;J_1(m)\sin\omega_\mathrm{m} t) \\ \approx{} & E_0 \exp(\,\mathrm{i}\,\omega_0 t)\,(1 + \mathrm{i}\;m\sin\omega_\mathrm{m} t)\,. \end{aligned} \tag{1.12}$$

Note the missing factor ‘i’ in the first equation and the different signs as compared to Equation (1.10). We usually prefer Equation (1.10) over Equation (1.12) because the former is more symmetrical and easier to remember.

1.2.1.2 Amplitude modulation

A small *amplitude* modulation, on the other hand, yields spectra given by

$$E_0 \exp(\,\mathrm{i}\,\omega_0 t)\,(1 + m\cos\omega_\mathrm{m} t) = E_0 \exp(\,\mathrm{i}\,\omega_0 t)\left(1 + \frac{m}{2}\exp[\,\mathrm{i}\,\omega_\mathrm{m} t] + \frac{m}{2}\exp[-\,\mathrm{i}\,\omega_\mathrm{m} t]\right) \tag{1.13}$$

for a modulation with $\cos\omega_\mathrm{m} t$ and

$$E_0 \exp(\,\mathrm{i}\,\omega_0 t)\,(1 + m\sin\omega_\mathrm{m} t) = E_0 \exp(\,\mathrm{i}\,\omega_0 t)\left(1 - \mathrm{i}\,\frac{m}{2}\exp[\,\mathrm{i}\,\omega_\mathrm{m} t] + \mathrm{i}\,\frac{m}{2}\exp[-\,\mathrm{i}\,\omega_\mathrm{m} t]\right) \tag{1.14}$$

for a modulation with $\sin\omega_\mathrm{m} t$. This can easily be understood and remembered with the help of phasor diagrams, as explained e.g. in [MPQ203, Section 2.2].

1.2.1.3 Frequency modulation

When looking at laser noise, we also have to consider a frequency modulation of the light field. A sinusoidal frequency modulation at the frequency ω_m with the modulation depth $\Delta\omega$ can be expressed by

$$\begin{aligned} E(t) &= E_0 \exp(\,\mathrm{i}\,\phi(t)), \\ \phi(t) &= \int (\omega_0 + \Delta\omega\sin\omega_\mathrm{m} t)dt. \end{aligned} \tag{1.15}$$

Note that one might be tempted to write

$$\phi(t) = (\omega_0 + \Delta\omega\sin\omega_\mathrm{m} t)t, \quad \textbf{(wrong)} \tag{1.16}$$

but this yields wrong results[5]. From Equation (1.15) it follows immediately that

$$\begin{aligned} \phi(t) &= \omega_0 t - \frac{\Delta\omega}{\omega_\mathrm{m}}\cos\omega_\mathrm{m} t, \\ E(t) &= E_0 \exp(\,\mathrm{i}\,\omega_0 t)\exp\left(-\,\mathrm{i}\,\frac{\Delta\omega}{\omega_\mathrm{m}}\cos\omega_\mathrm{m} t\right). \end{aligned} \tag{1.17}$$

Hence a sinusoidal frequency modulation behaves like a phase modulation of the same frequency with the modulation index

$$m_\mathrm{FM} = \frac{\Delta\omega}{\omega_\mathrm{m}}. \tag{1.18}$$

---

[5] The frequency, given by $d\phi/dt$, would become

$$\omega = \omega_0 + \Delta\omega\sin\omega_\mathrm{m} t + \Delta\omega\,\omega_\mathrm{m}\,t\,\cos\omega_\mathrm{m} t,$$

and the last term, which is proportional to t, is wrong.

In communications theory (see e.g. Reference [Razavi]), one distinguishes between *narrowband* FM, which is characterized by $m \ll 1$ and its opposite, *wideband* FM.

The spectrum of a narrowband FM signal contains (apart from the carrier) mainly the first upper and lower modulation sidebands, separated from the carrier by ω_m. It is described by Equations (1.10) and (1.18).

A wideband FM signal, on the other hand, contains many spectral components at multiples of ω_m from the carrier. As an example, Figure 1.9 shows the spectrum of a 100 kHz carrier, modulated at 1 kHz ($\omega_\mathrm{m} = 2\pi \cdot 1\,\mathrm{kHz}$) with a modulation depth of $\Delta\omega = 2\pi \cdot 10\,\mathrm{kHz}$, i.e. $m_\mathrm{FM} = 10$.

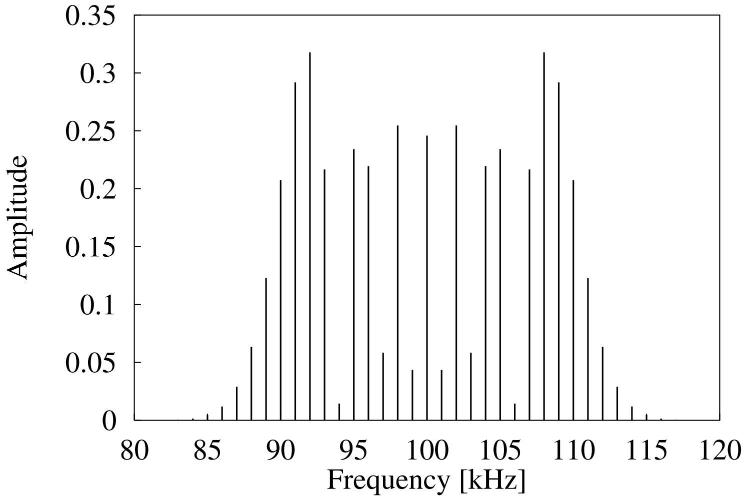

Figure 1.9: Spectrum of a frequency modulated signal with $m_\mathrm{FM} = 10$. The phase of each component is one out of 1, i, -1 or $-\mathrm{i}$, but the figure shows only the absolute values.

1.2.2 Description of mirrors and beamsplitters

Next we have to treat the splitting of light in two parts by a partially reflecting surface. Such a surface (e.g. a partially reflective mirror, see Figure 1.10) can be described by its amplitude reflectivity ρ and amplitude transmittance τ, which obey

$$\rho^2 + \tau^2 + \mathcal{A} = 1, \tag{1.19}$$

where $\mathcal{A}$ represents the power loss and ρ and τ are nonnegative real numbers with $0 \leq \rho, \tau \leq 1$. Strictly speaking, the reflectivity may be different from the two sides, but we can ignore this possibility for the low-loss optics generally used in gravitational wave detectors.

Now the amplitudes b and c that emerge from the mirror can be represented as linear

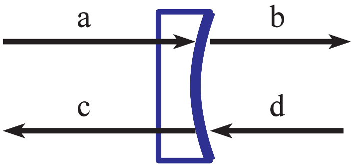

Figure 1.10: Amplitudes at a mirror.

combinations of the incoming amplitudes a and d:

$$\begin{pmatrix} b \\ c \end{pmatrix} = \begin{pmatrix} \mathrm{i}\,\tau & \rho \\ \rho & \mathrm{i}\,\tau \end{pmatrix} \cdot \begin{pmatrix} a \\ d \end{pmatrix}. \tag{1.20}$$

The factors 'i' are necessary to ensure energy conservation. Equivalently the matrix $\left(\begin{smallmatrix} \tau & \mathrm{i}\,\rho \\ \mathrm{i}\,\rho & \tau \end{smallmatrix}\right)$ can be used[6]. Other matrices are possible (such as $\left(\begin{smallmatrix} \tau & \rho \\ -\rho & \tau \end{smallmatrix}\right)$) but less desirable because of their asymmetry. Note that J. Mizuno in his work [MPQ203, Mizuno99] uses an equivalent expression which couples the amplitudes on the right side, b and d, to those on the left side of the mirror, a and c:

$$\begin{pmatrix} b \\ d \end{pmatrix} = \frac{\mathrm{i}}{\tau} \begin{pmatrix} 1-A & -\rho \\ \rho & -1 \end{pmatrix} \cdot \begin{pmatrix} a \\ c \end{pmatrix}. \tag{1.21}$$

This form allows the multiplication of matrices that represent components following each other 'in line'. Since, however, in the end a set of linear equations needs to be solved anyway, the author sees no particular advantage in this notation and uses Equation (1.20) throughout this work.

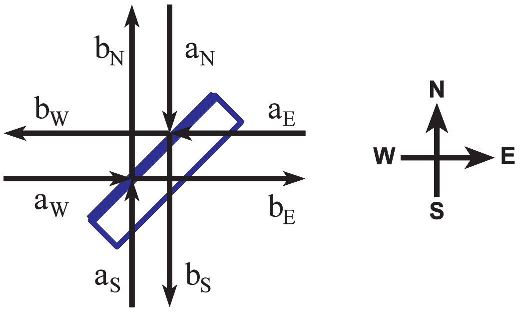

Figure 1.11: Amplitudes at a beamsplitter.

A beamsplitter (see Figure 1.11) can similarly be described by two sets of linear equa-

---

[6] These relationships were probably derived many times independently by many people. The first reference known to the author is [Rüdiger78]. The subject is also briefly treated in [Siegman].

tions:

$$\begin{aligned} \begin{pmatrix} b_\mathrm{e} \\ b_\mathrm{n} \end{pmatrix} &= \begin{pmatrix} \mathrm{i}\,\tau & \rho \\ \rho & \mathrm{i}\,\tau \end{pmatrix} \cdot \begin{pmatrix} a_\mathrm{w} \\ a_\mathrm{s} \end{pmatrix}, \\ \begin{pmatrix} b_\mathrm{w} \\ b_\mathrm{s} \end{pmatrix} &= \begin{pmatrix} \mathrm{i}\,\tau & \rho \\ \rho & \mathrm{i}\,\tau \end{pmatrix} \cdot \begin{pmatrix} a_\mathrm{e} \\ a_\mathrm{n} \end{pmatrix}. \end{aligned} \tag{1.22}$$

In practice all we need to remember is to use '$\mathrm{i}\,\tau$' as amplitude transmittance and 'ρ' as amplitude reflectivity.

1.2.3 Treatment of 'lengths' and 'tunings'

At this point it is convenient to explain the treatment of 'armlengths' and 'tunings' in our interferometer models (the simple models given explicitly in Section 1.3, the more detailed models of Section 1.4 and also the autoalignment models). The following may seem mathematically trivial, but is essential for successful application of the presented models to real interferometers. For simplicity we use the word 'length' for all distances between mirrors, beamsplitters etc.

We are not interested in the absolute value of any length to the precision of the light wavelength. There are more than 10^8 wavelengths in one roundtrip through the arms of our prototype (60 m), and even more in GEO 600. So far it has never been necessary in our prototype (and it may even be impossible) to determine the exact integral number of wavelengths in any macroscopic length. The macroscopic length is important for modulation frequencies (no more than 50 MHz) and signal frequencies (no more than a few 100 kHz, including calibration signals), and hence an accuracy of order 1 mm is sufficient.

On the other hand, the resonance condition of an interferometer (e.g. a Michelson interferometer or a Fabry-Perot cavity) is determined by mirror motions measured in small fractions of a wavelength, and is usually periodic with the period of one (or one half) wavelength.

Severe numerical problems would result if we expressed both the absolute armlength and its fine tuning in one single number. Therefore we split this information in two parts: The macroscopic length L and the tuning φ. The length L is expressed in meters and changes the phase of modulation and signal sidebands, as explained below. The tuning φ is expressed in radians, where 2π is equivalent to a pathlength difference of one wavelength λ and is used to change the relative phase of interfering light beams by multiplying the relevant light amplitudes with $\exp(\mathrm{i}\,\varphi)$.

As an example, consider a component of a light beam with the angular frequency $\omega = \omega_0 + \omega_1$, where $\omega_1 \ll \omega_0$. Typically ω_0 is the carrier frequency $\omega_0 = 2\pi\, c/\lambda$, whereas ω_1 is a small frequency offset, such as caused by a phase modulation[7]. The

---

[7] For the laser light used in GEO 600, $\omega_0/(2\pi)$ equals $2.8 \cdot 10^{14}$ Hz, whereas the highest modulation frequency will be no more than 50 MHz, i.e. more than six orders of magnitude smaller.

field of the light beam varies with

$$a_0 \exp[\,\mathrm{i}\,(-\omega t + kz)] \tag{1.23}$$

along the z-axis (the propagation axis). We write this expression as

$$a_0 \exp(-\,\mathrm{i}\,\omega_0 t)\exp(\,\mathrm{i}\,k_0\,z)\exp(-\,\mathrm{i}\,\omega_1 t)\exp(\,\mathrm{i}\,k_1\,z), \tag{1.24}$$

where $k_0 = \omega_0/c$ and $k_1 = \omega_1/c$. We consider a fixed point in space $z \neq 0$ (such as after propagating a macroscopic length). The term $\exp(-\,\mathrm{i}\,\omega_0 t)$ will be common to all interfering beams in all our applications. It can therefore be dropped since in the end we compute measurable photocurrents by forming expressions like $|a|^2 = aa^*$, where it yields unity.

The next term $\exp(\,\mathrm{i}\,k_0\,z)$, the microscopic phase of the carrier, is also omitted from the calculations, because it will be represented by a suitable phase φ (often called 'tuning'), which is defined as is most convenient for the particular application and is usually restricted to the range $-\pi < \varphi < \pi$.

We keep the terms $\exp(-\,\mathrm{i}\,\omega_1 t)$, which will reveal the time dependence of the detected photocurrent, and $\exp(\,\mathrm{i}\,k_1\,z)$ which describes the corresponding phase delays in the macroscopic length z. For simplicity we will call k_1 also a 'wavenumber', although its typical values are $\pm\omega_{\mathrm{mod}}/c$ or zero.

Having dropped the term $\exp(\,\mathrm{i}\,k_0\,z)$ means that all phase shifts are referred to the carrier phase, which is taken to be zero at the point of interest, unless a phase or tuning φ has explicitly been introduced.

1.3 Internal, external and Schnupp modulation

1.3.1 Internal modulation in the sideband picture

In order to illustrate the application and versatility of the sideband picture, we now treat again the case of internal modulation using sidebands.

We assume a simple Michelson interferometer with perfect mode matching and alignment, i.e. the interfering beams have the same transversal spatial structure, such that we can also omit all transversal geometric factors. Misalignments can, however, also be treated in a sideband picture, as will be done in Section 2.2 on autoalignment.

Referring to Figure 1.12, we call the amplitude of the incoming laser light a_0. We define the origin of time $t = 0$ at the moment the beam is split at the beamsplitter. In the first arm we then have

$$a_1 = \mathrm{i}\,\tau\,a_0, \tag{1.25}$$

where τ is the beamsplitter's amplitude transmittance.

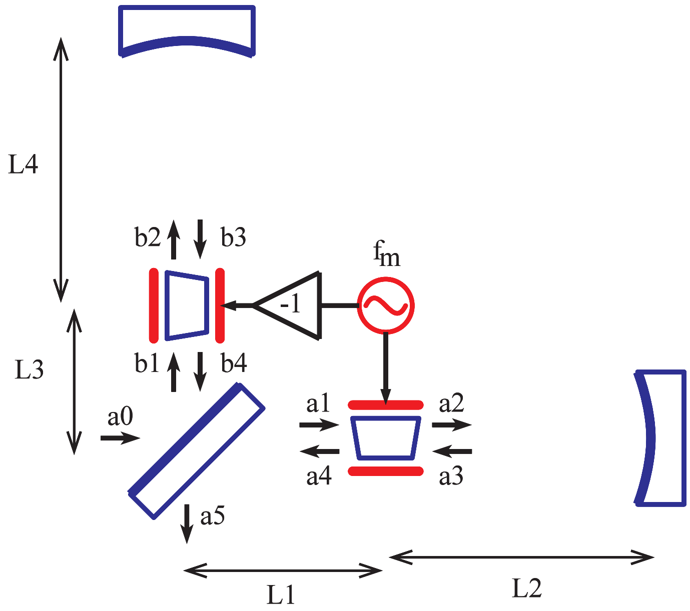

Figure 1.12: A Michelson interferometer with internal modulation. The light amplitudes a_0 … a_5 and b_1 … b_4 are shown, as well as the lengths L_1 … L_4. The two Pockels cells are driven in anti-phase from the modulation oscillator at the frequency f_m.

The action of the Pockels cell can now be described as

$$a_2 = a_1 \left(J_0(m) + 2\,\mathrm{i}\,J_1(m)\cos[\omega_\mathrm{m} t - k_\mathrm{m} L_1]\right). \tag{1.26}$$

The term '$-k_\mathrm{m} L_1$', where $k_\mathrm{m} = \omega_\mathrm{m}/c$, describes the phase of the modulation oscillator at the time of the beam's passage through the Pockels cell. This description is useful for the present discussion of internal modulation. For other cases (see e.g. the discussion of Schnupp modulation in Sections 1.3.3 and 1.4), the time delay acquired by traversing a finite distance will be associated with the phase of the beam.

Following the beam to the end mirror and back to the beamsplitter we get

$$\begin{aligned} a_3 &= a_2, \\ a_4 &= a_3\big(J_0(m) + 2\,\mathrm{i}\,J_1(m)\cos[\omega_\mathrm{m} t - k_\mathrm{m}(L_1 + 2L_2)]\big). \end{aligned} \tag{1.27}$$

Here we made the assumption of a perfectly reflecting end mirror. If losses are to be included, we just need to multiply a_3 with the mirror reflectivity.

Similarly we get for the second arm

$$\begin{aligned} b_1 &= \rho a_0, \\ b_3 = b_2 &= b_1\big(J_0(m) - 2\,\mathrm{i}\,J_1(m)\cos[\omega_\mathrm{m} t - k_\mathrm{m} L_3]\big), \\ b_4 &= b_3\big(J_0(m) - 2\,\mathrm{i}\,J_1(m)\cos[\omega_\mathrm{m} t - k_\mathrm{m}(L_3 + 2L_4)]\big). \end{aligned} \tag{1.28}$$

Finally we recombine both beams at the beamsplitter:

$$a_5 = \mathrm{i}\,\tau b_4 - \rho a_4 \exp(\mathrm{i}\,\varphi), \tag{1.29}$$

where φ is the Michelson phase and the '–' sign was chosen because then $\varphi = 0$ corresponds to the dark fringe. Note that in principle we could also express the Michelson phase via the arm lengths $L_1 \ldots L_4$, but we prefer not to do that (see Section 1.2.3).

The detected photocurrent is proportional to the power in that beam, i.e.

$$I_5 = |a_5|^2 = a_5 \cdot a_5^*, \tag{1.30}$$

where constant factors have been omitted.

When the Equations (1.25) ... (1.29) are inserted, this expression becomes rather lengthy and is not given here. It contains various terms with a $\cos \omega_\mathrm{m} t$ dependency as well as terms without any $\omega_\mathrm{m} t$ dependency and higher harmonic terms such as $\cos 2\omega_\mathrm{m} t$ and $\sin 2\omega_\mathrm{m} t$.

Most interesting is the coefficient of the $\cos \omega_\mathrm{m} t$ term, which represents (after demodulation) our output signal. A MATHEMATICA program to compute that term (as well as the DC term and the higher harmonics, if desired) is printed in Appendix E.1.2.

Here we have introduced some simplifications (perfect mirrors and beamsplitter, equal armlengths). From the given equations it is, however, clear that more general results can be derived by the same method in a straightforward fashion. Because of their complexity they will, however, be useful only in special situations or with particular numerical values. The resulting expression (with the simplifications $L_1 = L_3$ and $L_2 = L_4$) is:

$$4J_0(m)J_1(m)\left(J_0(m)^2 - J_1(m)^2 - 2J_1(m)^2\cos(2k_\mathrm{m}L_2)\right) \times \\ \sin\varphi\,\cos(k_\mathrm{m}L_2)\,\cos[\omega_\mathrm{m}t - k_\mathrm{m}(L_1 + L_2)] \tag{1.31}$$

We now examine the factors of this result. The factor $\sin\varphi$ tells us the most important property of the signal: it is linearly proportional to the Michelson phase φ near the dark fringe operating point $\varphi = 0$.

The very interesting factor $\cos(k_\mathrm{m}L_2)$ reflects the time delay which the light beam experiences between its two passages through the Pockels cell. If $k_\mathrm{m}L_2 = \pi/2$, or equivalently $2L_2 = \lambda_\mathrm{m}/2$, i.e. the total pathlength between the two passages equals half the wavelength λ_m of the modulation frequency, the output signal completely vanishes because the phase modulation on the way 'out' towards the end mirror is completely compensated on the way back to the beamsplitter. In earlier experiments in the 30 m prototype, L_2 was around 30 m and f_m was chosen near 10 MHz, such that $k_\mathrm{m}L_2 \approx 2\pi$ and the maximum signal was obtained [Schilling].

Finally, the factor $\cos[\omega_\mathrm{m}t - k_\mathrm{m}(L_1 + L_2)]$ indicates that the modulation of the photocurrent at ω_m appears with a time delay equivalent to the one-way travel time in the total armlength. In our prototype such effects were always ignored since the reference signal for the demodulator needed an adjustable phase-shift anyway. For the large interferometers it might however become necessary to carefully compensate such time delays in order to minimize the influence of phase noise from the modulation oscillator [Strain].

The first long factor with the Bessel functions shows how the signal depends on the modulation index m. For small modulation indices $m \ll 1$ this factor becomes $2m$. For larger modulation indices, it reaches a maximum absolute value of around 0.8 at $m = 0.63$, if $\cos(2k_{\mathrm{m}}L_2) = 0$.

This example shows the usefulness of the sideband picture. In Appendix D it is applied to a Fabry–Perot cavity. The principles involved are exactly the same as explained above. However, in a cavity (and hence in a recycled interferometer), the linear equations coupling the light amplitudes to each other form loops and lead in general to a linear system of equations in the unknown amplitudes. The solution of such a linear system is theoretically very straightforward, but may lead to algebraically more complicated expressions for the amplitudes.

The method has been expanded by K. Strain, M. Regehr and J. Mizuno [Mizuno99] (see Section 1.4).

1.3.2 External modulation

Another scheme to read out the Michelson phase at the dark fringe is *external modulation* [Drever83a, Man90]. It was used for a few years in the Garching prototype and also during the first half of this work. It had been proposed for GEO 600, but has now been replaced by Schnupp modulation (which is discussed in Section 1.3.3 and the rest of this Chapter).

In external modulation, the ‘signal beam’, which emerges as the interfering sum of the beams from the two arms, is arranged to interfere with another beam, called the ‘local oscillator beam’. Before they interfere, a phase modulation is applied to one of the two beams, usually the local oscillator beam. The resulting power of the interference pattern will contain a component at the modulation frequency, which is proportional to the Michelson phase, provided that everything is at its proper operating point.

In practice, this procedure can be carried out in several ways. The conceptually simplest setup is shown in Figure 1.13. The local oscillator beam is split off by the pickoff mirror **PO** before the light enters the interferometer, hence it has constant amplitude and a fixed phase. It is then phase modulated in the electro-optic modulator **EOM**, which is driven from the stable oscillator **Osc**.

In the second beamsplitter **BS2**, the signal beam and local oscillator beam are made to interfere. Two interference products emerge, which in principle carry the same information. For simplicity the diagram shows the detection of only one of them (with photodiode **PD**). For optimal signal-to-noise ratio, both beams need to be detected, otherwise a factor of $\sqrt{2}$ is lost. This loss was accepted in our prototype, but would be unacceptable in a real gravitational wave detector.

This setup of Figure 1.13 has various practical problems. First, the alignment of the two beams at BS2 is very difficult. They have travelled very different paths, and only the signal beam position and direction is influenced by the alignment of the long arms. Second, proper mode matching is equally difficult. And finally, there are very

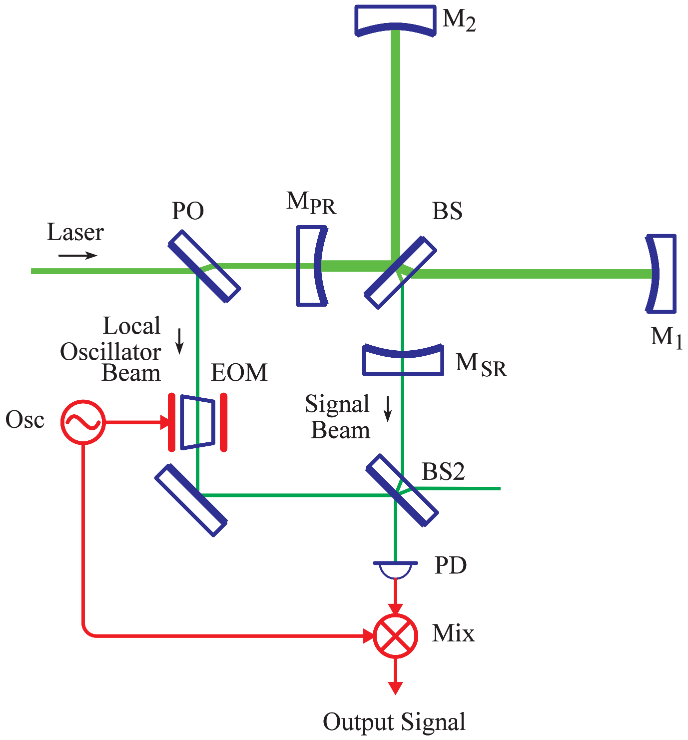

Figure 1.13: Schematic diagram of external modulation. The local oscillator beam is taken from the injected light.

strict requirements on the frequency stability of the laser source, because the local oscillator beam has a much shorter path to BS2 than the signal beam. For these reasons, this setup is used only in table–top demonstration experiments, but not in suspended interferometers.

Figure 1.14 shows a clever alternative setup, which was employed in the Garching prototype. The local oscillator beam is picked off the light circulating in one arm by the rear side of the beam splitter (this idea was first proposed by Lise Schnupp [Schilling]). Normally this rear side is coated for minimal reflectance; however, in the setup described here it is intentionally given a small finite reflectivity (approx. 300 ppm in the Garching prototype).

Both signal and local oscillator beam travel towards the South in parallel. They hit the 'recombination plate' RP, which has the same dimensions as the beamsplitter and which is suspended either parallel (Figure 1.14) or orthogonal to it. The use of such a recombination plate was proposed by P. Nelson [Nelson]. Figure 1.15 shows it in detail.

Interference takes place in the central spot of RP's front surface, which is given a 50:50 beamsplitter coating. In an annulus around this central spot, the front surface is AR (anti-reflective) coated. Both output beams emerge in parallel. This configuration avoids the mode-matching problems and reduces very strongly the sensitivity of the system to misalignments. Furthermore the local oscillator beam is taken from the same light that circulates in the arms and hence has good coherence with the signal

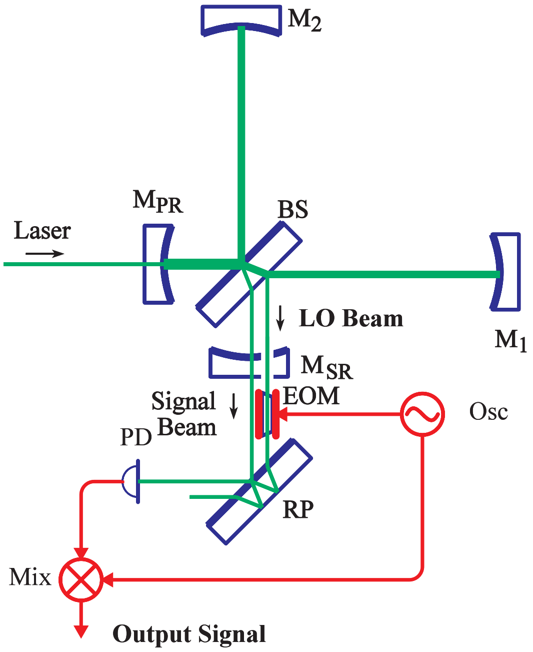

Figure 1.14: External modulation with a recombination plate (shown in detail in Figure 1.15). In practice this configuration is preferable to the one shown in Figure 1.13.

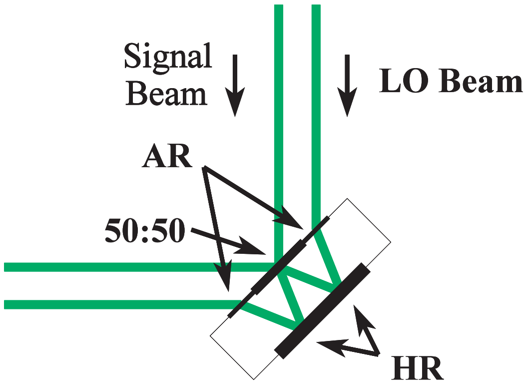

Figure 1.15: Detailed view of the recombination plate. The type of coating in each spot is indicated by 'HR' for high reflectivity, 'AR' for anti-reflection coating, and '50:50' for a semi-reflective beamsplitter coating and symbolized by the linewidth.

beam.

The phase relationship between the two interfering beams (which will soon be found to be important and is called the 'Mach-Zehnder phase' ψ) can be changed by slightly rotating the recombination plate about an axis perpendicular to the page in Figure 1.15.

We now compute the output signal that is expected with external modulation, assuming for simplicity, perfect modematching (i.e. the transversal geometry of all interfering beams is the same). The amplitudes of the beams returning from the first and second arm are given by

$$\begin{aligned} a_1 &= c_1 \, \exp(\mathrm{i}\,\varphi/2), \\ a_2 &= -c_2 \, \exp(-\mathrm{i}\,\varphi/2). \end{aligned} \tag{1.32}$$

The factor $\exp(\mathrm{i}\,\omega_0 t)$ describing the common light frequency has been omitted (as described in Section 1.2.3). The phase φ corresponds to the Michelson phase, earlier described as $\Delta\varphi$. The negative sign in the second equation is included for later convenience in order to have $\varphi = 0$ represent the desired dark-fringe operating point. Both c_1 and c_2 are positive constants of approximately equal magnitude. The signal beam is then given by

$$a_\mathrm{s} = (a_1 + a_2)/\sqrt{2}\,. \tag{1.33}$$

The local oscillator beam is given by

$$a_\mathrm{LO} = c_\mathrm{LO} \, \exp(\mathrm{i}\,\psi)\big(J_0(m) + 2\,\mathrm{i}\,J_1(m)\cos\omega_\mathrm{m} t\big). \tag{1.34}$$

The positive constant c_LO will generally be much smaller than c_1 or c_2. The phase ψ ('Mach-Zehnder phase') describes the phase shift between signal beam and local oscillator beam and is of great importance. The modulation of the local oscillator beam is described by the term containing the Bessel functions, the argument of which is the modulation index (see Equation 1.10).

The two output beams of the Mach-Zehnder are then given by

$$\begin{aligned} o_1 &= (a_\mathrm{s} + a_\mathrm{LO})/\sqrt{2}\,, \\ o_2 &= (a_\mathrm{s} - a_\mathrm{LO})/\sqrt{2}\,. \end{aligned} \tag{1.35}$$

The detected photocurrent in the two photodiodes is proportional to $|o_1|^2$ and $|o_2|^2$, respectively. These expressions are rather lengthy and not given here. They can be computed with the MATHEMATICA program printed in Appendix E.1.3. The subsequent coherent demodulation extracts only those components swinging with the modulation frequency ω_m. They are (without the $\cos\omega_\mathrm{m} t$ term)

$$\begin{aligned} u_1 &= \sqrt{2}\, c_\mathrm{LO}\, J_1(m)\left(c_1 \sin\left[\frac{\varphi}{2} - \psi\right] + c_2 \sin\left[\frac{\varphi}{2} + \psi\right]\right), \\ u_2 &= -u_1. \end{aligned} \tag{1.36}$$

With the simplification $c_2 = c_1$ one obtains

$$u_1 = -\sqrt{2}\, c_1\, c_{\mathrm{LO}}\, J_1(m) \sin\frac{\varphi}{2} \cos\psi. \tag{1.37}$$

Various interesting facts can be seen from this result. The signal is proportional to the amplitudes of both the beam in the arm and the local oscillator beam. The term $\sin\frac{\varphi}{2}$ shows that it is a useful signal with maximum slope at the proper point of operation. The term $\cos\psi$ indicates the dependence on the Mach-Zehnder phase. It is clear that ψ must be controlled, because otherwise the output signal might vanish or change sign. It is exactly this dependence on the additional degree of freedom ψ that makes external modulation more difficult to control than, for example, Schnupp modulation.

As we have seen, the output signal (demodulated dark fringe photocurrent) in an interferometer using external modulation has an extra factor $\cos\psi$ which requires active control of the Mach-Zehnder phase ψ.

Herein lies a challenging problem that is typical for many complex interferometers: A group of control loops (Michelson and Mach-Zehnder in this case) can only work properly when every loop of that group is already working. (For another example see Section 1.7).

In other words, if the Michelson is not locked to a dark fringe, there is no stable power recycling. Then the light inside the interferometer will fluctuate wildly in power (by many orders of magnitude) as well as in phase, because the uncontrolled suspended mirrors move freely. No meaningful error signal for the Mach-Zehnder phase ψ can be obtained.

However, without a controlled Mach-Zehnder phase, the Michelson error signal can vanish or have the wrong sign. Thus, initially, neither of the two loops is locked and neither has a useful error signal.

A simulation of these interferometer states, when lock has not yet been acquired for all loops, is possible, but very difficult. The LIGO project is currently writing an 'end-to-end' simulation code with this purpose in mind, which is based both on FFT beam propagation codes and following the interferometer state over small discrete timesteps [Yamamoto]. A complete description also needs to include the intermediate error signals and subsequent actions of the relevant control loops. In the GEO 600 project there is no such effort to simulate such error signals. It is one of the main purposes of the Garching 30 m prototype and in particular of this work to investigate the lock acquisition experimentally.

Appenix A.7 discusses in more detail the external modulation, which was used for the first half of this work, and eventually replaced by Schnupp modulation.

1.3.3 Schnupp modulation

The third modulation technique is *Schnupp modulation*, alternatively known as 'pre-modulation' or 'frontal modulation'. It will be used in all planned large-scale detectors, including GEO 600, and it has also been used in the Garching 30 m prototype during the second part of this work.

The basic idea is to create a controlled modulation at the output port by applying a phase modulation to the laser beam *before* it enters the interferometer *and* introducing an intentional armlength difference ΔL between the two long arms.

In the following description a simple Michelson interferometer without recycling (see Figure 1.16) will be used as an example. For the mathematical description of Schnupp modulation in this simple case, a variation of the sideband method will be used, which has proved to be most flexible and which is used in the simulation programs described in Section 1.4.

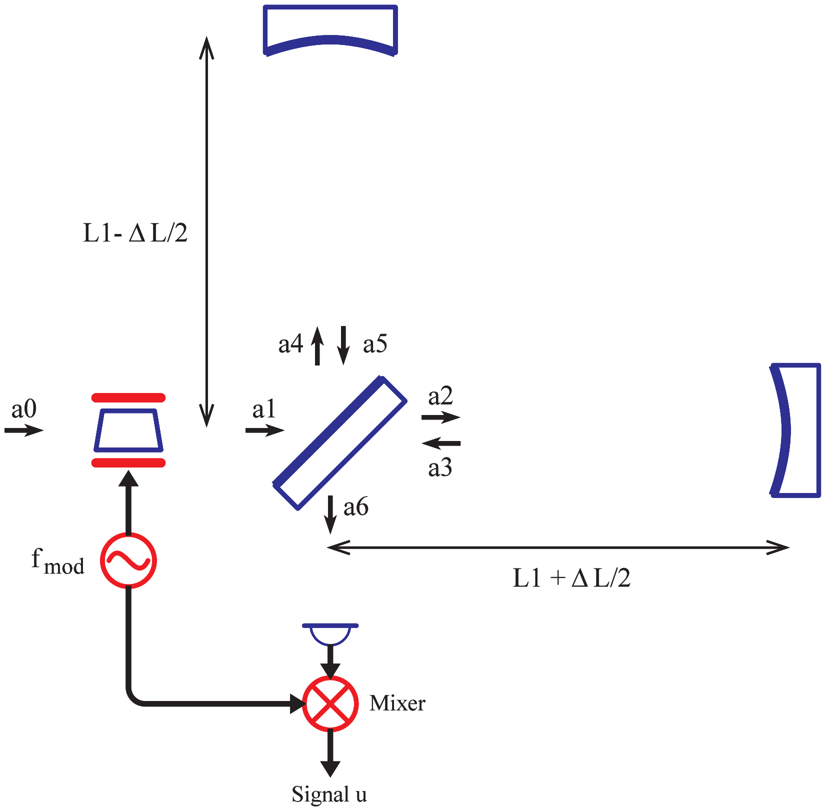

Figure 1.16: A simple Michelson interferometer employing Schnupp modulation. The light amplitudes $a_0 \ldots a_6$ used to derive the signal are shown.

Referring to Figure 1.16 and equation (1.10), we can write for the light amplitude a_1

$$a_1 = a_0 \left[J_0(m) + \mathrm{i}\, J_1(m) \exp(\mathrm{i}\, \omega_{\mathrm{m}} t) + \mathrm{i}\, J_1(m) \exp(-\mathrm{i}\, \omega_{\mathrm{m}} t) \right]. \tag{1.38}$$

Immediately behind the beamsplitter we have

$$\begin{aligned} a_2 &= \mathrm{i}\,\tau a_1 = \mathrm{i}\,\tau a_0 \left[J_0(m) + \mathrm{i}\, J_1(m) \exp(\mathrm{i}\, \omega_{\mathrm{m}} t) + \mathrm{i}\, J_1(m) \exp(-\mathrm{i}\, \omega_{\mathrm{m}} t) \right] \quad \text{and} \\ a_4 &= \rho a_1 = \rho a_0 \left[J_0(m) + \mathrm{i}\, J_1(m) \exp(\mathrm{i}\, \omega_{\mathrm{m}} t) + \mathrm{i}\, J_1(m) \exp(-\mathrm{i}\, \omega_{\mathrm{m}} t) \right]. \end{aligned} \tag{1.39}$$

Now these beams a_2 and a_4 propagate along the arms, traversing the distances $2L_1+\Delta L$ and $2L_1-\Delta L$, respectively.

The phase shift induced on the ω_m modulation, which is essential for the function of Schnupp modulation, is now taken into account by propagating the carrier and each sideband with its own 'wavenumber' $k=\omega/c$ (see Section 1.2.3):

$$\begin{aligned} k_- &= -\omega_\mathrm{m}/c && \text{for the lower sideband at } \omega_0-\omega_\mathrm{m},\\ k_0 &= 0 && \text{for the carrier at } \omega_0,\\ k_+ &= \omega_\mathrm{m}/c && \text{for the upper sideband at } \omega_0+\omega_\mathrm{m}. \end{aligned} \tag{1.40}$$

Hence the beams returning from the arms are given by

$$\begin{aligned} a_3 = &\,\mathrm{i}\,\tau a_0\Big[J_0(m)\\ &\quad+\mathrm{i}\,J_1(m)\exp\Big(\mathrm{i}\left(\omega_\mathrm{m}t+k_+(2L_1+\Delta L)\right)\Big)\\ &\quad+\mathrm{i}\,J_1(m)\exp\Big(\mathrm{i}\left(-\omega_\mathrm{m}t+k_-(2L_1+\Delta L)\right)\Big)\Big],\\ a_5 = &\,\rho a_0\Big[J_0(m)\\ &\quad+\mathrm{i}\,J_1(m)\exp\Big(\mathrm{i}\left(\omega_\mathrm{m}t+k_+(2L_1-\Delta L)\right)\Big)\\ &\quad+\mathrm{i}\,J_1(m)\exp\Big(\mathrm{i}\left(-\omega_\mathrm{m}t+k_-(2L_1-\Delta L)\right)\Big)\Big]. \end{aligned} \tag{1.41}$$

The two beams a_3 and a_5 recombine to form the output beam a_6 (and another beam returning towards the laser, which is not considered here). We have

$$a_6=\rho a_3-\,\mathrm{i}\,\tau a_5\exp(\mathrm{i}\,\varphi). \tag{1.42}$$

The phase φ describes the 'tuning' of the Michelson interferometer, and the '$-$' sign was chosen such that $\varphi=0$ conveniently corresponds to the dark-fringe operating point.

The power in the output beam is given by $|a_6|^2$, which again has various terms at the frequencies 0, ω_m and $2\omega_\mathrm{m}$. Extracting the terms at ω_m yields the following expression (see the program in Appendix E.1.4):

$$u_{\omega_\mathrm{m}}=-2J_0(m)J_1(m)\sin\varphi\,\sin\frac{\omega_\mathrm{m}\Delta L}{c}\,\sin\left(\omega_\mathrm{m}\left[t+\frac{2L_1}{c}\right]\right). \tag{1.43}$$

After demodulation in the mixer the output signal is given by

$$u=-2J_0(m)J_1(m)\sin\varphi\sin\frac{\omega_\mathrm{m}\Delta L}{c}. \tag{1.44}$$

The output signal has the desired dependence on the Michelson phase φ, being linearly proportional to φ near the desired operating point $\varphi=0$. The effective modulation index is given by

$$m_\mathrm{eff}=2J_0(m)J_1(m)\sin\frac{\omega_\mathrm{m}\Delta L}{c}\approx m\sin\frac{\omega_\mathrm{m}\Delta L}{c}. \tag{1.45}$$

The dependence on ΔL can be written as $\sin(2\pi\Delta L/\lambda_\mathrm{m})$, using the wavelength λ_m of the modulation frequency. It reaches its first maximum for $\Delta L = \lambda_\mathrm{m}/4$, when the total pathlength difference ($2\Delta L$) between both arms is $\lambda_\mathrm{m}/2$ (this is no longer true in a system with recycling, see Section 1.5.4 below).

1.4 Simulation tools

For a useful simulation of the 30 m prototype and GEO 600 the models presented in the previous sections need to be extended to include

- both power- and signal-recycling mirrors,
- arbitrary (non-ideal) reflectivities,
- arbitrary arm lengths (such as the armlength asymmetry needed for the Schnupp modulation),
- the frequency response of the output signals.

Although analytical solutions can in principle be obtained by the methods described so far, they become too complicated to be intuitively understandable. It is hence desirable to find a general method to simulate a complex interferometer. The main application of that model will be numerical simulations.

This has been carried out by J. Mizuno in collaboration with K. Strain and resulted in the simulation program described in this section, which will be referred to as "Jun's program" in the following sections. The same has also been done in the LIGO project [Yamamoto], but the resulting program, called TWIDDLE, has unfortunately not been available to us when this work was written. However, during a workshop on simulation tools held in Garching in April 1998 [STAIC] both programs were compared and found to yield identical results.

1.4.1 The interferometer model

The simulation assumes the general dual-recycling interferometer with Schnupp modulation as shown in Figure 1.17.

The four directions seen from the beamsplitter are called North, East, West and South. The West direction is taken to be the input port, South the output and North and East are the long arms. In each direction from the beamsplitter **BS**, which has an amplitude reflectivity ρ_BS, there are mirrors $\mathrm{M_N}$, $\mathrm{M_E}$, $\mathrm{M_W}$ and $\mathrm{M_S}$ with amplitude reflectivities ρ_N, ρ_E, ρ_W and ρ_S respectively at distances L_N, L_E, L_W and L_S from the beamsplitter's semireflective surface. Furthermore, there are 'tunings' φ_N, φ_E, φ_W and φ_S associated with each of the mirrors, again measured with respect to the beamsplitter. They cause a phase shift of $\exp(-2\,\mathrm{i}\,\varphi_x)$ for a beam reflected by the mirror M_x.

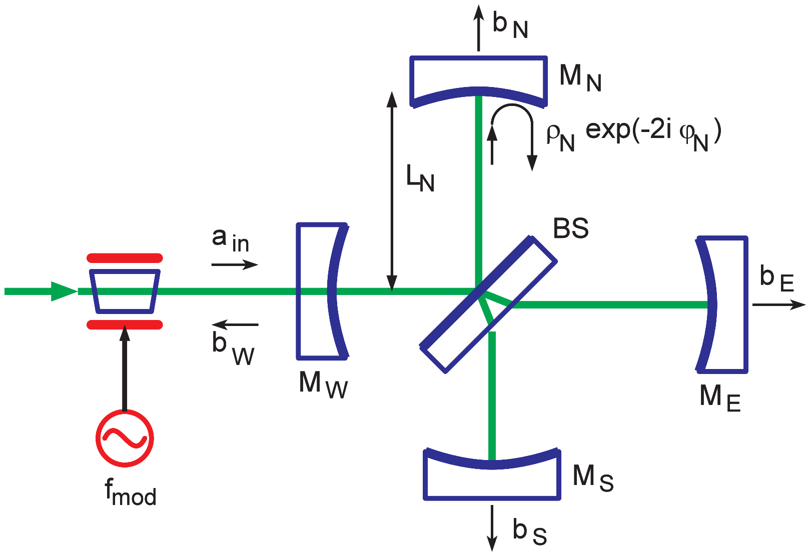

Figure 1.17: The dual recyling interferometer simulated by Jun's program. For simplicity, the arm length L, mirror reflectivity ρ and tuning φ are symbolically shown only for the north arm, but are similarly present in the other arms as well.

All four mirrors and the beamsplitter are assumed lossless, i.e. their amplitude transmittance is given by $\tau = \sqrt{1-\rho^2}$. Losses can be introduced in the interferometer by assigning a reflectivity $\rho < 1$ to the end-mirrors $\mathrm{M_N}$ and $\mathrm{M_E}$.

The above quantities can loosely be split into two groups:

The design is defined by the lengths L_N, L_E, L_W and L_S and the reflectivities ρ_N, ρ_E, ρ_W, ρ_S and ρ_BS. Some of these quantities may be subject to optimization for a particular observational purpose, but none of them can be quickly changed, and they can be considered constant during any particular experiment.

The state of the interferometer is defined by the tunings φ_N, φ_E, φ_W and φ_S. They can and will vary during lock acquisition, and possibly during operation.

As far as the simulation is concerned, the interferometer is completely characterized by the above quantities.

If light of the frequency $\omega_0 + \omega_1$ is injected through the West mirror $\mathrm{M_W}$, all light amplitudes inside the interferometer can be computed by solving a set of linear equations composed of equations such as (1.20) and (1.22)[8]. As explained in Section 1.2.3, ω_1 is considered a small offset to the carrier frequency ω_0 which is taken as reference and whose numerical value is irrelevant. The tunings φ_N, φ_E, φ_W and φ_S refer to the carrier frequency ω_0, and light of the frequency $\omega_0 + \omega_1$ acquires an additional phase shift given by $\exp(\,\mathrm{i}\,k_1 \Delta L)$, when it traverses the distance ΔL (see Section 1.2.3).

---

[8] Actually Jun's program uses equation (1.21) and solves the resulting equations using a clever matrix notation explained in Reference [Mizuno99].

The solution of these equations yields in general all unknown equilibrium amplitudes and in particular the four light amplitudes that leave the interferometer through the four mirrors, and which are denoted b_N, b_E, b_W and b_S in Figure 1.17.

In the present version used to simulate the 30 m prototype and GEO 600, a phase modulation (Schnupp modulation) is applied to the light before it enters the interferometer. The resulting amplitudes are computed separately for the carrier and the two sidebands, and then combined to find the photocurrent components at DC, the modulation frequency and its second harmonic, as explained below.

There are two main types of output from the simulation, the *static response* and the *frequency response*, which will be explained in the following sections.

1.4.2 Static response

For the static response, the design and state of the interferometer are described as in the previous section. Light that is phase modulated with modulation frequency ω_m and modulation index m is injected through the West mirror. The amplitude of this injected light has three frequency components:

$$\begin{aligned} a_\mathrm{in} &= J_0(m) + \mathrm{i}\,J_1(m)\exp(\mathrm{i}\,\omega_\mathrm{m}t) + \mathrm{i}\,J_1(m)\exp(-\mathrm{i}\,\omega_\mathrm{m}t) \\ &= a_0 + a_+\exp(\mathrm{i}\,\omega_\mathrm{m}t) + a_-\exp(-\mathrm{i}\,\omega_\mathrm{m}t). \end{aligned} \tag{1.46}$$

One output port is chosen, e.g. South. The linear equations describing the interferometer are solved separately for each of the three frequency components, resulting in complex amplitudes b_0, b_+ and b_- at the carrier frequency and its two modulation sidebands, respectively. A photodetector at the chosen output port will detect the photocurrent proportional to

$$I = |b|^2 = \left|b_0 + b_+\exp(\mathrm{i}\,\omega_\mathrm{m}t) + b_-\exp(-\mathrm{i}\,\omega_\mathrm{m}t)\right|^2. \tag{1.47}$$

This photocurrent has components at DC, ω_m and $2\omega_\mathrm{m}$, and can be written as a sum of five components:

$$I = H_0 + 2H_{1\mathrm{p}}\cos\omega_\mathrm{m}t - 2H_{1\mathrm{q}}\sin\omega_\mathrm{m}t + 2H_{2\mathrm{p}}\cos 2\omega_\mathrm{m}t - 2H_{2\mathrm{q}}\sin 2\omega_\mathrm{m}t, \tag{1.48}$$

using the following expressions:

$$\begin{aligned} H_0 &= |b_0|^2 + |b_+|^2 + |b_-|^2 && \text{at DC,} \\ H_{1\mathrm{p}} &= \Re\{b_-^* b_0 + b_0^* b_+\} && \text{at } \omega_\mathrm{m} \text{ in phase,} \\ H_{1\mathrm{q}} &= \Im\{b_-^* b_0 + b_0^* b_+\} && \text{at } \omega_\mathrm{m} \text{ in quadrature,} \\ H_{2\mathrm{p}} &= \Re\{b_-^* b_+\} && \text{at } 2\omega_\mathrm{m} \text{ in phase,} \\ H_{2\mathrm{q}} &= \Im\{b_-^* b_+\} && \text{at } 2\omega_\mathrm{m} \text{ in quadrature.} \end{aligned} \tag{1.49}$$

Here the asterisk ‘*’ denotes complex conjugation. The equivalence of equations (1.47) and (1.48) can be shown by straightforward algebraic transformations.

Hence H_0, which is real and positive, represents the DC component (average) of the detected photocurrent. The real numbers $H_{1\mathrm{p}}$ and $H_{1\mathrm{q}}$ yield the ω_m components of the photocurrent, $H_{1\mathrm{p}}$ representing the 'in-phase' component and the $H_{1\mathrm{q}}$ the 'quadrature' component, where 'in-phase' and 'quadrature' refer to the ω_m Schnupp modulation. Similarly, $H_{2\mathrm{p}}$ and $H_{2\mathrm{q}}$ yield the $2\omega_\mathrm{m}$ components of the photocurrent, 'in-phase' and 'quadrature' now referring to $2\omega_\mathrm{m}$.

In practice the most important components are $H_{1\mathrm{p}}$ and $H_{1\mathrm{q}}$. A linear combination of them given by

$$H_1(\chi) = H_{1\mathrm{p}}\cos(\chi) + H_{1\mathrm{q}}\sin(\chi) \tag{1.50}$$

is obtained experimentally by demodulating the photocurrent in a mixer. The local oscillator port of the mixer is driven with the modulation frequency ω_m, which has been phase shifted by χ. The linear combination $H_1(\chi)$ can also be computed as

$$H_1(\chi) = \Re\{(b_-^* b_0 + b_0^* b_+)\exp(-\mathrm{i}\,\chi)\}. \tag{1.51}$$

Since in-phase and quadrature component can contain different information about the interferometer state, it may be desirable to additionally demodulate the other quadrature[9] (with $\chi + 90°$). The local oscillator phase χ as well as the demodulation of both quadratures will be further discussed in Section 1.4.6.

The usual application of the static response is to plot one of its components (such as $H_{1\mathrm{p}}$) versus one parameter of the interferometer (such as one of the tunings φ).

As a realistic example, the Michelson error signal $H_{1\mathrm{p}}$ of the 30 m prototype with power recycling (but no signal recyling) is shown in Figure 1.18, together with the corresponding power in the PR cavity and DC power at the output. The MATHEMATICA program to compute these results is shown in Appendix E.2.1.

For a certain Michelson detuning far away from the dark fringe ($\varphi_\mathrm{MI} = 0.28\,\mathrm{rad}$), almost all injected power (91 %)[10] appears at the output. This can be understood by considering the PR cavity to consist of the PR mirror as the input coupler and the Michelson (consisting of the beamsplitter and two long arms) as the 'rear mirror' which has a variable reflectivity depending on φ_MI. The light that is 'transmitted' through this imaginary 'rear mirror' is the light that appears at the output port. For the tuning φ_MI =0.28 rad, this cavity is impedance matched and hence transmits all light (losses excepted) to its output.

---

[9] The planned control scheme for LIGO [Regehr95] uses only one modulation frequency for all longitudinal degrees of freedom and relies upon separate demodulation of in-phase and quadrature signals from several photodiodes to get sufficient information for all degrees of freedom.

[10] The missing 9 % are due to losses and, mainly, due to the fact that unity amplitude is assumed *before* the Schnupp modulation is applied. Thus some power is in the modulation sidebands, which have different resonance conditions in the interferometer (see also Section 1.5.4).

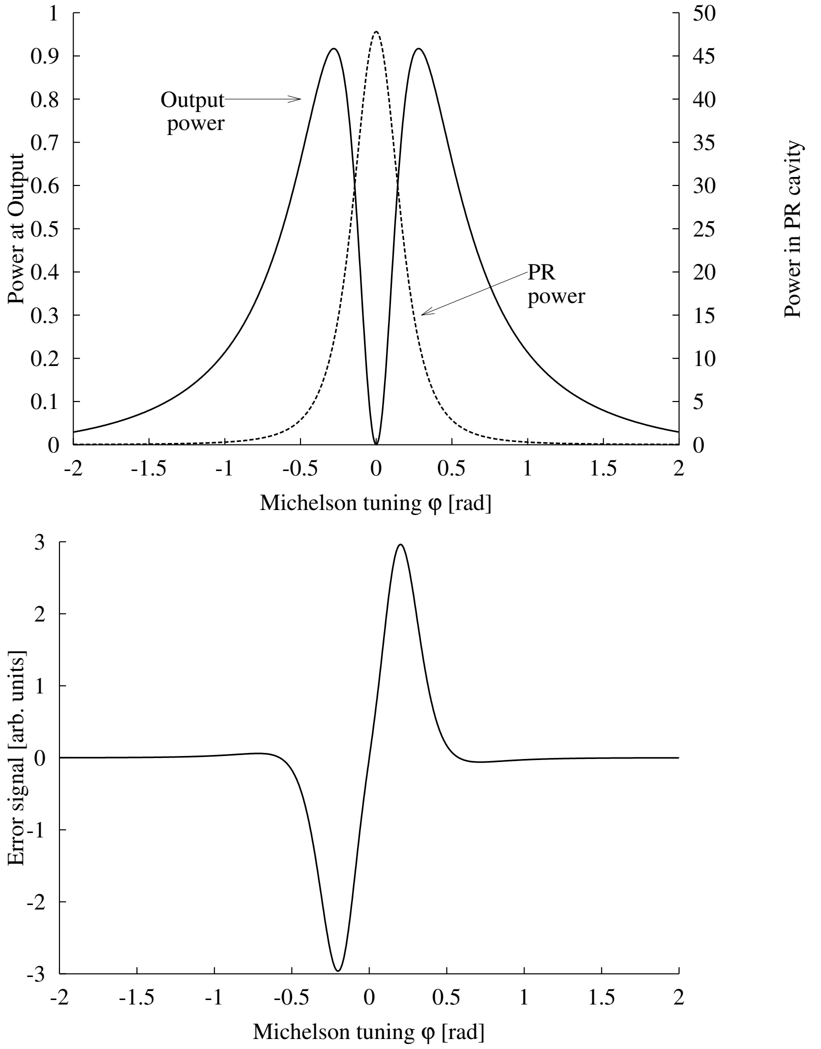

Figure 1.18: Simulation of power recycling in the 30 m prototype. The lower curve shows the Michelson error signal $H_{1\mathrm{p}}$ as a function of the Michelson tuning φ_{MI}. The upper curves show the corresponding DC power at the output and the power buildup in the PR cavity, for unity injected power.

1.4.3 Frequency response: An introduction

The ‘static response’ described in the previous section assumes the state of the interferometer to be fixed, i.e. any changes happen on a timescale significantly slower than all light travel times and storage times in the interferometer.

Many interesting effects happen to signals of timescales comparable to, or faster than, those storage times. In a dual-recycled system for example, the storage time of the SR cavity will be comparable to the expected signal period. Furthermore, in designing control loops for the interferometer, it is essential to know the phase-shifts of signals detected from the interferometer. To simplify the following discussion, we take the Michelson tuning φ_{MI}, i.e. the differential tuning of the two end mirrors, as an example of the parameter to be varied. If necessary, any of the tunings, or even any linear combination of them, can take this role.

To compute these frequency-dependent effects, there is another type of output of Jun’s program, called *frequency response*. As before, the state of the interferometer is given and considered fixed. The output of the program is again computed for one output port, e.g. South. It again has five distinct components: DC, ω_{m} in-phase and quadrature, and $2\omega_{\mathrm{m}}$ in-phase and quadrature, which are called G_0, $G_{1\mathrm{p}}$, $G_{1\mathrm{q}}$, $G_{2\mathrm{p}}$ and $G_{2\mathrm{q}}$ respectively. This section describes the meaning and application of the frequency response, whereas its computation is presented in Section 1.4.5.

In the ‘static response’, the parameter φ_{MI} was set to a certain value and the photocurrents were computed for that state of the interferometer. The computation was repeated for many values of φ_{MI}, but every single value was considered fixed. For the frequency response however, φ_{MI} is sinusoidally dithered[11] by an infinitesimal amount at a given frequency (the *signal frequency* $f_{\mathrm{sig}} = \omega_{\mathrm{sig}}/2\pi$).

The output signals (the five components of the photocurrent at the chosen output port) will then contain a sinusoidal component at the signal frequency f_{sig}. The magnitude and phase of these f_{sig} components, divided by the infinitesimal stimulus, constitute the frequency response of the interferometer. They are equivalent to ‘transfer functions’ used in the analysis of electronic circuits and are likewise usually plotted as Bode diagrams.

Now there are two distinct frequencies with corresponding phases, causing possible confusion and additional complications. The situation can be clarified by giving typical numbers for the Garching 30 m prototype.

The Schnupp modulation frequency ω_{m} is around 10 MHz and is imposed on the light entering the interferometer as phase modulation by a Pockels cell. The light power at the chosen output port has components at DC, 10 MHz and 20 MHz. With appropriate filters, phase-shifters and mixers, five distinct signals can be extracted from that light, represented by G_0, $G_{1\mathrm{p}}$, $G_{1\mathrm{q}}$, $G_{2\mathrm{p}}$ and $G_{2\mathrm{q}}$. At the output of the mixers and filters, all five signals are at frequencies $\ll 10\,\mathrm{MHz}$. The result of the simulation are the f_{sig} components in these five signals.

---

[11] The term ‘modulation’ is avoided here because of possible confusion with the Schnupp modulation.

Experimentally most interesting is a combination of $G_{1\mathrm{p}}$ and $G_{1\mathrm{q}}$ such as $G_1(\chi) = G_{1\mathrm{p}} \cos\chi + G_{1\mathrm{q}} \sin\chi$. The demodulation phase χ refers to the 10 MHz local oscillator associated with the Schnupp modulation and is implemented experimentally by a 10 MHz phase shifter in the local oscillator port of the mixer.

The Michelson phase φ_{MI} is kept near zero by the dark fringe lock. This constitutes the nominal operating point: all tunings are zero (the simulation can, of course, also be done for arbitrary other operating points). A very small sinusoidal dithering at the *signal frequency* (in this example, $f_{\mathrm{sig}} = 375\,\mathrm{Hz}$) is applied to φ_{MI} via coil-magnet actuators on the end mirrors (the actual amplitude of the motion was less than 1 pm). All five signals described above will in general have a 375 Hz component in them. The magnitude and phase (at f_{sig}) of these components depend on the state of the interferometer, but also on the signal frequency f_{sig}. All five signals G_0, $G_{1\mathrm{p}}$, $G_{1\mathrm{q}}$, $G_{2\mathrm{p}}$ and $G_{2\mathrm{q}}$ will represent the magnitude *and phase* of the 375 Hz component in the respective mixer output. Consequently they come out of the calculation as complex numbers, their argument representing the phase at 375 Hz, which is not to be confused with the 10 MHz demodulation phase χ.

Picking one of the five signals, e.g. $G_{1\mathrm{p}}$, we can plot the magnitude and phase of its f_{sig} component as a function of f_{sig}. This constitutes the typical application of the frequency response output.

As an example, Figure 1.19 shows the frequency response of $G_{1\mathrm{p}}$ for the *dual* recycled 30 m prototype, with the same parameters as in the example in the previous section. The Mathematica code is shown in Appendix E.2.2

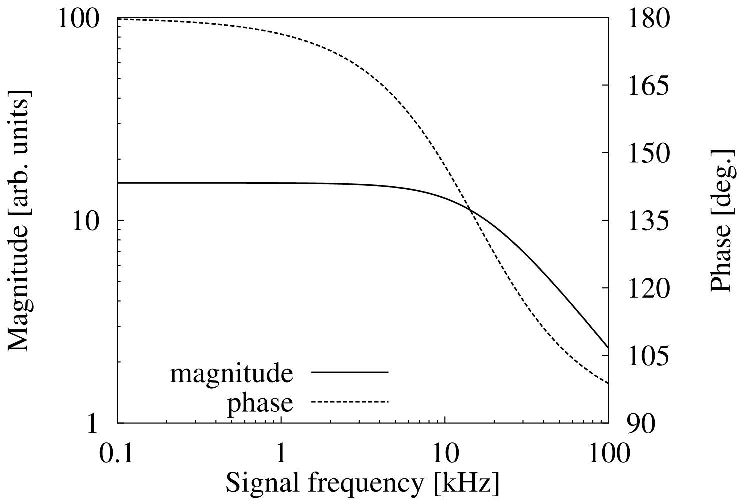

Figure 1.19: Frequency response of the Michelson error signal of the dual recycled 30 m prototype.

The frequency response behaves like a one-pole low-pass filter with a corner frequency of 15.4 kHz, determined by the SR cavity linewidth (see Section 1.5.3 and Appendix D.3.1). The knowledge of this frequency response is essential both to optimize the parameters of the interferometer for a desired gravitational wave frequency and also for designing the control loops that are needed to keep the interferometer at the chosen operating point. For this 'simple' case the frequency response could have been predicted without the simulation program (see, e.g., [Meers89]), but for more complicated cases, such as detuned dual recycling, the simulation is indispensable.

1.4.4 Simulating the effects of gravitational waves

In the above examples we have always dithered the differential Michelson phase φ_{MI} and assumed that a gravitational wave will have a similar effect on the interferometer. That is true if the direction of propagation of the gravitational wave is favorably oriented to the arms of the detector, and its polarization is right. The simplest case is when the wave is impinging orthogonally on the plane of the detector and is linearly polarized with its main polarization axes parallel to the arms. In this case the differential phase shift is given by

$$\varphi_{\mathrm{MI}}(t) = 2\,h(t - L/c)\,\frac{\omega_0 L}{c}\,\frac{\sin(\omega_{\mathrm{sig}} L/c)}{\omega_{\mathrm{sig}} L/c}, \tag{1.52}$$

for a simple Michelson interferometer, where $h(t)$ is the strain of the gravitational wave, assumed sinusoidal with angular frequency ω_{sig}, L is the physical armlength and ω_0 the angular frequency of the laser light. Equation (1.52) is a 'standard' result; for a derivation see for example Reference [Lobo92] (or [Heinzel95]).

If orientation and/or polarization are different from the simplest case cited above, the phase shift will be multiplied by a factor between -1 and 1. For some directions and/or polarizations, the effect may be zero. Further details can be found in References [Forward78] and [Schutz87].

The frequency dependence of the phase shift φ_{MI} in Equation (1.52) is also interesting. There are periodic zeroes in the response, the first one for $\omega_{\mathrm{sig}} L/c = \pi$ (see also Reference [Schilling97]). This corresponds to the case when the light's round-trip travel time in the arms is equal to one full period of the gravitational wave. Any phase shift acquired on the way 'out' will be cancelled in the return trip back 'in'. Hence the simple model of the gravitational wave dithering just the position of the end mirrors fails in this case.

In a delay-line system, Equation (1.52) remains valid if L is replaced by NL where N is the number of 'folds' of the beams in each arm ($N = 2$ in GEO 600). In contrast to the common usage in Garching, for this work L is defined to be the physical armlength and N the number of 'folds'.[12]

For systems with dual recycling or Fabry–Perot cavities in the arms, it turns out that Equation (1.52) is valid with L being the physical armlength (or NL for a delay line). The gravitational wave produces a phase shift according to Equation (1.52), which converts a fraction of the carrier into signal sidebands. These sidebands then circulate

---

[12] While Herriot delay lines were studied, there were good reasons to define these quantities differently, but in this work such Herriot delay lines are not treated and a simple Michelson is taken as reference, e.g. in Equation (1.52).

in the interferometer. In the model, signal sidebands with an amplitude proportional to the phase-shift given by Equation (1.52) are treated as if they were injected in the arms. All further effects can adequately be described by the interferometer model given above, and are similar to the effects of 'dithering' the armlength.

For GEO 600, NL equals 1200 m, and the signal frequency where the first zero occurs is at 125 kHz. This is more than one decade higher than any anticipated signal and we can therefore identify the effect of a gravitational wave with that of dithering the armlengths for all practical purposes.

1.4.5 Computation of the frequency response

To compute the frequency response described in Section 1.4.3, all parameters of the interferometer, including the tunings which set its operating point, are considered fixed.

The computation begins with the three (carrier-referred) light frequencies $-\omega_\mathrm{m}$, 0, and ω_m which are produced by the Schnupp modulation and hence contained in the injected light. They circulate in the interferometer, and at any given mirror their amplitudes, called b_-, b_0 and b_+, can be computed as described in Section 1.4.2.

The sinusoidal dithering of a mirror causes a phase modulation of the light reflected from that mirror and hence additional sidebands appear in the reflected light. Assuming a (small) modulation index ε, there will be new sidebands with amplitudes called e as shown in Figure 1.20.

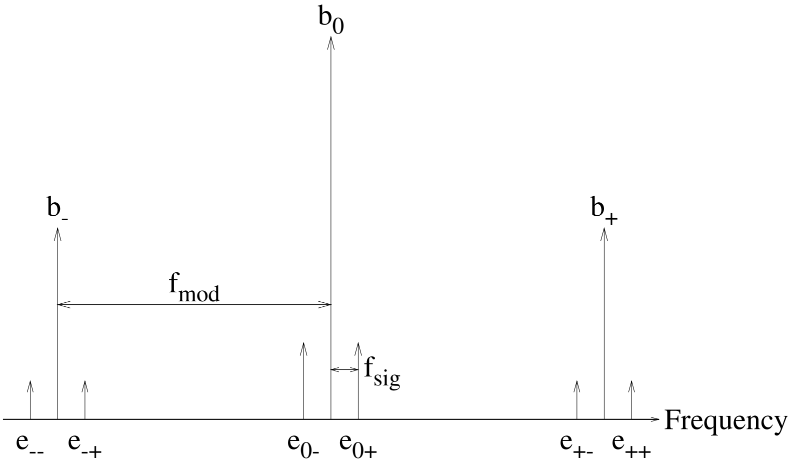

Figure 1.20: The nine light frequencies involved in computing the requency response.

Their complex amplitudes and corresponding frequencies (with respect to the carrier) are

$$\begin{aligned}
e_{--} &= \mathrm{i}\,(\varepsilon/2) b_- && \text{at} && -\omega_\mathrm{m} - \omega_\mathrm{sig}, \\
e_{-+} &= \mathrm{i}\,(\varepsilon/2) b_- && \text{at} && -\omega_\mathrm{m} + \omega_\mathrm{sig}, \\
e_{0-} &= \mathrm{i}\,(\varepsilon/2) b_0 && \text{at} && -\omega_\mathrm{sig}, \\
e_{0+} &= \mathrm{i}\,(\varepsilon/2) b_0 && \text{at} && +\omega_\mathrm{sig}, \\
e_{+-} &= \mathrm{i}\,(\varepsilon/2) b_+ && \text{at} && +\omega_\mathrm{m} - \omega_\mathrm{sig}, \\
e_{++} &= \mathrm{i}\,(\varepsilon/2) b_+ && \text{at} && +\omega_\mathrm{m} + \omega_\mathrm{sig}.
\end{aligned} \tag{1.53}$$

Since the modulation index ε is considered infinitesimally small, the Bessel functions can be approximated by their first terms (see equation (1.10)). Higher order sidebands and all second order effects, such as loss from the carrier and Schnupp sidebands (b_-, b_0 and b_+) due to the dithering, are ignored.

If the dithering takes place at an end mirror, these additional sidebands can be considered to be additionally injected through that end mirror, with amplitudes proportional to b_-, b_0 and b_+ at that end mirror. If the dithering is to take place at a mirror internal to the interferometer (such as the beamsplitter), the lengths on both sides of the mirror are considered dithered simultaneously in anti-phase. This is explained in detail in Reference [Mizuno99], where it is also shown how an internal dithering can be replaced by an equivalent 'virtual input' at an end mirror.

Now there are light components at *nine* frequencies independently circulating in the interferometer, the six of Equation (1.53) and $-\omega_\mathrm{m}$, 0, ω_m. The gain and phase shift that each component experiences in the interferometer will in general differ from any other and can be computed individually from the set of linear equations describing the interferometer. At the chosen output port, nine light amplitudes are obtained, which will be called $\hat{b}_-$, $\hat{b}_0$, $\hat{b}_+$, $\hat{e}_{--}$, ... , $\hat{e}_{++}$. This is schematically illustrated in Figure 1.21.

The output signals of interest are the ω_sig components in the DC photocurrent and in each of the four possible mixer outputs (two demodulated signals at ω_m, and two at $2\omega_\mathrm{m}$). They are computed as follows:

$$\begin{aligned}
G_0 &= 2\,F_0, \\
G_{1\mathrm{p}} &= 2\left[F_{1+} + (F_{1-})^*\right], \\
G_{1\mathrm{q}} &= 2\left[F_{1+} - (F_{1-})^*\right], \\
G_{2\mathrm{p}} &= 2\left[F_{2+} + (F_{2-})^*\right], \\
G_{2\mathrm{q}} &= 2\left[F_{2+} - (F_{2-})^*\right],
\end{aligned} \tag{1.54}$$

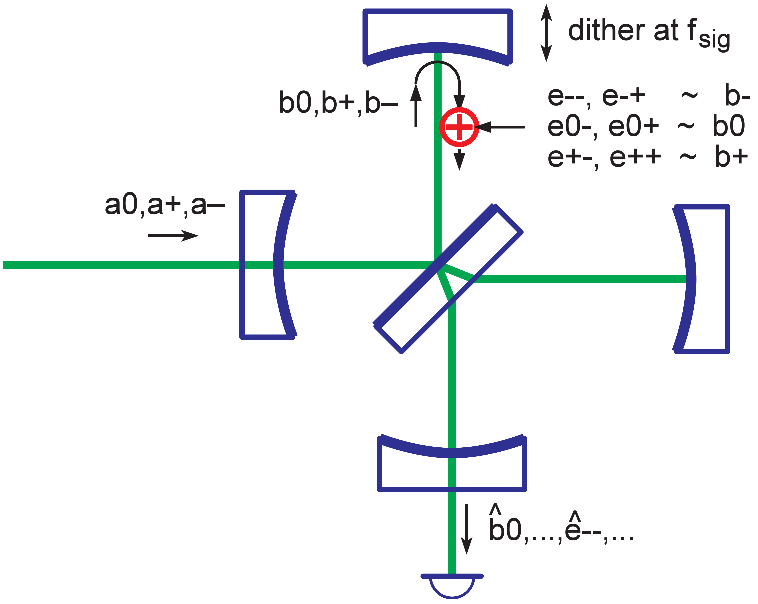

Figure 1.21: Schematic representation of the amplitudes used to compute the frequency response. Due to the Schnupp modulation (not shown), the injected light has three frequency components a_-, a_0, and a_+. They circulate independently in the interferometer, yielding b_-, b_0, and b_+ at the dithered mirror (North in this example) and $\hat{b}_-$, $\hat{b}_0$ and $\hat{b}_+$ at the chosen output port (South in this example). At the dithered mirror, six additional components $e_{--}, \ldots, e_{++}$ are produced proportional to the b components there. These also circulate individually with different resonance conditions and appear at the output as $\hat{e}_{--}, \ldots, \hat{e}_{++}$.

using the intermediate results

$$
\begin{aligned}
F_0 &= (\hat{e}_{--})^*\hat{b}_- + (\hat{b}_-)^*\hat{e}_{-+} + (\hat{e}_{0-})^*\hat{b}_0 + (\hat{b}_0)^*\hat{e}_{0+} + (\hat{e}_{+-})^*\hat{b}_+ + (\hat{b}_+)^*\hat{e}_{++}\,,\\
F_{1-} &= (\hat{b}_-)^*\hat{e}_{0-} + (\hat{e}_{-+})^*\hat{b}_0 + (\hat{b}_0)^*\hat{e}_{+-} + (\hat{e}_{0+})^*\hat{b}_+\,,\\
F_{1+} &= (\hat{e}_{--})^*\hat{b}_0 + (\hat{b}_-)^*\hat{e}_{0+} + (\hat{e}_{0-})^*\hat{b}_+ + (\hat{b}_0)^*\hat{e}_{++}\,,\\
F_{2-} &= (\hat{e}_{-+})^*\hat{b}_+ + (\hat{b}_-)^*\hat{e}_{+-}\,,\\
F_{2+} &= (\hat{e}_{--})^*\hat{b}_0 + (\hat{b}_-)^*\hat{e}_{0+}\,.
\end{aligned}
\tag{1.55}
$$

The terms F_0, F_{1-}, F_{1+}, F_{2-} and F_{2+} can be identified as interference products of all combinations between two light amplitudes separated in frequency by $\omega_{\rm sig}$, $\omega_{\rm m} - \omega_{\rm sig}$, $\omega_{\rm m} + \omega_{\rm sig}$, $2\omega_{\rm m} - \omega_{\rm sig}$ and $2\omega_{\rm m} + \omega_{\rm sig}$, respectively.

All of them are proportional to the (signal frequency) modulation index ε, and hence the transfer functions for $\varepsilon \to 0$ can be obtained by formally dividing them by ε (in practice, ε is set to unity in Equation (1.53) and never appears in the program).

For very low signal frequencies $\omega_{\rm sig} \to 0$ all five output signals $G_0, \ldots, G_{2\rm q}$ should become purely real, and their value should be

$$
\lim_{\omega_{\rm sig}\to 0} G_x = \left.\frac{\partial H_x}{\partial \varphi}\right|_{\varphi=\varphi_{\rm operating}}\,, \tag{1.56}
$$

when compared with the static response H_x at the same mixer output, and φ is the dithered tuning. This can be used as one check for the consistency of the simulation.

Similarly to the case of the static response, the most important output signal will generally be a linear combination of $G_{1\rm p}$ and $G_{1\rm q}$ given by

$$
G_1(\chi) = G_{1\rm p}\cos\chi + G_{1\rm q}\sin\chi, \tag{1.57}
$$

where χ is the phase of the local oscillator at $\omega_{\rm m}$ that is used for downmixing.

1.4.6 Demodulation phase χ and reconstruction of the signal

In interpreting the frequency response and comparing it with experiments, a problem arises in arriving at the proper choice of the demodulation phase χ. Both $G_{1\rm p}$ and $G_{1\rm q}$ are complex numbers and in general they may have four independent components. This applies in particular to the case of detuned dual recycling, and will be discussed in general in this section.

We assume a monochromatic input signal to the interferometer with a (complex) amplitude x, i.e.:

$$
\varphi(t) = \Re\{x\exp(\mathrm{i}\,\omega_{\rm sig}t)\}, \tag{1.58}
$$

where φ is the dithered tuning of interest (e.g. the Michelson phase). The signal frequency $\omega_{\rm sig}$ will be considered fixed and we look only at its amplitude x.

The interferometer reacts on this input signal x and finally yields a photocurrent with components in the neighborhood of ω_m, which can be demodulated in two quadratures[13]. The demodulated output signal in both quadratures is called y_p and y_q, respectively, and is given by

$$y_\mathrm{p} = G_{1\mathrm{p}}\, x + n_\mathrm{p}\,, \tag{1.59}$$

$$y_\mathrm{q} = G_{1\mathrm{q}}\, x + n_\mathrm{q}\,. \tag{1.60}$$

The noise terms n_p and n_q represent additional the noise in the output channels, such as the shot noise and the electronic noise of the photodetector. The noise in the two quadratures is assumed to be uncorrelated, white, and to be of equal average value n, i.e.

$$n = \langle n_\mathrm{p} \rangle_\mathrm{rms} = \langle n_\mathrm{q} \rangle_\mathrm{rms} \tag{1.61}$$

in a fixed observation bandwidth of interest.

These are significant simplifications. If the light power at the output is dominated by the modulation sidebands (such as in properly operated dual recycling), the noise cannot really be considered white. Detailed investigations (see [Meers91] and [Niebauer91]) show, however, that the loss in signal-to-noise ratio (SNR) due to these corrections is only of the order of 1 dB. These corrections are ignored in the following discussion. Another assumption is that after downmixing no further noise is added, i.e. A/D-converters, amplifiers, etc. are considered perfect (their noise contribution is considered negligible compared to the noise already present in the signal).

The transfer functions $G_{1\mathrm{p}}$ and $G_{1\mathrm{q}}$ can be computed by an interferometer simulation program such as Jun's program. The interesting questions are:

- In the data aquisition process intended to record the Michelson phase (and hence the gravitational wave signal), both quadratures will need to be demodulated. What is the best way to reconstruct the signal x such that the maximal signal-to-noise ratio (SNR) is obtained?
- For analog loops, such as the dark fringe lock or the SR mirror lock in the 30 m prototype, normally only one mixer will be used. What is the best demodulation phase? And how much SNR is lost compared with demodulating both quadratures?
- To compare various transfer functions, what is a good 'figure of merit' of the transfer functions?

1.4.6.1 Two mixers

If both y_p and y_q are obtained, they must be added coherently to obtain the maximal SNR. Since the signal may appear with different phase shifts in the two quadratures,

---

[13] The same discussion applies for demodulation at $2\omega_\mathrm{m}$. Demodulation at this frequency is, however, much less commonly utilized due to spurious $2\omega_\mathrm{m}$ signals caused by various nonlinearities.

the first step is to 'shift back' their phases before they can be added:

$$\begin{aligned} y'_\mathrm{p} &= y_\mathrm{p}\,\frac{|G_{1\mathrm{p}}|}{G_{1\mathrm{p}}}\,, \\ y'_\mathrm{q} &= y_\mathrm{q}\,\frac{|G_{1\mathrm{q}}|}{G_{1\mathrm{q}}}\,. \end{aligned} \tag{1.62}$$

The signal components in y'_p and y'_q are now coherent, with both channels still having the same noise level (remember that the in-phase and quadrature demodulation takes place at ω_m, whereas the phase shift described by Equation (1.62) is at the signal frequency). The magnitude of the signal component is different in both channels and given by $|G_{1\mathrm{p}}|$ and $|G_{1\mathrm{q}}|$, respectively.

For optimal SNR, they should be added with proper weighting. The optimal weights can be derived with the theory of optimal filtering, but can also be found by a direct calculation. The result is that the weight of each channel should be proportional to the magnitude of its signal component, i.e.:

$$y_\mathrm{opt} = |G_{1\mathrm{p}}|\,y'_\mathrm{p} + |G_{1\mathrm{q}}|\,y'_\mathrm{q} = y_\mathrm{p}\frac{|G_{1\mathrm{p}}|^2}{G_{1\mathrm{p}}} + y_\mathrm{q}\frac{|G_{1\mathrm{q}}|^2}{G_{1\mathrm{q}}}. \tag{1.63}$$

Substituting Equations (1.59) and (1.60) in the last expression yields

$$y_\mathrm{opt} = \left(|G_{1\mathrm{p}}|^2 + |G_{1\mathrm{q}}|^2\right) x + |G_{1\mathrm{p}}| n_\mathrm{p} + |G_{1\mathrm{q}}| n_\mathrm{q}. \tag{1.64}$$

For the noise components n_p and n_q, the phase of the transfer functions is irrelevant. Because n_p and n_q are uncorrelated, they must be added quadratically, yielding:

$$y_\mathrm{opt} = \left(|G_{1\mathrm{p}}|^2 + |G_{1\mathrm{q}}|^2\right) x + \sqrt{|G_{1\mathrm{p}}|^2 + |G_{1\mathrm{q}}|^2}\; n. \tag{1.65}$$

Hence the optimal reconstructed signal $\hat{x}$ is given by

$$\begin{aligned} \hat{x} &= \frac{y_\mathrm{opt}}{|G_{1\mathrm{p}}|^2 + |G_{1\mathrm{q}}|^2} \\ &= x + \frac{n}{\sqrt{|G_{1\mathrm{p}}|^2 + |G_{1\mathrm{q}}|^2}}\,. \end{aligned} \tag{1.66}$$

We can thus take the variable

$$u := \sqrt{|G_{1\mathrm{p}}|^2 + |G_{1\mathrm{q}}|^2} \tag{1.67}$$

either as a figure of merit for the transfer functions (for constant noise) or as measure of the SNR (for constant signal).

It is straightforward to show that an arbitrary phase shift χ common to both mixers' local oscillators does not affect the obtainable SNR[14]. In other words, any local oscillator phase can be used for the first mixer, as long as the second mixer's local oscillator is in quadrature to the first mixer's local oscillator.

---

[14] The signal $\hat{x}$ remains constant if $G_{1\mathrm{p}}$ is replaced by $(G_{1\mathrm{p}}\cos\chi + G_{1\mathrm{q}}\sin\chi)$ and $G_{1\mathrm{q}}$ by $(-G_{1\mathrm{p}}\sin\chi + G_{1\mathrm{q}}\cos\chi)$.

Note that $G_{1\mathrm{p}}$ and $G_{1\mathrm{q}}$ will in general be frequency dependent with a possibly complicated frequency response. The optimal SNR obtained above can then only be reached by digitizing both channels y_p and y_q and performing the calculation of Equation (1.66) digitally in the data aquisition or data processing program. This requires a knowledge of the transfer functions $G_{1\mathrm{p}}$ and $G_{1\mathrm{q}}$. In practice, for detuned dual recycling, some kind of calibration signal will be beneficial to monitor (and stabilize) these transfer functions (see Section A.8).

1.4.6.2 One mixer

During the experiments described in this work, the 30 m prototype had no digital data acquisition, and only one mixer (with adjustable phase shifter) was used for each signal. For each of the relevant mixer outputs (PR cavity tuning, Michelson tuning and SR tuning), the local oscillator phase χ was experimentally adjusted such that the maximum signal was obtained for one particular signal frequency (see Section 1.8.1). Hence the maximum signal obtainable with only one mixer and the corresponding phase χ are important and discussed in this section. For the following algebra, $G_{1\mathrm{p}}$ and $G_{1\mathrm{q}}$ are separated into their real and imaginary parts:

$$\begin{aligned} G_{1\mathrm{p}} &= a + \mathrm{i}\, b, \\ G_{1\mathrm{q}} &= c + \mathrm{i}\, d, \end{aligned} \tag{1.68}$$

with $a, b, c, d \in \mathbb{R}$. (Remember that the complex numbers $G_{1\mathrm{p}}$ and $G_{1\mathrm{q}}$ represent the signal at ω_sig in the two demodulator channels). Demodulating the ω_m component in the photocurrent with the demodulation phase χ yields the output signal

$$y(\chi) = G_1(\chi)\, x + n = (G_{1\mathrm{p}} \cos\chi + G_{1\mathrm{q}} \sin\chi)\, x + n. \tag{1.69}$$

According to the assumptions about the noise, the noise level n is independent of χ. The signal x can therefore be reconstructed from the output y as

$$\hat{x} = \frac{y(\chi)}{G_1(\chi)} = x + \frac{n}{|G_1(\chi)|}. \tag{1.70}$$

Similar to Equation (1.67), we can hence take

$$u = |G_1(\chi)| \tag{1.71}$$

either as a figure of merit for the transfer functions (for constant noise) or as measure of the SNR (for constant signal). We ask which demodulation phase χ yields the maximum output signal. To simplify the mathematics we look at the squared magnitude u^2:

$$u^2 = |G_1(\chi)|^2 \longrightarrow \max. \tag{1.72}$$

Straightforward algebra yields

$$u^2 = (a^2 + b^2) \cos^2\chi + (c^2 + d^2) \sin^2\chi + (ac + bd) \sin(2\chi). \tag{1.73}$$

Solving $\partial u^2/\partial\chi = 0$ for χ yields the optimal demodulation phase

$$\chi_{\rm opt} = \pm\frac{1}{2}\arccos\left(\frac{a^2+b^2-c^2-d^2}{w}\right), \tag{1.74}$$

where the abbreviation

$$w = \sqrt{(b+c)^2+(a-d)^2}\sqrt{(b-c)^2+(a+d)^2} \tag{1.75}$$

has been introduced. The '+' or '−' sign in Equation (1.74) must be used for

$$ac+bd > 0 \quad \text{or} \quad ac+bd < 0. \tag{1.76}$$

Note that $ac+bd$ can be computed as $\Re\{G_{\rm 1p}\cdot G^*_{\rm 1q}\}$. Substituting $\chi_{\rm opt}$ in u yields

$$u^2_{\rm opt} = \frac{1}{2}\left(a^2+b^2+c^2+d^2+w\right). \tag{1.77}$$

To obtain this result, the following identities valid for $x \in [-1,1]$ were applied:

$$\begin{aligned}\cos\left(\frac{1}{2}\arccos x\right) &= \sqrt{\frac{1+x}{2}},\\ \sin\left(\frac{1}{2}\arccos x\right) &= \sqrt{\frac{1-x}{2}}.\end{aligned} \tag{1.78}$$

In the expression for $u^2_{\rm opt}$ (Equation (1.77)), no case distinction is necessary.

In experimental practice, the optimal phase $\chi_{\rm opt}$ will be chosen for one particular signal frequency[15]. In the simulation this corresponds to solving Equation (1.74) for that frequency (note that a, b, c and d are the components of the frequency-dependent transfer functions), and then using this phase $\chi_{\rm opt}$ for *all* signal frequencies of interest. This kind of calculation was done to compare experiment and theory in the *detuned* case of dual recycling (see Section 1.10 and the program in Appendix E.2.4).

We now examine a few special cases for a fixed signal frequency:

- If one of the $\omega_{\rm m}$ quadratures vanishes, for example $G_{\rm 1q} = 0$, we get the expected results:

$$\begin{aligned} c = d &= 0,\\ w &= a^2+b^2,\\ \chi_{\rm opt} &= 0,\\ u_{\rm opt} &= \sqrt{a^2+b^2} = |G_{\rm 1p}|.\end{aligned} \tag{1.79}$$

  The magnitude of the signal (and also the SNR) is the same as if two mixers were used.

---

[15] In the 30m prototype, this was done by dithering the parameter of interest (e.g. the Michelson phase) at an audible frequency and then adjusting the demodulation phase for maximal output signal, which was monitored with headphones (see Section 1.8.1).

- If the signal appears with equal amplitude and the same phase in both ω_{m} quadratures, i.e. $G_{1\mathrm{p}} = G_{1\mathrm{q}}$, we get:

$$\begin{aligned} a = c &= \hat{a}/\sqrt{2}, \\ b = d &= \hat{b}/\sqrt{2}, \\ w &= \hat{a}^2 + \hat{b}^2, \\ \chi_{\mathrm{opt}} &= +\frac{\pi}{4}, \\ u_{\mathrm{opt}} &= \sqrt{\hat{a}^2 + \hat{b}^2} = \sqrt{|G_{1\mathrm{p}}|^2 + |G_{1\mathrm{q}}|^2}, \end{aligned} \tag{1.80}$$

  again as expected. Now the case distinction in Equation (1.74) becomes important, and similar results are obtained for $G_{1\mathrm{p}} = -G_{1\mathrm{q}}$ with $\chi_{\mathrm{opt}} = -\pi/4$. The magnitude of the signal (and also the SNR) is the same as if two mixers were used.

- Another interesting special case occurs if $G_{1\mathrm{p}}$ and $G_{1\mathrm{q}}$ are 90° out of phase. For example, suppose $b = c = 0$. This means that with a demodulation phase $\chi = 0$ we obtain the signal with amplitude a, whereas with $\chi = 90°$ we obtain the signal with amplitude d, but 90° out of phase (at ω_{sig}) as compared to a. The above equations then yield:

$$\begin{aligned} b = c &= 0, \\ w &= |a+d| \cdot |a-d| = |a^2 - d^2|, \\ \chi_{\mathrm{opt}} &= \begin{cases} 0; & |a| > |d|, \\ \frac{\pi}{2}; & |a| < |d|. \end{cases} \\ u_{\mathrm{opt}} &= \max(|a|, |d|). \end{aligned} \tag{1.81}$$

  In the extreme case of $a = d$, the recovered signal u is independent of the demodulation phase: $u \equiv |a|$. This is a factor of $\sqrt{2}$ worse than the result obtainable with two mixers, $\sqrt{|G_{1\mathrm{p}}|^2 + |G_{1\mathrm{q}}|^2} = |a|\sqrt{2}$. This extreme case may seem artificially constructed. Indeed it is, but we will see that in *detuned* dual recycling almost any relationship between $G_{1\mathrm{p}}$ and $G_{1\mathrm{q}}$ can appear.

1.4.6.3 Loss in SNR by using only one mixer

The ratio of the optimal SNR with two mixers, SNR_2, to the SNR with one mixer (assuming optimal demodulation phase χ for the frequency of interest), called SNR_1, is in the general case given by (see Equations (1.67) and (1.77)):

$$r_{21} := \frac{\mathrm{SNR}_2}{\mathrm{SNR}_1} = \sqrt{\frac{2(a^2+b^2+c^2+d^2)}{a^2+b^2+c^2+d^2+w}}. \tag{1.82}$$

After some algebra one obtains

$$r_{21} = \sqrt{\frac{2}{1+f}} \tag{1.83}$$

with

$$\begin{aligned} f &= \sqrt{\frac{1+\alpha^2+2\alpha\cos(2\beta)}{1+\alpha}}\,, \\ \alpha &= \left|\frac{H_{1\mathrm{p}}}{H_{1\mathrm{q}}}\right|^2, \\ \beta &= \angle\left(\frac{H_{1\mathrm{p}}}{H_{1\mathrm{q}}}\right). \end{aligned} \tag{1.84}$$

It can be seen that the loss in SNR by using only one mixer with the optimized demodulation phase χ_{opt} instead of using two mixers is between 0 dB and 3 dB. For $\cos(2\beta) = 1$, i.e. when $H_{1\mathrm{p}}$ and $H_{1\mathrm{q}}$ are either in phase or 180° out of phase, there is no loss in SNR (but note that this is in general only true for the one signal frequency for which χ is optimized). The maximal loss, 3 dB, appears when $H_{1\mathrm{p}}$ and $H_{1\mathrm{q}}$ are 90° out of phase and $\alpha = 1$ (see the example of Equation (1.81)).

Since for a gravitational wave detector no avoidable loss in SNR can be tolerated, the main output will certainly have two mixers. Another reason for two mixers is that (at least in detuned dual recycling) the optimal demodulation phase χ_{opt} is frequency dependent and changes by up to 90° around the sensitivity maximum. For the following discussions of the interferometer's frequency response, we will take $\sqrt{|G_{1\mathrm{p}}|^2 + |G_{1\mathrm{q}}|^2}$ (Equation (1.67)) as measure of the frequency response (see also Equation (1.85) below).

1.5 Signal recycling: Frequency response

The frequency response meant here is the detector's output signal per unit amplitude phase modulation of the Michelson, as a function of the signal frequency, i.e. the frequency dependent response of the detector to a (hypothetical) gravitational wave signal.

It will be computed as the frequency response *from* signal sidebands differentially entered into the arms (such as by a gravitational wave) *to* the photocurrent at the South port (the dark fringe port), demodulated at ω_{m}, i.e. $G_{1\mathrm{p}}$ and $G_{1\mathrm{q}}$ at the South port.

The frequency response of the dual-recycled 30 m prototype will be discussed using results of Jun's program (see Section 1.4). Only a few examples will be given for longer interferometers such as GEO 600, because optimal parameters still need to be found. The optical parameters of the prototype are given in Appendix A.4.

1.5.1 'Broadband' and 'detuned'

At this point it is useful to introduce and clarify the terms 'broadband' and 'detuned'.

The term 'broadband' is defined for this work to mean that operating point of the SR cavity where the carrier frequency is resonant (also indicated by $\varphi_{\mathrm{SR}} = 0 \mod 2\pi$). It corresponds to a maximum in the frequency response at zero signal frequency. The frequency response behaves like a one-pole low-pass filter with a corner frequency of $\mathrm{FWHM}_{\mathrm{SR}}/2$ (see Section 1.5.3 below, Appendix D.3.1 and Figure 1.19 for an example).

All other operating points are called 'detuned' (i.e. the SR cavity is not tuned to the carrier, $\varphi_{\mathrm{SR}} \neq 0 \mod 2\pi$). The frequency response typically has a maximum at some other signal frequency $\neq 0$. The bandwidth of that sensitivity peak is typically $\mathrm{FWHM}_{\mathrm{SR}}$. Detuned dual recycling is further discussed in Section 1.10.

This terminology is not optimal, since the signal bandwidth in the broadband case is from 0 to $\mathrm{FWHM}_{\mathrm{SR}}/2$, whereas in the detuned case it is $\mathrm{FWHM}_{\mathrm{SR}}$ centered around some higher non-zero frequency, i.e. twice as wide. In practice, however, different reflectivities of M_{SR} will be optimal for the two cases, and therefore the 'broadband' response will usually have a wider bandwidth than the 'detuned' response. Lacking better terms, we will continue to use 'broadband' and 'detuned' as defined above.

1.5.2 Transfer function and signal-to-noise ratio

The output signal, caused by signal sidebands entered into the arms, consists of two factors: The frequency response for the signal sidebands and the throughput of the Schnupp modulation sidebands. One condition for an optimal shot-noise limited signal-to-noise ratio (SNR) is that the light power in the Schnupp modulation sidebands must dominate all other light at the output port, in particular it must dominate the 'waste' light in higher transversal modes caused by imperfect contrast. Since this condition is fulfilled for the dual-recycled prototype, and must be fulfilled for GEO 600, we assume it to be true in the following discussion. Then the SNR (to first order) is independent of the power in the Schnupp sidebands, assuming all other parameters remain constant (in particular the power circulating in the PR cavity).

This can be seen as follows: Doubling the *amplitude* of the Schnupp sidebands will double the useful output signal, because the photocurrent at ω_{m} is proportional to the product of the Schnupp sideband amplitude and the signal sideband amplitude (Equations (1.54) and (1.55)). Simultaneously the average power at the dark fringe port will be increased by a factor of four (because the Schnupp sidebands dominate that power), resulting in a doubled shot noise. Hence the SNR remains constant.

However the direct output of Jun's program, i.e. the function $\sqrt{|G_{1\mathrm{p}}|^2 + |G_{1\mathrm{q}}|^2}$, is proportional to the product of the above two factors and is hence not a faithful measure of SNR, when the power in the Schnupp sidebands is not constant.

One possibility to compare the interferometer response under varying conditions (which may involve varying amplitudes of the Schnupp modulation sidebands at the output), is to define a normalized response by

$$G_{\mathrm{n}} = \frac{\sqrt{|G_{1\mathrm{p}}|^2 + |G_{1\mathrm{q}}|^2}}{\sqrt{H_0}} \tag{1.85}$$

The denominator is the square root of the average (DC) power at the corresponding output (Equation (1.49)). The quotient G_{n} is proportional to the shot-noise limited sensitivity (i.e. a larger quotient means better sensitivity), because the shot noise is proportional to the square root of the DC photocurrent (see also the remark following Equation (1.61)). The main proportionality constants, which are not taken into account by Equation (1.85), involve the armlength (see Equation (1.52)), and the injected laser power (see, e.g., Equation (1.93)). Transfer functions in this work are compared under the assumption of constant armlength and constant injected laser power.

The complete computation of an interferometer's SNR involves many other aspects which are beyond the scope of this work, such as thermal noise in the test masses or nonstationary shot noise. Furthermore, even in the purely optical transfer functions, there are technical tradeoffs such as a maximum practical light power inside the interferometer before thermal lenses become important. Hence no attempt is made in this work to define or compute anything like an absolute shot-noise limited sensitivity. Instead, the emphasis is on 'changes' in sensitivity caused by changes in the configuration, such as parameter variation or tuning of the interferometer.

1.5.3 Signal sideband transfer function

The transfer function for the signal sidebands can be computed with Jun's program. Often it is, however, sufficient to employ the much simpler model of a two-mirror *signal recycling cavity* (see Figure 1.4). The 'rear mirror' of that cavity is the combination of both end mirrors and will usually have a much higher reflectivity than the signal recycling mirror. Furthermore it can normally be assumed that the small armlength difference has no effect. Then the results of Appendix D can be applied. The transfer function for light amplitudes produced inside the cavity is given by

$$H_{\mathrm{bb}} = \frac{-\mathrm{i}\,\tau_{\mathrm{SR}}\exp(\mathrm{i}\,kL)}{1-\rho_{\mathrm{SR}}\exp(2\,\mathrm{i}\,kL)}, \tag{1.86}$$

where k is the 'wavenumber' of the signal sideband given by

$$k = \pm\frac{2\pi f_{\mathrm{sig}}}{c} = \pm\frac{\omega_{\mathrm{sig}}}{c} \tag{1.87}$$

for the upper and lower signal sideband, respectively (see Section 1.2.3). This situation is shown in Figure 1.22.

The SR cavity is resonant for the carrier frequency. Hence both signal sidebands experience the same absolute gain. The final output signal is proportional to the light amplitude in the signal sidebands. The cavity bandwidth FWHM is defined in terms of power, such that for amplitudes it corresponds to the 3 dB corner frequency. The whole system behaves like a one-pole low-pass filter with a corner frequency of

$$B_{\mathrm{bb}} = \frac{\mathrm{FWHM}_{\mathrm{SR}}}{2} = \frac{c\,T_{\mathrm{SR}}}{8\pi L}, \tag{1.88}$$

which amounts to 15.4 kHz for the 3.88 % SR mirror of the prototype (see Equation (1.89) and Appendix D.3.1).

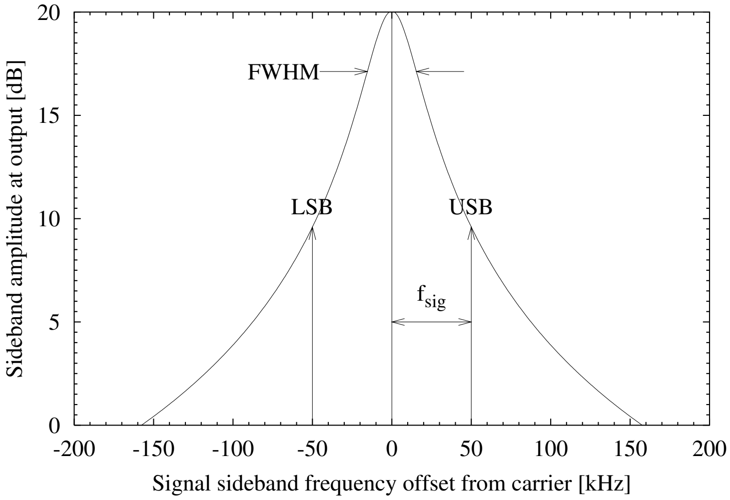

Figure 1.22: Amplitude transfer function in broadband signal recycling, using the parameters of the prototype (30 m armlength and 3.88 % SR mirror transmission). The signal frequency used for the example is 50 kHz.

Generally this FWHM bandwidth of the SR cavity is given by

$$\mathrm{FWHM_{SR}} = \frac{c\,T_{\mathrm{SR}}}{4\pi L}. \tag{1.89}$$

For the 30 m prototype, the numeric value is roughly

$$\mathrm{FWHM_{SR}} = 8\,\mathrm{kHz} \times \left[\frac{T_{\mathrm{SR}}}{1\,\%}\right], \tag{1.90}$$

while for GEO 600 ($NL = 1200\,\mathrm{m}$) we have

$$\mathrm{FWHM_{SR}} = 200\,\mathrm{Hz} \times \left[\frac{T_{\mathrm{SR}}}{1\,\%}\right]. \tag{1.91}$$

The gain for low-frequency signals (below B_{bb}) is given by

$$H_{\mathrm{bb,DC}} = \frac{2}{\tau_{\mathrm{SR}}}, \tag{1.92}$$

which amounts to 10.15 for the prototype. It is referred to an otherwise similar system without signal recycling.

One main experimental result of the broadband DR experiment at the prototype was the confirmation of this gain factor (see Section 1.8.2).

If the above approximations are not valid, the precise frequency response can be computed with Jun's program (see e.g. Figure 1.19).

This gain is equivalent to the improvement in SNR of the detector as compared to the same detector without signal recycling, if everything else remains constant. One parameter that will *not* remain constant by the addition of signal recycling is the amplitude of the Schnupp sidebands at the output. For the present comparison it can, however, be assumed that they are optimized in each case such that their effect is cancelled.

Figure 1.23 shows the signal gain obtainable by signal recycling in the prototype for various transmissions of $\mathrm{M_{SR}}$. The reduced gain of the topmost curve is caused by finite losses of the interferometer (which are included in the model as a power loss of 0.1 % at each end mirror).

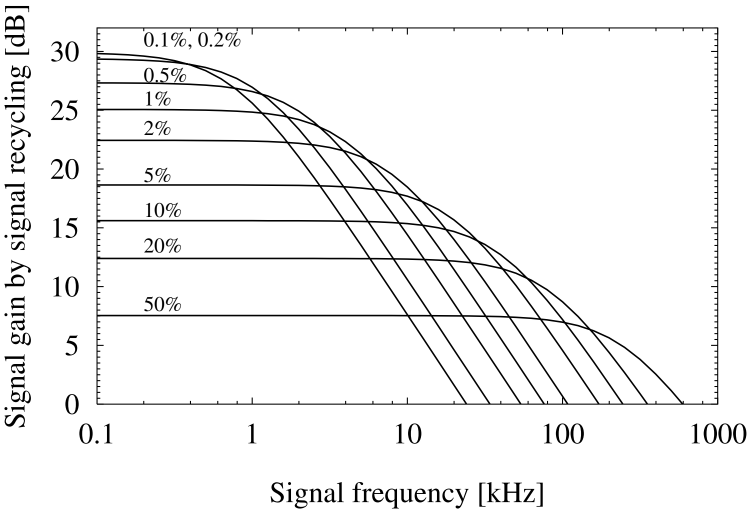

Figure 1.23: Signal gain obtainable in the 30 m prototype by signal recycling, compared against the signal without $\mathrm{M_{SR}}$. The numbers printed are the power transmissions τ_{SR}^2 of $\mathrm{M_{SR}}$. It is assumed that the local oscillator (Schnupp modulation sidebands) is the same for each curve.

The curves were obtained by computing G_{n} (Equation (1.85)) with Jun's program and referencing them to the case without $\mathrm{M_{SR}}$. They can be approximately predicted by Equations (1.88) and (1.92).

It has previously been shown [MPQ203, Section 3.1.3] that the shot-noise limited sensitivity of a general Michelson-based interferometer can be approximated by

$$\widetilde{h} \gtrapprox \sqrt{\frac{2\hbar\lambda}{\pi c}\frac{B}{E}}\,, \tag{1.93}$$

where B is the effective bandwidth of the detector and E is the light energy stored in the arms. The dependence on the bandwidth is also apparent in equations (1.88) and (1.92), which can be combined to yield

$$H_{\mathrm{bb,DC}} \sim \frac{1}{\sqrt{B_{\mathrm{bb}}}}. \tag{1.94}$$

A higher value of H means more signal with the same noise, and hence better sensitivity, whereas the $\widetilde{h}$ of equation (1.93) is defined reciprocally, i.e. a lower value means better sensitivity.

1.5.4 Schnupp modulation sideband throughput

As far as the signal sidebands are concerned, the PR cavity and SR cavity could be considered separate in the preceding section. For reasons explained below, this is no longer true for the Schnupp modulation sidebands. They resonante in the complete interferometer formed by the beamsplitter and a mirror in each of the four directions.

We are mainly interested in the efficiency with which the Schnupp modulation sidebands are transferred to the main detection port (South), where they are needed as local oscillator to detect the Michelson phase. We will use the term ‘throughput’ to denote this coupling efficiency, which in general depends both on the Schnupp modulation frequency and on the state of the interferometer.

There are two coupling mechanisms between the PR cavity and the SR cavity. The first applies to signals that are produced differentially (i.e. in anti-phase) in the arms. On their first encounter with the beamsplitter, such signals go in the other direction compared to the carrier. In particular, the signal sidebands are transferred into the SR cavity, where they circulate. This is the only relevant coupling mechanism for the signal sidebands and is explained in Section 1.1.2.

The second coupling mechanism is only present in systems with Schnupp modulation and is caused by the armlength difference between the two arms. It will turn out to be proportional to the sideband frequency and is hence relevant only for the Schnupp modulation sidebands with their much higher frequency. Because of its importance it is explained here again in detail (see also Section 1.3.3).

Assume a Michelson interferometer with armlengths $L + \Delta L/2$ and $L - \Delta L/2$ (see Figure 1.24) at the dark-fringe operating point for the carrier. All carrier light will be reflected back to where it came from. Now consider a light beam of frequency ω with respect to the carrier. Its corresponding wavenumber offset is $k = \omega/c$.

The light returning from the first arm has travelled a distance $2L + \Delta L$ and has hence the amplitude

$$a_1 = \mathrm{i}\,\tau a_0 \exp[\,\mathrm{i}\,k(2L + \Delta L)], \tag{1.95}$$

whereas the light beam returning from the second arm has the amplitude

$$a_2 = -\rho a_0 \exp[\,\mathrm{i}\,k(2L - \Delta L)], \tag{1.96}$$

where the ‘$-$’ sign ensures the dark-fringe condition for the carrier. Upon their recombination at the beamsplitter the two interference products a_3 and a_4 are formed, which

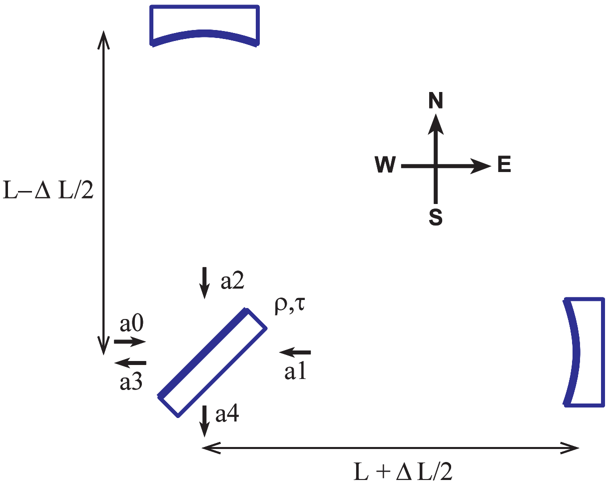

Figure 1.24: A Michelson interferometer with an armlength difference ΔL. The incoming beam a_0 is split into two parts. When they return from the two arms (as a_1 and a_2), a phase difference has evolved between them. After recombination at the beamsplitter, new beams a_3 and a_4 are formed.

travel West and South, respectively. Their amplitudes are

$$\begin{aligned}
a_3 &= \mathrm{i}\,\tau a_1 + \rho a_2 \\
&= -a_0 \exp(\mathrm{i}\,2kL)[\rho^2 \exp(\mathrm{i}\,k\Delta L) + \tau^2 \exp(-\mathrm{i}\,k\Delta L)] \\
&\approx -a_0(\rho^2+\tau^2)\exp(\mathrm{i}\,2kL)\cos(k\Delta L) \quad \text{for} \quad \rho^2 \approx \tau^2, \\
a_4 &= \rho a_1 + \mathrm{i}\,\tau a_2 \\
&= 2a_0\rho\tau \exp(\mathrm{i}\,2kL)\sin(k\Delta L).
\end{aligned} \tag{1.97}$$

With a symmetric 50:50 beamsplitter, these expressions simplify to

$$\begin{aligned}
a_3 &= -a_0 \exp(\mathrm{i}\,2kL)\cos(k\Delta L), \\
a_4 &= a_0 \exp(\mathrm{i}\,2kL)\sin(k\Delta L).
\end{aligned} \tag{1.98}$$

It can be seen that a fraction $\sin(k\Delta L)$ of the amplitude is directed in the other direction compared with where the light entered the Michelson. Light originally circulating in the PR cavity is directed south towards $\mathrm{M_{SR}}$ and hence enters the SR cavity, and vice versa. The PR cavity and SR cavity can be understood as a system of coupled optical resonators, with a frequency dependent coupling taking place at the beamsplitter. This is symbolically shown in Figure 1.25.

As example, Figure 1.26 shows the 'throughput' of the Schnupp modulation sidebands for the parameters of the 30 m prototype, as computed with Jun's program. All lengths are those of the prototype. For the SR and PR mirrors, two sets of values are plotted, those of the actual experiment ($\tau^2_{\mathrm{PR}} = 7\,\%$, $\tau^2_{\mathrm{SR}} = 3.88\,\%$) and another set with $\tau^2_{\mathrm{PR}} = 1\,\%$ and $\tau^2_{\mathrm{SR}} = 2\,\%$. The frequency range shown corresponds to the second harmonics of the cavity free spectral ranges, because frequencies in this range were used in the experiment.

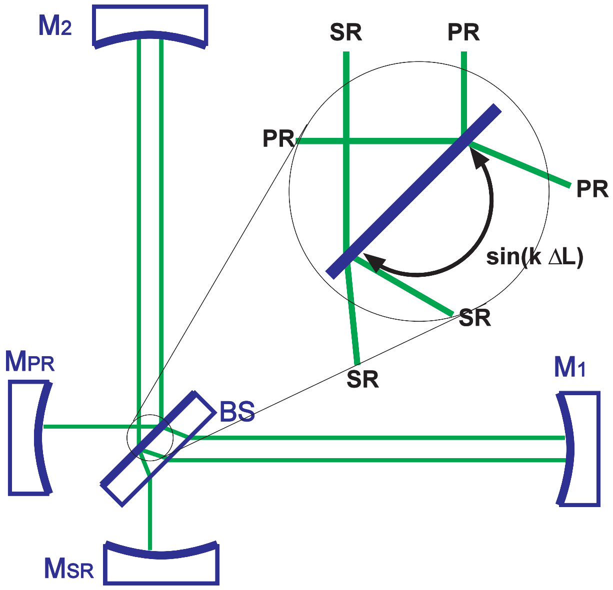

Figure 1.25: Symbolic representation of a dual recycled interferometer with armlength difference ΔL in the dark-fringe condition. For the carrier, PR cavity and SR cavity are independent in this idealized model. For light of other frequencies ($k \neq 0$) there is a coupling between these cavities. Beams in the long arms are shown spatially separated, although in reality they are superimposed.

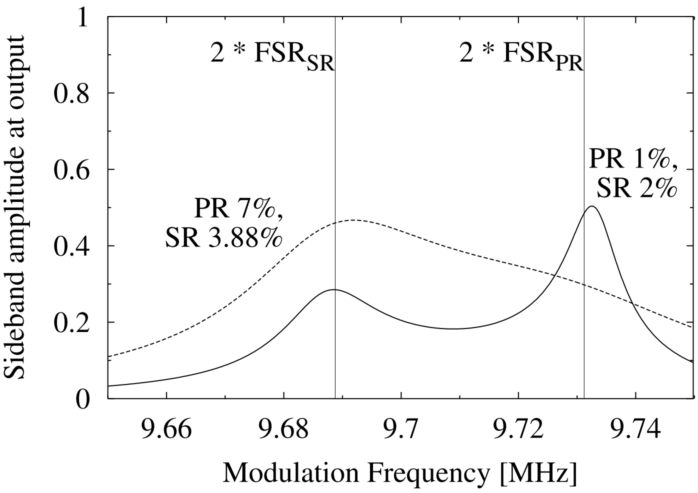

Figure 1.26: Throughput of Schnupp modulation sidebands in the 30 m prototype. Shown is the light amplitude at the South port for light of unity amplitude and the frequency shown referred to the carrier injected in the East port. The vertical lines indicate the position of the free spectral ranges of the two cavities (multiplied by two).

In particular for the more strongly reflective mirrors, the coupled resonances can clearly be seen. Figure 1.27 shows the same function for frequencies ten times higher, i.e. near the 20th multiple of the cavitiy free spectral ranges. The two resonances of the PR cavity and SR cavity are now separated more clearly.

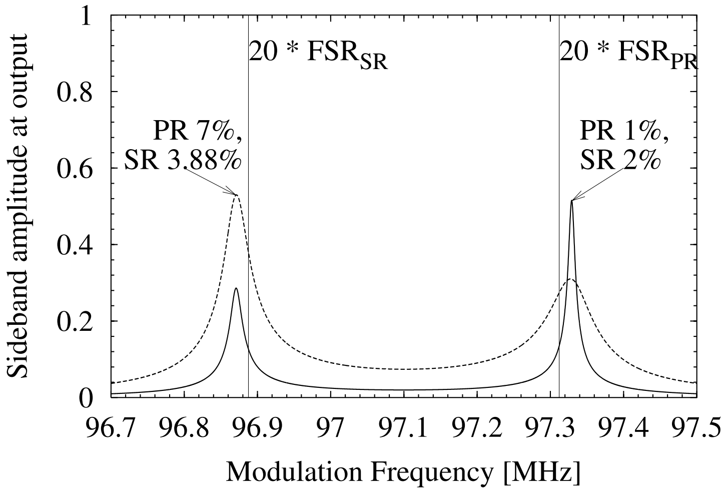

Figure 1.27: Throughput of Schnupp modulation sidebands in the 30 m prototype for modulation frequencies near the 20th free spectral ranges of the PR and SR cavities. All other parameters are the same as in Figure 1.26.

It is interesting that the curves shown can also be reproduced by the equivalent electrical circuit of Figure 1.28. The phenomenon of separating the two resonances by the coupling is exactly equivalent to the same effect in the electrical circuit. In both cases (optical and electrical) it appears also if the two (undamped and uncoupled) resonance frequencies are identical. This electrical model is, however, only of limited practical use because with Jun's program a simulation of the optical system is not much more difficult than a simulation of the electrical circuit. The equivalence holds only for frequencies near one particular multiple of the cavity free spectral ranges and the analogy fails for a detuned interferometer. Furthermore there is no clear equivalence between the parameters of the optical system and those of the electrical circuit.

In practice one will usually strive to choose a Schnupp modulation frequency near or at the throughput maximum, because then the necessary level of modulation at the output can be obtained with the lowest possible modulation index in the Pockels cell, thus reducing the power loss of the carrier and also technical problems such as heating of the crystal and RF pickup in adjacent photodiode preamplifiers.

The armlength difference ΔL is another parameter that influences the Schnupp sideband throughput. One will normally strive to keep it as small as possible, in order to minimize coupling of laser frequency noise into the output signal (see Section 1.8.3).

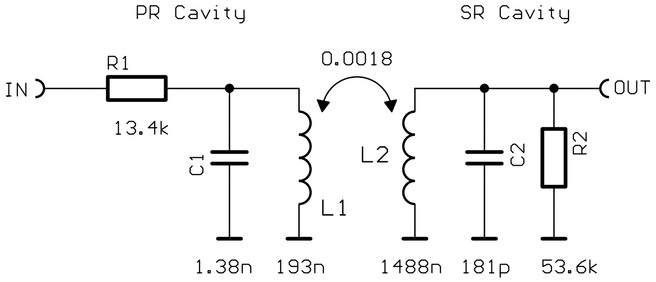

Figure 1.28: An electrical model of coupled resonators. The frequency response of this circuit (for voltages) is exactly identical to the curve shown in Figure 1.26 (with 1 % and 2 % mirrors). The resonance frequencies of the (undamped) L-C resonators were set exactly identical to the free spectral ranges of the SR cavity and PR cavity, multiplied by two.

1.6 Control of signal recycling

One of the main purposes of this work was to investigate control schemes for the dual recycled interferometer. ‘Control’ in this section means longitudinal control of the mirrors, and possibly control of the laser frequency, to ensure the proper interference conditions inside the interferometer (assuming the alignment to be perfect). The discussion in this section mixes general aspects with descriptions of the specific experimental realization in the 30 m prototype.

In a dual recycling interferometer there are three degrees of freedom, if the laser frequency is assumed to be fixed:

Michelson The Michelson interferometer must be in the dark fringe condition. The relevant degree of freedom is the (microscopic) armlength difference. A differential motion of both end mirrors is used as actuator.

PR cavity The incoming carrier light must be resonant in the PR cavity. The length of the PR cavity is equal to the distance from M_{PR} to the ‘average’ of the two end mirrors. Possible actuators are M_{PR} and a common mode motion of the two end mirrors. Another possibility to ensure resonance is to change the laser frequency (see Section 1.6.1.2 below).

SR mirror Finally the microscopic position (tuning) of M_{SR} must be controlled. The control signal is fed directly to M_{SR}.

The control problem has several aspects:

Error signals Jun’s program is used to predict the error signals at the desired operating point. Parameters such as modulation frequencies and armlength differences can be optimized for the ‘best’ error signal. The coupling of the various feedback loops to each other can be investigated.

Actuators The error signals will be passed through loop filters and ultimately need to be fed back to the interferometer. Directly moving the mirrors with the coil–magnet (or electrostatic) actuators provided for that purpose is the obvious possibility. Factors to be investigated are the actuator transfer functions, orthogonality with other degrees of freedom (such as coupling into the alignment) and permissible noise levels. Feedback to the laser frequency is another possible actuation which simultaneously influences several degrees of freedom (see Section 1.6.1.2 below).

Loop filters The loop filters must be designed to provide the necessary gain, in conjunction with the sensors' and actuators' response. Loop stability is the most important question. Unconditionally stable loops are generally preferred for easier lock acquisition.

Lock acquisition Unfortunately it turns out that the three degrees of freedom listed above are not independent. In particular, proper error signals for the Michelson and the SR mirror can only be obtained *after* all three loops are already locked. The question of how to get from the unlocked state (all three degrees of freedom uncontrolled and mirrors freely swinging) to the locked state is very complex. With our simulation tools it is impossible to predict the transient behaviour of the interferometer. Therefore we had to rely on experiment to find a suitable scheme for lock acquisition.

Summarizing the following sections, the number of degrees of freedom is reduced from three to two by having one very robust loop (that for the PR cavity) continuously working, such that the PR cavity is reliably resonant, being almost independent from the state of the rest of the interferometer. Then the mirrors are left swinging randomly. Most of the time the two error signals for the Michelson and SR mirror will be very small and hence cause only negligible feedback action on the mirrors. In their random motion, the remaining degrees of freedom sometimes get near the desired operating point, at which moment the error signals start to get meaningful and the mirrors are 'pushed' in the right direction. After a few (converging) oscillations around the operating point, the system 'drops' into that point and stays there. This takes no more than a few seconds, provided that the alignment is good and the loop gains and demodulation phases are set properly. More details will be given below. An overview of the longitudinal control loops is shown in Figure 1.29.

1.6.1 PR cavity loop

1.6.1.1 Error signal

In normal operation, the PR cavity behaves like a medium-finesse Fabry-Perot, its length being the distance between $\mathrm{M_{PR}}$ and the 'average' of the end mirrors. The error signal is obtained with the usual Pound-Drever-Hall scheme [Drever83b] with a modulation frequency that is not resonant in the cavity. In the prototype the modulation frequency was 12 MHz, which is 2.46 times the PR cavity FSR. At the dark fringe

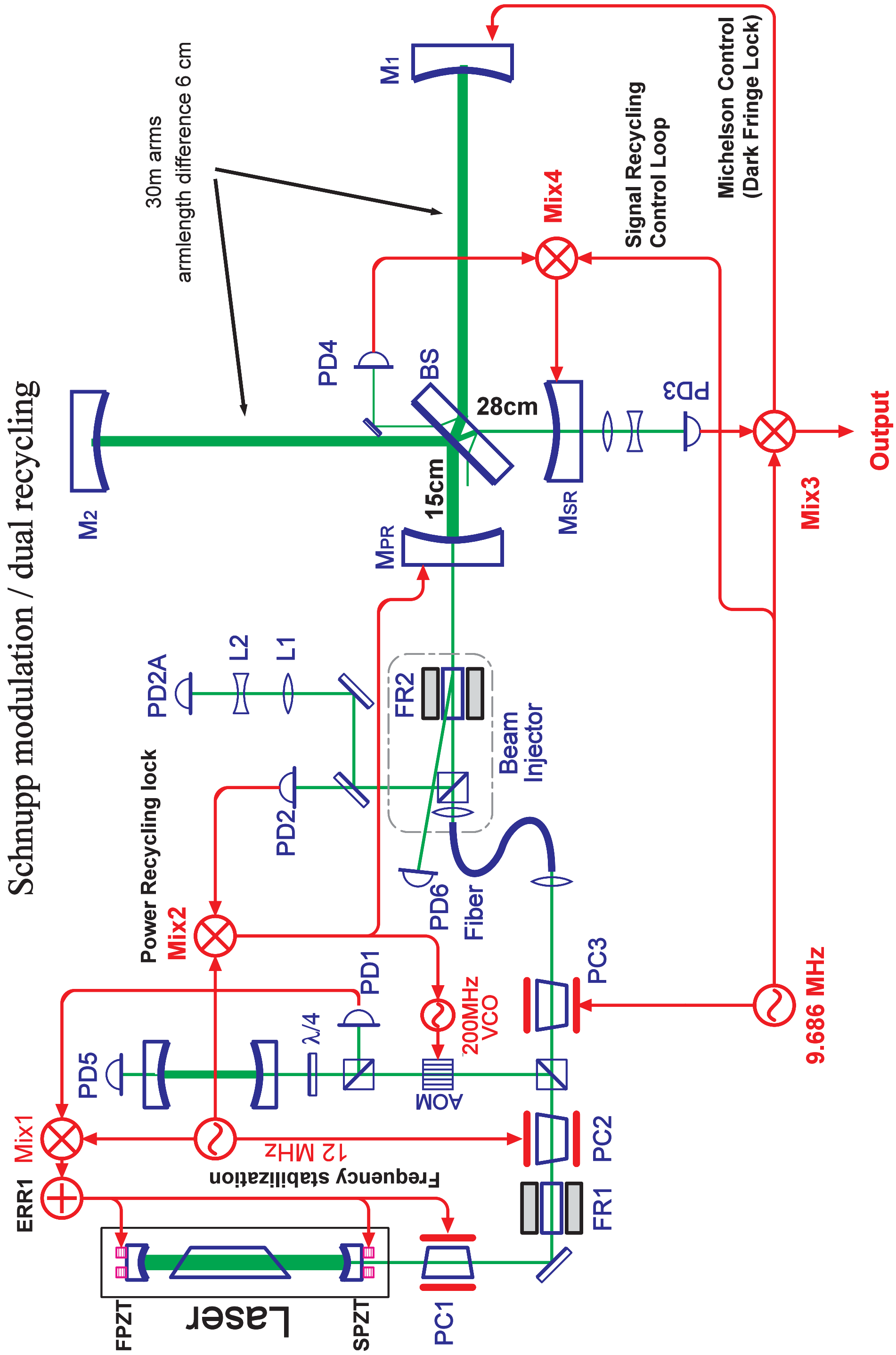

Figure 1.29: Overview of the longitudinal control loops for dual recycling in the 30 m prototype.

operating point, the carrier is resonant in the PR cavity, whereas the 12 MHz modulation sidebands are not resonant. Hence the usual Pound-Drever-Hall error signals are expected. In the prototype, the resonant photodiode PD2 (in Figure 1.29) detects the light that is reflected from the PR cavity and is used to generate the error signal together with mixer Mix2. Figure 1.30 shows the computed error signal as a function of the tuning of M_{PR} at the normal operating point.

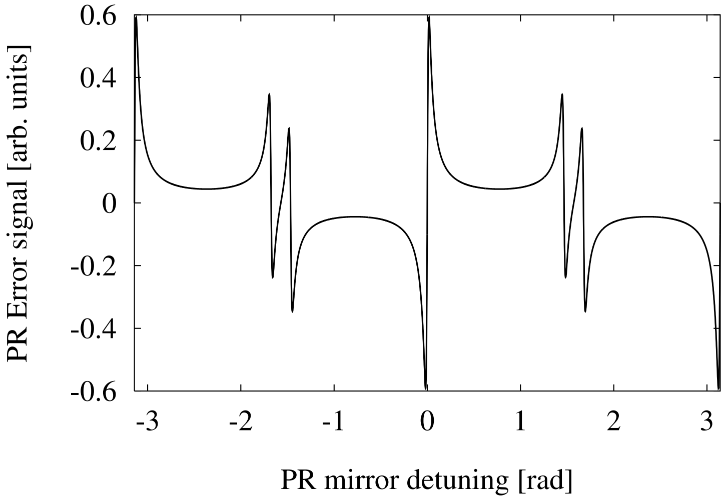

Figure 1.30: PR cavity error signal at the normal operating point.

The strange structure near $\pi/2$ is caused by the fact that the modulation frequency (12 MHz) is not a small fraction of the FSR, as is more usual with Pound-Drever-Hall systems for short cavities, but is rather a non-integer multiple of the FSR. The 'usual' Pound-Drever-Hall signal (central feature with sidebands 12 MHz away) is periodically repeated every FSR (4.8656 MHz) in an overlapping fashion.

If the interferometer is on a dark fringe, the PR cavity error signal is almost independent of the SR cavity tuning. This is, however, not true for an arbitrary state of the interferometer, such as during lock acquisition.

Figure 1.31 shows the PR cavity error signal for six randomly chosen states of the interferometer. The zero position in these plots has been shifted to the desired resonance of the PR cavity, which was determined by the program shown in Appendix E.2.3.

In any case there is a zero-crossing of the error signal. Since the PR cavity loop has been designed with a large gain margin, it will try to lock onto this zero-crossing. Fortunately it was found that the PR loop does lock the PR cavity correctly in almost any state of the interferometer.

It can be seen in Figures 1.30 and 1.31 that there are extra zero crossings of the error signal (near $\varphi_{PR} = \pi/2$ in Figure 1.30), that have the same sign as the 'correct' zero crossing at $\varphi_{PR} = 0$. It was found experimentally that sometimes the PR loop does indeed lock on this 'wrong' operating point. However, because the gain (visible in

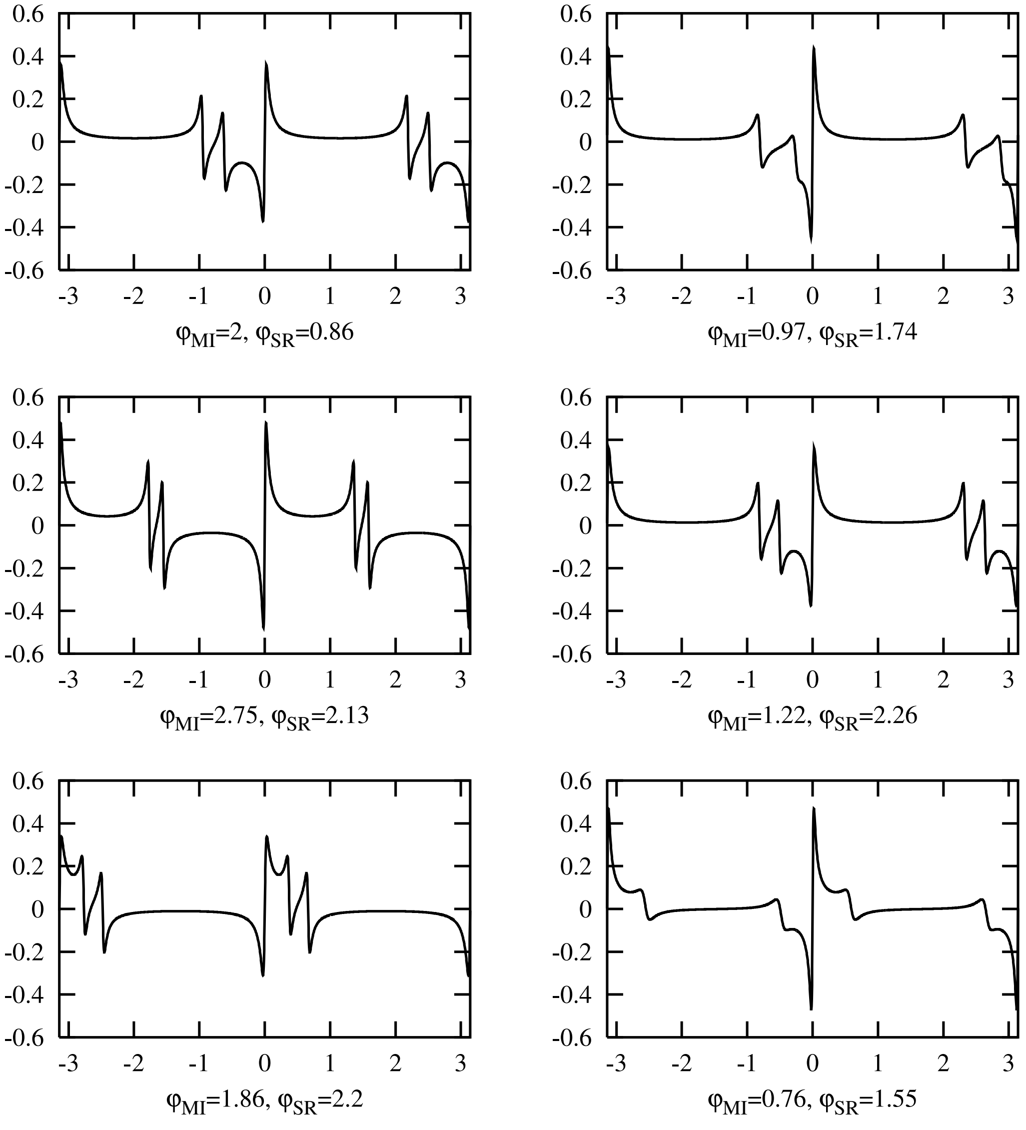

φ_{MI}=2, φ_{SR}=0.86

φ_{MI}=0.97, φ_{SR}=1.74

φ_{MI}=2.75, φ_{SR}=2.13

φ_{MI}=1.22, φ_{SR}=2.26

φ_{MI}=1.86, φ_{SR}=2.2

φ_{MI}=0.76, φ_{SR}=1.55

Figure 1.31: PR cavity error signal at six random operating points of the Michelson (tuning φ_{MI}) and SR mirror (tuning φ_{SR}). The x-axis in these plots is the PR mirror tuning φ_{PR} with an offset such that the desired resonance is at zero.

the plot as slope of the zero-crossing) is much lower, this 'incorrect' condition is not very stable, and the loop usually jumps to the correct operating point during lock acquisition.

1.6.1.2 Actuator

Our strategy for lock acquisition requires the PR cavity loop to lock onto the resonance of the PR cavity under a large variety of cirumstances (i.e. Michelson and SR mirror not yet locked, swinging randomly and/or being pushed around by their respective loops). This demand requires a large gain margin and a control bandwidth much larger than the bandwidth of these other two loops (which is between a few 100 Hz and a few kHz). Feedback to the PR mirror alone cannot provide such a wide control bandwidth. Hence it is necessary to use another actuator with wider bandwidth. A suitable actuator is the laser frequency.

Changing the laser frequency immediately changes the tuning of the PR cavity with a coupling efficiency given by

$$\frac{\partial \varphi_{\mathrm{PR}}}{\partial \nu_{\mathrm{Laser}}} = \frac{\pi}{\mathrm{FSR}_{\mathrm{PR}}} \approx \frac{2\pi}{c}\, 30\,\mathrm{m} \approx 0.6\,\mathrm{rad/MHz}. \tag{1.99}$$

The tuning of the SR cavity is simultaneously changed with about the same efficiency. Due to the armlength difference, the Michelson tuning is also affected by the laser frequency, but with a much smaller coupling efficiency given by

$$\frac{\partial \varphi_{\mathrm{MI}}}{\partial \nu_{\mathrm{Laser}}} \approx \frac{2\pi}{c}\, 2 \cdot 6\,\mathrm{cm} \approx 2.4\,\mathrm{mrad/MHz} \tag{1.100}$$

(see also Section 1.8.3). Hence to a first approximation we may say that by changing the laser frequency we simultaneously tune the PR and SR cavity but not the Michelson.

In earlier experiments in the Garching 30 m prototype (power recycling with external modulation, before the introduction of signal recycling) [Schnier97], the PR cavity error signal was directly fed back to the laser frequency. There are three actuators available for this purpose: two piezos changing the length of the laser cavity and an external Pockels cell acting as phase corrector (see Appendix A.2). The piezos have mechanical resonances which limit their useful frequency range. The overall open-loop gain was a delicate function of the individual actuator gains, crossover frequencies, etc.

During the installation of dual recycling[16], it was, however, found that this direct feedback was too unstable for initially setting up the dual-recycled interferometer.

Hence we have implemented a prestabilization system for the laser frequency. A small fraction of the light is directed on a reference cavity after it has been shifted in frequency by a double-passed acousto-optic modulator (AOM). The laser frequency is locked to the reference cavity with a Pound-Drever-Hall loop, which uses as actuators the two piezos

---

[16] This installation was done in the spring of 1998 in collaboration with Ken Strain and Ken Skeldon from Glasgow.

changing the length of the laser cavity and the external Pockels cell. The bandwidth of this loop is around 300 kHz. This loop (to lock the AOM-shifted laser frequency to the reference cavity) is called '*first loop*' (the reason will become clear in Section 1.7). It is described in more detail in Appendix A.2.

The AOM is driven by a voltage controlled oscillator (VCO) operating at 200 ± 20 MHz. By changing the VCO's input voltage, the frequency of the laser light that enters the interferometer can be changed by ±40 MHz, because the *shifted* laser frequency is locked to the resonance of the reference cavity. This 'laser frequency control' input has a simple flat frequency response up to around 100 kHz, limited by the response of the first loop and additional time delays in the VCO and AOM. The measured frequency response of the VCO/AOM as an actuator for the laser frequency is shown in Figure 1.32. The fitted curve has a single pole at 28 kHz (from the reference cavity) and a time delay of 2 μs (fit by LISO). After electronically compensating the 28 kHz pole, it is used as the actuator for the PR cavity loop with a control bandwidth of up to 70 kHz. The PR cavity loop (which locks the laser frequency and and the PR cavity to each other) is called *'second loop'* in this work. For very slow signals that exceed the range of the VCO/AOM, there is another feedback path that changes the length of the PR cavity via the PR mirror M_{PR}. The crossover frequency between the AOM and M_{PR} is at a few Hz.

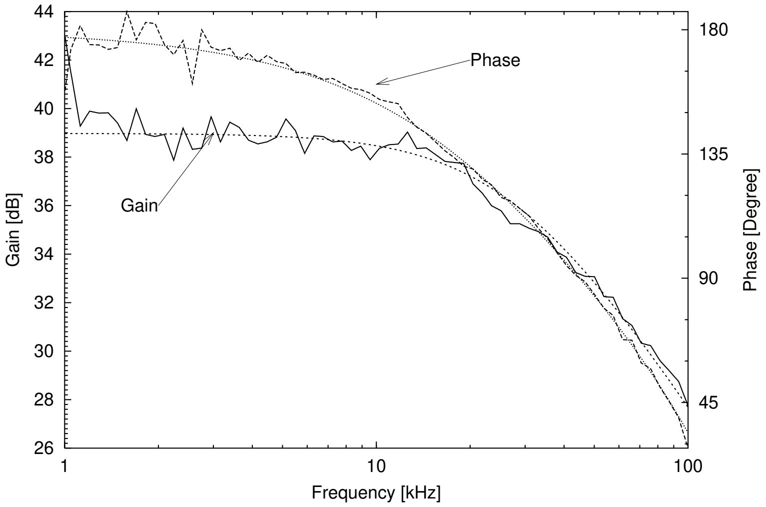

Figure 1.32: Frequency response of the AOM used as an actuator to change the laser frequency via the first loop.

The advantages of using this setup are:

- The frequency of the light entering the interferometer is much more stable, around 5 Hz/$\sqrt{\text{Hz}}$ instead of several 100 kHz/$\sqrt{\text{Hz}}$ at Fourier frequencies of a few 100 Hz. This simplifies lock acquisition of the dual recycled interferometer.
- The feedback loop acting directly on the laser gets its error signal from the refer-

ence cavity, which is much more stable than the interferometer swinging during lock acquisition, and the error signal has constant gain.

- The design of the PR cavity loop is much simplified by the simple actuator (VCO input) now available. During lock acquisition, the finesse of the PR cavity and hence the gain of the PR cavity loop change by several orders of magnitude. Designing a stable loop with an error signal showing such gain variations is much easier if the actuator has a simple frequency response.
- The new setup more closely resembles the planned control system of GEO 600.

To put it in other words, the task of locking the laser frequency to the PR cavity has two problems: The actuators (piezos and Pockels cell) have a problematic frequency response requiring a well-defined loop gain. But the error signal has a huge gain variation during lock acquisition. With the setup described above, a new laser frequency control with a simpler frequency response input is introduced and hence the design of the PR cavity loop becomes manageable. Furthermore, the fluctuations of the laser frequency during lock acquisition are very much reduced, simplifying lock acquisition of the two remaining loops (Michelson and SR cavity).

In the prototype, there is, however, a distinct disadvantage of this approach: that is, noise. The first loop suffers from having low light levels. Around 4 % of the main beam is split off by an uncoated glass plate. After double-passing the AOM, only around one tenth of that light is left over, which, furthermore, is quite distorted in its beam shape. On the laser table, there is not enough space for optimal mode matching lenses. Also, the reference cavity has a low finesse; around 200. All these facts together result in a remaining frequency noise of the prestabilized laser of around $5\,\mathrm{Hz}/\sqrt{\mathrm{Hz}}$ at a few kHz, dominated by sensor noise. This setup was built during the first installation of dual recycling, where the intention was to achieve and study lock acquisiton of the dual recycled interferometer, and the emphasis was put on loop stability rather than noise. Figure 1.33 shows the estimated frequency noise of the prestabilized laser. Note that this is *not* directly measured, but rather deduced from the measurement shown in Figure 1.34 below by correcting for the estimated loop gain of the second loop. Hence the curve shown should only be considered as a rough estimate of an upper limit for the prestabilized laser frequency noise.

The second loop sensor noise is much lower, such that in principle the frequency fluctuations of the prestabilized laser could be further reduced. However, the unity gain frequency of the second loop is only a few tens of kHz, and its gain drops as $1/f$. Figure 1.34 shows the resulting frequency noise (laser frequency referred to PR cavity).

This curve was measured via photodetector **PD2** of Figure 1.29. Its calibration is described in Appendix A.5.2. For autoalignment purposes, there is another photodetector (shown as **PD2A** in Figure 1.29) in the experiment detecting another fraction of the same beam. The measurement was repeated with that (semi-out-of-loop) detector, yielding the same result.

The remaining frequency noise shown in Figure 1.34 often dominates the noise at the main output of the interferometer (see Section 1.8.3). It is coupled there due to the

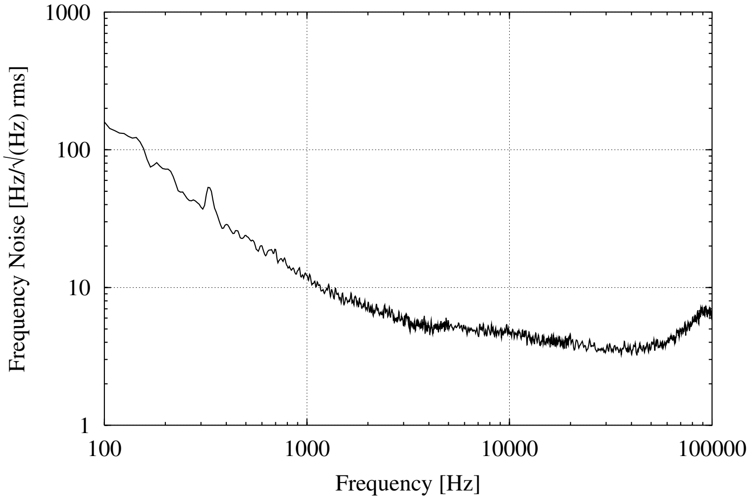

Figure 1.33: Estimated frequency noise of the prestabilized laser (this was *not* directly measured, see text).

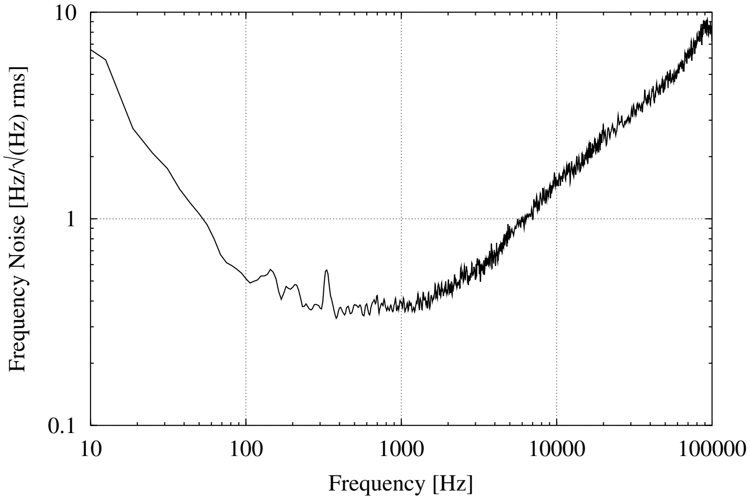

Figure 1.34: Frequency noise (laser frequency referred to PR cavity) with first and second loop in operation.

armlength difference. In the prototype, there would be several possibilities to improve the situation:

The performance of the first loop might be improved by increasing the light level, improving the throughput through the AOM, improving the mode matching and/or using a reference cavity of higher finesse. All these measures are possible in principle, and the author believes that at least one of them should be sufficient to gain a satisfactory improvement. However, they require a major reorganization of the laser table and were not implemented due to time limitations.

The loop gain of the second loop could also be improved. At present it is limited by the actuator's phase delay shown in Figure 1.32. It was believed that feeding back the high-frequency component of the error signal to the first-loop error point (labelled **ERR1** in Figure 1.29) and/or the first loop's phase correcting Pockels cell (**PC1**) might allow for an increase in the second loop unity gain frequency and hence its loop gain. This was tried both by the author and, more thoroughly, by A. Freise and H. Grote during a week-long stay in Garching, but it was not successful. The reason was that these two additional actuators still interact with the first loop. Any frequency correction that they apply is 'seen' by the reference cavity and hence shows up in the first-loop error signal. From there it is amplified and fed back to the three actuators of the first loop. The result is that all the complicated features in the frequency response of these actuators (in particular the 200 kHz resonances of the fast piezo) also show up in the frequency response of the proposed two new actuators, making their frequency response quite complicated and of little use.

A possible solution would be to use another Pockels cell located behind the first loop pickoff (such as **PC3**, which presently only applies the 9.7 MHz Schnupp modulation), as an additional fast actuator for the second loop. Again, this would be possible in principle but not easy to implement in practice and has not been tried due to time limitations.

A further possibility would be to eliminate the first loop altogether and feed the PR cavity error signal directly back to the laser frequency via the three actuators (similar to the frequency stabilization used with external modulation, see Figure A.15). This would probably cure the noise problems, but, on the other hand, make lock acquisition more difficult, because in such a setup the range of interferometer states allowing the PR cavity loop to lock would most likely be smaller than in the present setup (see also Section 1.7).

1.6.1.3 Keeping the PR cavity resonant in the simulation

In the simulation programs, there is a minor complication if the situation in the prototype is to be realistically described. The PR cavity tuning φ_{PR} is defined such that *at the proper operating point* the condition $\varphi_{\mathrm{PR}} = 0$ corresponds to the resonance of the power recycling cavity for the carrier frequency. This is, unfortunately, no longer true if the Michelson is not at the dark fringe condition (as during lock acquisition).

Experimentally, the PR cavity is nearly always kept resonant by the second loop. The bandwidth of that loop is larger than those of the remaining two loops (Michelson and SR). To simulate the Michelson and SR error signals under this condition requires the correct PR cavity tuning φ_{PR} to be found, to make the PR cavity resonant (for arbitrary tunings of the Michelson and SR cavity), because the second loop will enforce this tuning in the experiment.

In the simulation, this can be done by temporarily 'removing' the PR mirror (i.e. setting its reflectivity to zero), injecting carrier light from the West direction and computing the phase of that light when it returns to the West port. The MATHEMATICA code necessary to compute this phase in Jun's model is shown in Appendix E.2.3.

Figure 1.35 shows the resulting PR cavity tuning φ_{PR} that is necessary to make the PR cavity resonant, as a function of the Michelson tuning φ_{MI} for the 30 m prototype with only power recycling, and then for dual recycling (with $\varphi_{\mathrm{SR}} \equiv 0$).

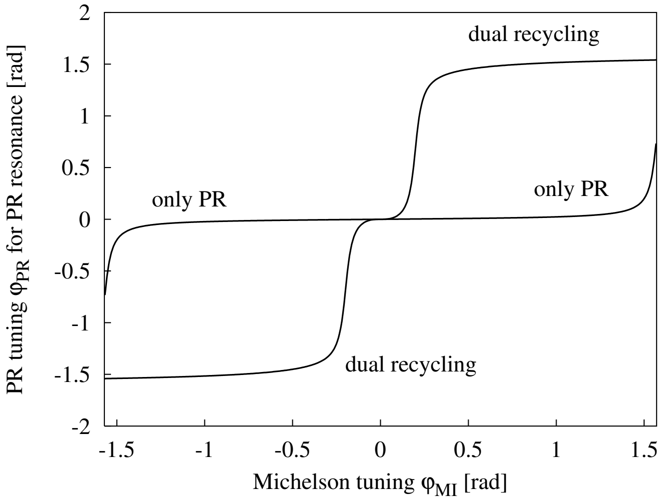

Figure 1.35: The PR cavity tuning φ_{PR} that is necessary to make the PR cavity resonant.

1.6.2 Michelson control

The error signal for the Michelson is obtained by demodulating the photocurrent from the South port at the Schnupp modulation frequency (around 9.7 MHz). In the prototype, the resonant photodiode PD3 together with mixer Mix3 (in Figure 1.29) generate the error signal. In principle, this works as was shown in Section 1.3.3 for a simple Michelson without recycling. The presence of the recycling mirrors does, however, complicate the behaviour of the error signal for operating points other than the dark fringe.

The following discussion uses the parameters of the 30 m prototype, with the only modification being the presence or absence of the signal recycling mirror, as individually indicated.

1.6.2.1 Error signal without signal recycling

The properties of the Michelson error signal are already rather complex in a power-recycled system without signal recycling when Schnupp modulation is used for the readout. The reason is that the Schnupp modulation sidebands, which act as local oscillator for the detection of the signal at the output port, are subject to a complicated resonance of their own in the system (see also Section 1.5.4).

Figure 1.36 shows the throughput of the upper Schnupp sideband from the input (i.e. after the EOM) to the South output. It can be seen that at the proper operating point ($\varphi_{\mathrm{MI}} = 0$), there is only a small amount of Schnupp sidebands available at the output to be used as local oscillator. This is because the armlength difference (6 cm) was optimized for dual recycling but is too small for a system with only power recycling. It can also be seen that the Schnupp sidebands at the output show resonance phenomena including a phase reversal at tunings $\varphi_{\mathrm{MI}} \neq 0$.

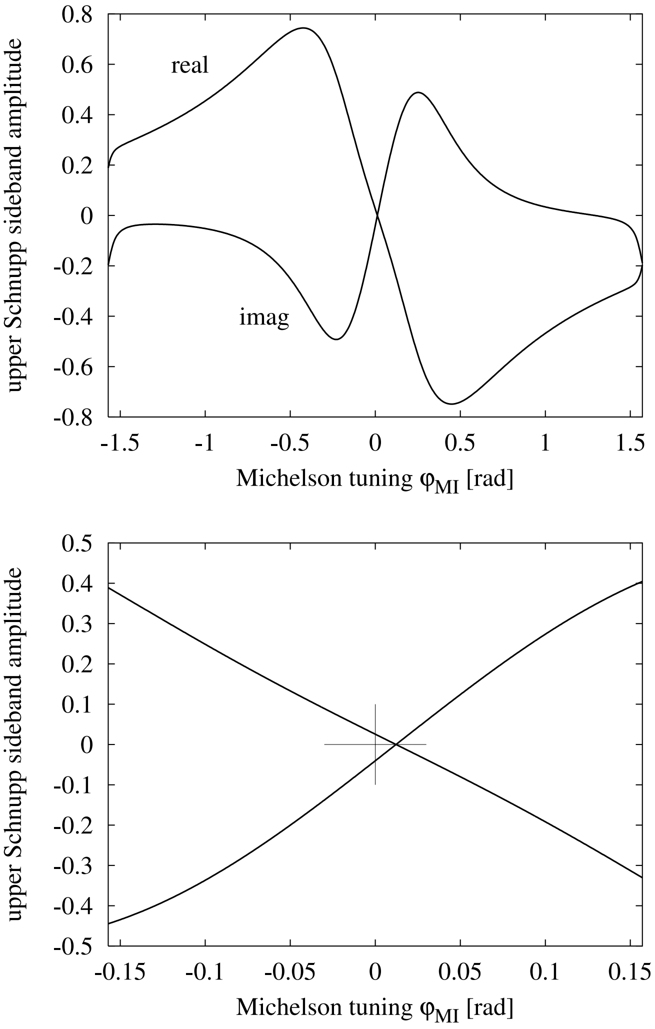

Figure 1.36: Throughput of the upper Schnupp sideband from the EOM to the South port for the 30 m prototype *without* signal recycling, referred to unity input amplitude. The lower curve shows the central part of the upper curve. The corresponding curves for the lower Schnupp sideband are similar, but mirrored at the y-axis $\varphi_{\mathrm{MI}} = 0$.

Figure 1.37 shows the resulting Michelson error signal. Most interesting is the phase reversal of the error signal near tunings $\varphi_{\mathrm{MI}} \approx \pm 0.5$. It is caused by the phase reversal of the local oscillator just mentioned. The 'height' of the phase-reversed peak is smaller than might be expected from Figure 1.36, because at these detunings the PR cavity buildup is already reduced (lower curve of Figure 1.37). The same phenomenon will show up in even stronger form for the case of dual recycling.

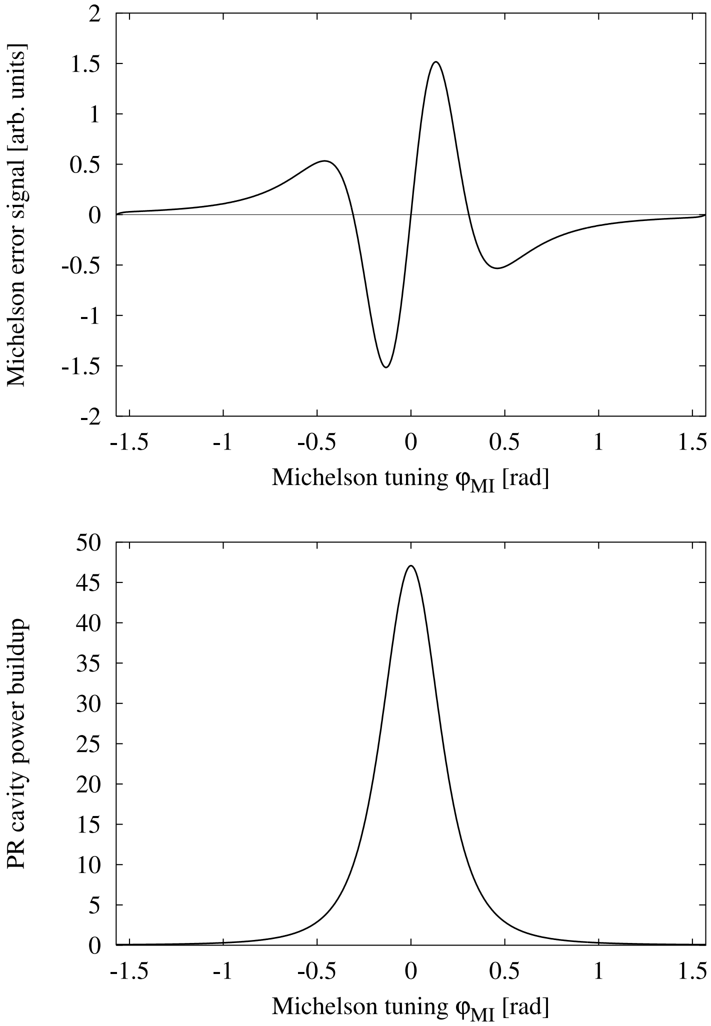

Figure 1.37: Michelson error signal and PR cavity power buildup for the 30 m prototype *without* signal recycling.

The practical consequences of this phase reversal mainly affect the lock acquisition. Clearly the loop designed to keep the Michelson on the dark fringe can only operate in the region where the error signal has the correct sign. In the other regions the loop will strive to move the Michelson even further away from the dark fringe. Fortunately it turned out in the prototype experiments that the loop will nevertheless usually work.

During acquisition the Michelson phase swings freely by several radians, crossing again and again the ‘good’ region of the error signal. If the mirror motion is not too fast at this point, and the loop gain is properly adjusted, then the loop will ‘catch’ the swinging mirrors and hold them at the dark fringe.

It remains to be seen whether this simple lock acquisition scheme will also work for GEO 600, where the relevant cavities have much higher finesse and the ‘good’ region will span a smaller part of the possible Michelson tunings.

1.6.2.2 Error signal with dual recycling

The presence of the SR mirror further complicates things. For example, if the SR mirror is in its zero position (the proper position for broadband SR), the signal sidebands have much more optical gain in the dark fringe condition (this is, after all, the purpose of signal recycling). The additional gain is approximately given by the factor $2/\tau_{\mathrm{SR}}$, compared with the case without the signal recycling mirror (see Equation (1.92) in Section 1.5.3).

If, on the other hand, the SR mirror happens to be in the ‘opposite’ position (represented in the simulation by the tuning $\varphi_{\mathrm{SR}} = \pi/2$), the optical gain for the signal sidebands is only $\tau_{\mathrm{SR}}/2$ in the dark fringe condition (see Appendix D). Hence there is a gain variation of $4/\tau_{\mathrm{SR}}^2$ for the signal sidebands, which amounts to a factor of about 100 for the 3.88 % SR-mirror of the prototype.

In practice however, the Schnupp sidebands, which act as local oscillator at the detection port, also experience a variation in gain and phase depending on φ_{SR}, which makes the situation even worse. Figure 1.38 shows the throughput of the upper Schnupp sideband from the input (i.e. after the EOM) to the South output *with* signal recycling (compare Figure 1.36). The effective gain of the Michelson error signal at the dark fringe varies by a factor of around 9000 instead of 100, when φ_{SR} is varied from 0 to $\pi/2$.

During lock acquisition, neither the Michelson nor the signal recycling mirror will be in their expected position. Instead they swing around freely in the two-dimensional continuum of possible interferometer states.

Figure 1.39 shows the computed Michelson error signal for this continuum of states, again under the assumption that the PR cavity is always kept on resonance (see Section 1.6.1.3). This assumption is made throughout the rest of this Section, even if not explicitly mentioned. Shown is the static response $H_1(\chi_{\mathrm{opt}})$ (Equation (1.50)), where χ_{opt} is the optimal demodulation phase for one mixer (Equation (1.74)), determined for low signal frequencies at the nominal broadband operating point. This is what most closely resembles the actual error signal in the prototype, as it is observed at the output of mixer **Mix3** in Figure 1.29.

Several interesting observations can be made from these diagrams. In a huge fraction of the parameter space, the error signal is negligible (but compare Figure 1.40). Consequently the Michelson dark fringe lock will not act very much on the mirrors in these

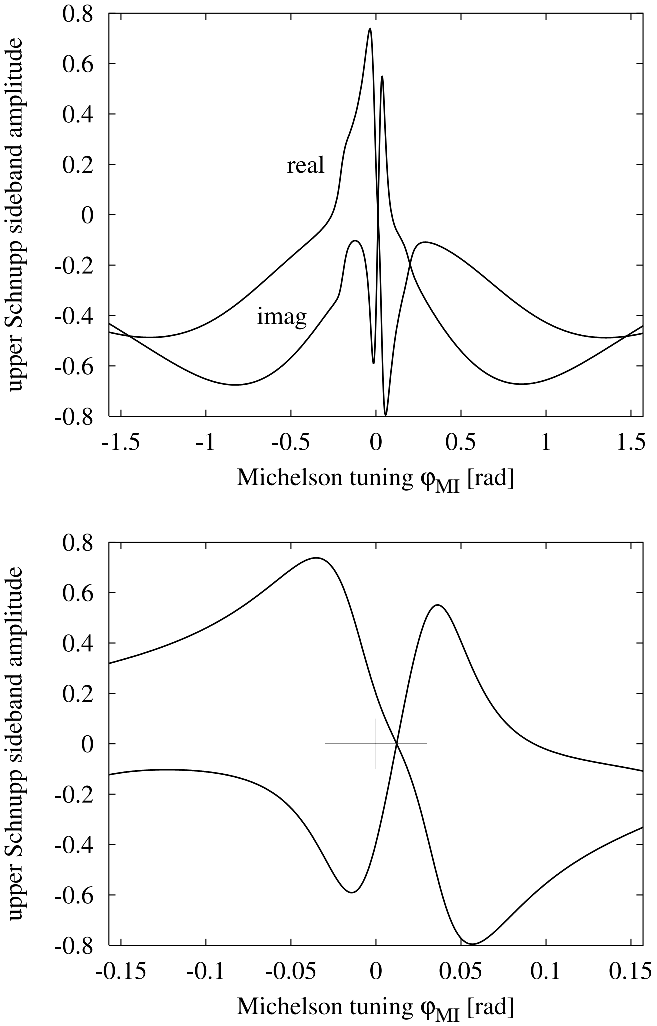

Figure 1.38: Throughput of the upper Schnupp sideband from the EOM to the South port for the 30 m prototype with dual recycling, referred to unity input amplitude. The lower curve shows the central part of the upper curve. The corresponding curves for the lower Schnupp sideband are similar, but mirrored at the y-axis $\varphi_{\mathrm{MI}} = 0$.

regions and more or less leave the mirrors swinging freely. This does in fact help the lock acquisition.

The error signal is strictly zero for $\varphi_{\mathrm{MI}} \equiv 0$, independent of the SR mirror tuning φ_{SR}. This means that, to a first approximation, at the dark fringe operating point, a small motion of the signal recycling mirror (i.e. fluctuation of φ_{SR}) will *not* directly cause a spurious Michelson error signal. This is very desirable, because the Michelson error signal will contain the gravitational wave information and so any potential noise source for that signal is highly undesirable.

The lowest curve shows the Michelson error signal for an assumed tuning $\varphi_{\mathrm{SR}} \equiv 0$ of the

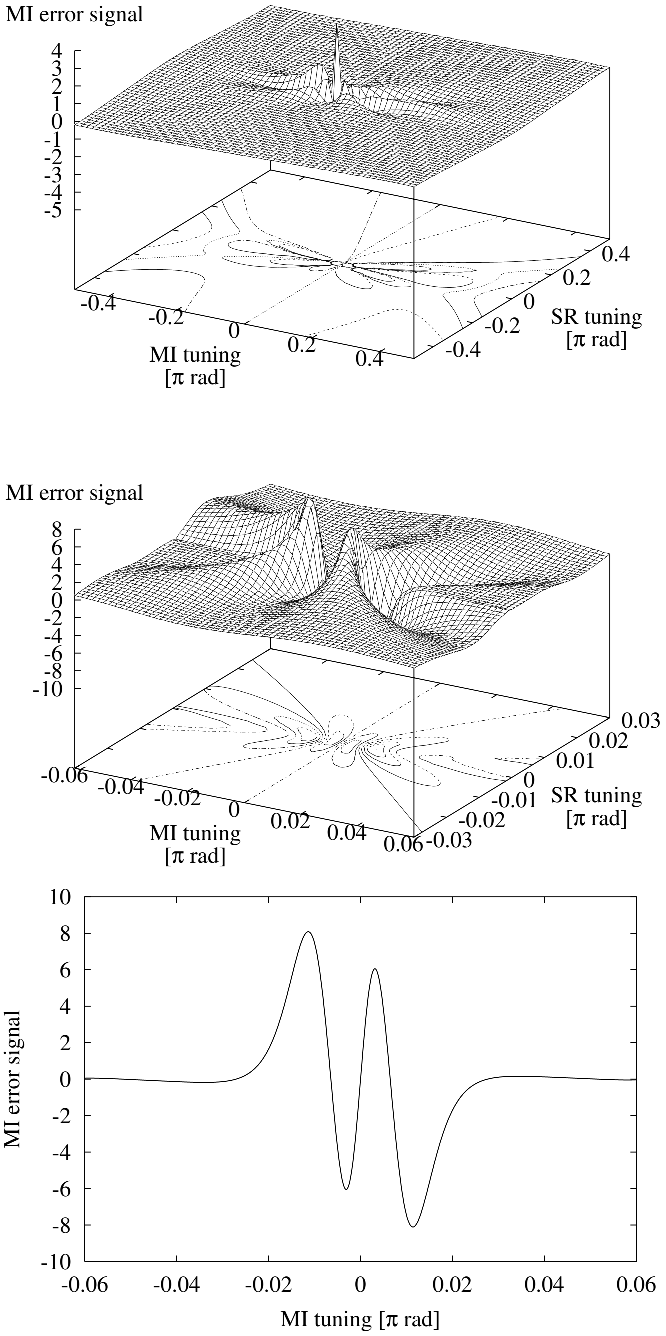

Figure 1.39: Michelson error signal (in arbitrary units) as a function of the tunings φ_{MI} and φ_{SR}, with the PR cavity being kept resonant. The lower curve shows the error signal for $\varphi_{\mathrm{SR}} \equiv 0$. The tunings φ_{MI} and φ_{SR} are expressed as multiples of π in these plots.

SR mirror. In the prototype, this situation cannot be experimentally realized, because the SR mirror will not stay at $\varphi_{\mathrm{SR}} = 0$, if the Michelson is detuned as much as is shown in the Figure. Nevertheless it is interesting to see that the error signal exhibits a similar phase reversal effect as was already apparent in the case of only power recycling (Figure 1.37), but now the effect is even stronger[17].

Figure 1.40 shows the gain in dB of the Michelson error signal. It was computed as the frequency response $\sqrt{|G_{1\mathrm{p}}|^2 + |G_{1\mathrm{q}}|^2}$ (Equation (1.67)) for small signal frequencies, and the gain at the nominal operating point $\varphi_{\mathrm{MI}} = \varphi_{\mathrm{SR}} = 0$ is taken as 0 dB reference. Although not very clearly visible from the diagram, the maximal gain does indeed occur in the center of the diagram, i.e. at the nominal operating point. It is interesting to see, however, that there is a large area of strongly detuned states that have surprisingly high gain.

These states are, however, not attractive as operating points because at these operating points there is much more DC (average) light power arriving at the photodetector (**PD3** in Figure 1.29), and hence the (shot-noise limited) SNR will be reduced. The DC light power is shown in Figure 1.41, referred to unity at the nominal operating point. It was computed as the static response H_0 (Equation (1.49)).

Finally Figure 1.42 shows the theoretical SNR of the Michelson error signal (G_{n} from Equation (1.85)). It was computed by dividing the gain from Figure 1.40 by the square root of the DC light power (Figure 1.41). Again the nominal operating point was taken as 0 dB reference. This plot shows clearly the superiority of the nominal operating point.

1.6.2.3 Actuator and loop filter

In the prototype, the end mirrors are suspended as single pendulums. Their associated local control modules (see Appendix A.3.1) have control inputs that permit the application of small forces directly to the mirror (via coils and magnets). In this way a signal applied differentially (in anti-phase) to both end mirrors serves to control the Michelson tuning, and is now described here. As discussed in Appendix A.3.1, the transfer function of this input, as an actuator for the Michelson phase, has the form of a two-pole low-pass filter.

This transfer function was transformed into a useful open-loop gain by the addition of two $f^{1/2}$ filters active between 3 Hz and 10 kHz (see Appendix B.4). In order to suppress potential disturbances from the resonances above 10 kHz, a two-pole low-pass filter (3 kHz corner frequency) was also included. The resulting open-loop gain for a typical unity-gain frequency of 300 Hz is shown in Figure 1.43. Since this gain turned out to be insufficient to suppress the large fluctuations of the Michelson phase well enough at low frequencies for stable operation of the autoalignment system (in particular near the pendulum resonsance near 1 Hz), an additional filter was added that can be progressively activated via a potentiometer. For that purpose a biquadratic filter with a complex pole at 1 Hz ($Q = 1$) and a complex zero at 20 Hz ($Q = 2$) was

---

[17] The effect is reduced if the PR and SR cavities have the same length (see Section 1.11).

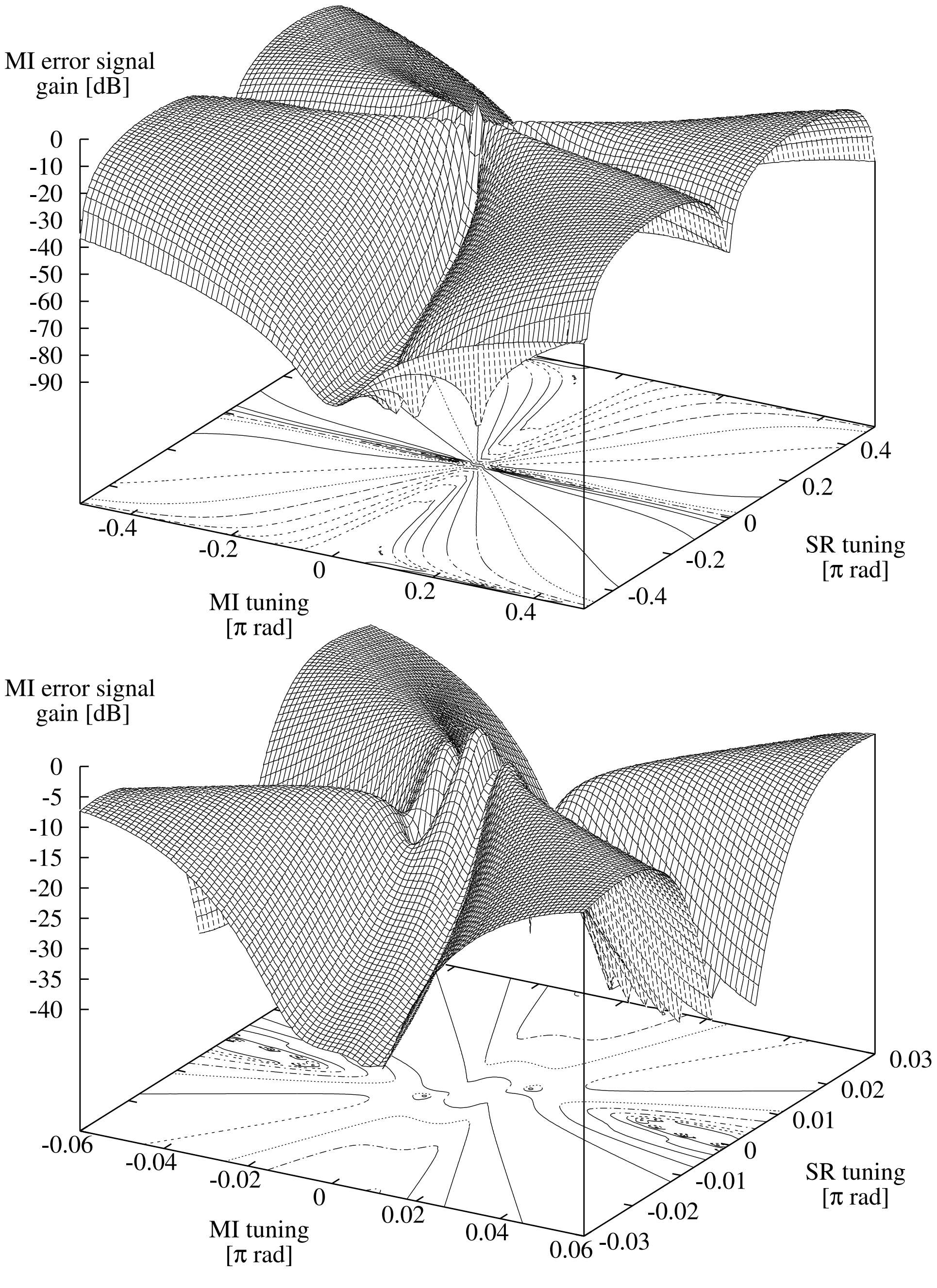

Figure 1.40: The gain (in dB) of the Michelson error signal, referred to the gain at the nominal operating point $\varphi_{\mathrm{MI}} = \varphi_{\mathrm{SR}} = 0$, for small signal frequencies.

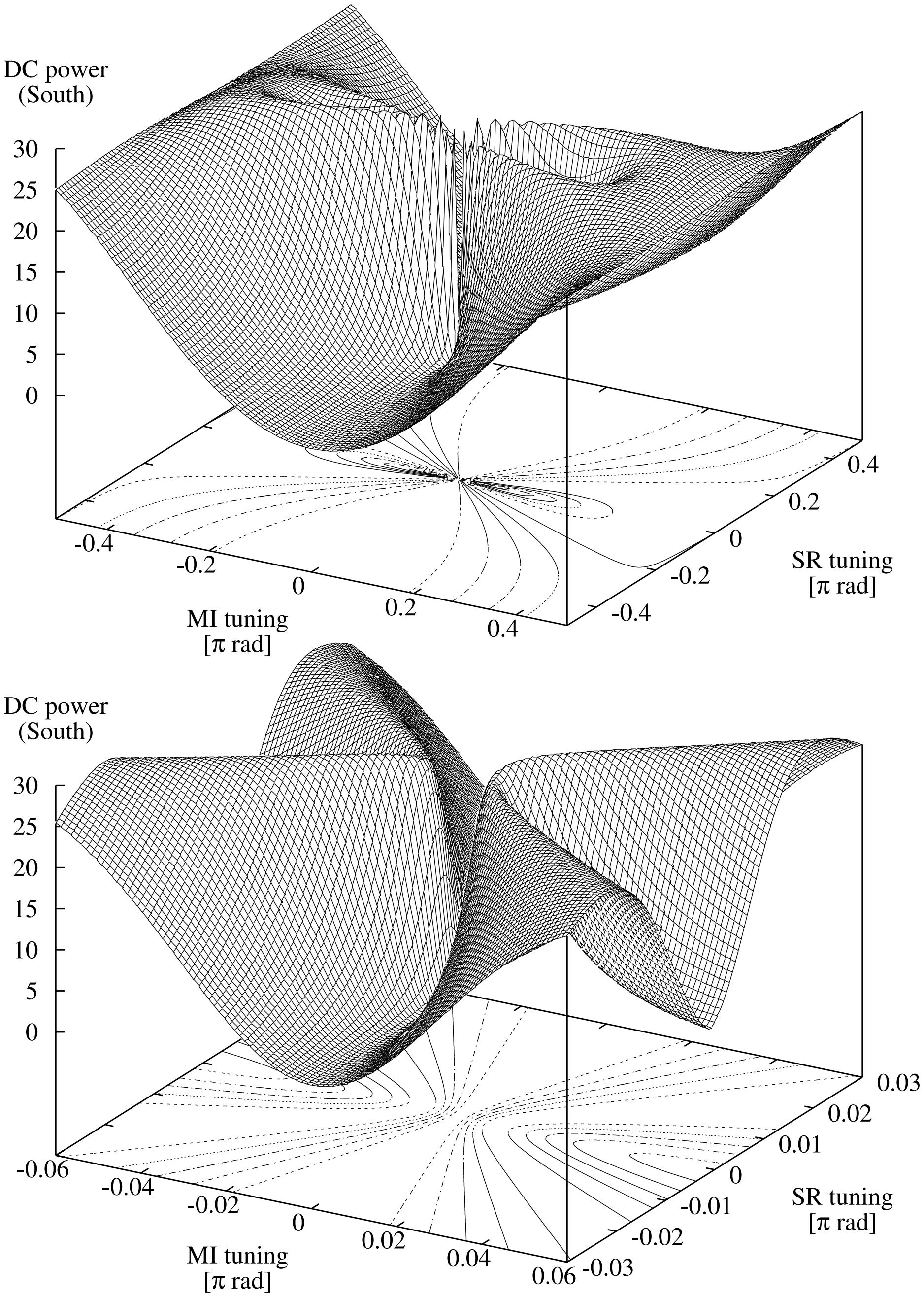

Figure 1.41: The DC (average) light power arriving at the photodetector, referred to unity at the nominal operating point. Note that this diagram was computed from H_0 (Equation (1.49)) and therefore includes the power due to the Schnupp sidebands.

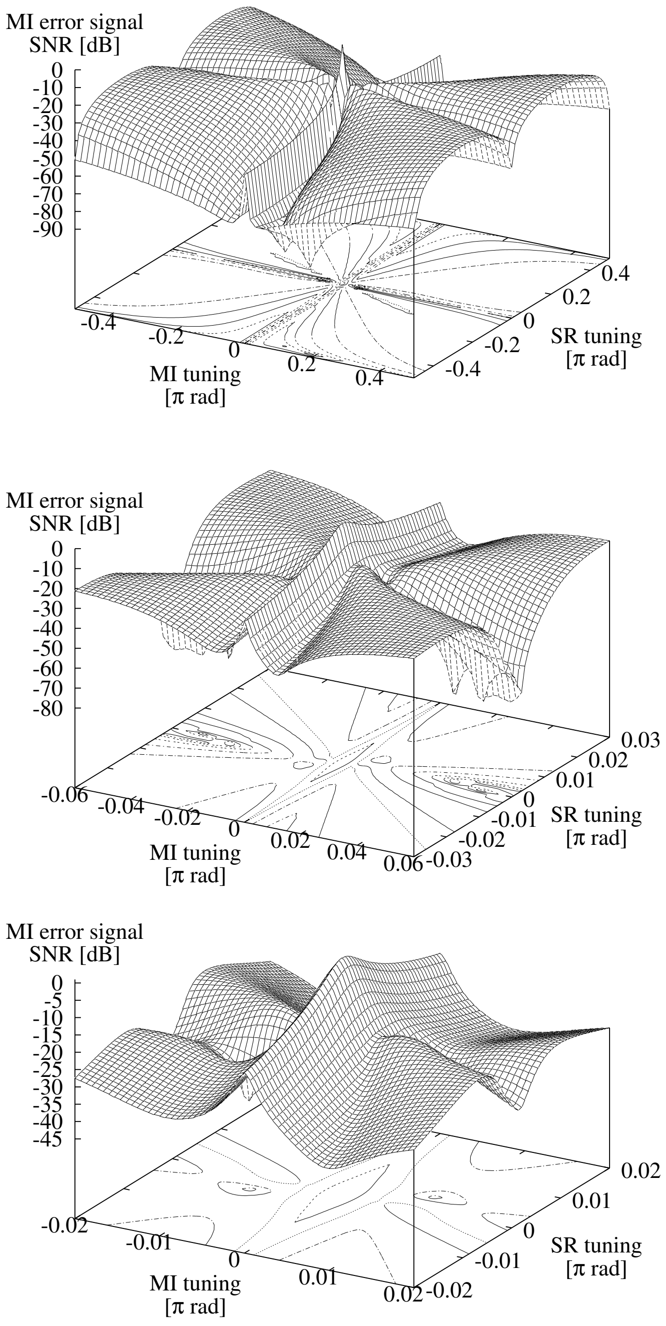

Figure 1.42: The signal-to-noise ratio (in dB) of the Michelson error signal, referred to the SNR at the nominal operating point $\varphi_{\mathrm{MI}} = \varphi_{\mathrm{SR}} = 0$, for small signal frequencies.

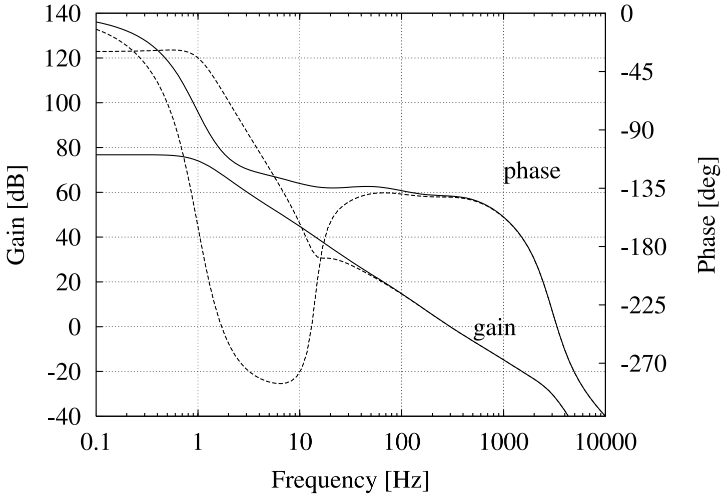

Figure 1.43: Open loop gain of the Michelson dark fringe lock, for a typical unity-gain frequency of 300 Hz. The dashed curves show the open-loop gain with the additional DC gain active.

chosen, which was realized as an Akerberg-Mossberg filter [Wangenheim]). Its action is also shown in Figure 1.43.

During lock acquisition of the dual recycled interferometer, this additional filter needed to be deactivated. Furthermore, the loop gain of the Michelson lock needed to be reduced until it was lower than that of the SR mirror loop (see also Section 1.7). Once lock was acquired, the loop gain could be increased and the additional filter be activated. The unity-gain frequency could then be increased up to more than 1 kHz. In practice, a unity-gain frequency of around 300 Hz provided useful and stable operation.

1.6.3 SR mirror control

1.6.3.1 Error signal

Although the demodulated signal at the South port, which is used as the Michelson error signal, does in general depend on the tuning of the signal recycling mirror M_{SR} (see Figure 1.39), it cannot be used as the M_{SR} error signal. As was shown in the last Section (1.6.2.2), the dependence on the M_{SR} tuning vanishes in the dark fringe state of the Michelson.

Hence it is necessary to find another way to control M_{SR}. In the first demonstration of dual recycling [Strain91], this was achieved by injecting additional light *through the South port* into the interferometer. To avoid interference with the main light circulating in the interferometer, this additional light was of orthogonal polarization and, furthermore, shifted in frequency with an AOM.

It is, however, preferable to avoid this further complication and to use the light that is already present in the interferometer to generate an error signal for M_{SR}. If possible, it would be easiest if the same Schnupp modulation which is already being applied (to read out the Michelson phase) could also be used to control signal recycling. It turns out that this is indeed possible if we look at the light circulating *in the arms*.

This concept was first investigated in a series of table-top experiments in Hannover (without power recycling) [Maass95, Barthel97, Freise98] and finally implemented in the Garching 30 m prototype as one main part of this work. The main results have recently been published [Heinzel98].

The generation of an M_{SR} error signal can be understood if one considers the (idealized) interferometer in the dark fringe condition. Then there will be no carrier light between the beamsplitter and M_{SR} (compare Figure 1.2). The only light arriving at M_{SR} will be the Schnupp modulation sidebands, which are directed there via the armlength difference (see Section 1.5.4). The only effect of an assumed motion of M_{SR}, which we want to detect, is to change the phase of those Schnupp sidebands that are reflected back into the interferometer.

Hence the resonance condition of the Schnupp sidebands is modified and we can expect to see their phase (with respect to the carrier) changed everywhere inside the interferometer, including the South output port. However at this port, it is impossible to detect this phase change because no carrier is present. In the power recycling cavity, on the other hand, the carrier is resonant and very strongly present. Beating the phase-shifted Schnupp sidebands with the carrier will then produce an error signal that depends on the tuning of M_{SR}.

In principle, light from anywhere inside the power recycling cavity could be used to detect this beat signal. In particular, light from either of the two arms will contain the desired information. In the last table-top experiment in Hannover [Freise98], the light transmitted through one end mirror was used for that purpose. In the Garching 30 m prototype we have chosen to use the weak beam reflected off the rear of the beamsplitter (see Figure 1.29). This beam is a small fraction (around 300 ppm) of the light which is on its way into the East arm. The rear of the beamsplitter had intentionally been given this finite reflectance for the former external modulation setup (see Section 1.3.2). The beam is detected by the resonant photodiode PD4 in Figure 1.29, and the error signal is then generated in the associated mixer Mix4.

It is mentioned for completeness here that some simulations have also been carried out to compute possible error signals for M_{SR} which are detected at the *West* port of the interferometer (i.e. in the light reflected from the power recycling mirror) instead of the light from one arm (this had been proposed by David McClelland[18] for detuned dual recycling). All such simulations[19] showed, however, the same qualitative behaviour of the error signal as with detection in one arm. Detection in the West port (reflected light) is therefore no longer considered in this work.

A detailed investigation of the error signal is possible with Jun's program. Figure 1.44

---

[18] See also the footnote 27 on page 95.

[19] This holds also for detuned dual recycling (see Section 1.10.2) and the special case of equal lengths of PR and SR cavity (see Section 1.11).

shows the computed error signal, equivalent to Figure 1.39 for the Michelson error signal. It was computed from the static response $H_1(\chi_{\text{opt}})$ at the East output port (Equation (1.50)), where χ_{opt} is the optimal demodulation phase for one mixer (Equation (1.74)), determined for low signal frequencies at the nominal broadband operating point. This is what most closely resembles the actual error signal in the prototype, as it is observed at the output of mixer **Mix4** in Figure 1.29.

Several interesting facts can be seen in the plots. If the Michelson is in the dark fringe condition ($\varphi_{\text{MI}} = 0$), the SR error signal shows a more regular behaviour than the Michelson error signal. In particular, there is no phase reversal of the error signal (compare Figure 1.39).

On the other hand, if M_{SR} is locked ($\varphi_{\text{SR}} = 0$), the error signal is *not* constantly zero, but does depend on the Michelson tuning φ_{MI}. This is different from the behaviour of the Michelson error signal. The (desired) sensitivity of the SR error signal to a motion of M_{SR} is 3.3 times larger than the (spurious) sensitivity to a differential motion of the end mirrors. However, since the Michelson lock must be rather tight anyway during operation, this dependence is not expected to present a problem.

Figure 1.45 shows the frequency response of the SR error signal at the nominal operating point. The data computed with Jun's program were fitted with LISO. The response is dominated by a single pole at 100 kHz. The structure near 300 kHz can be fitted by a complex pole at 345 kHz ($Q = 0.98$) and a complex zero at 318 kHz ($Q = 0.86$). No attempt was made to find a physical explanation for these response poles.

1.6.3.2 Actuator and loop filter

In the prototype the signal recycling mirror M_{SR} is suspended as a single pendulum that is very similar to the end mirrors (see Section 1.6.2.3 and Appendix A.3). The test mass is a fused silica plate much thinner than those of the end mirrors. Consequently (and possibly also because of imperfect adjustment of the gain ratio for the three coils) there is some coupling of the longitudinal motion to the (undesired) rotational and tilting motion of the plate[20]. The resulting transfer function is slightly more complicated than the simple two-pole low-pass filter valid for the end mirrors. It was measured and could be fitted with a model consisting of a complex pole at 0.8 Hz ($Q = 0.46$), another complex pole at 1.5 Hz ($Q = 1.75$) and a complex zero at 2.4 Hz ($Q = 2.25$).

Apart from the standard overall gain control and optional inverter, the loop filter consisted of an integrator active between 10 mHz and 1 Hz and a differentiator active between 1 Hz and 1 kHz. The resulting open-loop gain is shown in Figure 1.46 for a typical unity-gain frequency of 500 Hz. This filter was designed and built very quickly during the initial installation of dual recycling. Since it worked satisfactorily, it was never changed, although a more complicated filter (such as the one described in Section 1.6.2.3) might yield slightly better performance.

---

[20] Another reason may be that the SR mirror is *not* fixed in the center of the test mass, as opposed to the end mirrors. That was because the test mass was designed to hold two SR mirrors next to each other such that the SR mirror reflectivity could quickly be switched by moving the test mass

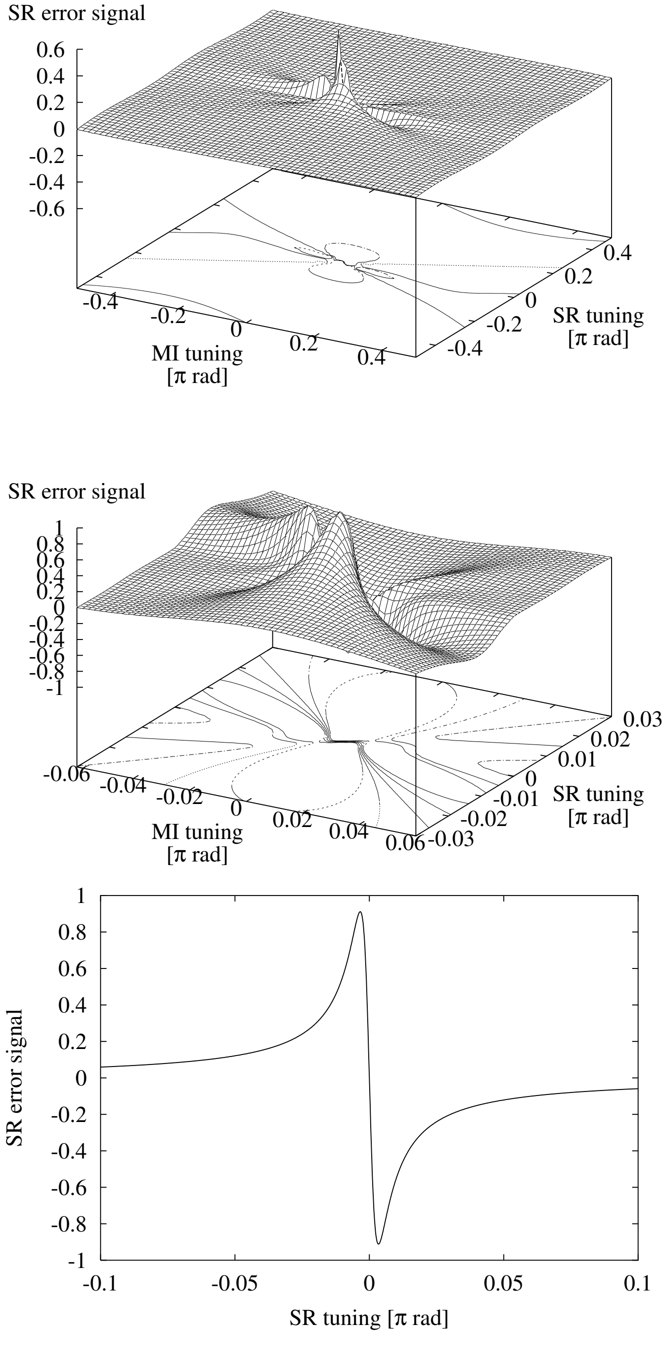

Figure 1.44: SR error signal as a function of the tunings φ_{MI} and φ_{SR}, with the PR cavity being kept resonant. The lower curve shows the error signal for the dark fringe state $\varphi_{\mathrm{MI}} \equiv 0$. The tunings φ_{MI} and φ_{SR} are expressed as multiples of π in these plots.

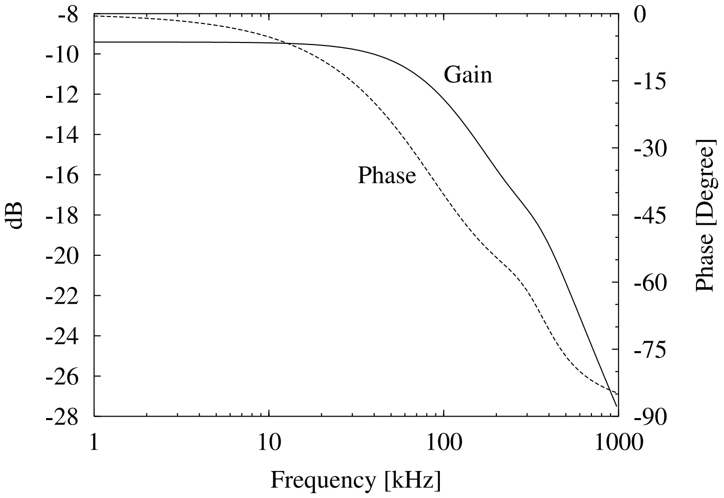

Figure 1.45: Frequency response of the SR error signal in the 30 m prototype at the nominal operating point.

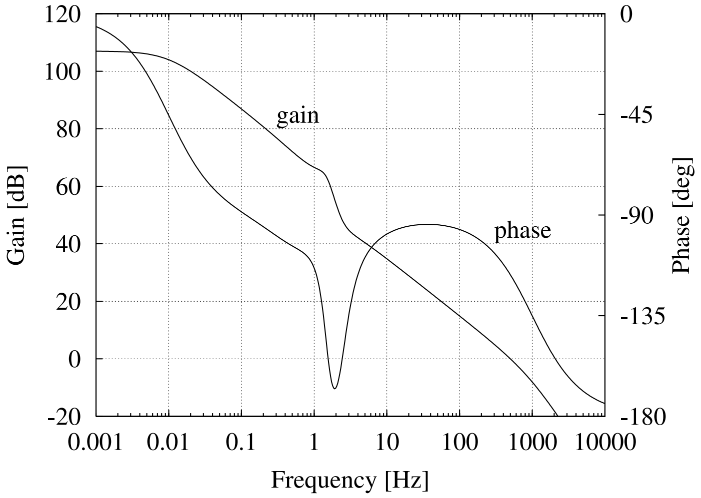

Figure 1.46: Open-loop gain of the SR mirror control loop.

1.6.4 Power recycling gain in dual recycling

Supplementing the previous diagrams, which show various aspects of the dual recycled interferometer as a function of the two tunings φ_{MI} and φ_{SR}, Figure 1.47 shows the average (DC) total power in the power recycling cavity. It was computed as the sum of the power in the North arm and the power in the East arm. If one compares this

---

orthogonally to the beam direction.

diagram with Figure 1.41, there is not the strict correspondence that one might at first expect (exit through the South arm being the main loss mechanism for the PR cavity). This is because the impedance matching condition for the injected light varies considerably over the plotted parameter space, and thus the amount of light directly reflected from the PR cavity also varies by a factor of almost 10.

1.7 Lock acquisition

This section describes how the lock acquisition of the dual recycled interferometer was found to work experimentally, and attempts to give an explanation using the simulations presented in the previous sections.

During several months of experiments at the 30 m prototype, the following procedure to acquire lock of all loops proved to be the most successful (see also Section 1.8.1 on the alignment procedure).

1. The first loop (laser frequency stabilization to the reference cavity) must be locked (see Section 1.6.1.2). This is independent of the rest of the interferometer, apart from the fact that the second loop (PR cavity lock) interacts with the first loop via the AOM. It was helpful to interrupt this interaction during lock aquisition by setting the gain of the second loop to zero. Lock acquisition was at first done manually by slowly scanning either the laser frequency or the reference cavity length (both via piezos). Then, in the neighborhood of a resonance, the first loop tried to lock. Because the precise gain setting of that loop is somewhat critical, it was often necessary to manually reduce the gain until lock of the first loop was accomplished and then increase it again to reduce the remaining frequency noise. Later this manual procedure was replaced by an electronic circuit that effectively performs the same task. The circuit is described in Appendix B.13.

2. Once the laser frequency is stabilized, the gain of the second loop (which locks the laser frequency to the PR cavity) is again restored to its normal value (this task is now also performed by the electronic circuit). The second loop then continually tries to lock the laser frequency to the ‘power recycling cavity’, which at this point wildly fluctuates in its behaviour (because both the Michelson and the SR mirror are still swinging freely). It is believed to be important for the final success of lock acquisiton that the second loop manages to lock the laser frequency to the swinging interferometer under most conditions of the interferometer (see also Sections 1.6.1.2 and 1.6.1.3).

3. The remaining two degrees of freedom, Michelson and SR mirror, could only be locked simultaneously. Thus both loop gains were set to an appropriate value and the interferometer was left swinging. Fortunately it turned out that under correct conditions (in particular, good alignment of the interferometer, proper loop gain

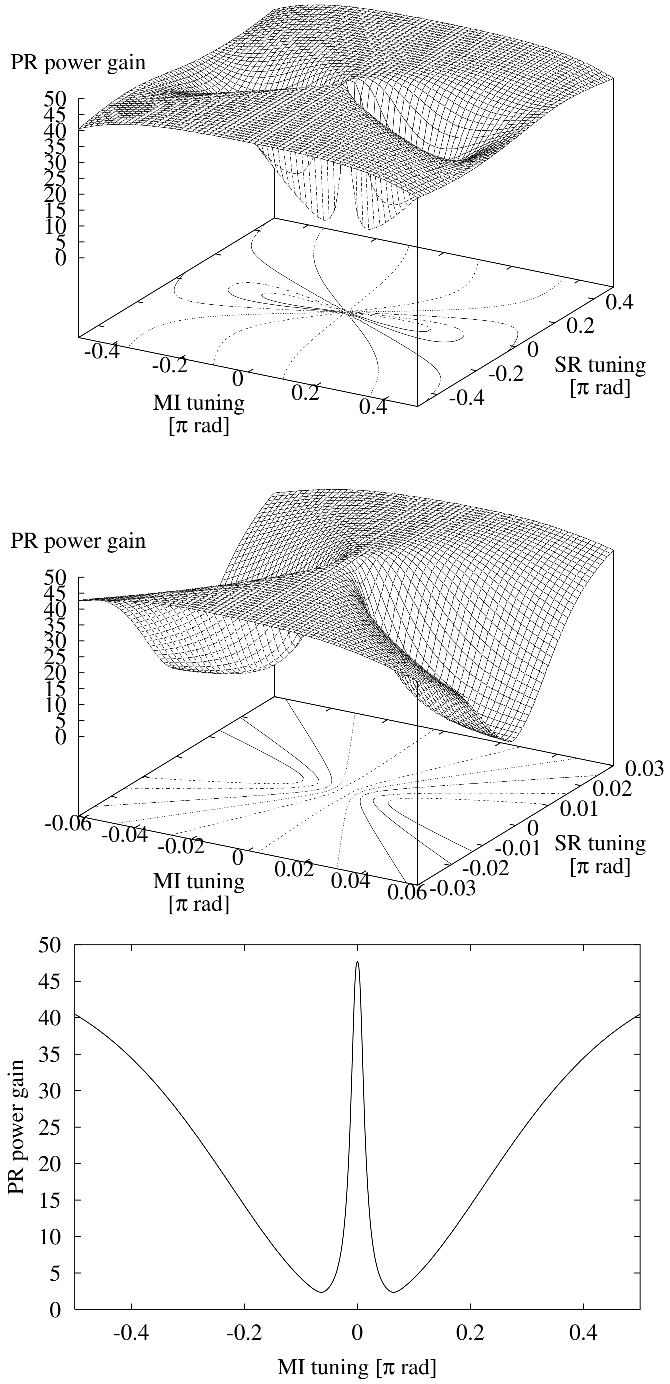

Figure 1.47: Power buildup in the PR cavity (sum of the power in the East arm and the power in the North arm for unity input power) as a function of the tunings φ_{MI} and φ_{SR}, with the PR cavity being kept resonant. The lower curve shows the power for $\varphi_{\mathrm{SR}} \equiv 0$. The tunings φ_{MI} and φ_{SR} are expressed as multiples of π in these plots.

and demodulation phase for the last two error signals)[21] it usually only takes a few seconds before the interferometer falls into lock by itself, without any external interaction, and stays there. This process is described in some more detail below.

4. Once the dual recycled interferometer is locked, some parameters can be optimized, as described in Section 1.8.1.

The lock, once achieved, was usually quite stable. At best, lock was typically lost after 15 to 30 minutes due to either a failure of the first loop (when the relative drift of the laser frequency compared to reference cavity exceeded the actuator's range) or 'seismic' disturbances (including stepping too strongly on the laboratory floor's hot spot near the central vacuum tank), which caused the dynamic range of one of the interferometer loops to be exceeded.

For the lock acquisition described above to work it was found necessary (or at least very helpful) that the Michelson loop gain was smaller than the SR mirror loop gain. Typical gain settings corresponded to unity-gain frequencies (after lock was achieved) of around 100 Hz for the Michelson and 500 Hz for the SR mirror. After lock was achieved, the Michelson gain could be increased, even until it was bigger than the SR mirror loop gain. This behaviour may have to do with the simpler structure of the SR mirror error signal (compare Figures 1.39 and 1.44), but there is no hard evidence for this belief.

Both error signals were recorded during a few typical lock acquisition transients. Some examples are shown in Figure 1.48.

The upper curve of Figure 1.48 is perhaps most typical. At first ($t < -0.2\,\mathrm{s}$), both Michelson and SR mirror are freely swinging and occasionally encountering one of the peaks of Figures 1.39 and 1.44. At about $t = -0.18\,\mathrm{s}$, both of them arrive in the central region. Then a complicated nonlinear oscillation starts and lasts for a few cycles, and finally both degrees of freedom are locked. Lock acquisition was confirmed by a constant high PR gain and by the sudden appearance of the calibration signal (375 Hz) in the Michelson output signal (unfortunately these were both not recorded in Figure 1.48 due to lack of channels in the oscilloscope).

Figure 1.49 shows an enlarged detail of the final phase of the oscillation. No attempt was made to simulate or understand it. As can be seen from the other two examples in Figure 1.48, sometimes the oscillation lasted longer, or was missing altogether on other occasions.

1.7.1 Other stable states

During lock acquisition, in particular if parameters were not yet well readjusted after an idle period, the dual recyled interferometer could sometimes lock in other states

---

[21] After the initial installation of dual recycling, it took Ken Strain and the author only one day to acquire lock for the first time. The author thinks this was quite lucky (at least several weeks had been expected), but also and mainly due to the expertise of Ken Strain.

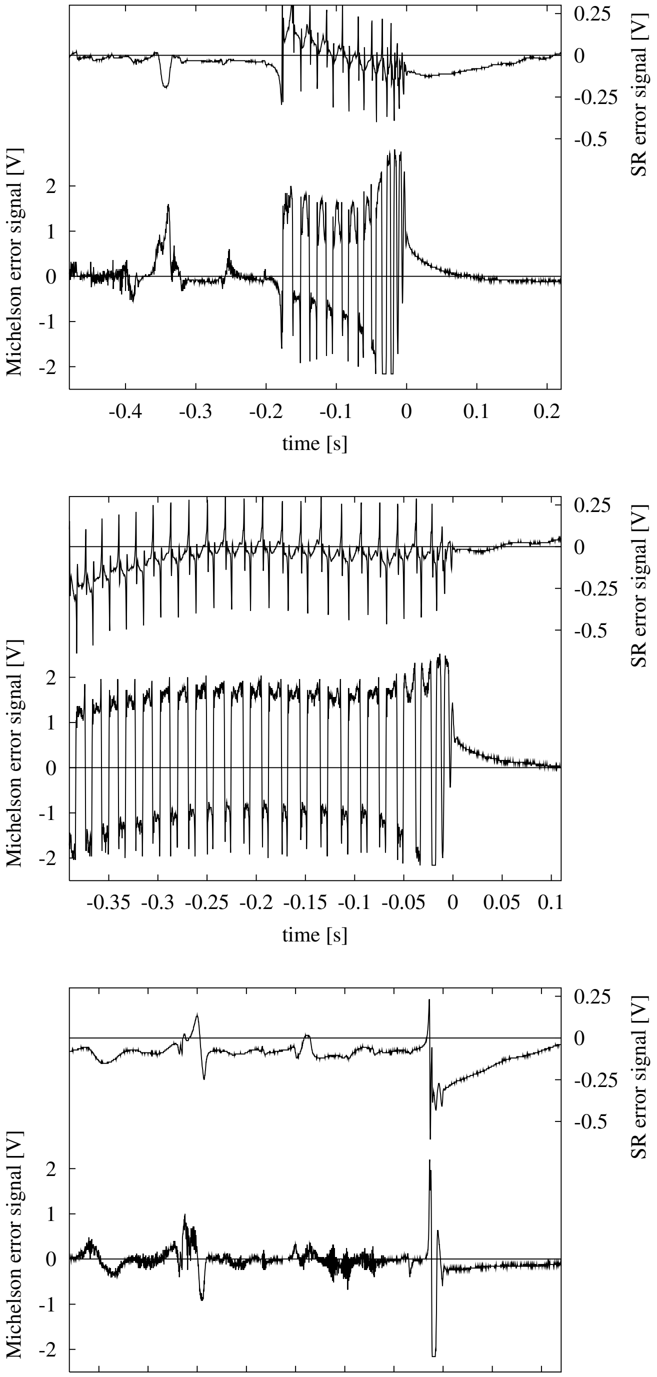

Figure 1.48: Some lock acquisition transients recorded in the dual-recycled 30 m prototype. The time axis has been shifted such that $t = 0$ corresponds to the approximate time of lock acquisition.

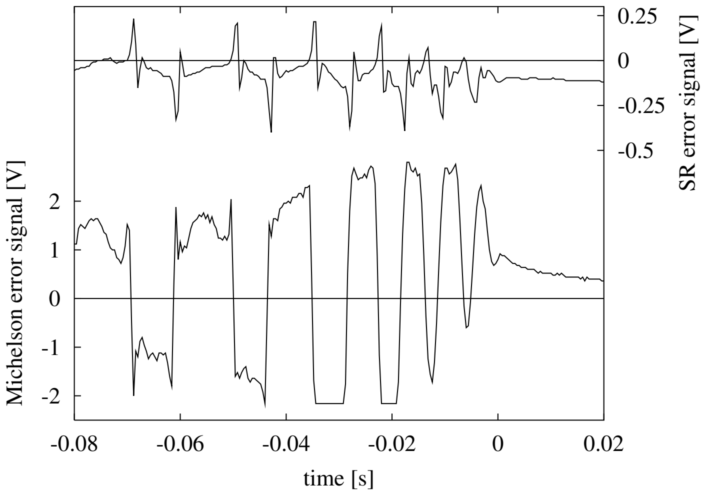

Figure 1.49: Detail of the lock acquisition transient from the upper curve of Figure 1.48.

than the desired dual recycling state. Some of these states were reasonably stable, while others had so little loop gain that a small disturbance quickly threw them out of lock. They could easily be identified by observing the power of the beams in the interferometer and at the output. It was found, not very surprising, that the stability of these states depended critically on the loop gains for the Michelson and SR mirror lock, and, equally important, on the demodulation phases χ_{MI} and χ_{SR} that were used to generate the error signals for these two loops. Luckily it was always possible to lock the interferometer in the desired dual-recycling state after a few readjustments of these gain and phase settings.

One of the more interesting states, that was sometimes observed, is shown in Figure 1.50. The thickness of the lines symbolically represent the relative beam powers in each arm.

As another verification of our models, this state was also simulated with Jun's program. The required tunings are $\varphi_{\mathrm{MI}} = 3\pi/2$, $\varphi_{\mathrm{SR}} = \pi/4$ and $\varphi_{\mathrm{PR}} = \pi/4$ (or an equivalent symmetric combination). It was found that indeed error signals with zero crossings at this operating point could be obtained, in particular if the demodulation phases χ_{MI} and χ_{SR} had some offset against their optimized values for dual recycling. The gain of both error signals was, however, much lower than in the normal state. The following table shows the relative power in each arm (computed with Jun's program) for unity input power.

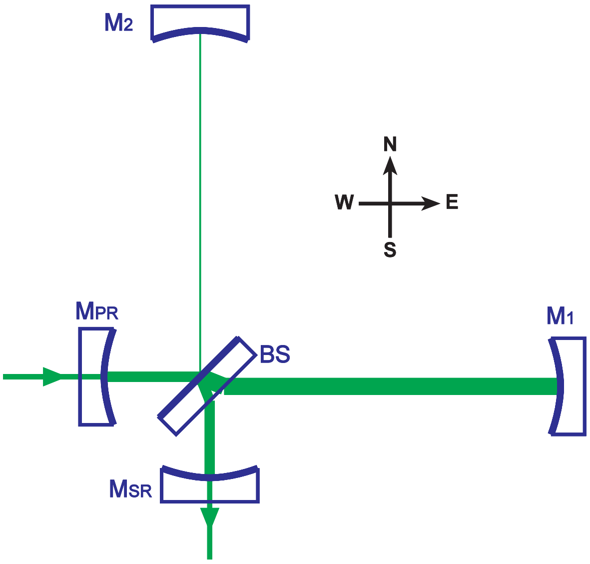

Figure 1.50: One of the other stable states of the dual recycled 30 m inteferometer, which was sometimes observed when gain and phase settings were not yet optimized.

State	Tunings $\varphi_{\rm MI}$	$\varphi_{\rm SR}$	$\varphi_{\rm PR}$	Power North	East	West	South
Normal	0	0	0	24.4	23.6	47.1	0.92
Funny	$3\pi/2$ $\pi/2$	$\pi/4$ $3\pi/4$	$\pi/4$ $3\pi/4$	0.004	39.5	18.8	20.7

Different interpretations of this state are possible. It can, for example, be considered as a power-recycled Michelson with the East arm as PR cavity, with two short ‘arms’, and even with signal recycling in the North arm. This dual-recycled Michelson is, however, fed from the laser through one of its ‘arms’, an otherwise very unusual arrangement. The simulation also showed that the gain of the error signals and the signal-to-noise ratio at the output were, as expected, worse than in the normal dual recycling state.

1.8 Operation of dual recycling

1.8.1 Initial alignment and adjustments

This section briefly describes the procedure that was typically used to first aquire lock in the dual recycled prototype, after it hadn’t been used for a while. After a warm-up period of one or two hours for the laser, the elements on the laser table were readjusted until the first loop was locked (see Section 1.7). Then the coupling of the light into the fiber was optimized. The suspended interferometer was usually so badly misaligned that no interference took place. Realignment starts with a simple Michelson (i.e. M_{PR} and M_{SR} tilted and acting only as attenuators). The spots at the output port are clearly visible and can easily be superimposed by manual alignment.

This does, however, not yet mean that the two beams returning from the arms do indeed retrace their path, which is necessary for power (and signal) recycling. This common mode alignment of the end mirrors is the most tricky part in manual alignment. It was initially approximated by observing the (very weakly visible) spots on the power recycling mirror and then, as soon as possible after lock was aquired, optimized with the autoalignment system (see Chapter 2).

The next step is to re-align the power recycling mirror such that a power-recycled Michelson (still without signal recycling) results. This interferometer could usually be locked (by increasing the Michelson loop gain), and the locked state was used to optimize the alignment of the power recycling cavity.

Then finally M_{SR} is re-aligned. At this moment the interferometer output, which had been rather dim so far, starts to flash brightly. The interferometer is swinging through a two-dimensional continuum of states, while the second loop is mostly locked, such that the incoming laser light is usually resonant in the strange interferometer formed by the swinging mirrors (see Section 1.7). In many states a large fraction of the injected power appears at the output (see Figure 1.41). Furthermore, since both power- and signal-recycling cavity are nondegenerate, higher order transversal modes may be resonant in parts of the system at tunings where the fundamental mode is not resonant. This gives the flickering light at the output port a wild and rapidly changing transversal structure.

If the power-recycling cavity had been well aligned before the re-alignment of M_{SR}, and all loop gains etc. are set not too far from their optimum, then the dual-recyling interferometer will usually lock quickly, as described in Section 1.7. Once locked, many parameters can be adjusted. To begin with, the alignment of all suspended mirrors (apart from M_{SR}) is optimized with the autoalignment system.

The alignment of M_{SR} must be carried out manually, because there is not yet an autoalignment system for it. For that purpose (and many others as well), a small test signal at an audible frequency is fed to the Michelson interferometer via coil-magnet actuators on one end mirror. The frequency should be as high as easily possible, because low frequencies may be affected by the loop gain of the Michelson dark fringe lock (see also Appendix A.5.1).

The amplitude of that test signal in the Michelson output is monitored via headphones (and often a band-pass filter). This is a very sensitive indicator for the alignment of the SR cavity, which can now be optimized. The same procedure is also used to optimize the Michelson demodulation phase χ_{MI}.

The demodulation phase χ_{SR} for the SR error signal is similarly optimized with another audible test signal, which is fed to M_{SR} and monitored in the SR error signal.

1.8.2 Confirmation of dual recycling

After the initial installation and lock acquisition of dual recycling, it was necessary to confirm its proper operation. The first test was the enhancement of the amplitude of the 375 Hz calibration signal at the Michelson output. For that measurement, M_{SR} was temporarily misaligned by about 3 mrad, such that beams reflected from it would no longer hit the end mirrors, and M_{SR} thus acted as a simple attenuator. Then the interferometer (a power-recycled Michelson without signal recycling) was locked by increasing the Michelson gain. The amplitude of the 375 Hz signal at the Michelson output was measured with a spectrum analyzer and recorded as reference. Then M_{SR} was re-aligned to its proper position, the dual recycled system was locked and the amplitude of the 375 Hz signal was measured again. The ratio of these two amplitudes was compared with theory.

The expected ratio consists of three factors:

- The enhancements of the signal sidebands due to signal recycling. For the 3.88 % mirror of the prototype, this factor is given by $2/\tau_{SR} = 10.15$ (see Section 1.5.3).
- The improved coupling of the Schnupp modulation sidebands to the output, where they act as local oscillator (compare Section 1.5.4 and Figures 1.36 and 1.38). This factor[22] amounts to around 9.
- The attenuation due to the misaligned M_{SR} in the reference measurement yields another factor of $1/\tau_{SR}^2 = 25.8$.

Using Jun's program with the best numbers available, the expected total ratio was 2335. Upon the initial installation of dual recycling, however, a ratio of only around 500 was consistently measured. Considerable effort was invested in trying to eliminate all possible errors, including errors in the simulation. In the end, after all other possibilities had been excluded[23], the signal recycling mirror (which had had about 4 % transmittance) was replaced by an old mirror of unknown origin, which happened to be flat and have a suitable transmittance, which was measured as 3.88 %. Immediately upon its installation in the prototype, a ratio of 1900 was measured, and that old mirror is still installed as the signal recycling mirror. Visual inspection of the previously used mirror showed that its coating was very inhomogeneous, apparently due to some severe accident in the coating process, and that entire batch of mirrors has now been discarded.

The measured ratio of 1900, compared with the expected total ratio of 2335, was considered sufficient evidence for the correct operation of dual recycling, if one takes into account the idealizations of the model (perfect mode matching etc.).

Further indications of correctly operating dual recycling were obtained from the improved shape of the mode emerging at the dark fringe port (see Section 1.9) and, later, the correspondence of measurement and theory in the detuned case (see Section 1.10).

---

[22] The exact value is 9.24, if the demodulation phase in mixer **Mix3** of Figure 1.29 is optimized separately for the two cases, and to 8.93, if it remains untouched between the measurements.

[23] A significant fraction of these experiments was carried out in collaboration with B. Willke.

1.8.3 Noise behaviour of the dual recycled prototype

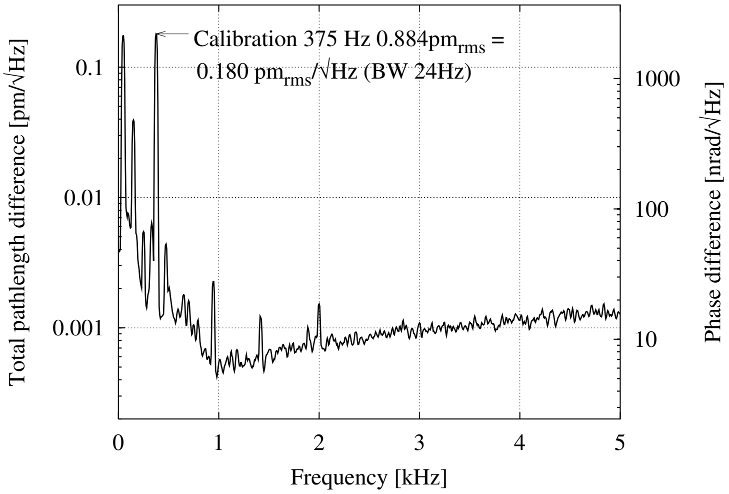

Figure 1.51: Noise spectrum of the dual recycled 30 m prototype.

Figure 1.51 shows a typical noise spectrum of the dual recycled 30 m prototype. The calibration was performed as described in Appendix A.5.1. The lowest noise occurs near 1 kHz at a level of around $5 \cdot 10^{-15}\,\mathrm{m}/\sqrt{\mathrm{Hz}}$, similar to the results with external modulation (see Figure A.17).

It was shown (see below) that this noise is largely dominated by the frequency noise of the laser light that enters the interferometer. The expected effect of the frequency noise with the known armlength difference can be computed as follows [Winkler]:

A laser frequency fluctuation of the amount $\delta\nu$ will simulate the effect of a gravitational wave of amplitude

$$h = \frac{\Delta L}{L}\frac{\delta\nu}{\nu}, \tag{1.101}$$

where L is the physical armlength, ΔL the armlength difference and ν the laser frequency. The corresponding phase difference (of the interfering beams) is related to h by

$$\delta\varphi = \frac{4\pi\, L}{\lambda}\, h = \frac{4\pi\,\nu\, L}{c}\, h. \tag{1.102}$$

Combining the above two equations yields

$$\delta\varphi = 4\pi\frac{\Delta L}{c}\,\delta\nu. \tag{1.103}$$

This conversion factor is independent of the Fourier frequency of the frequency fluctuation. This can be understood in the sideband picture, if one remembers that the amplitude of the sidebands that describe the frequency fluctuation is inversely proportional to the Fourier frequency (see Section 1.2.1.3), whereas their coupling to the output is proportional to the Fourier frequency (see Section 1.5.4). Thus the amplitude of the sidebands at the output, and hence the spurious signals which they cause, are independent of the Fourier frequency.

For the prototype, the conversion factor from frequency noise to phase noise at the Michelson output is thus expected to be $4\pi \cdot 6\,\mathrm{cm}/c = 2.5 \cdot 10^{-9}\,\mathrm{rad/Hz}$. According to this calculation, however, the measured frequency noise of $0.4\,\mathrm{Hz}/\sqrt{\mathrm{Hz}}$ at $1\,\mathrm{kHz}$ (Figure 1.34) would result in a phase noise of about $1\,\mathrm{nrad}/\sqrt{\mathrm{Hz}}$, whereas approximately $5\,\mathrm{nrad}/\sqrt{\mathrm{Hz}}$ were measured (Figure 1.51).

A repetition and recalibration of both measurements (Figures 1.34 and 1.51, see Appendix A.5) confirmed both measurements. Nevertheless a measurement of the ‘transfer function’ of laser frequency noise to output phase noise (without injecting additional signals) showed a good correlation. Furthermore, an experiment was performed to subtract the frequency noise (using the second loop error signal) from the Michelson output. This gave indeed a lower noise level at the subtracted Michelson output (but proved to be rather unstable, as the coefficient used in the subtraction was rather critical and tended to drift considerably on timescales of one minute or so). These facts indicate that the output phase noise is indeed dominated by laser noise, although the coupling efficiency is apparently higher than computed from Equation (1.103).

Several explanations are possible. If the Michelson is not exactly on a dark fringe, the coupling increases. Simulations with Jun’s program have shown that an offset of $\varphi_{\mathrm{MI}} = 0.001\,\mathrm{rad}$ is sufficient to increase the coupling to a value five times bigger than predicted from Equation (1.103), i.e. sufficient to explain the measurements. Offsets in the Michelson loop (and in all other loops that use RF demodulation to generate their error signal) were not uncommon due to drifting AM in the Pockels cells that apply the phase modulation (see Appendix A.2) and due to RF pickup in the photodiode preamplifiers.

Another possible explanation is that laser frequency noise, which is generated by shot noise in the first loop error signal and then impressed on the laser frequency via the high loop gain and fed back to the piezos in the laser (see Section A.2). This unfortunately not only changes the laser frequency but also alters its alignment and amplitude. Fluctuations in alignment and amplitude do also couple into the Michelson output. This may yield another contribution to the increased coupling which was observed.

Unfortunately the precise relationships were very difficult to investigate, due to the ever present drifts in the laser beam characteristics and the modulation AM components. It was, however, experimentally observed at the Michelson output by applying a test signal to dither the laser frequency, that offsets in the Michelson loop (and also the PR loop) did indeed change the coupling efficiency.

Furthermore, the calibration of the frequency noise measurement shown in Figure 1.34 was rather difficult and depended on many varying factors (see Appendix A.5.2), so that some uncertainty (probably up to a factor of two) exists in the absolute scaling of

Figure 1.34. The measurements shown in Figures 1.34 and 1.51 were done on different days under somewhat different conditions of the interferometer.

Laser frequency noise is a serious problem in an interferometer that uses Schnupp modulation. Any frequency (or phase) fluctuation of the injected light will be separated from the carrier by the beamsplitter and transferred to the South direction (either directly to the output port or to the SR cavity), as described in Section 1.5.4. In a system with signal recycling, such light injected into the SR cavity will be indistinguishable from the light caused by true signals, and will thus be amplified in the SR cavity just as true signals would be.

For the 30 m prototype, some possible improvements of the laser frequency stabilization are discussed in Section 1.6.1.2. In GEO 600, a much better laser and frequency stabilization (including two suspended mode-cleaner cavities) will be used, and it is hoped that laser frequency noise will not limit the sensitivity of GEO 600.

1.9 Contrast improvement and ‘mode healing’ effect

One very important feature of signal recycling (and, in particular, of dual recycling) has become known as ‘mode-healing’ effect [Meers91b, McClelland93, Mavaddat95].

There are two aspects to it: First, the contrast at the output port is improved due to signal recycling. This effect was clearly observed in our experiment. Second, in a dual recycled system, the power recycling gain should also improve. The experimental parameters of the prototype during this work were such that this effect was (as expected) too small to be observed.

To understand these effects, we first consider a basic Michelson interferometer with power recycling, but no signal recycling, which is operated on the dark fringe, with one of the modulation methods described in Section 1.3 used for readout.

The contrast of an interferometer is never perfect. We use the term ‘contrast’ to represent the fraction of the light power leaking out towards the detection port (South) relative to that incident on the beamsplitter from the input side (West). The modulation sidebands are not included in this definition. More common definitions of ‘contrast’ or ‘visibility’ cannot easily be applied to a power-recycled system, where a true ‘bright fringe’ never exists.

In the earlier experiments using external modulation (and no signal recycling), the contrast was found to be never better than 1:1000. If we ignore the modulation sidebands for a moment, the remaining light at the South port consists of higher order transversal modes, which are generated by differential mirror imperfections in the long arms. The fundamental mode component in that light is eliminated as far as possible by the dark fringe lock (the limit being unequal reflectivities in the two arms). The amplitude of the remaining light can be expanded into a set of orthogonal modes, mostly used are Gauss-Hermite modes or Gauss-Laguerre modes.

Any components of the two first Gauss-Hermite modes (01 and 10) can be interpreted as misalignments of the Michelson and are thus also suppressed (by the autoalignment system). Hence the remaining light is dominated by higher order modes (see the left half of Figure 1.53 for an example). This light is effectively lost from the power recycling cavity and thus limits the power recycling gain.

Furthermore, at the detection port the power in the Schnupp modulation sidebands (which are required to detect the Michelson phase) must be bigger than the power of the 'waste' light, if the optimal sensitivity is to be approached. Since (in all practical schemes) this power is also taken from the power recycling cavity, the power-recycling gain that can be achieved is limited even more.

With the introduction of signal recycling, it becomes possible to distinguish between the fundamental mode and higher order transversal modes thanks to the Guoy phase shift. If the SR cavity is designed to be non-degenerate (as is usual), then the higher order modes will in general not be resonant, when the carrier is resonant. For simplicity we treat here only the case of broadband dual recycling, i.e. when the fundamental mode of the carrier is resonant in the SR cavity.

To compute the resonance condition for the higher order sidebands in the signal recycling cavity, we first need to find the geometry of the cavity eigenmode. From the length of the cavity ($L = 30.942\,\mathrm{m}$) and the radius of curvature of the end-mirrors ($R = 33\,\mathrm{m}$), we find the Rayleigh range of the SR-cavity as

$$z_\mathrm{R} = \sqrt{L(R-L)} = 7.98\,\mathrm{m}, \tag{1.104}$$

and the Guoy phase shift between mode n and mode $n+1$ for a one-way trip along the arm as

$$\eta = \arctan(L/z_\mathrm{R}) = 1.318\,\mathrm{rad} = 75.54^\circ. \tag{1.105}$$

The index n is given by $l+m$ for a Gauss-Hermite mode with indices l and m (indicating l and m node lines in the horizontal and vertical direction, respectively). For a Gauss-Laguerre mode with indices l and m (indicating m circular node lines and l radial node lines) the relevant index is $n = |l| + 2m$ [MPQ203, Appendix G] [Siegman].

The resonance condition in the Fabry-Perot cavity is mainly determined by the factor

$$d = \frac{1}{1 - \rho_1\rho_2 \exp(-2\,\mathrm{i}\,kL)} \tag{1.106}$$

(see Appendix D), which multiplies all amplitudes in the cavity. If we assume the carrier's fundamental mode to be resonant ($kL = 0 \mod 2\pi$) and include the Guoy phase shift for the transversal mode with index n we obtain

$$d = \frac{1}{1 - \rho_1\rho_2 \exp(-2\,\mathrm{i}\,n\eta)} \tag{1.107}$$

Figure 1.52 shows the power buildup for higher order modes in the SR cavity, referred to the power buildup for the fundamental mode. It was computed as $|d|^2$ (Equation (1.107)) with the parameters of the prototype. It can be seen that most of the higher order modes are strongly suppressed. The appearance of individual higher order modes which are almost as well resonant as the fundamental mode (such as the 31st mode in Figure 1.52) depends critically on the exact value of the cavity length and mirror curvature.

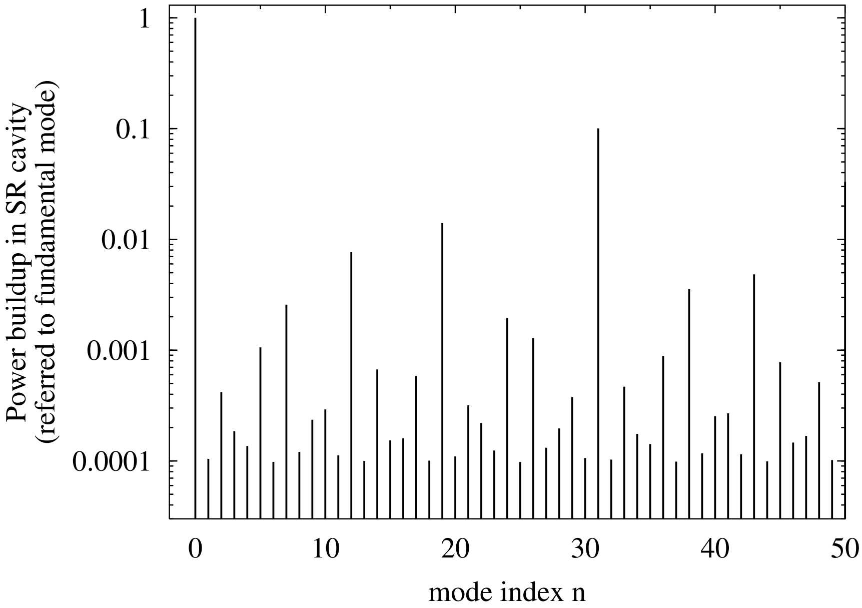

Figure 1.52: Suppression of higher order transversal modes in the signal recycling cavity of the prototype.

The effect of this suppression of the higher order modes is that most of the ‘waste light’ generated by differential distortions of the end mirrors does not reach the main photodetector. Hence a smaller amplitude of the modulation sidebands is sufficient to achieve the optimal performance. This effect alone already allows to increase the power circulating in the PR cavity (because a smaller modulation index is needed for the Schnupp modulation).

The effect of ‘cleaning’ of the light that arrives at the detection port was clearly observed in our experiment. Figure 1.53 shows the shape of the beam that leaves the interferometer towards the main photodetector, recorded with a CCD camera. The left picture shows the shape of the output beam *without* signal recycling. It is dominated by ‘waste’ light in a combination of many higher order modes. The right picture shows the same beam with dual recycling in operation. Now the beam is dominated by the Schnupp modulation sidebands, which are in the fundamental transversal mode.

The measured contrast with dual recycling was 1:3700, including the power in the Schnupp sidebands, which dominate the light at the output. Because the Schnupp sidebands are necessary for operation, the contrast without them could not be measured. It was, however, estimated to better than 1:10000.

Another experimental observation concerns the amount of intentional misalignment

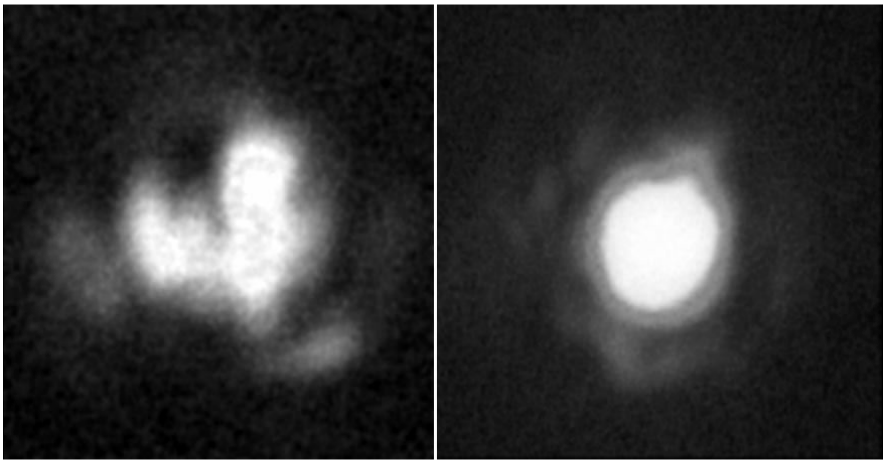

Figure 1.53: The shape of the beam leaving the interferometer towards the main detection photodiode. The left picture shows the case *without* signal recycling, while the right picture was taken with dual recycling working.

(of the end mirrors) that is tolerable before lock is lost. It was found that (after disabling the autoalignment system) the end mirrors could be misaligned more than twice as far as had been possible without signal recycling. Furthermore, the shape of the beam emerging at the South port starts to show the characteristic shape of a misaligned Michelson (which looks like a Gauss-Hermite '01' mode) only at much larger misalignments.

The complete theory of 'mode-healing' is rather complicated. From the above considerations it is easy to believe that the contrast at the dark fringe port improves, in accordance with the observation. If there is less light leaving the interferometer through the South port, it is also plausible (from energy conservation) that the power recycling gain increases, provided that the imperfect contrast is a major loss mechanism of the power recycling cavity. However, what exactly happens to the modes in the interferometer is not easily understandable.

Table-top experiments [Meers91b] and numerical simulations [Mavaddat95] have shown that the power recycling gain does indeed increase, if the 'distortion' is dominated by lower order modes such as misalignments. One possible interpretation is that an equilibrium mode is formed in the 'power recycling cavity'[24], which is *not* a pure fundamental mode. This mode experiences smaller losses than a fundamental mode would. It is, however, still close enough to a fundamental mode such that the 'overlap' with the mode coming from the laser is good and an efficient coupling of the incoming power into that mode is possible.

In our experiment no such effect could be expected to be observable, because the power recycling gain (about 50) was limited by the relatively high transmittance of the power

---

[24] Using the term 'power recycling cavity' here is common but not very precise. It is, of course, the whole interferometer including in particular the SR mirror that forms the equilibrium mode.

recycling mirror (7 %), and all other losses of the power recycling cavity were negligible compared to those 7 %.

1.10 Detuned signal recycling

1.10.1 Frequency response of detuned signal recycling

In analogy to Section 1.5.2, we treat separately the signal transfer function and the Schnupp sideband throughput, the product of which constitutes the interferometer transfer function, as computed by Jun's program.

1.10.1.1 Signal transfer function

In detuned signal recycling, the resonance frequency of the SR cavity is *not* the carrier frequency, but instead has an offset to the carrier which will be called f_{det}. This is achieved by maintaining the signal recycling mirror $\mathrm{M_{SR}}$ at a position that has a microscopic offset (*detuning*) to the position where the carrier would be resonant. The tuning φ_{SR} (expressed in radians) is related to f_{det} by

$$f_{\mathrm{det}} = \mathrm{FSR_{SR}} \frac{\varphi_{\mathrm{SR}}}{\pi}. \qquad (1.108)$$

The denominator is only π instead of 2π because of the definition of φ_{SR} in the model (see Section 1.4.1).

Then, in general, the two signal sidebands (which are at frequencies $\pm f_{\mathrm{sig}}$ with respect to the carrier) will experience different resonance conditions in the SR cavity. Often only one sideband (the upper one was chosen in the following example) will be resonantly amplified, whereas the other sideband has low gain (or is even suppressed) and can be neglected. This situation is shown in Figure 1.54 (compare Figure 1.22). Note that in an ideal interferometer, there is no carrier in the SR cavity.

If the signal frequency f_{sig} is swept through some range around f_{det}, both signal sidebands move symmetrically about the carrier. In the simplified picture given here, the upper sideband traces the resonance of the SR cavity and is maximally enhanced for $f_{\mathrm{sig}} = f_{\mathrm{det}}$, while the lower sideband can be neglected.

If we compare the detuned signal transfer function with the broadband case discussed in Section 1.5.3, the following important properties can be observed (see also Figure 1.56 below):

- The detuned transfer function reaches its maximum at f_{det}, and the 3 dB bandwidth of that maximum is equal to the SR cavity's FWHM, i.e. twice as wide as the bandwidth[25] in the broadband case.

---

[25] The term 'bandwidth' here refers to the *signal* bandwidth, where only positive frequencies are considered.

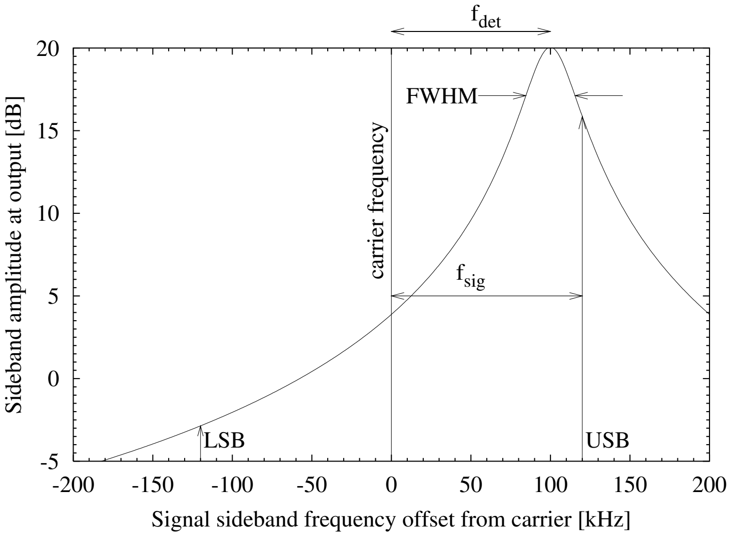

Figure 1.54: Amplitude transfer function in detuned signal recycling, using the parameters of the prototype (30 m armlength and 3.88 % SR mirror transmission). The signal frequency used for the example is 120 kHz, and the frequency offset f_{det} is 100 kHz.

- The value at the maximum is only one half of the broadband transfer function at DC (if we assume equal detection of all sidebands).
- The magnitude of the detuned transfer function at DC will be lower than both the broadband transfer function at DC and the detuned transfer function at its maximum. This effect will be stronger with increasing frequency offset f_{det} and increasing finesse of the SR cavity.

In this simple model, the signal transfer function can be approximated by that of a second order low-pass filter (see Appendix D.3.2) under certain conditions. For very small detunings ($f_{\text{det}} \lessapprox$ FWHM), the transfer function is a 'mixture' of the broadband case and detuned case and cannot be described by the simple model given above. Such small detunings will, however, rarely be useful in practice.

1.10.1.2 Schnupp sideband throughput

The resonance of the Schnupp sidebands in the interferometer, which is already rather complicated in the broadband case (see Section 1.5.4), is even more complex in the detuned case. The upper and the lower Schnupp sideband have different resonance conditions. Figure 1.55 shows the throughput of the upper and lower Schnupp sidebands to the output for the 30 m prototype at a detuning of $\varphi_{\text{SR}} = 0.065$ rad, which corresponds to a peak sensititvity at $f_{\text{det}} = 100$ kHz. If we compare this plot with Figure 1.26, it can be seen that the maximal modulation throughput is reached at a very different Schnupp modulation frequency (at an offset of approximately f_{det} as compared with the broadband case). The lower plot shows the resulting dependence of the frequency response of the interferometer on the Schnupp modulation frequency for two signal frequencies (a very low frequency and 100 kHz).

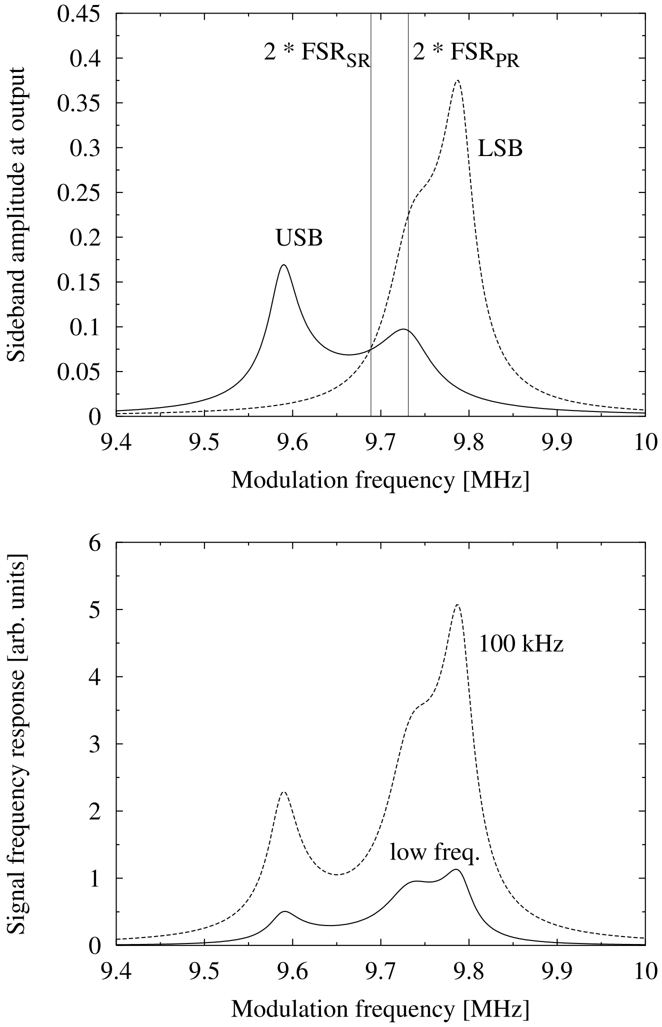

Figure 1.55: Schnupp sideband throughput in detuned dual recycling. The upper plot shows the amplitude of the upper and lower Schnupp modulation sidebands at the output (assuming unity input amplitude). The lower plot shows the dependence of the interferometer frequency response on the Schnupp modulation frequency, for signals of low frequency and 100 kHz, respectively.

If the lower curves of Figure 1.55 are normalized by dividing them by the square root of the average (DC) power arriving at the South port (according to Equation (1.85)), we find that the shot-noise limited sensitivity of the interferometer is almost independent of the Schnupp modulation frequency (this assumes that all other parameters, in particular the carrier power in the PR cavity, remain constant). This idealized shot-noise limited sensitivity varies only by around 1 % when the modulation frequency is varied between 9 MHz and 10 MHz.

Nevertheless one will usually strive for an efficient modulation throughput for the same reasons already given towards the end of Section 1.5.4. In detuned dual recycling, the generation of the error signal for the signal recycling mirror also depends on the Schnupp modulation frequency (see Section 1.10.2 below), such that in practice a compromise may be necessary in choosing the Schnupp modulation frequency.

1.10.1.3 Transfer function of the interferometer

The transfer function of the interferometer is the product of the signal transfer function and the Schnupp sideband throughput, which were discussed in the two previous sections. In order to take into account some complications which were neglected in the simplified discussion of the previous two sections, the transfer function is computed with Jun's program. Then both signal sidebands and both Schnupp modulation sidebands are properly taken into account including their phase.

Since, as we have seen, the throughput of the Schnupp modulation sidebands (and hence the amplitude of the output signal) depends on the tuning φ_{SR} as well as on the Schnupp modulation frequency, we will use the 'normalized' transfer functions

$$G_{\mathrm{n}} = \frac{\sqrt{|G_{1\mathrm{p}}|^2 + |G_{1\mathrm{q}}|^2}}{\sqrt{H_0}} \tag{1.109}$$

(see Equation (1.85)). Figure 1.56 shows these transfer functions for the parameters of the prototype and several detunings φ_{SR}. The value of the broadband ($\varphi_{\mathrm{SR}} = 0$) transfer function at low frequencies was taken as 0 dB reference.

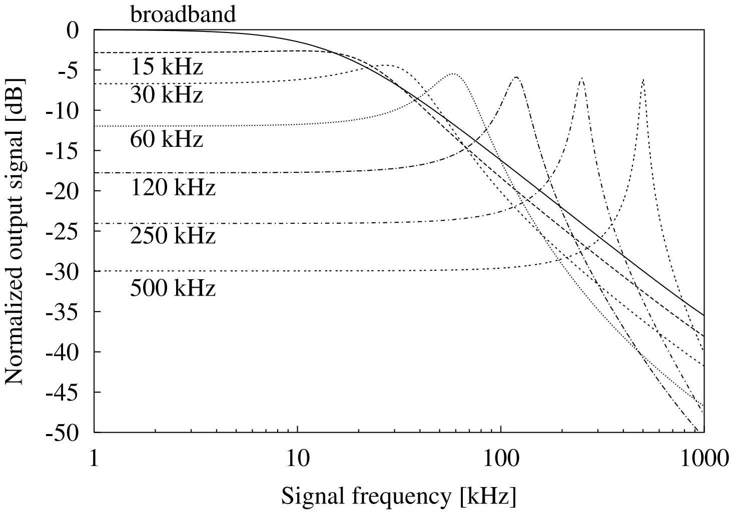

Figure 1.56: Normalized transfer functions of the dual recycled 30 m prototype for various detunings φ_{SR}. For the peak frequencies shown, the corresponding detunings were computed using Equation (1.108), e.g. $\varphi_{\mathrm{SR}} = 0.324$ for $f_{\mathrm{det}} = 500\,\mathrm{kHz}$.

Several of the points mentioned in Section 1.10.1.1 can be confirmed by this figure. For example, the smallest detuning (for $f_{\mathrm{det}} = 15\,\mathrm{kHz}$) is not very useful.

1.10.2 Control of detuned dual recycling

Just as in the broadband case, error signals must be generated for both the Michelson phase $\varphi_{\rm MI}$ and the SR mirror tuning $\varphi_{\rm SR}$, preferably by using only one Schnupp modulation frequency for both signals. The nominal operating point is now at $\varphi_{\rm SR} \neq 0$ (determined by $f_{\rm det}$, see Equation (1.108)), whereas we still have $\varphi_{\rm MI} = 0$ corresponding to the dark fringe of the carrier (see Figure 1.41).

A series of experiments was performed at the 30 m prototype and a method of obtaining such error signals (and to lock the interferometer) in a detuned state was successfully demonstrated[26]. This method is discussed here, together with some associated problems. Further work will be necessary to find a fully satisfactory control scheme for the detuned operation of GEO 600.

The error signals are, in principle, generated in a way similar to the broadband case (see Sections 1.6.2.2 and 1.6.3.1 and Figure 1.29). In particular, the Michelson error signal is obtained by demodulating the photocurrent at the South port with the Schnupp modulation frequency (around 9.7 MHz), whereas the SR error signal is obtained by demodulating the photocurrent generated by a weak beam picked off one arm with the same Schnupp modulation frequency. It should be noted that some variations of this method had already been discussed for some time by various people[27].

The two demodulation phases used in the two mixers that generate the error signals will be called $\chi_{\rm MI}$ and $\chi_{\rm SR}$, respectively. Experimentally they are adjusted by phase shifters in the local oscillator lines which drive **Mix3** and **Mix4** in Figure 1.29. Our method is based on choosing appropriate values for the Schnupp modulation frequency and the demodulation phases $\chi_{\rm MI}$ and $\chi_{\rm SR}$. The Michelson error signal will, under most conditions, have a zero crossing at $\varphi_{\rm MI} = 0$. The first difficulty lies in generating an error signal for the signal recycling mirror that has a zero crossing at the (predetermined) tuning $\varphi_{\rm SR} \neq 0$.

Looking at Figure 1.44, one might be tempted to use the error signal shown there and add a DC offset to it, such that the locking point is shifted away from $\varphi_{\rm SR} = 0$. This is, however, not very desirable because the gain of the error signal and hence the locking point will depend on many variables of the apparatus, such as injected light power, Schnupp modulation index, PR gain, alignment etc.

In the following it will be shown that under certain conditions an SR error signal can be generated that has a zero crossing at $\varphi_{\rm SR} \neq 0$ which does not depend on these variables. In the following discussion, which assumes the parameters of the 30 m prototype, the desired locking point will be assumed to be at $f_{\rm det} = 100\,$kHz, corresponding to $\varphi_{\rm SR} = 0.065$ (see Equation (1.108)).

The basic idea is to shift the Schnupp modulation frequency from its optimum in the

---

[26] These experiments were carried out in collaboration with A. Freise.

[27] These 'various people' include in particular Ken Strain and Jun Mizuno. During the workshop on simulation tools held in Garching in April 1998 [STAIC], David McClelland proposed a similar scheme which would use the light reflected from the PR cavity (instead of the light from one arm) to generate the SR error signal.

broadband case (see Section 1.5.4) by approximately f_{det}. Figure 1.57 shows (as a first attempt) both the Michelson error signal and the SR error signal that are generated if the Schnupp modulation frequency is shifted by $f_{\mathrm{det}} = 100\,\mathrm{kHz}$ (from $2 \cdot \mathrm{FSR}_{\mathrm{SR}} = 9688\,\mathrm{kHz}$ to $9788\,\mathrm{kHz}$)[28]. The plot was generated under the following assumptions: The nominal operating point is given by $\varphi_{\mathrm{MI}} = 0$ and $\varphi_{\mathrm{SR}} = 0.065$. The x-axis of both plots shows one of the two tunings, while the other tuning remains at the nominal operating point. The PR cavity tuning is computed such that the PR cavity is always resonant (see Section 1.6.1.3).

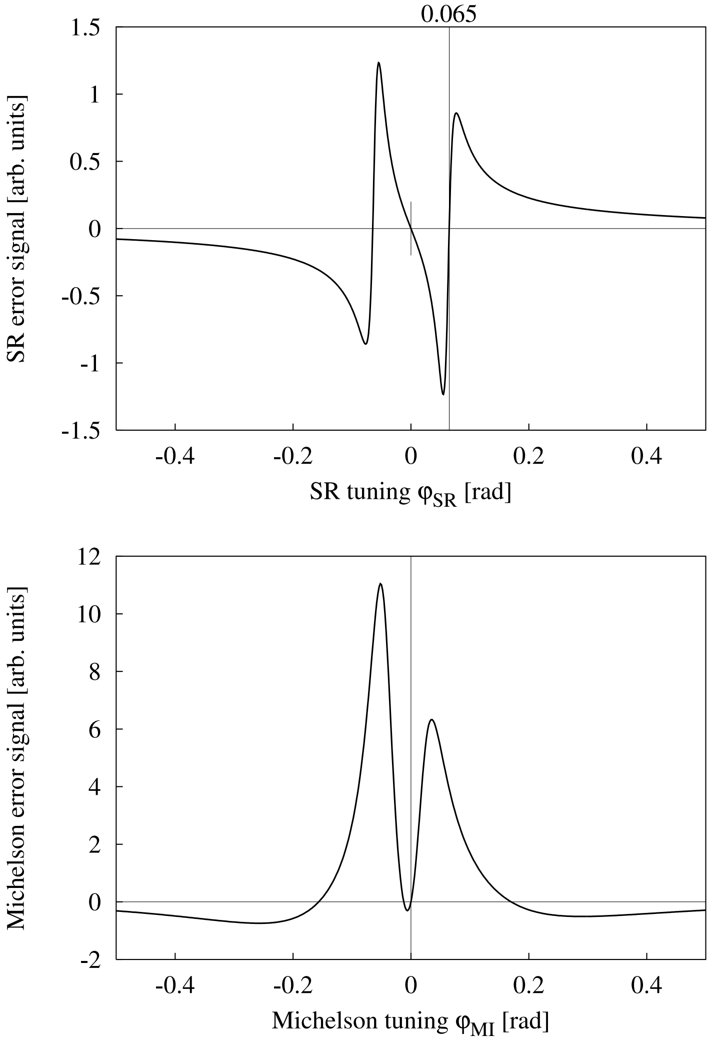

Figure 1.57: Error signals for detuned dual recycling (see text). The nominal operating point is indicated by the long thin lines.

---

[28] For simplicity an integer multiple of $\mathrm{FSR}_{\mathrm{SR}}$ is assumed as optimal Schnupp modulation frequency for broadband operation, although in reality the coupled cavities' resonance (see Sections 1.5.4 and 1.10.1.2) must be studied.

The Michelson demodulation phase χ_{MI} was computed from Equation 1.74 for a maximal frequency response at the operating point (for low signal frequencies, this corresponds to a maximal slope of the plotted curve at $\varphi_{\mathrm{MI}} = 0$, see Equation (1.56)). The plotted Michelson error signal is then found as $H_1(\chi_{\mathrm{MI}})$ (see Equation (1.50)), where detection at the South port is assumed.

The SR demodulation phase χ_{SR} was determined as

$$\chi_{\mathrm{SR}} = \frac{\pi}{2} + \frac{H_{1\mathrm{q}}}{H_{1\mathrm{p}}}, \tag{1.110}$$

where $H_{1\mathrm{p}}$ and $H_{1\mathrm{q}}$ were computed at the operating point, assuming detection at the East port. This is the very demodulation phase that yields a zero-crossing at the operating point.

The SR error signal is satisfactory, having two steep zero-crossings at $\varphi_{\mathrm{SR}} = \pm 0.065$. There is also another zero-crossing at $\varphi_{\mathrm{SR}} = 0$, which is, however, irrelevant, because it has the opposite polarity. Both locking points of φ_{SR} ($+0.065$ and -0.065) yield the same frequency response, i.e. Figure 1.56 remains unchanged.

Unfortunately the Michelson error signal is rather problematic. It does have a zero-crossing at the operating point $\varphi_{\mathrm{MI}} = 0$, which even has sufficient slope there (compare Figure 1.55). But the locking range (i.e. the range on both sides of the operating point where the error signal has the correct sign) is very small on one side. The next zero-crossing occurs already at -0.013 rad. This makes lock acquisition difficult and the whole system potentially unstable.

If the sign of the SR tuning φ_{SR} is changed (i.e. $\varphi_{\mathrm{SR}} = -0.065$ in the example), the Michelson error signal undergoes a point reflection about the origin (of the lower plot in Figure 1.57). This means in particular that the zero-crossing at $\varphi_{\mathrm{MI}} = 0$ retains its slope and polarity, and hence $\varphi_{\mathrm{SR}} = -0.065$ is an equivalent operating point, where lock acquisition might occur with the same probability. The small locking range of the Michelson error signal is now on the other side (i.e. between 0 and 0.013 rad). Thus the two operating points are not completely equivalent in all respects. In the prototype experiments, however, no attempt was made to identify the sign of φ_{SR} and it is quite possible that the system was locked with different signs on different occasions.

In the prototype experiments, the tiny locking range was slightly improved by a compromise: The Schnupp modulation frequency offset was reduced (we used 48 kHz above $2\,\mathrm{FSR}_{\mathrm{SR}}$ instead of 65 kHz for a detuning of $\varphi_{\mathrm{SR}} = 0.042$ rad, which corresponds to $f_{\mathrm{det}} = 65$ kHz, see Section 1.10.3). This deteriorates the shape of the SR error signal, but improves the shape of the Michelson error signal (see below). The locking range for the Michelson error signal can also be improved by de-adjusting the Michelson demodulation phase χ_{MI} from its optimal value (which was adjusted for maximal gain at low signal frequencies), at the expense of having a reduced slope at $\varphi_{\mathrm{MI}} = 0$. Under the same conditions as shown in Figure 1.57, the closest undesired zero-crossing can thus (by changing χ_{MI}) be shifted from -0.013 rad to about -0.04 rad. It can be imagined to use such ‘misadjustments’ of the Schnupp modulation frequency and χ_{MI} during lock acquisition, which are then slowly and carefully re-adjusted to their optimal values during operation.

If these tricks prove to be insufficient for GEO 600, there are at least two other possibilities to obtain good error signals for both φ_{MI} and φ_{SR}. Of course, two different modulation frequencies could be used to generate the two error signals. Then it would be possible to optimize the Schnupp modulation frequency independently for both error signals. The Michelson error signal has its 'normal' form (such as shown in Figure 1.39) if it is produced with a Schnupp modulation frequency near $\mathrm{FSR}_{\mathrm{SR}}$ or one of its multiples. The SR error signal, on the other hand, has its best form if the Schnupp modulation frequency has an offset of approximately f_{det} from $\mathrm{FSR}_{\mathrm{SR}}$.

If two modulation frequencies were used, there would be two alternatives to choose from: They could be chosen near the *same* multiple of $\mathrm{FSR}_{\mathrm{SR}}$, i.e. approximately f_{det} apart. This would allow the use of only one Pockels cell with one resonant transformer for both of them. Problems may be expected from beat signals at the difference frequency (near f_{det}) in both mixers, which will probably be undesirable (after all, f_{det} is approximately the sensitivity maximum of the detector, where gravitational wave signals are sought).

Otherwise the two modulation frequencies could be chosen near *different* multiples of $\mathrm{FSR}_{\mathrm{SR}}$ (in GEO 600, we have $\mathrm{FSR}_{\mathrm{SR}} \approx 125\,\mathrm{kHz}$). This should reduce or eliminate the beat frequency problems but would require another Pockels cell (or a rather difficult driver/transformer).

There is, however, still another possibility to get reasonable error signals for both φ_{MI} and φ_{SR} without using two modulation frequencies. It turns out that, if one single Schnupp modulation frequency is chosen near a *higher* multiple of $\mathrm{FSR}_{\mathrm{SR}}$, the SR error signal is almost unaffected (it still looks very similar to the one shown in Figure 1.57). The Michelson error signal, however, changes its shape considerably, and the locking range may increase. This was only tested in simulations with the parameters of the 30 m prototype, and Figure 1.58 shows an example. Here a modulation frequency of $20\,\mathrm{FSR}_{\mathrm{SR}} + 100\,\mathrm{kHz} = 96.98\,\mathrm{MHz}$ has been chosen rather arbitrarily.

Although the shape of the Michelson error signal is now somewhat peculiar, it has a locking range of more than 0.1 rad in both directions from the operating point $\varphi_{\mathrm{MI}} = 0$. These simulations have not been followed any further, since, with the parameters of GEO 600, considerably different results may be expected.

One feature of the discussed control scheme is that the operating point of the SR cavity (i.e. φ_{SR} and equivalently f_{det}) is determined by both the Schnupp modulation frequency *and* the local oscillator phase χ_{SR} that is used in generating the SR error signal. For example, Figure 1.59 shows the dependence of the SR error signal on χ_{SR} (computed as in Figure 1.57, in particular with a modulation frequency of 9788 kHz). If χ_{SR} is varied by ± 0.5 rad around the phase that gives a zero-crossing at $\varphi_{\mathrm{SR}} = 0.065$, the zero crossings move between 0.0594 rad and 0.0722 rad, corresponding to sensitivity peaks between 92 kHz and 111 kHz.

This is both an advantage and a problem. It is an advantage, because the precise frequency of the sensitivity peak (f_{det}) may be moved (by small amounts) by adjusting χ_{SR} without changing any other parameters of the system. This might be useful if either one fixed frequency is to be observed (such as an expected pulsar signal), or else a frequency is to be tracked (such as the identified signal of a coalescing binary). The

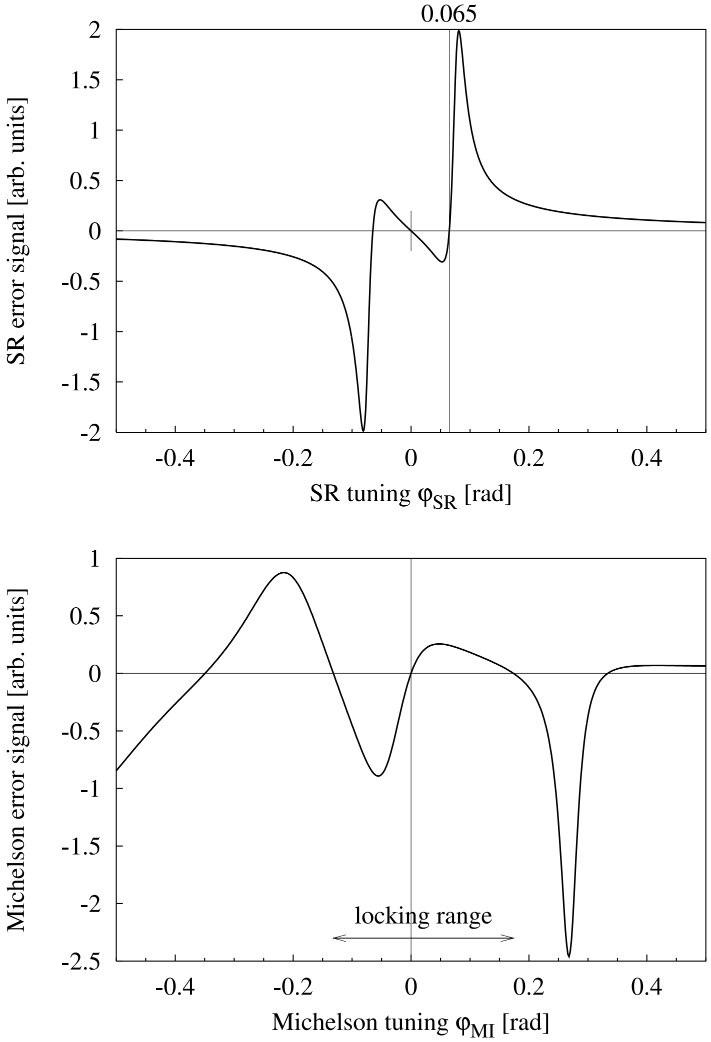

Figure 1.58: Error signals for detuned dual recycling, for a modulation frequency near 97 MHz (see text).

dependence of $f_{\rm det}$ on $\chi_{\rm SR}$ may also be a problem, because it requires a very stable demodulation phase $\chi_{\rm SR}$. This is a technical problem involving the stability of the resonant transformer that feeds the Pockels cell, and of the phase shifter that feeds the mixer generating the error signal. It is likely that these problems can be solved, in particular if calibration signals are periodically (or even continually) applied in the interferometer.

1.10.3 Experimental demonstration of detuned dual recycling

In the experiments on detuned dual recycling, the control scheme discussed in the previous section was used. Apart from testing the control scheme, the main goal of

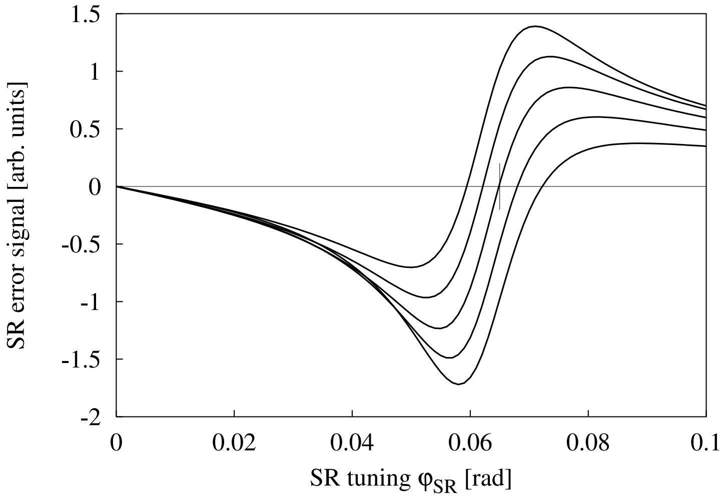

Figure 1.59: SR error signals as a function of the demodulation phase χ_{SR}. The five curves shown were computed with offsets of -0.5, -0.25, 0, $+0.25$ and $+0.5$ rad referred to the demodulation phase χ_{SR} used in Figure 1.57.

the experiments was to verify the frequency response for test signals that simulate gravitational wave signals. With the parameters of the prototype, a clearly visible peak in the frequency response occurs only at frequencies higher than about 50 kHz. Thus the first step was to find an actuator that could simulate gravitational wave signals at such frequencies. Luckily it turned out the the coils and magnets already present on one end mirror (M_1 in Figure 1.29) could be used for that purpose (after modification of the current drivers).

Figure 1.60 shows the transfer function that was observed. Test signals were fed to the current driver connected to coils behind the mirror, and were observed at the Michelson output (**Mix3** in Figure 1.29) while the interferometer was operated in broadband dual recycling mode. Many resonances are visible in the range of 20 … 100 kHz. Some of them are resonances of the test mass itself,[29] while others were not identified. This transfer function was measured with our HP 3562A network analyzer. The phase of the transfer function was also recorded.

The experiment itself was relatively straightforward, compared with the simulations of Section 1.10.2. One of the resonances (near 69 kHz) was selected, and a test signal at that frequency was injected via the current driver. The goal was to detune the interferometer such that the sensitivity peak would be near $f_{det} \approx 70$ kHz (which corresponds to $\varphi_{SR} \approx \pm 0.045$ rad).

The two variables available for control of the detuning φ_{SR}, were the Schnupp modulation frequency and the demodulation phase χ_{SR}, as discussed in Section 1.10.2. First

---

[29] According to a simple calculation following [McMahon64], the three lowest resonances should be at 20.7, 20.8 and 26.3 kHz. In the measured spectrum there are indeed two resonances near 21 kHz and another one near 27 kHz visible.

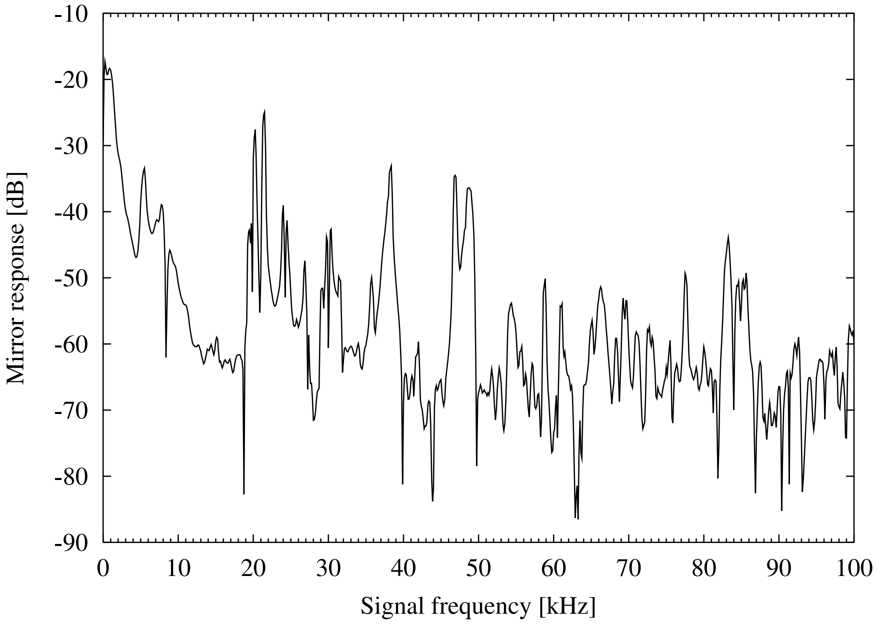

Figure 1.60: Transfer function of the end mirror M_1 driven by coil-magnet actuators, which were used to simulate gravitational wave signals.

the interferometer was locked in broadband operation. Then these two variables (and the other demodulation phase χ_{MI}, which also changes in the process[30]) were slowly and carefully adjusted until the 69 kHz signal appeared with maximal amplitude at the output, while the interferometer would still lock. The best modulation frequency thus found was 9736 kHz. In this state the frequency response of Figure 1.60 was again measured. The difference between these two measurements (i.e. the ratio of the two transfer functions) was expected to show the effect of the detuning while cancelling the effect of the mirror resonances, and was compared with the simulations. Figure 1.61 shows the first results obtained.

The theoretical curve was obtained as the ratio of two functions $G_1(\chi_{\mathrm{MI}})$ (see Equation (1.57)), which were computed separately for the conditions of the respective measurement. The parameters that were changed between the two calculations were the SR tuning φ_{SR} (from 0 to 0.042 rad), Schnupp modulation frequency (from 9688 kHz to 9736 kHz) and the Michelson demodulation phase χ_{MI} (from -0.47 rad to -1.65 rad). The three parameters (φ_{SR} for the detuned measurement, and χ_{MI} for both measurements) were found with a non-linear least-squares fit. If the phase of the transfer function is ignored, and only the absolute gain is used, an even better fit for the gain alone can be found.

The measured additional gain around 70 kHz and especially the good agreement of the

---

[30] This was caused not only by the purely optical effects, which can be predicted by Jun's program, but also by additional technical frequency-dependent phase shifts in the resonant transformer that drives the Pockels cell and in resonant circuits in the electronic phase-shifters.

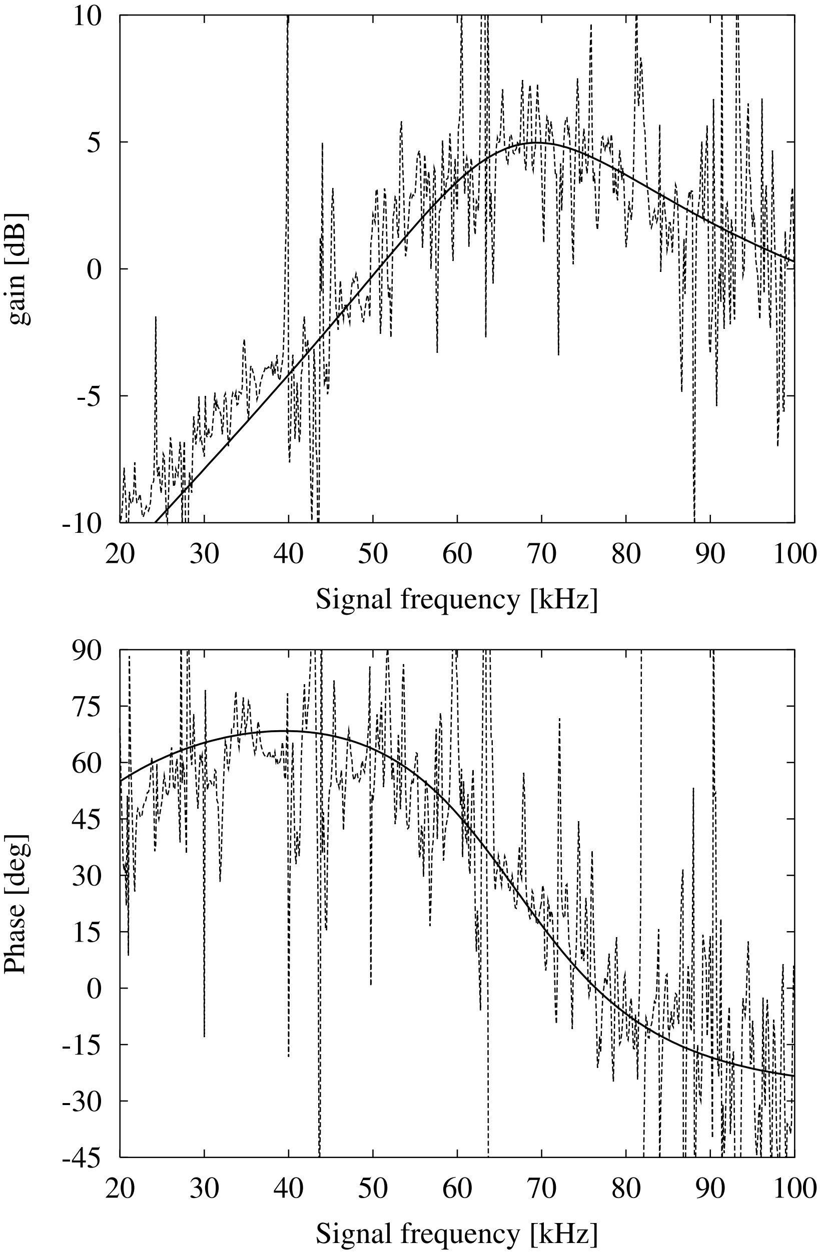

Figure 1.61: Change in the transfer function of the dual recycled interferometer due to detuning. Shown are the measured data and the computed curve (see text).

phase shift visible in Figure 1.61 show clearly that our models are basically correct and that we have indeed locked the interferometer in a detuned state.

Furthermore it turned out that the whole system continued to behave as 'friendly' as before; in particular the lock acquistion tended to happen by itself, just as described in Section 1.7 for the broadband case[31], and the autoalignment system also continued to work as before. In practice, all we needed to do in order to operate the interferometer in a detuned state was to change the Schnupp modulation frequency and the two demodulation phases (χ_{MI} and χ_{SR}). Since these three variables could in principle be calibrated by a set of reference measurements, the author sees no fundamental problem in detuning the interferometer to a desired sensitivity maximum f_{det} by some automated mechanism. Hence there is optimism that even for the very different parameters of GEO 600, a similar scheme might be found.

Figure 1.62 shows the Michelson and SR error signals computed with the parameters of that measurement. It can be seen that by choosing a modulation frequency offset somewhat smaller than f_{det} (48 kHz instead of 65 kHz) and suitable demodulation phases (χ_{MI} and χ_{SR}), useable error signals were generated for both the Michelson and the SR mirror with a single Schnupp modulation frequency.

In order to verify the measurements and to try other locking points, the same experiment was repeated a few days later. Now another network analyzer was used to generate and detect the test signals, our new HP 8751A, which also works for frequencies > 100 kHz, and which allows the source to be programmed in such a way that only certain frequencies are generated. This feature was used to generate test signals only near some of the resonances of Figure 1.60, because the response for other frequencies (in between the resonances) is so small in either state of the interferometer, that no useful information can be extracted. The modulation frequency in these experiments was 9740 kHz. Figure 1.63 shows the results of these measurements for two different detunings φ_{SR}.

Note that in the experiment the two different detunings were set by only changing the SR error signal demodulation phase χ_{SR} without changing any other parameters (for the measurements, however, the Michelson demodulation phase χ_{MI} was readjusted between measurements). The fitted curves were computed using the following parameters (which were again found by a nonlinear fit):

First (upper) curve: The SR detuning φ_{SR} was 0.0444, corresponding to $f_{\mathrm{det}} = 68$ kHz. The Michelson demodulation phase χ_{MI} during the broadband reference measurement was 0.14 rad, whereas χ_{MI} during the detuned measurement was -1.66 rad.

Second (lower) curve: The SR detuning φ_{SR} was 0.0572, corresponding to $f_{\mathrm{det}} = 88$ kHz. The Michelson demodulation phase χ_{MI} during the broadband reference measurement was 0.06 rad, whereas χ_{MI} during the detuned measurement was -1.40 rad.

---

[31] This was true under the same assumptions as were given there, in particular good initial alignment of the whole interferometer.

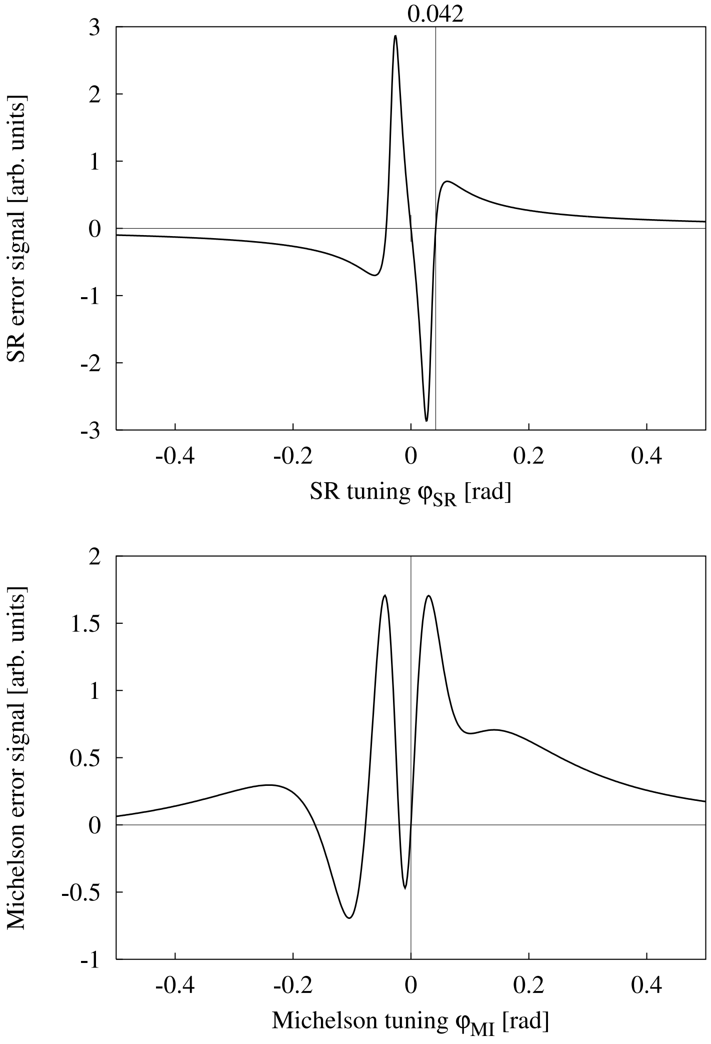

Figure 1.62: Computed error signals for detuned dual recycling, using the parameters that occurred in the experiment (9736 kHz modulation frequency, $\varphi_{\mathrm{SR}} = 0.042\,\mathrm{rad}$, $\chi_{\mathrm{MI}} = -1.65\,\mathrm{rad}$).

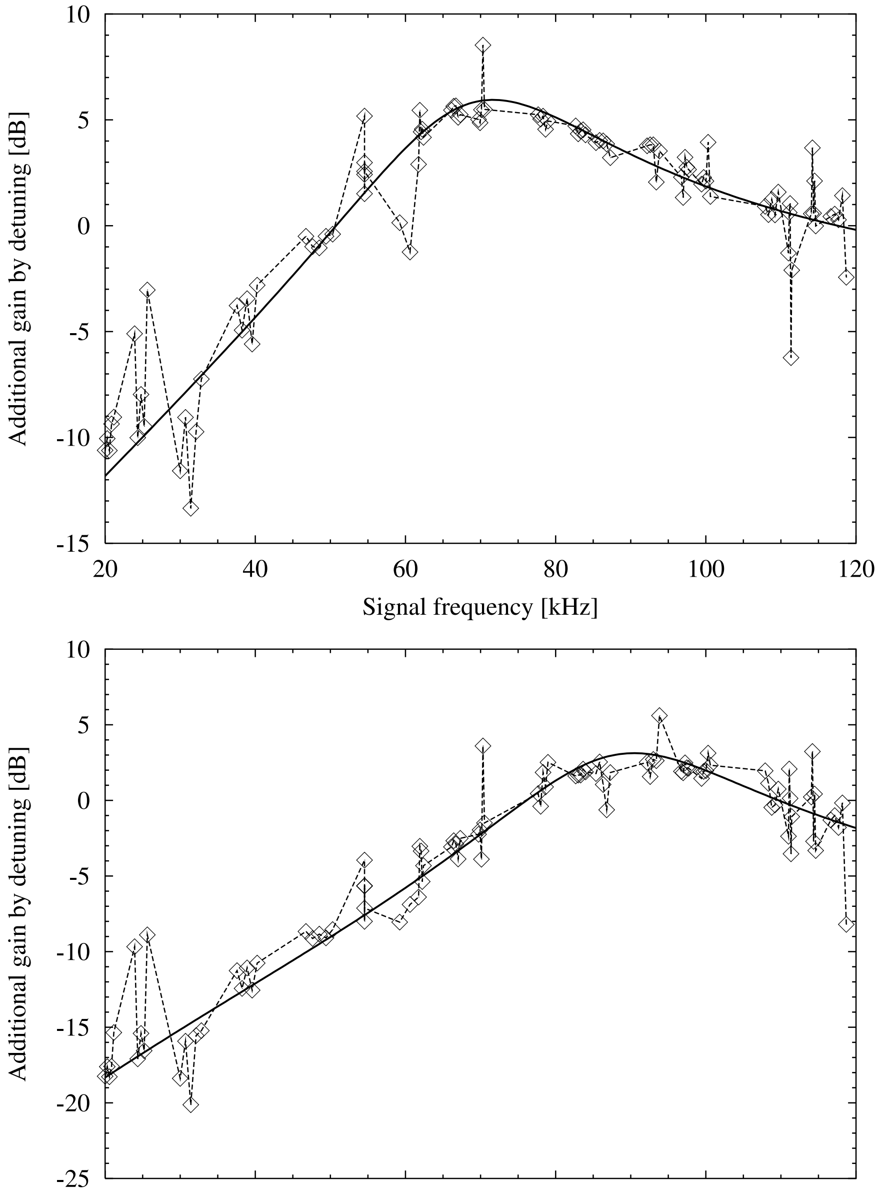

Figure 1.63: Change in the transfer function of the dual recycled interferometer due to detuning. Shown are the measured data and the computed curve (see text).

Unfortunately, the phase of the transfer functions was too noisy to be of any use and was thus ignored.

1.11 Must PR and SR cavity have different lengths?

In the 30 m prototype, PR cavity and SR cavity have slightly different lengths (the distance from the beamsplitter (BS) to $\mathrm{M_{PR}}$ is 15 cm, whereas from BS to $\mathrm{M_{SR}}$ it is 28.5 cm, see Appendix A.4). This is due to constructional reasons, but was also believed to be necessary for the operation of detuned dual recycling. To investigate this question, some simulations with Jun's program were run that assume equal lengths of the PR and SR cavities. For those simulations, all the parameters of the prototype were used, except for the distances $\mathrm{BS}-\mathrm{M_{PR}}$ and $\mathrm{BS}-\mathrm{M_{SR}}$, which were both set to 21.75 cm (the average of their previous values). The FSR of both cavities would then be 4855 kHz (as compared to 4865 and 4845 kHz with the true lengths). Note that an armlength difference between the two long arms (6 cm in the prototype) is always necessary with Schnupp modulation (see Section 1.5.4).

These few simulations cannot, of course, give a generally valid answer to the question asked in the title of this Section. For the parameters of the prototype, they do, however show *no significant difference*, i.e. the prototype experiments could probably have also been carried out with equal lengths. No simulations were done with a larger length difference.

In the broadband case ($\varphi_{\mathrm{SR}} = 0$), the SR error signal is essentially unchanged (compare the lowest curve of Figure 1.44). The Michelson error signal, on the other hand, even improves as compared to the lowest curve of Figure 1.39. The amplitude of the 'overshoot' with the wrong sign is reduced to about one third of its previous value.

For the detuned case, the situation is also largely unchanged. Error signals very similar to those discussed in Section 1.10.2 were predicted by the simulation. As an example, Figure 1.64 is the direct equivalent to Figure 1.57, for equal lengths of PR- and SR-cavity. The Michelson error signal has the same problems as before, which probably could be cured with the same measures.

For GEO 600, these results are only of limited direct applicability, because of the very different parameters. However, it should not be taken for granted that a difference between the lengths of the PR- and the SR-cavities is intrinsically necessary, if a control scheme similar to that described in Section 1.6 is used.

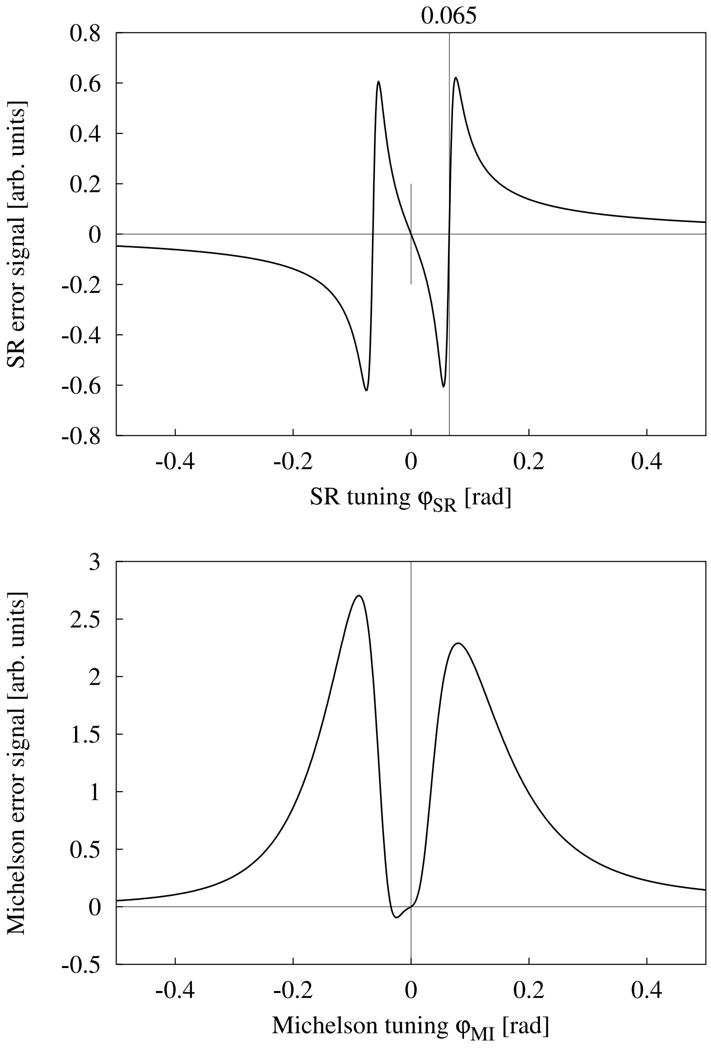

Figure 1.64: Error signals for detuned dual recycling under the same conditions as in Figure 1.57, but with equal lengths of PR- and SR-cavity.

Chapter 2

Autoalignment

This chapter describes the autoalignment system for the 30 m prototype that was developed by the author. It was built during the first half of this work using the configuration with external modulation (see Section 1.3.2, Appendix A.7 and Figure A.15). After external modulation had been replaced by Schnupp modulation and dual recycling had been introduced, the system continued to function without modification. There is, however, not yet an autoalignment system for the signal recycling mirror M_{SR}, and the discussion in this chapter assumes a Michelson interferometer with power recycling only. A summary of the material presented in Sections 2.1 to 2.9 is about to be published [Heinzel99]. Some alignment error signals for GEO 600 are computed in Section 2.10.

2.1 Introduction

To make the interferometer work optimally all optical components need to be well aligned, and to remain so for extended periods of time. 'Alignment' in this chapter refers to angular alignment of mirrors and beamsplitter, assuming the relevant longitudinal loops to be working, in particular the PR cavity to be resonant in its fundamental mode. In the following we consider only a single angular dimension α for each component, the orthogonal direction to be handled equivalently. In this chapter, we count an angle as positive if it is rotated *clockwise* from a reference direction. Figure 2.1 schematically shows all possible misalignments in one dimension.

The required performance can only be achieved with an automatic alignment system. There are three different methods known to the author that can be used for automatic alignment of interferometers:

- The *differential wavefront sensing technique*, first developed by H. Ward and others [Morrison94]. This is the method that we use and extend here, and which is described below.
- The *Anderson* method [Anderson84, Sampas90] for aligning a Fabry–Perot cavity requires a phase modulation of the incoming beam with a fixed frequency given by

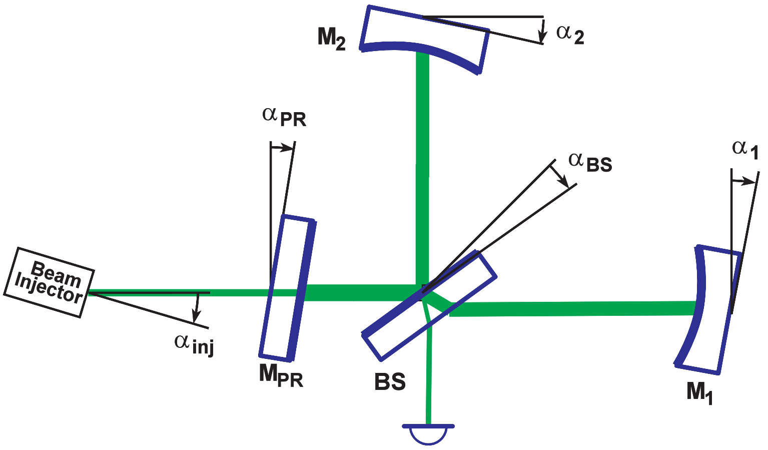

Figure 2.1: Schematic diagram of a power-recycled Michelson interferometer showing all possible angular misalignments α in one dimension. Beams are shown in their nominal positions, whereas the components are shown misaligned by exaggerated angles.

the difference of resonance frequencies of the fundamental and first higher order modes in the cavity. The error signal is obtained with a quadrant photodiode looking at the *transmitted* light. Since for a high PR gain we do not want much light to be transmitted through the end mirrors, and because this method is not easily applicable to a Michelson interferometer, we do not discuss it any further in this chapter. The VIRGO project plans to use a combination of the above two methods and has shown in a table-top prototype [Babusci97] that error signals according to theory can be obtained.

- The most straightforward method of *dithering* all degrees of freedom with different low modulation frequencies has been used to align a Fabry–Perot cavity [Kawabe94]. For various reasons we do, however, not believe that this is a practical scheme for gravitational wave detectors.

Referring to Figure 2.1, we can separately consider the following alignment tasks:

Michelson alignment: For optimal interference contrast, the axes of the beams returning from the two arms need to coincide when they recombine at the beamsplitter. The two degrees of freedom to be controlled are (1) the 'differential' term[1] $\alpha_{\mathrm{diff}} = \alpha_1 + \alpha_2$ of the end-mirror alignments, and (2) its equivalent in the other dimension. Good alignment of the Michelson interferometer is also necessary to suppress the coupling of beam jitter into noise in the output signal [Rüdiger81].

Power recycling cavity alignment: If we assume the incoming laser beam to be fixed in space, the PR cavity's axis needs to coincide with the incoming beam's

---

[1] Due to the reflection at the beamsplitter experienced by only one beam, the differential alignment of the end mirrors corresponds to $\alpha_1+\alpha_2$, whereas the common-mode alignment corresponds to $\alpha_1-\alpha_2$.

axis in order to obtain optimal coupling of the laser light into the PR cavity. There are four degrees of freedom to be controlled: (1) the PR mirror's alignment α_{PR}, (2) the common mode term $\alpha_{\mathrm{comm}} = \alpha_1 - \alpha_2$ of the end mirror alignments, and (3, 4) their equivalents in the other dimension.

Spot positions on mirrors: If the above two systems are working, there are two more uncontrolled optical components: The beam injector[2] (which is usually also suspended as a pendulum), and the beamsplitter. These two components define the position of the beam spot on the far mirrors M_1 and M_2, respectively. Although these spot positions in principle do not affect the operation of the interferometer, in practice one also needs to control these four degrees of freedom for various reasons, such as wandering spot positions on mirrors and photodetectors, scattered light variations, inhomogeneities of mirror coatings, etc.

Thus there are 5×2 degrees of freedom in a power-recycled Michelson interferometer (beam injector, PR mirror, beamsplitter and two end mirrors) to be controlled in order to fix all beams in space. The beam positions are then completely defined by the lateral positions of the beam injector and of the sensors that determine the beam spot positions on the end mirrors.

2.2 Misalignments in the mode picture

Small angular misalignments of a Gaussian laser beam can conveniently be described by adding a small component of the first order Gauss-Hermite mode to the dominating fundamental mode [Rüdiger81, Anderson84]. A mismatch in beam size or waist position can similarly be described by a mixture of the fundamental mode with higher order modes. Because of symmetry reasons, in this case the Gauss-Laguerre modes are more convenient. Since we do not expect these mismatches to be as troublesome as angular misalignments (their main effect will be a sub-optimal coupling of the incoming beam into the PR cavity) and because we do not plan to incorporate an automatic system to correct these mismatches, they are not considered in this chapter. In the following we assume perfect mode-matching.

Hefetz et al. [Hefetz97] develop a general formalism to describe arbitrary misaligned fields using operators in modal space. Here, however, we concentrate on the practical computation of alignment error signals. Our analysis is restricted to the two lowest modes and emphasizes experimental aspects such as the geometry of the interferometer, various possible modulation schemes for a power-recycled Michelson interferometer, and the manipulation of the beam with lens systems to separate the error signals.

The electrical field amplitude of a Gaussian beam propagating along the z-axis, with

---

[2] By 'beam injector' we mean the last component determining the position and angle of the beam hitting the PR mirror. In our prototype this is a fiber output coupler suspended as a pendulum, whereas in the large interferometers it will probably be a suspended beam-steering mirror.

its waist at $z = 0$, is given by (see e.g. [Yariv])

$$E_{l,m}(x,y,z) = E_0 \frac{w_0}{w(z)}\, u_l(x,z)\, u_m(y,z) \exp\left[\mathrm{i}\left((l+m+1)\eta(z) - k\frac{x^2+y^2}{2R(z)}\right)\right] \tag{2.1}$$

with the spot radius

$$w(z) = w_0\sqrt{1+\left(\frac{z}{z_\mathrm{R}}\right)^2}\,, \tag{2.2}$$

the Rayleigh range z_R given by

$$z_\mathrm{R} = \frac{\pi w_0^2}{\lambda}\,, \tag{2.3}$$

the radius of curvature of the wavefronts

$$R(z) = z\left(1+\frac{z_\mathrm{R}^2}{z^2}\right)\,, \tag{2.4}$$

the Guoy phase shift

$$\eta(z) = \arctan(z/z_\mathrm{R}), \tag{2.5}$$

and the modal functions

$$u_i(x,z) = C_i\, H_i\left(\frac{x\sqrt{2}}{w(z)}\right) \exp\left(-\frac{x^2}{w^2(z)}\right) \tag{2.6}$$

containing the Hermite polynomials $H_i(x)$ and normalization constants C_i. In equation (2.1), the propagation term $\exp(\mathrm{i}\,(\omega t - kz))$ has been omitted and we assume $n \equiv 1$, i.e. beams propagating in vacuum. In the following we again omit the second spatial dimension y and need to consider only the transverse functions

$$u_0(x,z) = C\exp\left(-\frac{x^2}{w^2(z)}\right)\,, \tag{2.7}$$

$$u_1(x,z) = C\frac{2x}{w(z)}\exp\left(-\frac{x^2}{w^2(z)}\right)\,, \tag{2.8}$$

$$C = \sqrt[4]{\frac{2}{\pi w^2(z)}}. \tag{2.9}$$

Out of several possible normalizations for the u_i, we have here chosen the one that later gives the simplest coupling coefficients and also satisfies $\int_{-\infty}^{\infty}[u_0(x,z)]^2\,dx = \int_{-\infty}^{\infty}[u_1(x,z)]^2\,dx = 1$. For future reference we also compute the following integrals:

$$\int_{-\infty}^{\infty} u_0(x,z)u_1(x,z)dx = 0, \tag{2.10}$$

$$\int_0^{\infty} u_0(x,z)u_0(x,z)dx - \int_{-\infty}^{0} u_0(x,z)u_0(x,z)dx = 0, \tag{2.11}$$

$$\int_0^{\infty} u_0(x,z)u_1(x,z)dx - \int_{-\infty}^{0} u_0(x,z)u_1(x,z)dx = \sqrt{\frac{2}{\pi}}. \tag{2.12}$$

Note that the functions u_0 and u_1 do not contain the wavefront curvature. The effects of the curvature are, however, taken into account in the formalism below. We will use a TEM$_{00}$ beam described by u_0 as reference and compare a slightly misaligned TEM$_{00}$ beam against this reference. We assume the misaligned beam to have the same waist size and longitudinal waist position as the reference.

At the beam waist ($z = 0$), the u_1 component is in phase with u_0 for lateral displacements Δx, and in quadrature for angular misalignments β between the beams' axes:

$$u_0(x-\Delta x,0) \approx u_0(x,0) + \frac{1}{w_0}\,\Delta x\, u_1(x,0), \tag{2.13}$$

$$u_0(x,0)\exp\left(\mathrm{i}\,\frac{2\pi}{\lambda}\,\beta\, x\right) \approx u_0(x,0) + \mathrm{i}\,\frac{\pi w_0}{\lambda}\,\beta\, u_1(x,0). \tag{2.14}$$

We will need to consider such a beam after propagation away from the waist ($z \neq 0$). It can be shown that the above approximations can consistently be generalized as follows. A real (in-phase) u_1 component corresponds to a lateral separation of the beams' centers with the scaling factor $w(z)$, whereas an imaginary component corresponds to an angle γ *between the wavefronts* with a scaling factor of $\lambda/[\pi w(z)]$. In the case of a tilt of the beams' axes by the angle β (about the beam waist as pivot), that angle is given by $\gamma(z) = \beta\, z_\mathrm{R}^2/(z^2 + z_\mathrm{R}^2)$. We thus have:

$$u_0(x-\Delta x,z) \approx u_0(x,z) + \frac{1}{w(z)}\,\Delta x\, u_1(x,z), \tag{2.15}$$

$$u_0(x,z)\exp\left(\mathrm{i}\,\frac{2\pi}{\lambda}\,\gamma\, x\right) \approx u_0(x,z) + \mathrm{i}\,\frac{\pi w(z)}{\lambda}\,\gamma\, u_1(x,z)\,. \tag{2.16}$$

These equations are valid for small misalignments, i.e. $\Delta x \lesssim w(z)$, $\gamma \lesssim \lambda/[\pi w(z)]$.

In general we will have to consider combinations of lateral displacements and angular misalignments, i.e. beams given by (at their waist):

$$u_0(x,0) + \kappa_1\, u_1(x,0) + \kappa_2\,\mathrm{i}\, u_1(x,0) = u_0(x,0) + \kappa\exp(\mathrm{i}\,\theta^\mathrm{w})\, u_1(x,0)\,. \tag{2.17}$$

We describe the 'character' of the misalignment at the waist by the angle $\theta^\mathrm{w} = \arctan(\kappa_2/\kappa_1)$, and its 'amount' by $\kappa = \sqrt{\kappa_1^2+\kappa_2^2}\,$.

When a misaligned beam propagates, the first order mode u_1 acquires an additional phase shift with respect to u_0 which is given by the Guoy phase $\eta(z) = \arctan(z/z_\mathrm{R})$ and which alters the ratio of lateral to angular misalignment. At a distance z from the waist we then have

$$u_0(x,z) + \kappa\exp(\mathrm{i}\,[\theta^\mathrm{w} + \eta(z)])\, u_1(x,z)\,. \tag{2.18}$$

For example, if we start with a beam that has a pure lateral displacement Δx at its waist ($\theta^\mathrm{w} = 0$) and consider its propagation away from the waist, we find that the real part of the coefficient of u_1 decreases. If, however, we take into account the scaling factor $w(z)$, the physical displacement Δx remains constant. At the same time an imaginary part of the coefficient of u_1 evolves, which corresponds to an angle γ between the wavefronts caused by the now finite wavefront curvature.

In the following we will have to consider propagation through a system of lenses and segments of free space, characterized by its overall phase shift Φ. After the sytem we then have $\theta^{\mathrm{d}} = \theta^{\mathrm{w}} + \Phi$ describing the character of the misalignment. $\theta^{\mathrm{d}} = 0$ corresponds to a displacement between the beam's centers with parallel wavefronts, whereas $\theta^{\mathrm{d}} = 90^\circ$ describes coinciding centers with an angle between the wavefronts. It will turn out that in the differential wavefront sensing scheme the detectors are only sensitive to that angle, such that $\theta^{\mathrm{d}} = 90^\circ$ yields the maximum signal.

2.3 Detection of misalignments

The alignment of an interferometer is determined by the superposition of the axes of two or more beams. In the differential wavefront sensing scheme, one of these must be phase modulated (usually at a frequency of several MHz). The intensity of the interference pattern will then in general contain a term at the modulation frequency. The integral of this term over the whole cross section contains information about the longitudinal phase relationship of the two interfering beams and is usually exploited for the corresponding longitudinal loop. If the two beams' axes are not perfectly superimposed, the RF term in the intensity of the interference pattern will have a spatial structure that we exploit to obtain error signals containing information about misalignments of the interferometer. This is the essence of the 'differential wavefront sensing' technique.

2.3.1 Fabry-Perot cavity

In the case of a Fabry-Perot cavity (such as the PR cavity), the Pound-Drever-Hall method [Drever83b] is used for longitudinal locking. The incoming beam is phase modulated with modulation index m at a frequency ω_{m} that is beyond the bandwidth of the cavity. The reflected beam consists of two components: the direct reflection from the coupling mirror (M_{PR} in our case), which still contains the phase modulation sidebands, and the beam leaking out of the cavity, which has no or negligible phase modulation. We take the directly reflected beam as reference and consider the beam leaking out of the cavity as misaligned against this reference. The amplitudes of the two beams can be written as (see also Section 1.2):

$$a_1 = c_1 u_0 \exp(\mathrm{i}\,\varphi)\big[J_0(m) + 2\,\mathrm{i}\,J_1(m)\cos(\omega_{\mathrm{m}} t)\big], \tag{2.19}$$

$$a_2 = -c_2 \left[u_0 + \kappa \exp(\mathrm{i}\,\theta^{\mathrm{d}}) u_1\right], \tag{2.20}$$

where c_1 and c_2 are positive constants, κ and θ^{d} represent the amount and character of the misalignment (see Equation (2.17) and Section 2.4) and φ is the phase difference between the fundamental mode terms of these two beams, arranged such that $\varphi = 0$ for the resonance of the cavity. Although only the first two Bessel functions J_0 and

J_1 appear in the equations, the following results can be shown to be valid for arbitrary modulation indices (assuming sinusoidal modulation and none of the modulation sidebands being resonant in the cavity).

We compute the light intensity $|a_1 + a_2|^2$ and determine the coefficients I_{ω_m} of the terms that oscillate with $\omega_\mathrm{m} t$. The longitudinal (Pound-Drever) error signal V_FP is found by integrating this I_{ω_m} term over the whole cross section of the beam:

$$V_\mathrm{FP} = \int_{-\infty}^{\infty} I_{\omega_\mathrm{m}}(x)dx = 4\, c_1 c_2\, J_1(m) \sin\varphi\,. \tag{2.21}$$

On the other hand, the alignment error signal W_FP is obtained with a split photodiode as the difference of the contributions from the two halves:

$$W_\mathrm{FP} = \int_{0}^{\infty} I_{\omega_\mathrm{m}}(x)dx - \int_{-\infty}^{0} I_{\omega_\mathrm{m}}(x)dx = 4\, c_1 c_2\, J_1(m) \sqrt{2/\pi}\,\kappa\, \sin(\varphi - \theta^\mathrm{d})\,. \tag{2.22}$$

A Mathematica program to compute these expressions is given in Appendix E.1.5. If the Pound-Drever loop is locked, we have $\varphi \approx 0$ and

$$W_\mathrm{FP} = -4\, c_1 c_2\, J_1(m) \sqrt{2/\pi}\,\kappa\, \sin\theta^\mathrm{d}. \tag{2.23}$$

Looking back at Equations (2.15) to (2.17) we see that we get a signal for an angular misalignment between the wavefronts ($\theta^\mathrm{d} = 90°$), but not for a lateral displacement. The signal is, as desired, proportional to the 'amount' κ of the misalignment

In the above calculations we have assumed that the beam hits the center of the photodiode. In Ref. [Morrison94] it is shown that any offset between the centers of the interference pattern and the photodiode causes a reduction of the signal and spurious signals from higher-order modes, such as second order modes corresponding to a mismatch in beam size or curvature. For this reason it is necessary to keep the beam always centered on the quadrant diode (see Section 2.6.2).

2.3.2 Michelson interferometer

For the Michelson interferometer, again a modulation technique is employed to read out the Michelson phase near a dark fringe. The planned large-scale interferometers will use either Schnupp modulation (see Section 1.3.3) or external modulation (Section 1.3.2). We now treat these two cases, which have both been successfully used with autoalignment in the 30-m prototype.

2.3.2.1 Schnupp modulation

In *Schnupp modulation*, the incoming laser beam is phase modulated with modulation index m at an angular frequency ω_m. An intentional length difference ΔL between the arms causes a fraction of the modulation sidebands to appear at the dark fringe port, where they act as local oscillator to detect the signal (and misalignment). We can write the amplitudes of the two beams from the arms as

$$\begin{aligned} a_1 &= c_1 \exp(-\mathrm{i}\,\frac{\varphi_{\mathrm{MI}}}{2}) \left[u_0 + \frac{\kappa}{2}\exp(\mathrm{i}\,\theta^{\mathrm{d}})u_1\right] \\ &\quad \times \left[J_0(m) + 2\,\mathrm{i}\,J_1(m)\cos(\omega_{\mathrm{m}}t + \varepsilon)\right] \qquad (2.24) \\ a_2 &= -c_2 \exp(\mathrm{i}\,\frac{\varphi_{\mathrm{MI}}}{2}) \left[u_0 - \frac{\kappa}{2}\exp(\mathrm{i}\,\theta^{\mathrm{d}})u_1\right] \\ &\quad \times \left[J_0(m) + 2\,\mathrm{i}\,J_1(m)\cos(\omega_{\mathrm{m}}t - \varepsilon)\right] \qquad (2.25) \end{aligned}$$

Here $c_1 \approx c_2$, φ_{MI} is the deviation of the Michelson phase from the dark fringe, and $2\varepsilon = 2\Delta L\,\omega_{\mathrm{m}}/c$ is the phase difference of the modulation after one roundtrip in the arms.

With the same method as above[3] we obtain as the signals for longitudinal locking (of the Michelson to a dark fringe) and alignment (see Appendix E.1.5):

$$V_{\mathrm{MI}} = 8c_1c_2\,J_0(m)J_1(m)\left[1 - \left(\frac{\kappa}{2}\right)^2\right]\sin\varepsilon\sin\varphi_{\mathrm{MI}}, \qquad (2.26)$$

$$W_{\mathrm{MI}} = -8c_1c_2\,J_0(m)J_1(m)\sqrt{2/\pi}\,\kappa\,\sin\varepsilon\cos\varphi_{\mathrm{MI}}\sin\theta^{\mathrm{d}}. \qquad (2.27)$$

The longitudinal loop (dark fringe lock) uses V_{MI} as error signal and keeps that error signal very close to zero, thus enforcing the dark fringe condition $\varphi_{\mathrm{MI}} = 0$. The alignment error signal W_{MI} is again proportional to the amount κ of the misalignment, and obtained only from the angular misalignment between the wavefronts.

2.3.2.2 External modulation

External modulation is described in Section 1.3.2. The autoalignment system of the 30 m prototype was developed with external modulation, which was later replaced by Schnupp modulation.

We now have to consider three interfering beams. We call their amplitudes a_1 and a_2 for the beams from the first and second arm, and a_3 for the local oscillator beam. According to the experimental setup described in Section 2.6 below, we assume a_3 to be taken from a_1 and thus perfectly aligned with it, whereas a_2 is misaligned against this reference. We can then write down the amplitudes

$$a_1 = c_1 u_0, \qquad (2.28)$$

$$a_2 = -c_2\left[u_0 + \kappa\exp(\mathrm{i}\,\theta^{\mathrm{d}})u_1\right]\exp(\mathrm{i}\,\varphi_{\mathrm{MI}}), \qquad (2.29)$$

$$a_3 = c_3 u_0\left[J_0(m) + 2\,\mathrm{i}\,J_1(m)\cos(\omega_{\mathrm{m}}t)\right]\exp(\mathrm{i}\,\psi). \qquad (2.30)$$

Here φ_{MI} represents the deviation of the Michelson phase from the dark fringe[4], ψ the phase of the Mach-Zehnder interferometer and c_1, c_2 and c_3 are positive constants with

---

[3] If higher order sidebands are included, the algebraic result needs to be transformed using the following relation of the Bessel functions (which follows from [Gradstein-Ryshik, Vol. 2, No. 8.538]): $\sum_{k=0}^{\infty}(-1)^k J_k(m)J_{k+1}(m) = \frac{1}{2}J_1(2m)$.

[4] Since in our setup the local oscillator beam is taken from one beam (a_1), we apply both the Michelson phase and the misalignment exclusively to the other beam (a_2) in this model.

$c_1 \approx c_2$ and $c_3 \ll c_1$. Both φ_{MI} and ψ are defined such that their nominal values at the operating point are zero. The signals for longitudinal locking (of the Michelson to a dark fringe) and alignment are found to be (see Appendix E.1.5):

$$V_{\mathrm{MI}} = -4c_3\, J_1(m)\, [c_2 \sin(\varphi_{\mathrm{MI}} - \psi) + c_1 \sin\psi]\,, \tag{2.31}$$

$$W_{\mathrm{MI}} = -4c_2c_3\, J_1(m)\sqrt{2/\pi}\,\kappa \sin(\varphi_{\mathrm{MI}} - \psi + \theta^{\mathrm{d}}). \tag{2.32}$$

At the proper operating point of the Mach-Zehnder, $\psi = 0$, we have

$$V_{\mathrm{MI}} = -4c_2c_3\, J_1(m)\, \sin\varphi_{\mathrm{MI}}, \tag{2.33}$$

$$W_{\mathrm{MI}} = -4c_2c_3\, J_1(m)\sqrt{2/\pi}\,\kappa \sin\left(\varphi_{\mathrm{MI}} + \theta^{\mathrm{d}}\right). \tag{2.34}$$

As before, an alignment error signal at the dark fringe operating point ($\varphi_{\mathrm{MI}} = 0$) is obtained only for an angular error, i.e. a tilt of the wavefronts at the detector (for $\theta^{\mathrm{d}} = 90°$).

2.3.3 Mach-Zehnder alignment

With external modulation, there is one more interferometer that needs to be aligned: the Mach-Zehnder interferometer. We now show how to obtain error signals that detect misalignments of the Mach-Zehnder.

We start with the same amplitudes as in Equations (2.28)–(2.30) above, but now assume the Michelson to be perfectly aligned and instead the local oscillator beam a_3 to be misaligned. For simplicity we now also assume $c_1 = c_2$. This leads to the light amplitudes

$$a_1 = c_1 u_0, \tag{2.35}$$

$$a_2 = -c_1 u_0 \exp(\mathrm{i}\,\varphi_{\mathrm{MI}}), \tag{2.36}$$

$$a_3 = c_3\, [J_0(m) + 2\,\mathrm{i}\, J_1(m) \cos(\omega_{\mathrm{m}} t)] \exp(\mathrm{i}\,\psi) \left[u_0 + \kappa \exp(\mathrm{i}\,\theta^{\mathrm{d}}) u_1\right]. \tag{2.37}$$

For the longitudinal signal, we obtain the same result as in Equation (2.31). The alignment signal is, however, different:

$$W_{\mathrm{MZ}} = -4c_1c_3\, J_1(m)\sqrt{2/\pi}\,\kappa \left[\sin(\varphi_{\mathrm{MI}} - \psi - \theta^{\mathrm{d}}) + \sin(\psi + \theta^{\mathrm{d}})\right]. \tag{2.38}$$

At the proper operating point ($\varphi_{\mathrm{MI}} = \psi = 0$) this signal vanishes. We need two more modulations in order to control the phase ψ (see Appendix A.7). Both φ_{MI} and ψ are modulated sinusoidally with small modulation index at some low frequency (375 Hz and 11 kHz in the prototype). By synchronous demodulation with the proper local oscillators, we can effectively obtain the derivatives

$$\frac{\partial W_{\mathrm{MZ}}}{\partial \varphi_{\mathrm{MI}}} = -4c_1c_3\, J_1(m)\sqrt{2/\pi}\,\kappa \cos(\varphi_{\mathrm{MI}} - \psi - \theta^{\mathrm{d}}), \tag{2.39}$$

$$\frac{\partial W_{\mathrm{MZ}}}{\partial \psi} = -8c_1c_3\, J_1(m)\sqrt{2/\pi}\,\kappa\, \sin\left(\frac{\varphi_{\mathrm{MI}}}{2}\right) \sin\left(\frac{\varphi_{\mathrm{MI}}}{2} - \psi - \theta^{\mathrm{d}}\right), \tag{2.40}$$

and by demodulating at both modulation frequencies in series we obtain

$$\frac{\partial^2 W_{\mathrm{MZ}}}{\partial\psi\partial\varphi_{\mathrm{MI}}} = -4c_1c_3\, J_1(m)\sqrt{\frac{2}{\pi}}\,\kappa\sin(\varphi_{\mathrm{MI}} - \psi - \theta^{\mathrm{d}}). \tag{2.41}$$

At the proper operating point, $\varphi_{\mathrm{MI}} = \psi = 0$, we have

$$\frac{\partial W_{\mathrm{MZ}}}{\partial\varphi_{\mathrm{MI}}} = -4c_1c_3\, J_1(m)\sqrt{\frac{2}{\pi}}\,\kappa\cos\theta^{\mathrm{d}}, \tag{2.42}$$

$$\frac{\partial W_{\mathrm{MZ}}}{\partial\psi} = 0, \tag{2.43}$$

$$\frac{\partial^2 W_{\mathrm{MZ}}}{\partial\psi\partial\varphi_{\mathrm{MI}}} = 4c_1c_3\, J_1(m)\sqrt{\frac{2}{\pi}}\,\kappa\sin\theta^{\mathrm{d}}. \tag{2.44}$$

In principle, either Equation (2.42) or Equation (2.44) could be used for detecting the Mach-Zehnder alignment error signals. In practice, however, Equation (2.44) might be preferable, because the associated 'common mode' term (Equation (2.21)) vanishes. Note that autoalignment of the Mach-Zehnder was not implemented in our prototype (see Section 2.4.3 below), so that the results of this Section (2.3.3) were not verified experimentally.

2.4 Misalignments caused by individual components

Next we have to consider what type of mode combination results from a misalignment of each individual component. For general cavities (such as the more complicated cavities of GEO 600), a general method and some results are presented in Section 2.10. For simpler cavities, such as those in our prototype, the results can also be derived directly. In each case we compute the effect of the misalignment, referenced back to the beam waist and expressed as θ^{w} (see Section 2.2).

2.4.1 PR cavity

We assume a plane front mirror M_{PR} (as in our prototype) and take as rear mirror misalignment the common mode of both end mirrors, which we now just call M_1. The waist of all beams in the PR cavity is at M_{PR}. Figure 2.2 illustrates the possible misalignments of the PR cavity.

A rotation of the end mirror M_1 by an angle α_{comm} causes a lateral displacement of the cavity eigenmode by the distance $\Delta x = \alpha_{\mathrm{comm}} R_1$, where R_1 is the radius of curvature of the end mirror. At the beam waist we thus have $\theta^{\mathrm{w}}_{\mathrm{comm}} = 0°$.

A rotation of M_{PR} by an angle α_{PR} causes a lateral displacement $\Delta x = \alpha_{\mathrm{PR}}(R_1 - L_{\mathrm{PR}})$ at the waist, and an angular misalignment α_{PR}. Thus the cavity eigenmode, with respect to this reference, can de described as

$$u_0(x,0) + \frac{\alpha_{\mathrm{PR}}(R_1 - L_{\mathrm{PR}})}{w_0}\, u_1(x,0) - \mathrm{i}\,\frac{\pi w_0}{\lambda}\,\alpha_{\mathrm{PR}}\, u_1(x,0), \tag{2.45}$$

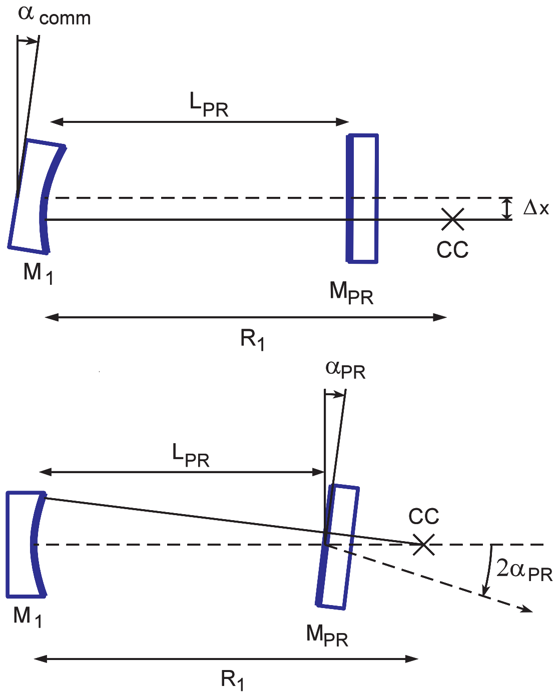

Figure 2.2: Two types of misalignments of the PR cavity. CC denotes the center of curvature of the end mirror(s), with radius of curvature R_1. The solid line that is orthogonal to M_1 and passes through CC is the axis of the cavity eigenmode. L_{PR} is the length of the PR cavity. In our prototype, $L_{\mathrm{PR}} \approx 31\,\mathrm{m}$ and $R_1 = 33\,\mathrm{m}$.

and the phaseshift between u_1 and u_0 at the waist is given by

$$\theta^{\mathrm{w}}_{\mathrm{PR}} = -\arctan\left(\frac{\pi w_0}{\lambda} \Big/ \frac{R_1 - L_{\mathrm{PR}}}{w_0}\right) = -\arctan\frac{z_{\mathrm{R}}}{R_1 - L_{\mathrm{PR}}}. \tag{2.46}$$

Note that the directly reflected incoming beam (our reference) experiences a rotation by $2\alpha_{\mathrm{PR}}$. This has the additional consequence that the whole interference pattern is tilted by an angle somewhere between α_{PR} and $2\,\alpha_{\mathrm{PR}}$. This makes it necessary to employ an additional mechanism to keep the pattern centered on the quadrant detector (see Section 2.6.2).

Since in general both M_{PR} and the end mirrors will be misaligned simultaneously, we will have a mixture of the two types of misalignments at the waist, described by $\theta^{\mathrm{w}}_{\mathrm{PR}}$ and $\theta^{\mathrm{w}}_{\mathrm{comm}}$. With two separate quadrant detectors, each detecting a fraction of the beam reflected from the PR cavity, it is possible to obtain independent signals for M_{PR} and the end mirrors' common mode, if an additional phase shift between u_0 and u_1 is introduced in one of the beams before detection.

For our prototype we have $R_1 = R_2 = 33\,\mathrm{m}$, $L_{\mathrm{PR}} = 31\,\mathrm{m}$[5], $z_{\mathrm{R}} = \sqrt{L_{\mathrm{PR}}(R_1 - L_{\mathrm{PR}})} =$

---

[5] The autoalignment system was built before the more precise measurements of Appendix A.14 were carried out, and $L_{\mathrm{PR}} = 31\,\mathrm{m}$ is assumed throughout the rest of this chapter. Using the more precise value of 30.807 m does not significantly change the results.

7.87 m and hence $\theta^{\mathrm{w}}_{\mathrm{PR}} = -75.7^\circ$. We placed the first quadrant detector (PD1 in Figure A.15) approximately $z = 1\,\mathrm{m}$ from the waist and thus obtained $\Phi = \eta(1\,\mathrm{m})$ and $\theta^{\mathrm{d}}_{\mathrm{PR}} = \theta^{\mathrm{w}}_{\mathrm{PR}} + \Phi = -68.5^\circ$, still giving $\sin(68.5^\circ) = 93\%$ of the maximum possible signal for $\mathrm{M_{PR}}$.

The signal for the end mirrors is obtained by the use of an adjustable lens system (L1 and L2 in Figure A.15) in front of the second detector PD2, initially designed for $\Phi = 90^\circ$ phase shift, but adjusted such that $\theta^{\mathrm{d}}_{\mathrm{PR}} = \theta^{\mathrm{w}}_{\mathrm{PR}} + \Phi = 0^\circ$ at PD2, corresponding to $\theta^{\mathrm{d}}_{\mathrm{comm}} = 75.7^\circ$ and 97% of the maximum possible signal. The lens system was adjusted experimentally by dithering the orientation of $\mathrm{M_{PR}}$ and adjusting for vanishing signal at the dithering frequency in PD2's output signal. It was not necessary to further separate the error signals. The design of the lens system is briefly described in Section 2.5 .

2.4.2 Michelson interferometer

Again we describe the misalignments of the Michelson at the beam waist, which is at a distance L_{PR} from the end mirrors. With *external modulation* the local oscillator beam was taken from the first arm as reflection from the back of the beamsplitter, which has a finite reflectivity of 290 ppm. Thus the beam returning from the first arm acted as angular reference. According to Figure 2.3, we have at the waist an angle $\alpha_{\mathrm{MI}} = 2\,\alpha_{\mathrm{diff}} = 2(\alpha_1 + \alpha_2)$ and a lateral displacement $\Delta x = -\alpha_{\mathrm{MI}} L_{\mathrm{PR}}$. Similar to the derivation of Equation (2.46), we find for the phase between u_1 and u_0

$$\theta^{\mathrm{w}}_{\mathrm{MI}} = \arctan\left(-\frac{z_{\mathrm{R}}}{L_{\mathrm{PR}}}\right), \tag{2.47}$$

which amounts to -14.25° in our prototype. Since the best signal is again obtained with $\theta^{\mathrm{d}}_{\mathrm{MI}} = 90^\circ$ at the detector (see Equation (2.32)), we need another lens system (L3 and L4 in Figure A.15) to introduce approximately 104.25° of extra phase shift between u_1 and u_0.

With *Schnupp modulation*, the 'local oscillator' consists of the phase modulation sidebands that leak out at the dark fringe port because of the armlength difference. Their geometry is determined by the eigenmode of the PR cavity, which we assume to be well aligned by its own autoalignment system. The ratio of lateral displacement to angular misalignment and hence $\theta^{\mathrm{w}}_{\mathrm{MI}}$ remain the same.

2.4.3 Mach-Zehnder alignment

We assume that both beamsplitter and RP are made such that their two surfaces are parallel to each other and that their material and shape are identical. For horizontal tilts, it is easy to see (using elementary geometry) that only a horizontal displacement of the beams results. For vertical tilts, the geometry is not so simple, but was computed using the ray-tracing program described in Appendix E.3. The results show that a vertical tilt of RP causes a combination of horizontal and vertical displacements, but no angle between the beams' axes (see Figure 2.4).

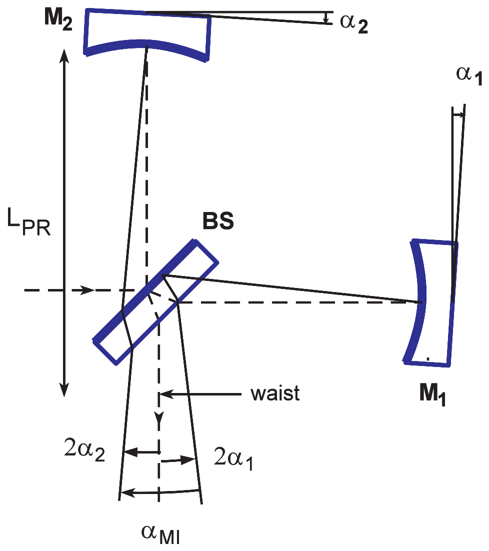

Figure 2.3: A misalignment of the Michelson interferometer is described by the differential mode of the end mirrors. The angle between the beams is $\alpha_{\mathrm{MI}} = 2\,\alpha_{\mathrm{diff}}$.

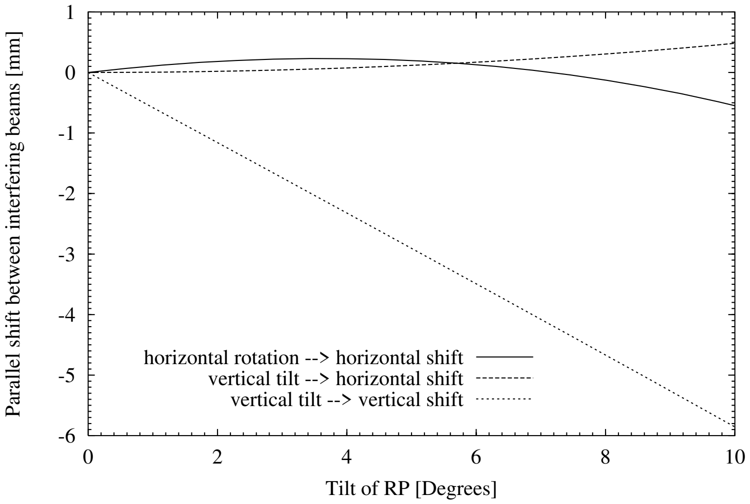

Figure 2.4: Parallel shifts between the two interfering beams in the Mach-Zehnder interferometer caused by a tilt of the recombination plate RP against the beamsplitter BS. The calculations were done assuming a beamsplitter and recombination plate of 3 cm thickness.

It follows from equations (2.42) and (2.44) that we could obtain error signals for the Mach-Zehnder alignment by using the quadrant detector on the detection bench which is anyway there for the Michelson alignment (PD3 in our prototype). Since the beam waist is near RP, the lateral displacement between the two interfering beams corresponds to $\theta^{\mathrm{w}}_{\mathrm{MZ}} = 0°$, which is not very different from the $\theta^{\mathrm{w}}_{\mathrm{MI}} = -14.25°$ valid for misalignments of the Michelson. Hence we may use the detector PD3 with the existing lens system (which adds $\Phi = 104.25°$ of extra phase shift), and demodulate the output signals twice according to equation (2.44) in order to obtain error signals.

In our prototype we did not install any automatic alignment system for RP. If we were rotating RP we would simultaneously change the phase shift between the two interfering beams. This phase shift needs to be well controlled to keep the interferometer in lock. The dynamic range of the only other control element for this phase shift, Pockels cell PC3, was too small to permit feedback of alignment correction signals to RP without throwing the interferometer out of lock.

2.5 Computation of lens systems

We now describe a lens system for the purposes mentioned above, which ideally fulfills the following requirements: arbitrary design value of phase shift Φ (usually around 90°), preferably adjustable around the design value, compactness and reasonable spot size on the quadrant detector.

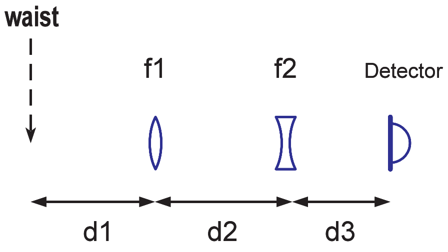

Figure 2.5: Scheme of the lens system used to introduce additional Guoy phase shift between u_1 and u_0.

One method to compute such lens systems uses the matrix formalism, as described e.g. in [Yariv, Siegman]. The beam at any point is described by the complex parameter q given by

$$q = \mathrm{i}\, z_\mathrm{R} + z \tag{2.48}$$

where z_R is the Rayleigh range, which is constant for any beam segment, and z is the distance from the waist. We denote by ‘ beam segment’ any portion of the beam propagating between lenses or other components.

The radius of curvature $R(z)$ and beam radius $w(z)$ at any position z can be found from the relation

$$\frac{1}{q(z)} = \frac{1}{R(z)} - \mathrm{i}\,\frac{\lambda}{\pi w^2(z)}, \tag{2.49}$$

and the Guoy shift from

$$\tan\eta(z) = \frac{z}{z_\mathrm{R}}. \tag{2.50}$$

The action of a thin lens with focal length f on the beam is given by

$$q_{i+1} = \frac{Aq_i + B}{Cq_i + D} \tag{2.51}$$

with the matrix

$$\begin{pmatrix} A & B \\ C & D \end{pmatrix} = \begin{pmatrix} 1 & 0 \\ -\frac{1}{f} & 1 \end{pmatrix} \tag{2.52}$$

The propagation of the beam for a distance d can either be described by another matrix

$$\begin{pmatrix} A & B \\ C & D \end{pmatrix} = \begin{pmatrix} 1 & d \\ 0 & 1 \end{pmatrix} \tag{2.53}$$

or more simply by $q_{i+1} = q_i + d$. If the matrix is used, several or all matrices describing a complex optical system could be multiplied together to form a single matrix. This approach is, however, not useful here, because the phase shift cannot be determined from this combined matrix. We are not interested in an absolute value of the Guoy shift, but only in the difference between the u_0 and u_1 modes. When the beam passes a thin lens, the phase shift must be continuous for physical reasons (imagine a very weak thin lens). Equations (2.51) and (2.52) predict, however, a jump in the phase shift, because in the new beam segment behind the lens, the phase shift is again counted as zero at the new waist. What we need, however, is the accumulated phase shift Φ through the whole system. It can be computed as follows:

- Start with $q = \mathrm{i}\, z_\mathrm{R}$ and $\Phi = 0$ at the waist of the beam of interest.
- For any beam segment with Rayleigh range z_R, which is traversed from $z = z_i$ to $z = z_{i+1}$, $(z_i < z_{i+1})$, add to Φ the phase shift $\arctan(z_{i+1}/z_\mathrm{R}) - \arctan(z_i/z_\mathrm{R})$.
- For any other optical element, transform the beam according to equations (2.51) and (2.52). Any thin optical element does not contribute to Φ.

With a Mathematica program we computed the phase shift and beam size in various lens systems and found reasonable solutions for the two cases of interest in our experiment, which require a phase shift of 90° and 104°, respectively. Each lens system consists of one converging lens (focal length f_1) and one diverging lens (f_2), separated by a distance $d_2 \approx f_1 + f_2$ (see Figure 2.5 and Table 2.1). The beam radius at the detector was designed to be approximately 2 mm. The lens systems can be adjusted via the distance d_2 between the two lenses. It turns out that very close to the desired position (which yields the design phase shift) the beam radius at the detector has a minimum, which simplifies the initial setup. By moving the second lens 1 cm in either direction, the phase shift Φ can be varied by more than ±30°, thus allowing final adjustment of the phase shift.

Almost the same effect could be obtained by using a converging second lens with the same absolute focal length, with two minor disadvantages: The overall length of the

	d_1 [cm]	$2w_1$ [mm]	f_1 [cm]	d_2 [cm]	$2w_2$ [mm]	f_2 [cm]	d_3 [cm]	$2w_\mathrm{D}$ [mm]	Φ_total [°]
PR Cavity	120	2.30	35	32.17	0.220	-3	50	1.78	90
Michelson	50	2.27	25	23.27	0.175	-2	55	2.10	104

Table 2.1: Parameters of the two lens systems used in our prototype (see also Figure 2.5). The beam diameters $2w$ are given at the first and second lens, and at the detector.

system would increase by $|2f_2|$ (since still $d_2 \approx f_1 + f_2$), and there would be a small real focus in front of the second lens. With the systems described above, the smallest beam diameter occurs at the second lens and is approximately twice as big as the real focus would be.

2.6 Experimental setup

The 30 m prototype is described in other parts of this work, in particular in Appendix A and in Appendix A.7, which describes the external modulation setup that was used during the development of the autoalignment system. An overview of the control loops is shown in Figure A.15. This section only describes the additional devices that are used for the autoalignment system.

2.6.1 Quadrant photodetectors

All three quadrant photodetectors PD1, PD2 and PD3 are built similarly. The preamplifier circuit used for each of the four quadrants is described in Appendix B.1 and shown in Figure B.6. Each preamplifier has one DC output signal and one RF output signal.

The DC and RF output signals are then separately processed with analog electronics to produce a total of six output signals from each quadrant detector. The RF signals V and W are the ones defined in Equations (2.21) and (2.22), and the DC signals $\overline{V}$ and $\overline{W}$ are their DC counterparts. X and Y represent the two orthogonal directions on the surface of the quadrant photodiode.

V : This signal is used for the longitudinal loops (PR cavity Pound-Drever loop and Michelson dark-fringe loop, respectively).

W_X, W_Y : These are the most important output signals for the autoalignment system, describing the tilt of the wavefronts of the interfering beams against each other.

$\overline{V}$: This signal (total DC photo current) is used for monitoring and normalization purposes.

$\overline{W}_X, \overline{W}_Y$: These two signals (differences of the DC photo currents) are fed to the beam-steering mechanism described in Section 2.6.2 below and are kept near zero by that beam-steerer.

Figure 2.6 shows the RF signal paths in the quadrant detector in more detail. The sum of all RF components, V, is produced by an adder and made available as output. The signals W_X and W_Y are demodulated in the quadrant detector. As demodulators we use two high-speed analog multipliers (Burr-Brown MPY600) which have differential high-impedance inputs (in the new designs being prepared for GEO 600 we prefer double-balanced diode mixers, which have a better dynamic range). The RF components from two diagonally opposite quadrants are demodulated in one mixer. After low-pass filtering (70 kHz), the sum and difference of these two signals represent the desired W_X and W_Y outputs.

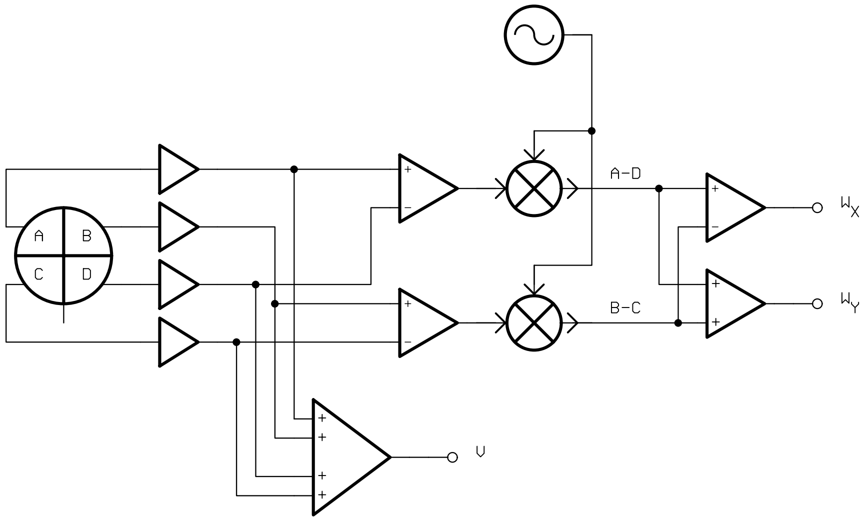

Figure 2.6: RF signal paths in the quadrant detector. The mixers are analog multipliers with differential inputs. The signal 'V' is demodulated in a separate mixer (Mix1 and Mix2 in figure A.15) and used as error signal for the Pound-Drever loop and Michelson dark fringe lock, respectively. The W_X and W_Y outputs are the error signals for the auto-alignment loops.

The DC signal paths are shown in Figure 2.7. The sum of all DC photocurrents, $\overline{V}$, is again obtained with an adder. The differences in DC photocurrents, $\overline{W}_X$ and $\overline{W}_Y$, are obtained from all 4 quadrants simultaneously with precision resistors and instrumentation amplifiers, because here we do have a large common-mode signal and thus want reasonable common-mode rejection.

2.6.2 Auxiliary beam-steering loops

As mentioned in Section 2.3, the quadrant detectors can produce reliable alignment error signals only when the interference pattern is centered on the photodiode. Since in the course of the alignment (either manual or automatic) the position and angle of

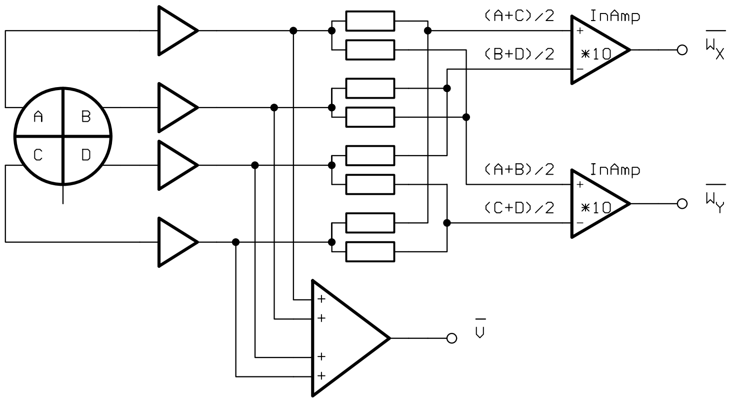

Figure 2.7: Low frequency signal paths in the quadrant detector. ‘InAmp’ are instrumentation amplifiers. The ‘$\overline{V}$’ output is used for monitoring, while the $\overline{W}_X$ and $\overline{W}_Y$ outputs are used as error signals for the auxiliary beam steering devices.

the beams leaving the vacuum chamber are changed (e.g. by rotating M_{PR}), we need an extra loop that centers the beam on the quadrant diode for each of the detectors PD1, PD2 and PD3. These loops make use of the DC output signals $\overline{W}_X$ and $\overline{W}_Y$ from the corresponding quadrant detector. To deflect the beam we use commercial magnet-mirror units modified for our purpose. The unity gain frequency of these loops is around 30–50 Hz, sufficient for our purposes.

A modification was necessary in the loop for PD3, because here the DC light level hitting the photodetector may vary widely during lock acquisition. Thus the $\overline{W}_X$ and $\overline{W}_Y$ signals from PD3 are divided by the DC sum signal $\overline{V}$ from the same detector before they are used as error signals. For GEO 600 two commercial galvanometer scanners mounted orthogonally will be used for each detector. In a prototype a unity gain frequency of 2 kHz was obtained with these units[6]. It is important for these beam-steering loops to have a bandwidth considerably higher than the main autoalignment loop of which they are a part.

2.7 Automatic alignment loops

2.7.1 Actuators

Each suspended component in our prototype has an associated local control module (see Appendix A.3.1). As described there, these modules have extra inputs which allow to apply the alignment control signals.

The transfer functions from the respective control inputs (translation, rotation, tilt) to an actual component movement have a similar simple shape, which can be approximated

---

[6] This prototype was developed by H. Grote during a stay in Garching.

by two-pole low-pass models

$$H_{\rm P}(s = {\rm i}\,\omega) = \frac{A_{\rm P}}{1 + \frac{s}{\omega_{\rm P} Q_{\rm P}} + \frac{s^2}{\omega_{\rm P}^2}}. \tag{2.54}$$

Their pole frequencies $f_{\rm P} = \omega_{\rm P}/(2\pi)$ are between 0.5 and 2 Hz, and the $Q_{\rm P}$ of these resonances is quite low, i.e. between 0.7 and 4, due to the active damping by the local control modules.

Figure 2.8 shows an example of such a transfer function, in this case for the common-mode 'tilt' motion of the end mirrors. We have fitted the model (2.54) to the measured transfer functions in order to obtain the parameters $A_{\rm P}$, $\omega_{\rm P}$ and $Q_{\rm P}$, which can then be used in the computation of loop filters.

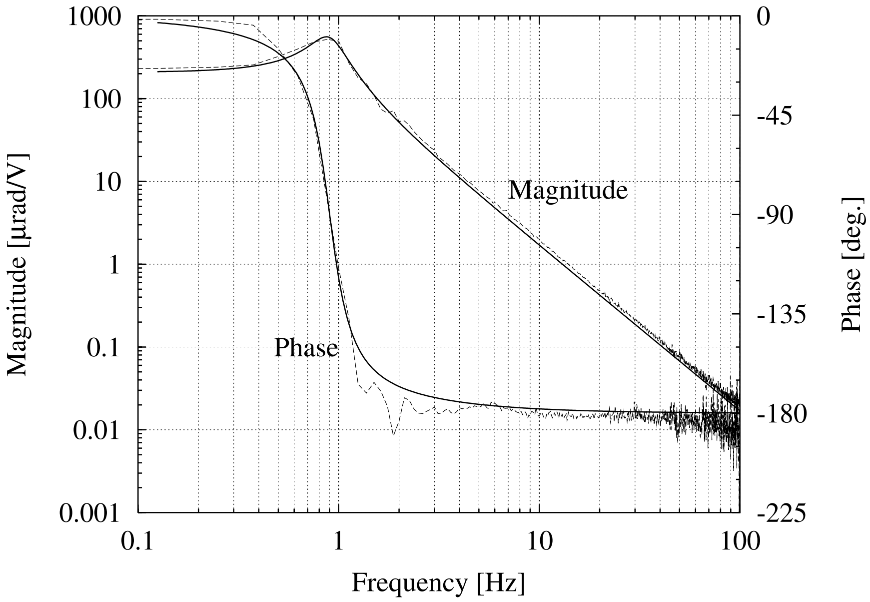

Figure 2.8: Transfer function from the common mode 'tilt' input for the end mirrors to the actual tilting motion (measured with PD2). The measured data was fitted to a two-pole low-pass model with $f_{\rm P} = 0.90$ Hz and $Q_{\rm P} = 2.63$.

For each channel, Table 2.2 shows these parameters, together with the overall factors $A_{\rm P}$ and the sensor gains $A_{\rm S}$, which were found with the calibration procedure described in Appendix A.5.3.

2.7.2 Loop filters

We have tried several variants of loop filters. The purpose of all of them is to allow the unity gain frequency to be around or above the pendulum resonance and to provide extra gain at low frequencies (below the resonance). Because the overall loop gain may

Mode	A_{P} [μrad/V]	f_{P} [Hz]	Q_{P}	A_{S} [V/rad]
EM diff. X	28.7	0.9	3.26	$3.0 \cdot 10^6$
EM diff. Y	20.8	0.9	3.0	$2.6 \cdot 10^6$
EM comm. X	287	0.89	2.99	$58 \cdot 10^3$
EM comm. Y	208	0.9	2.63	$47 \cdot 10^3$
PR X	2500	1.84	2.6	$23 \cdot 10^3$
PR Y	3500	1.67	1.99	$25 \cdot 10^3$

Table 2.2: Calibration parameters of the auto-alignment loops. 'EM diff.' is the differential mode of the end mirrors (Michelson alignment), 'EM comm.' their common mode (PR cavity alignment), and PR refers to the power recycling mirror. A_{P}, f_{P} and Q_{P} describe the pendulum response (Equation (2.54)). The sensor gain A_{S} includes everything from a mirror motion to a signal at the photodetector's output.

change according to many parameters, we have tried to normalize the error signals as far as possible by analog division (see Section 2.7.3) and also to use unconditionally stable loops wherever possible.

The favorite design consists of a '$f^{1/2}$ filter' active at frequencies above the pendulum resonance (see Appendix B.4). The result is an open-loop gain curve that rolls off approximately with $f^{-3/2}$ above the pendulum resonance and has a phase margin of around 45° (assuming there are no extra phase delays). At frequencies below the pendulum resonance, there is an integrator active to increase the gain at low frequencies and DC. Figure 2.9 shows the open loop gain of the Michelson alignment loop (x-channel), which was built according to this scheme.

An alternative design employs a biquadratic active filter to compensate the pendulum resonance. A new pole is introduced at a frequency above the loop's unity gain frequency, e.g. at 20 Hz. It is thus possible to obtain an open-loop gain that continuously rolls off as f^{-1} (or $f^{-3/2}$ if desired) even around the pendulum resonance frequency, at the cost of increased circuit complexity. Figure 2.10 shows the open loop gain of the end mirror common mode alignment loop (y-channel), which was built according to this scheme.

During the development of our system, we have built both kinds of filter, and both are still used in the prototype. For new systems we would prefer the first kind, because it is easier to build (no exact knowledge of the pendulum resonance is necessary) and because the biquadratic filter of the alternative design intrinsically has very small dynamic range (its step response has an enormous overshoot).

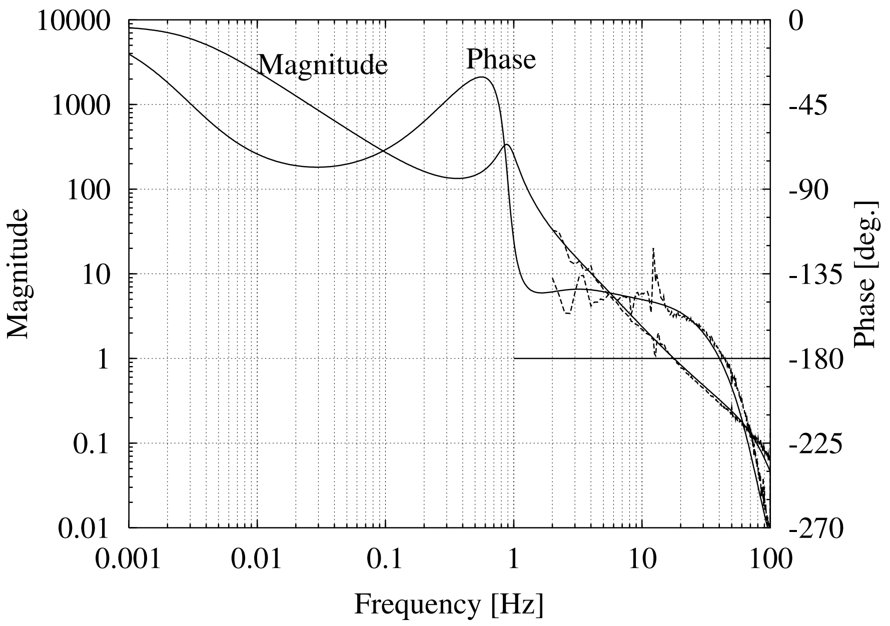

Figure 2.9: Open-loop gain of the Michelson alignment loop. Here the pendulum has $f_{\mathrm{P}} = 0.9\,\mathrm{Hz}$ and $Q_{\mathrm{P}} = 3.26$, and the loop includes a $f^{1/2}$-filter active between 1.5 Hz and 45 Hz, an integrator between 3 mHz and 0.3 Hz and a second order low-pass filter ($f = 85\,\mathrm{Hz}$, $Q = 1$). Measured data are shown between 2 Hz and 100 Hz, together with the computed extrapolation to lower frequencies.

2.7.3 Auxiliary signals for normalization

The two single-element photodetectors PD4 and PD5 in Figure A.15 are used to normalize the autoalignment error signals. PD4 detects a stray beam from the beam injector, which is a sample of the injected light hitting M_{PR}. PD5 detects a sample of the light power circulating in the PR cavity, which depends on the alignment of the interferometer, the condition of beamsplitters and mirrors, and in particular on the locking state of the longitudinal loops. Both PD4 and PD5 employ the broadband preamplifier circuit described in Appendix B.1.1.

The error signals for the Michelson interferometer (from PD3) are proportional to the product of the amplitudes of the beam returning from one arm and of the reference beam. Both of these amplitudes are proportional to the amplitude of the light circulating in the PR cavity, and hence the error signal is proportional to the power of that light. Therefore, the error signals are divided by the output from photodetector PD5 with an analog divider (AD734) before being fed to the loop filters.

The error signals for the PR cavity are, however, proportional to the product of the amplitudes of the beam injected into the interferometer and of the beam circulating in the PR cavity. The power of those two beams is measured with photodetectors PD4 and PD5, respectively. Therefore we compute the square root of the product of these powers with an analog circuit (AD734) and use it as denominator to normalize all four

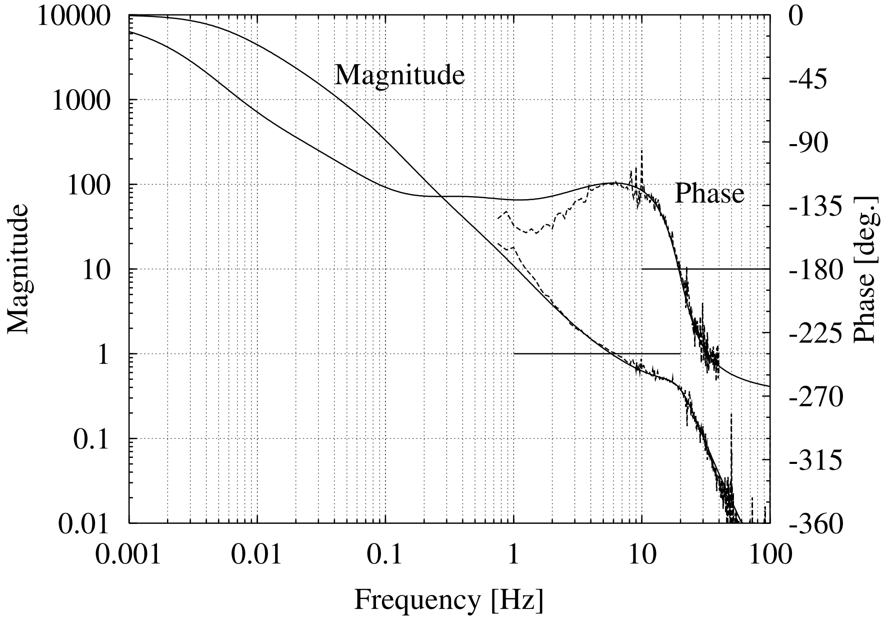

Figure 2.10: Open-loop gain curve of the end mirror common mode alignment loop (y-channel). The pendulum resonance is electronically compensated by a biquadratic filter that introduces the new pole at 20 Hz with $Q_{\mathrm{pole}} = 1.5$, an integrator starts at 5 mHz, and there is a $f^{-1/2}$ filter active between 80 mHz and 2.5 Hz. Measured data are shown between 0.75 Hz and 100 Hz, together with the computed extrapolation to lower frequencies.

PR cavity error signals from PD1 and PD2.

2.7.4 Alignment loops for Michelson and PR cavity

The system used for aligning the Michelson interferometer is the most important automatic alignment loop in our setup, because any noticeable Michelson misalignment immediately reduces the stability of the longitudinal loops. As described in the previous sections, the two error signals are obtained from the quadrant detector PD3. The loop filters were built according to the first design of Section 2.7.2, with an $f^{1/2}$ filter active from 1.5 Hz to 45 Hz, an integrator between 3 mHz and 300 mHz and an additional two-pole low-pass filter at 85 Hz in each channel. The unity gain frequency is around 10 Hz in normal operation and can be increased up to around 20 Hz if desired.

Error signals that describe the misalignment of the PR cavity are obtained from the quadrant detectors PD1 (for the PR mirror) and PD2 (for the end mirrors' common mode alignment). The loop filters for the PR mirror were built according to the second design of Section 2.7.2 above with the new pole introduced at 20 Hz ($Q_{\mathrm{pole}} = 1.5$), an $f^{-1/2}$ filter active between 80 mHz and 2.5 Hz, and an integrator starting at 5 mHz in each channel. The unity gain frequency is near 5 Hz in normal operation and can be increased up to about 10 Hz.

The Michelson loop and the PR cavity loop both act on the end mirrors, and the separation of 'common mode' and 'differential' signals is not perfect. Therefore there is some interaction between these loops. In particular we found that the Michelson loop should have a higher unity gain frequency than the two channels of the PR cavity loop that act on the end mirrors, and also that the Michelson loop should be switched on first. Otherwise, if one tries to automatically align the PR cavity with no or too little gain of the Michelson loop, a common mode signal fed back to the end mirrors invariably involves some differential mode component, which reduces the Michelson contrast or may even throw one of the longitudinal loops (and hence the whole interferometer) out of lock.

2.7.5 Spot positions on end mirrors

The loops that control the positions of the spots on the end mirrors are much less critical than those described above. The error signals for the beam spot positions are obtained from position sensitive detector (PSD) diodes (type SD-386-22-21-251 from Silicon Detector Corporation) with an active area of $100\,\mathrm{mm}^2$. The beam diameter at the end mirrors is $2w = 9\,\mathrm{mm}$, such that a part of the beam is cut off, but a useful error signal is nevertheless obtained. For the planned large-scale detectors, an array of separate diodes could be used. For this application, a PSD is more suitable than a quadrant diode, because the PSD measures the 'center of gravity' of the light, which is appropriate here, because the beam transmitted through the highly reflective mirror coating may have an irregular shape. The PSD diodes are operated with $-15\,\mathrm{V}$ of reverse bias and the photocurrent from each electrode is converted into a voltage by a transimpedance amplifier (see Appendix B.1.1). The sum of all photocurrents and the differences Δx and Δy are obtained with a circuit similar to the one shown in figure 2.7. The differences Δx and Δy are divided by the sum of all photocurrents and then used as error signals.

Although the beam injector's transfer function in itself is of the shape described in section 2.7.1, we find that the actual transfer function from a movement of the beam injector to a motion of the spot on the far mirror M_1 involves the reaction of the other loops described above. If these other loops were off, no motion of the spot position would occur at all, because that position is solely determined by the PR cavity eigenmode (and hence the alignment of M_{PR}, M_1 and M_2). Thus we have additional phase delays in the loop, which are caused by the reaction time of the other alignment loops.

Therefore the loop that controls the spot position on M_1 via the beam injector must be slower than the main alignment loops. In the prototype we have used an open loop gain of with a simple $1/f$ roll-off and a unity gain frequency of around $0.3\,\mathrm{Hz}$.

Although for the second of these loops (the one controlling the beamsplitter in order to fix the beam spot position on M_2) there are no other loops involved, and the actuator transfer function is that of the beamsplitter alone, we have nevertheless used the same open loop gain curve as for the beam injector.

The PSD diodes can be positioned behind the end mirrors with motorized mounts.

When everything is in lock, the spot positions on either of the end mirrors can thus be controlled by moving the PSD with the motors, while all other spot positions remain fixed and the Michelson and PR cavity are kept well aligned. The beam position on the end mirror can thus be fixed to any desired spot, such as the center of the mirror (to minimize torsional coupling) or to the spot that yields the best Michelson contrast.

In practice, this procedure works well for the beam injector and M_1, but only in a limited range for the beamsplitter and M_2, because by moving the beamsplitter we also move the beam that leaves the interferometer towards RP and PD3. Both the loop that controls the Mach-Zehnder phase ψ and the beam steerer that keeps the beam centered on PD3 must follow this movement, and the dynamic range of these loops limits the amount that the beamsplitter can be moved without everything falling out of lock.

2.7.6 Lock acquisition and error checking

The normalization of all error signals described in Section 2.7.3 involves analog division by a voltage that is proportional to some light level inside the interferometer. If any part of the system falls out of lock, most of these light levels quickly drop to very low levels. The normalized signal then gets very inaccurate or even saturated. To prevent feeding back such 'wrong' error signals to the suspended components, the denominators used for normalization are continually monitored by analog comparators. Once a denominator drops below a preset threshold, an analog sample-and-hold circuit is activated that holds the correction signal (output of the loop filter) at its last value. For initial manual alignment, there is another mode of operation which forces all correction signals to zero.

In practice these error checking systems worked sufficiently well if the error that led to the drop in light power was not caused by the autoalignment system itself. If, however, something is wrong with one of the autoalignment loops, then usually one or several components start to move away from their aligned positions, until the interferometer falls out of lock. The sample-and-hold systems then hold the components in positions that are already removed quite far from the optimum alignment, and lock acquisition has to be restarted from the initial positions of all components.

Thus we monitor the correction signals during operation, and manually adjust offsets from time to time such that the correction signals applied by the autoalignment loops are near zero. Then, in case of a lock reacquisition, the 'zero' position for all component orientations is already very close to the optimum position. In the planned large detectors, this task would be performed by a computerized control system, which is also responsible for monitoring the locking status, lock acquisition, etc. With such a system available, we would no longer use the sample-and-hold circuits but instead switch the correction signal to zero in case of insufficient light levels.

One important conclusion that we draw from our experiments is that this autoalignment system can only start to work after all longitudinal loops of the interferometer are already locked. Thus the interferometer must be started up with manual alignment, until the PR cavity and Michelson dark fringe are both locked. In particular care must be taken that the PR cavity locks in its fundamental TEM_{00} mode. Only then can the autoalignment system be activated.

2.8 Noise spectra

We have measured the noise spectra of all loops at their error points both with the loops switched on and off. They were divided by the sensor transfer function $H_S(s)$ to give the mirror motion in radians. The calibration procedure is described in Appendix A.5.3. For verification we have also measured the spectra of the correction signals applied to the mirrors when the loop was working. These were multiplied with the pendulum transfer function $H_P(s)$, such that they also express the mirror motion. A typical set of such measurements is shown in Figure 2.11.

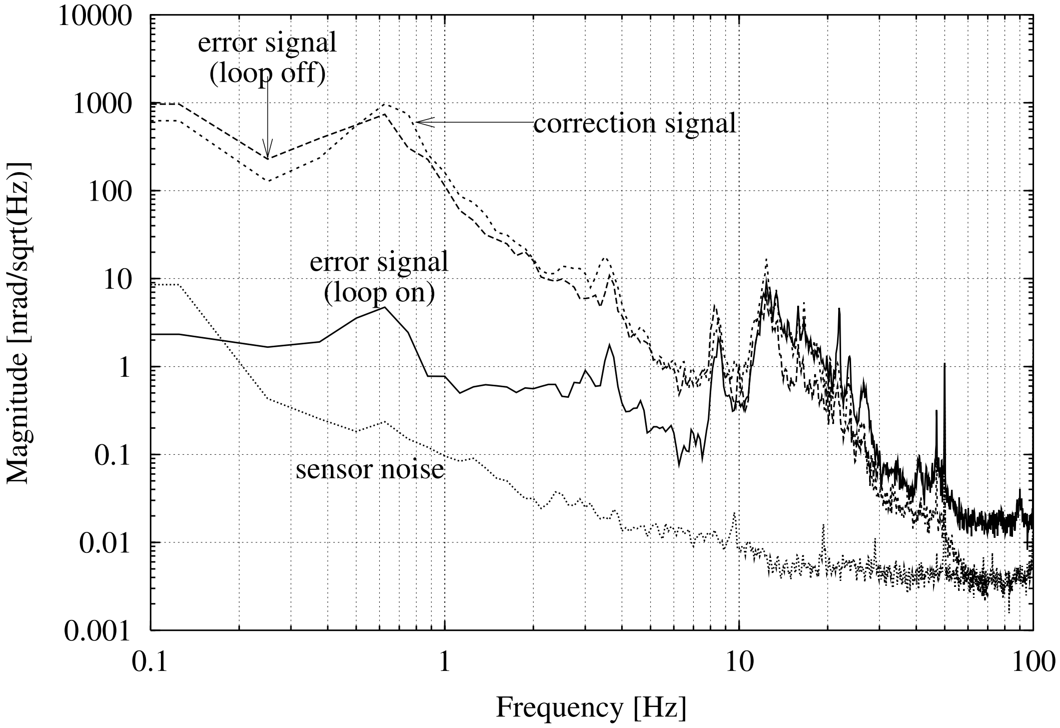

Figure 2.11: Noise spectrum of the x-channel of the Michelson alignment loop, calibrated in rad/$\sqrt{\text{Hz}}$ of differential end mirror motion.

The upper two curves show the error signal with the loop switched off and the correction signal with the loop in operation. The solid curve shows the error signal with the loop on. The lowest curve shows the sensor noise, measured with the same average photocurrent as that appearing during operation, produced by white light from an incandescent lamp. We have numerically integrated the noise spectra between 0.1 Hz and 100 Hz to obtain RMS values for the angular misalignments (see Table 2.3).

Mode	Loop off	Loop on [nrad$_{\text{RMS}}$]	Corr. signal
EM diff. X	461	11	522
EM diff. Y	1100	26	790
EM comm. X	1390	26	1540
EM comm. Y	234	34	1010
PR X	1300	270	1000
PR Y	2700	176	2730

Table 2.3: Integrated RMS alignment noise from 0.1 Hz to 100 Hz. 'EM diff.' is the differential mode of the end mirrors (Michelson alignment), 'EM comm.' their common mode (PR cavity alignment), and PR refers to the power recycling mirror.

Since some of the curves were measured on different days, and the environmental motion of our lab depends on outer conditions, there is considerable variability in the data, especially in the measurements with the loop off and those of the correction signal (which both represent the amount of alignment noise without the loop). These RMS values are usually dominated by a DC term, which also depends on how well the interferometer was manually aligned. The real usefulness of the autoalignment system is only incompletely described by these numbers, since the natural fluctuations increase even more towards frequencies below 0.1 Hz. These slow drifts are well compensated by the loops, but not easily measured.

The remaining fluctuations with the loop in operation are somewhat more reproducible. For the Michelson alignment, we find an RMS deviation of 11 and 26 nrad for the X and Y channels, respectively. That corresponds at the waist (near the beamsplitter) to an RMS lateral displacement between the axes of the two beams of 0.33 μm and 0.78 μm, respectively, or equivalently to a fraction of $2.8 \cdot 10^{-4}$ and $6.7 \cdot 10^{-4}$ of the beam radius w_0.

For the four other channels (those for the PR cavity) the results look qualitatively similar. In these channels, however, the sensor noise was higher by a factor of around 100. It was later found that during these measurements a spurious Fabry-Perot had been formed between the ends of the fiber that brings the light into the tank. The resulting excess noise on the light entering the interferometer had dominated the error signals.

Another important question to be addressed is that of extra noise being fed into the interferometer by the autoalignment loops. This is indeed a nontrivial problem since the loops need to act on the end mirrors. In our prototype, we used simple $1/f^2$ filtering with corner frequencies of 20 Hz or 85 Hz, as described in Section 2.7.4. Additionally there is the $1/f^2$ filtering action of the pendulum itself (see Section 2.7.1). For the large-scale interferometers, more elaborate filtering may be necessary in order to prevent feeding noise to the mirrors at measurement frequencies. This will depend on the necessary loop bandwidths of the alignments loops, which in turn depend on how much alignment noise there is to be controlled. In our prototype, the coil-magnet actuators directly acted on the test masses, whereas in GEO 600 they will act on an intermediate mass of a double or triple pendulum, which provides additional isolation, but also a more complicated transfer function.

2.9 Dark fringe contrast

Figure 2.12 shows how the light power at a dark fringe fluctuates without the auto-alignment system, and how the fluctuations are reduced after the alignment system was switched on. These environmental fluctuations shown are typical for a short time after

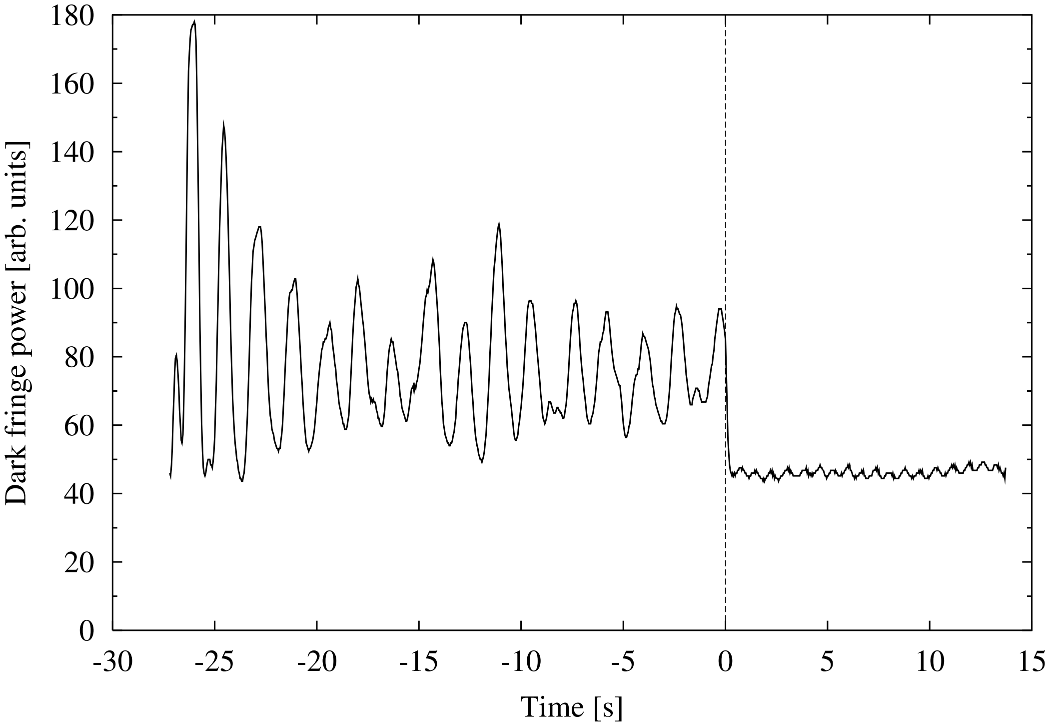

Figure 2.12: Power leaving the dark fringe port of the interferometer (measured with PD3) without and with auto-alignment (switched on at $t = 0$). The final level of 50 units corresponds to about 0.1 … 0.2 % of the power at the beamsplitter.

the interferometer was manually well aligned. Actually it is very difficult to align the interferometer manually, in particular the end mirrors' common mode. In practice the fine alignment of the interferometer was done using the auto-alignment system, which was then switched off to demonstrate the natural fluctuations. On longer timescales (several minutes or longer) the contrast without auto-alignment usually deteriorates even more than shown in Figure 2.12 due to slow alignment drifts.

2.10 Alignment error signals for GEO 600

This section presents the results of some computations that have been carried out by the author for the autoalignment system for GEO 600 which is being developed in Hannover at the time of this writing. The methods presented in Sections 2.1 to 2.9 are used and extended.

2.10.1 Ray-tracing program

The effects of mirror misorientations[7] in interferometers with three or more mirrors cannot easily be determined analytically in the general case. Therefore a Mathematica program for numerical 3-D ray tracing was written. It uses geometrical optics to find the axis of the eigenmode for a given combination of reflecting and/or refracting plane and spherical surfaces. The program is described and printed in Appendix E.3. The term 'beam' in this section refers to the geometrical axis of a beam, without taking into account the transverse shape or optical phase.

2.10.2 The GEO 600 power recycling cavity

Figure 2.13 shows a schematic diagram of the GEO 600 power recycling cavity (seen from the side) together with the coordinate system adopted in this section (2.10.2). In the GEO PR cavity the waist of the eigenmode is at M_{PR} and its Rayleigh-range is given by

$$z_{\mathrm{R}} = \sqrt{\frac{2L(R_{\mathrm{F}}-L)(2L^2+R_{\mathrm{F}}R_{\mathrm{N}}-2L(R_{\mathrm{F}}+R_{\mathrm{N}}))}{(2L-R_{\mathrm{F}})(2L-R_{\mathrm{F}}-2R_{\mathrm{N}})}} = 227\,\mathrm{m}, \tag{2.55}$$

where $L = 600\,\mathrm{m}$ is the armlength, and $R_{\mathrm{N}} = 600\,\mathrm{m}$ and $R_{\mathrm{F}} = 640\,\mathrm{m}$ are the radii of curvature of the near and far mirrors, respectively.

The following results do not depend critically on whether the near mirror M_{N} is above or below M_{PR}, nor on their vertical distance (25 cm). In this section, angles are counted positive if they describe a *clockwise* tilt from the reference direction.

As in Section 2.4 we determine the effect on the axis of the PR cavity eigenmode that is caused by a misorientation of each mirror. Some assumptions are: All longitudinal loops are locked, the PR cavity is resonant in its fundamental mode, mode matching is perfect and all misalignments are small.

A summary of the results of the ray-tracing program is given in Table 2.4 which was computed for misorientations in the y-direction (i.e. beam spots moving vertically),

---

[7] To avoid confusion, we call a mirror or other component **misoriented** in this section (2.10), if its angular orientation differs from its reference orientation. The resulting movement of beams (e.g. cavity eigenmodes) will be called **misalignment**. An interferometer is called **well-aligned** if there are neither misorientations nor misalignments, i.e. components as well as beams are in their reference positions.

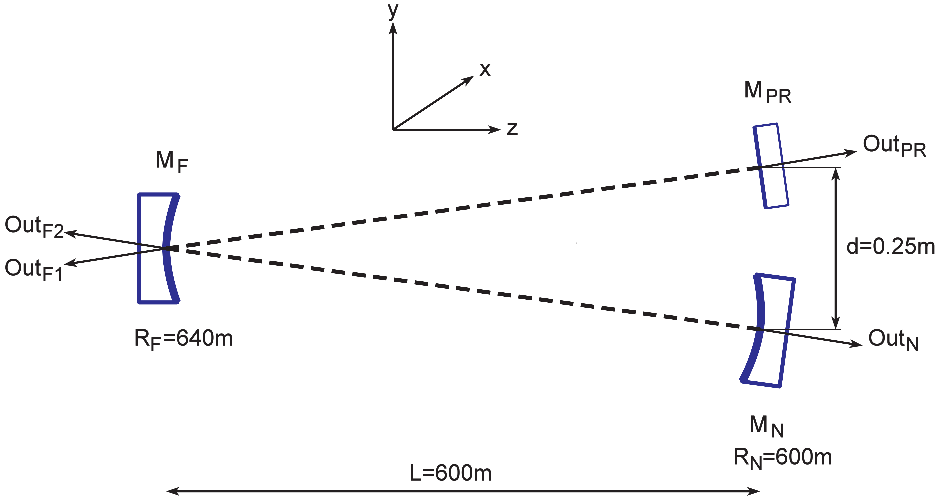

Figure 2.13: Schematic diagram of the GEO 600 PR cavity seen from the side.

Cause	Δy_{PR}	γ_{PR}	γ'_{PR}	θ^{w}
α_{PR}	$-600\,\mathrm{m}\cdot\alpha_{\mathrm{PR}}$	α_{PR}	$-\alpha_{\mathrm{PR}}$	20.7°
α_{F}	0	0	0	undefined
α_{N}	$600\,\mathrm{m}\cdot\alpha_{\mathrm{N}}$	0	0	0°

Cause	Δy_{F}	γ_{F1}	γ_{F2}	Δy_{N}	γ_{N}
α_{PR}	0	α_{PR}	$-\alpha_{\mathrm{PR}}$	$600\,\mathrm{m}\cdot\alpha_{\mathrm{PR}}$	$-\alpha_{\mathrm{PR}}$
α_{F}	0	0	$2\alpha_{\mathrm{F}}$	$-1200\,\mathrm{m}\cdot\alpha_{\mathrm{F}}$	$2\alpha_{\mathrm{F}}$
α_{N}	$600\,\mathrm{m}\cdot\alpha_{\mathrm{N}}$	0	$1.875\alpha_{\mathrm{N}}$	$-525\,\mathrm{m}\cdot\alpha_{\mathrm{N}}$	$1.875\alpha_{\mathrm{N}}$

Table 2.4: Results of the ray-tracing program for the GEO PR cavity.

with the results for the x-direction being identical. The following notations are used: Δy_{X} is the lateral displacement of the beam spot at the component X, and γ_{X} is the angle by which the beam segment 'Out$_{\mathrm{X}}$' is tilted due to the misorientation. The directly reflected incoming beam is tilted by the angle $2\alpha_{\mathrm{PR}}$, when M$_{\mathrm{PR}}$ is misoriented by the angle α_{PR}. Since the differential wavefront sensing method is sensitive to the angle between two interfering beams, in this case the beam 'Out$_{\mathrm{PR}}$' leaking out of the cavity and the directly reflected beam, we also include the angle $\gamma'_{\mathrm{PR}} = \gamma_{\mathrm{PR}} - 2\alpha_{\mathrm{PR}}$ in the table.

The 'character' of any small misalignment is described by the angle θ (see Section 2.2). The angle θ^{w} (at the waist) is given by $\theta^{\mathrm{w}} = \arctan(\gamma'_{\mathrm{PR}} z_{\mathrm{R}}/\Delta y_{\mathrm{waist}})$. The angle θ is altered by the propagation of the beam (from the waist to the detector), and can additionally be influenced by lens systems, such that any desired angle θ^{d} at the detector can be obtained, a feature needed for signal separation.

The corresponding analytical results for the more general case $R_{\mathrm{N}} \neq L$ are shown in

Cause	Δy_{PR}	γ_{PR}	Δy_{F}	γ_{F2}	Δy_{N}	γ_{N}
α_{PR}	$-\alpha_{\mathrm{PR}}(L + g\,h)$	α_{PR}	$-\alpha_{\mathrm{PR}}\,g\,h$	$-\alpha_{\mathrm{PR}}\,g\,R_{\mathrm{F}}$	$\alpha_{\mathrm{PR}}\,g\,R_{\mathrm{F}}R_{\mathrm{N}}$	$-\alpha_{\mathrm{PR}}\,g\,R_{\mathrm{F}}$
α_{F}	$2\alpha_{\mathrm{F}}\,g\,h$	0	$2\alpha_{\mathrm{F}}\,g\,h$	$2\alpha_{\mathrm{F}}\,g\,R_{\mathrm{F}}$	$-2\alpha_{\mathrm{F}}\,g\,R_{\mathrm{F}}R_{\mathrm{N}}$	$2\alpha_{\mathrm{F}}\,g\,R_{\mathrm{F}}$
α_{N}	$\alpha_{\mathrm{N}}\,g\,R_{\mathrm{F}}R_{\mathrm{N}}$	0	$\alpha_{\mathrm{N}}\,g\,R_{\mathrm{F}}R_{\mathrm{N}}$	$2\alpha_{\mathrm{N}}\,g\,R_{\mathrm{N}}$	$\alpha_{\mathrm{N}}\,g\,(R_{\mathrm{F}} - 2L)R_{\mathrm{N}}$	$2\alpha_{\mathrm{N}}\,g\,R_{\mathrm{N}}$

Table 2.5: Analytical results for the GEO PR cavity (L = arm length, $g = 1/(2R_{\mathrm{N}} + R_{\mathrm{F}} - 2L)$, $h = R_{\mathrm{F}}(L - R_{\mathrm{N}})$).

Table 2.5. They are mostly based on earlier calculations carried out by W. Winkler.

For the case of a curved power recycling mirror (such as might be simulated by thermal lensing), no analytical results are known. With the raytracing code it is, however, easy to compute numerical results for any given curvature.

The results shown in Table 2.4 are illustrated in Figures 2.14, 2.15 and 2.16. The well-aligned beams are drawn with dashed lines as reference, whereas the misaligned beams are drawn with solid lines. In Figure 2.14 it can be seen that a misorientation of $\mathrm{M_{PR}}$ changes both the lateral position and the angle of the eigenmode compared to the well-aligned reference. The ratio of the two effects (lateral vs. angular) is described by the angle $\theta^{\mathrm{w}}_{\mathrm{PR}} = 20.7°$.

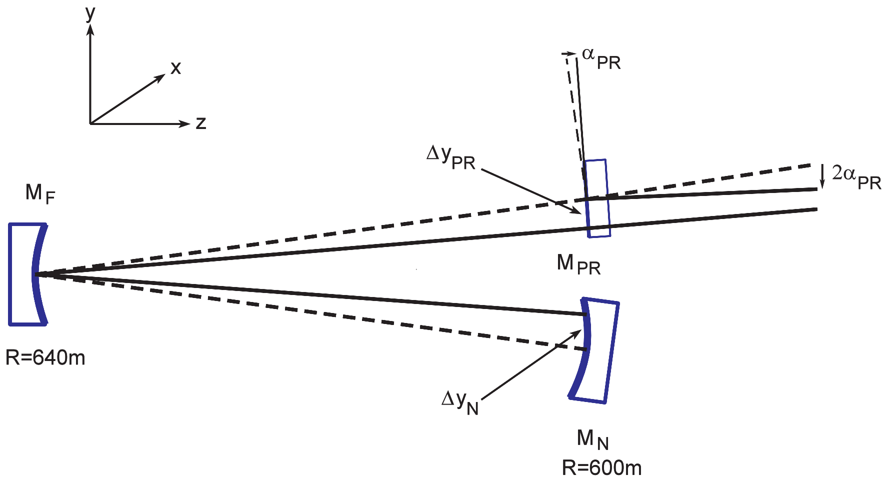

Figure 2.14: Misorientation of $\mathrm{M_{PR}}$ in the GEO 600 PR cavity. The dashed line is the well aligned reference. We have $\Delta y_{\mathrm{PR}} = -\alpha \cdot 600\,\mathrm{m}$, $\Delta y_{\mathrm{N}} = \alpha \cdot 600\,\mathrm{m}$ and $\theta^{\mathrm{w}}_{\mathrm{PR}} = 20.7°$.

A misorientation of $\mathrm{M_N}$, on the other hand, causes a pure lateral displacement and hence we have $\theta^{\mathrm{w}}_{\mathrm{N}} = 0°$ (Figure 2.15). And, finally, a misorientation of $\mathrm{M_F}$ causes no change in the cavity eigenmode at all, as far as the waist is concerned (Figure 2.16).

Therefore we may use two quadrant detectors (near the position of 'PDPR' in the present GEO design) with suitable lens systems to detect misorientations of $\mathrm{M_{PR}}$ and $\mathrm{M_N}$. Unfortunately, the signals for these two mirrors are not as easily separable as in the case of a simple plane-curved cavity, because $\theta^{\mathrm{w}}_{\mathrm{PR}} - \theta^{\mathrm{w}}_{\mathrm{N}}$ is only 20.7° instead of

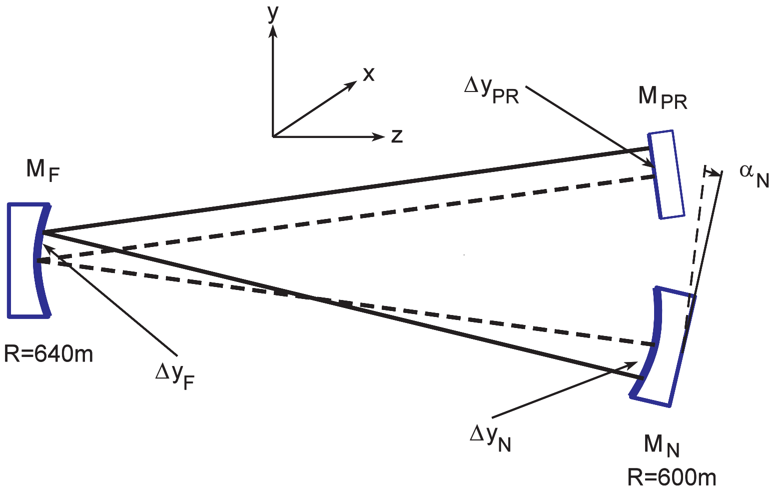

Figure 2.15: Misorientation of $\mathrm{M_N}$ in the GEO 600 PR cavity. The dashed line is the well aligned reference. We have $\Delta y_{\mathrm{PR}} = \alpha \cdot 600\,\mathrm{m}$, $\Delta y_{\mathrm{F}} = \alpha \cdot 600\,\mathrm{m}$, $\Delta y_{\mathrm{N}} = -\alpha \cdot 525\,\mathrm{m}$ and $\theta^{\mathrm{w}}_{\mathrm{N}} = 0°$. The angle between the reference and the misaligned beam between $\mathrm{M_F}$ and $\mathrm{M_N}$ is 1.875α.

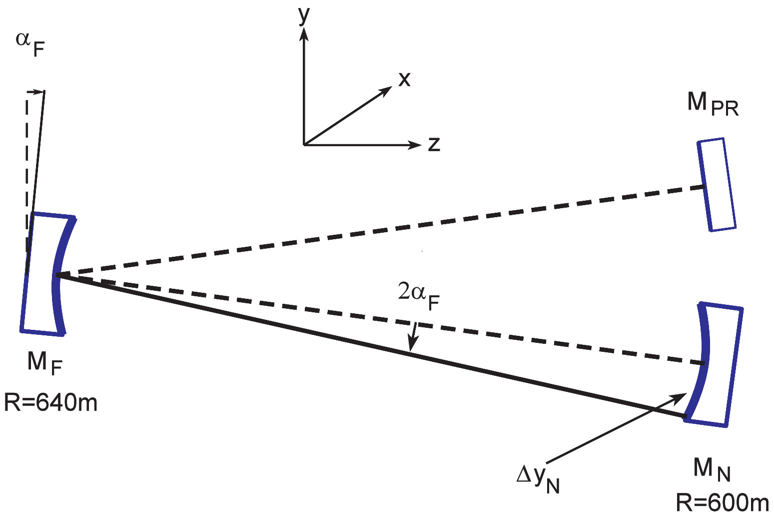

Figure 2.16: Misorientation of $\mathrm{M_F}$ in the GEO 600 PR cavity. The dashed line is the well aligned reference. We have $\Delta y_{\mathrm{N}} = -\alpha \cdot 1200\,\mathrm{m}$ and no effect on the cavity eigenmode at its waist.

near 90°. One possibility would be to induce additional phase shifts in front of the two detectors such that at the first detector we would have $\theta^{\mathrm{d}}_{\mathrm{PR}} = 20.7°$ and $\theta^{\mathrm{d}}_{\mathrm{N}} = 0°$. This first detector would then detect $\sin 20.7° \approx 35\%$ of the maximum possible signal for $\mathrm{M_{PR}}$ and no contribution from $\mathrm{M_N}$. The second detector could then be set up such that $\theta^{\mathrm{d}}_{\mathrm{PR}} = 0°$ and $\theta^{\mathrm{d}}_{\mathrm{N}} = -20.7°$, such as to detect 35 % of the maximum possible signal for $\mathrm{M_N}$ and no contribution from $\mathrm{M_{PR}}$. Other configurations are also possible if the signals are combined electronically.

Once $\mathrm{M_{PR}}$ and $\mathrm{M_N}$ are aligned, we may observe the spot position on $\mathrm{M_N}$ (either by using the transmitted light or by processing the output from a CCD camera which detects the light scattered from $\mathrm{M_N}$), and use it to derive an error signal for the alignment of $\mathrm{M_F}$ with a slower loop.

Finally, we may align the beam injector to fix the beam spot position on $\mathrm{M_F}$ (and, correspondingly, the beamsplitter for the second arm) with another slow loop. In the GEO configuration, we may, however, be handicapped by the fact that the 'spot' on $\mathrm{M_F}$ is composed of two beams which have a finite angle (0.25 m/600 m) between them and which interfere with each other. Figure 2.17 shows the predicted vertical cross section through the interference pattern on $\mathrm{M_F}$. The relative phase of the two interfering beams is *not* controlled by any of the currently designed loops and hence we may expect these fringes to be moving in an uncontrolled fashion. One possible approach would be to reduce the spot size with a telescope, and then use a PSD to detect the 'center of gravity' of that spot. This matter requires further investigation.

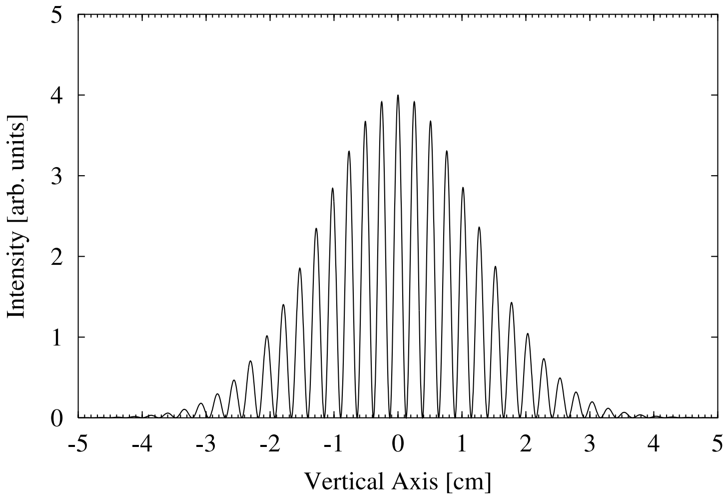

Figure 2.17: Predicted interference structure on the far mirror $\mathrm{M_F}$ of the GEO PR cavity. The intensity along a vertical line through the center of the mirror is shown. The separation between the fringes is 2.55 mm.

In summary, we propose to use the following loops (sorted by decreasing speed):

(1) Beam steerers for (2) and (3) below (six channels).

(2) Michelson alignment by differential wavefront sensing; feedback to M_N differential modes (two channels).

(3) PR cavity alignment by differential wavefront sensing; feedback to M_N common modes and to M_{PR} (four channels).

(4a) Spot positions on M_F via positional sensors; feedback to beam injector and beam splitter (four channels).

(4b) Spot positions on M_N via positional sensors; feedback to corresponding M_F (four channels).

2.10.3 The GEO 600 modecleaner cavities

Figure 2.18 shows a schematic view of a GEO 600 modecleaner cavity seen from above, together with the coordinate system adopted in this section (2.10.3).

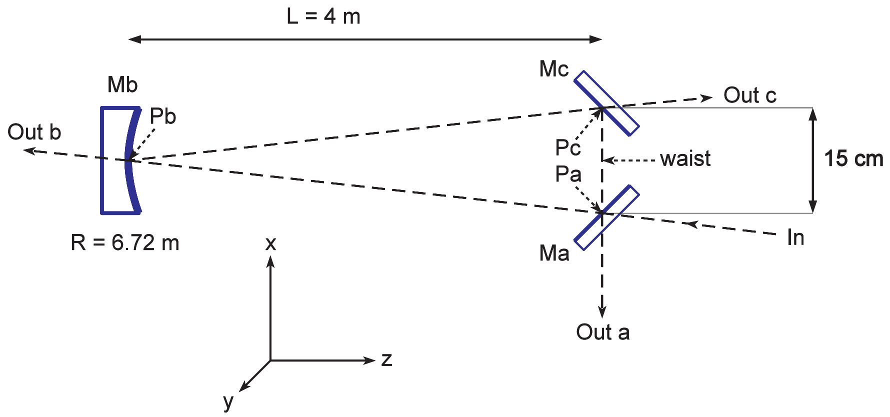

Figure 2.18: Schematic diagram of a GEO 600 modecleaner cavity seen from above.

The cavity consists of two flat mirrors (M_a and M_c) that are separated by a relatively short distance (15 cm in the present GEO design), and a curved mirror M_b with radius of curvature $R = 6.72\,\mathrm{m}$, which is at a distance $L = 4\,\mathrm{m}$ from the flat mirrors. The beam enters through M_a and travels clockwise to M_b, M_c, M_a, etc. There are four beams of interest leaving the cavity. The main output beams are 'Out_b' and 'Out_c' (the first GEO modecleaner uses 'Out_c' as main output, whereas the second one uses 'Out_b').

There are two beams coming from M_a: the directly reflected input beam and the beam 'Out_a' which is a fraction of the cavity eigenmode. The cavity is well aligned to the incoming beam (which we consider fixed), if these two beams are perfectly superimposed. By taking two quadrant diodes with two different lens systems and appropriately demodulating their outputs, we can obtain four independent error signals, similar to the case of a simple two-mirror Fabry-Perot cavity. The longitudinal locking signal is also obtained from these two interfering beams (using the Pound-Drever-Hall scheme).

In the three-mirror cavity, there are two additional degrees of freedom. They can be used to control the angle and/or direction of the output beams ‘Out$_a$’ and ‘Out$_c$’. This is described in more detail below.

In the ray-tracing program, we first compute the well-aligned case (i.e., all mirrors are hit in their center) as reference. We call P$_a$, P$_b$ and P$_c$ the points where the axis of the eigenmode intersects the mirrors M$_a$, M$_b$ and M$_c$, respectively. After misorienting one particular mirror by the small angle ε, we recompute the eigenmode axis, compare it with the well-aligned case and divide the difference by ε. The main results are (see Figure 2.19):

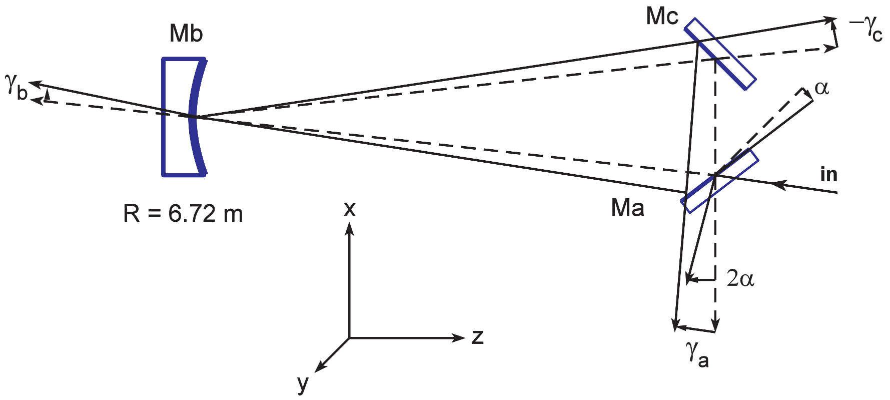

Figure 2.19: Modecleaner with misoriented input mirror. The dashed line is the well aligned reference. This is the most complicated case, since the direct reflection of the incoming beam is also tilted by $2\alpha_a$. For misorientations of the two other mirrors, the directly reflected incoming beam is unaffected.

- The shifts of the spots P$_a$, P$_b$ and P$_c$.
- The angles γ_a, γ_b and γ_c between the beams ‘Out$_a$’, ‘Out$_b$’, ‘Out$_c$’ and their respective references. For the vertical misalignments which are considered separately, we call these angles δ_a, δ_b and δ_c, respectively. We also compute the angle γ_d (δ_d) between the directly reflected incoming beam and its reference for the case that M$_a$ is misoriented.
- For ‘Out$_a$’ in the case of misorienting M$_a$, we also compute the angle $\gamma'_a = \gamma_a - \gamma_d$, which is the angle between the beam leaving the cavity and the directly reflected beam, because this is the angle between the interfering wavefronts that is detected by the quadrant diode.
- As described above we finally compute the angle θ which describes the ‘character’ of the misalignment at the waist. It is given by $\theta^w = \arctan(\gamma'_a z_R / \Delta z_{\mathrm{waist}})$.

The waist of the cavity eigenmode is located halfway between the mirrors $\mathrm{M_a}$ and $\mathrm{M_c}$. Its Rayleigh range is given by

$$z_\mathrm{R} = \sqrt{\frac{L_\mathrm{RT}}{2}\left(R - \frac{L_\mathrm{RT}}{2}\right)} = 3.28\,\mathrm{m}, \tag{2.56}$$

where $L_\mathrm{RT}/2$ is one half of the round-trip distance:

$$L_\mathrm{RT}/2 = \sqrt{L^2 + d^2/4} + d/2 = 4.076\,\mathrm{m}. \tag{2.57}$$

Horizontal misalignments: By ‘horizontal’ misalignments we mean that a mirror is rotated around the y-axis, i.e. beam spots move horizontally (in the plane of the modecleaner cavity, see also diagram ’D’ in Figure A.4). We introduce the linear combinations α_- and α_+ by

$$\alpha_- = \alpha_\mathrm{a} - \alpha_\mathrm{c}, \tag{2.58}$$
$$\alpha_+ = \alpha_\mathrm{a} + \alpha_\mathrm{c}, \tag{2.59}$$

and β_- and β_+ similarily. The results of the raytracing program are given in Table 2.6.

Cause	$\mathrm{P_a}$ Δx	$\mathrm{P_a}$ Δz	waist Δz	$\mathrm{Out_a}$ γ_a	$\mathrm{Out'_a}$ $\gamma'_\mathrm{a} = \gamma_\mathrm{a} - \gamma_\mathrm{d}$	θ^w
α_a	$-4.002\,\mathrm{m}\cdot\alpha_\mathrm{a}$	$-4.078\,\mathrm{m}\cdot\alpha_\mathrm{a}$	$-4.001\,\mathrm{m}\cdot\alpha_\mathrm{a}$	$1.028\,\alpha_\mathrm{a}$	$-0.972\,\alpha_\mathrm{a}$	38.6°
α_b	$0.187\,\mathrm{m}\cdot\alpha_\mathrm{b}$	$0.191\,\mathrm{m}\cdot\alpha_\mathrm{b}$	$0.000\,\mathrm{m}\cdot\alpha_\mathrm{b}$	$-2.542\,\alpha_\mathrm{b}$	$-2.542\,\alpha_\mathrm{b}$	90°
α_c	$3.851\,\mathrm{m}\cdot\alpha_\mathrm{c}$	$3.924\,\mathrm{m}\cdot\alpha_\mathrm{c}$	$4.001\,\mathrm{m}\cdot\alpha_\mathrm{c}$	$1.028\,\alpha_\mathrm{c}$	$1.028\,\alpha_\mathrm{c}$	40.2°
α_-	$-3.926\,\mathrm{m}\cdot\alpha_-$	$-4.001\,\mathrm{m}\cdot\alpha_-$	$-4.001\,\mathrm{m}\cdot\alpha_-$	$0.000\,\alpha_-$	$-1.000\,\alpha_-$	39.4°
α_+	$-0.076\,\mathrm{m}\cdot\alpha_+$	$-0.077\,\mathrm{m}\cdot\alpha_+$	$0.000\,\mathrm{m}\cdot\alpha_+$	$1.028\,\alpha_+$	$0.028\,\alpha_+$	(90°)

Cause	$\mathrm{P_b}$ Δx	$\mathrm{Out_b}$ γ_b	$\mathrm{P_c}$ Δx	$\mathrm{P_c}$ Δz	$\mathrm{Out_c}$ γ_c	d. refl. γ_d
α_a	$-0.191\,\mathrm{m}\cdot\alpha_\mathrm{a}$	$0.972\,\alpha_\mathrm{a}$	$3.851\,\mathrm{m}\cdot\alpha_\mathrm{a}$	$-3.924\,\mathrm{m}\cdot\alpha_\mathrm{a}$	$-1.028\,\alpha_\mathrm{a}$	$2\cdot\alpha_\mathrm{a}$
α_b	$10.362\,\mathrm{m}\cdot\alpha_\mathrm{b}$	$2.542\,\alpha_\mathrm{b}$	$0.187\,\mathrm{m}\cdot\alpha_\mathrm{b}$	$-0.191\,\mathrm{m}\cdot\alpha_\mathrm{b}$	$2.542\,\alpha_\mathrm{b}$	$0\cdot\alpha_\mathrm{b}$
α_c	$-0.191\,\mathrm{m}\cdot\alpha_\mathrm{c}$	$-1.028\,\alpha_\mathrm{c}$	$-4.002\,\mathrm{m}\cdot\alpha_\mathrm{c}$	$4.078\,\mathrm{m}\cdot\alpha_\mathrm{c}$	$0.972\,\alpha_\mathrm{c}$	$0\cdot\alpha_\mathrm{c}$
α_-	$0.000\,\mathrm{m}\cdot\alpha_-$	$2.000\,\alpha_-$	$7.853\,\mathrm{m}\cdot\alpha_-$	$-8.001\,\mathrm{m}\cdot\alpha_-$	$-2.000\,\alpha_-$	$1\cdot\alpha_-$
α_+	$-0.381\,\mathrm{m}\cdot\alpha_+$	$-0.057\,\alpha_+$	$-0.151\,\mathrm{m}\cdot\alpha_+$	$0.154\,\mathrm{m}\cdot\alpha_+$	$-0.057\,\alpha_+$	$1\cdot\alpha_+$

Table 2.6: Results of the ray-tracing program for horizontal misalignments of the GEO modecleaner.

Vertical misalignments: In the modecleaners, the horizontal and vertical axes are *not* similar. The results of the raytracing program for vertical misalignments (see diagram ’C’ in Figure A.4) are given in Table 2.7. Note, for example, that a small vertical tilt β_a of the input mirror $\mathrm{M_a}$ (which is hit under approximately 45° from the incoming beam) causes a deflection of the reflected beam by only $\delta_\mathrm{d} = 1.43\beta_\mathrm{a}$ as compared to $\gamma_\mathrm{d} = 2\alpha_\mathrm{a}$ in the horizontal case. Another example is the tilt of $\mathrm{M_b}$ which, if horizontal, causes a pure angular misalignment at the waist. A vertical tilt of $\mathrm{M_b}$, on the other hand, shifts the cavity eigenmode downwards parallelly, without changing any angles. Angles are again counted as positive when they refer to a clockwise tilt from the reference direction. As 'viewpoint' from where we look to determine whether a tilt is clockwise, we take the point with coordinates $(-1, 0, 0)$ in the coordinate system of Figure 2.18. For the angles δ_a and δ'_a (which describe the output beam $\mathrm{Out_a}$) we take $(0, 0, -1)$ as viewpoint, i.e. we look from the direction of $\mathrm{M_b}$.

Cause	$\mathrm{P_a}$	waist	$\mathrm{Out_a}$	$\mathrm{Out'_a}$	θ^w
	Δy	Δy	δ_a	$\delta'_\mathrm{a} = \delta_\mathrm{a} - \delta_\mathrm{d}$	
β_a	$1.889\,\mathrm{m} \cdot \beta_\mathrm{a}$	$1.942\,\mathrm{m} \cdot \beta_\mathrm{a}$	$0.701\,\beta_\mathrm{a}$	$-0.727\,\beta_\mathrm{a}$	$-50.9°$
β_b	$-6.720\,\mathrm{m} \cdot \beta_\mathrm{b}$	$-6.720\,\mathrm{m} \cdot \beta_\mathrm{b}$	$0.000\,\beta_\mathrm{b}$	$0.000\,\beta_\mathrm{b}$	$0°$
β_c	$1.994\,\mathrm{m} \cdot \beta_\mathrm{c}$	$1.942\,\mathrm{m} \cdot \beta_\mathrm{c}$	$-0.701\,\beta_\mathrm{c}$	$-0.701\,\beta_\mathrm{c}$	$-49.8°$
β_+	$1.942\,\mathrm{m} \cdot \beta_+$	$1.942\,\mathrm{m} \cdot \beta_+$	$0.000\,\beta_+$	$-0.714\,\beta_+$	$-50.3°$
β_-	$-0.053\,\mathrm{m} \cdot \beta_-$	$0.000\,\mathrm{m} \cdot \beta_-$	$0.701\,\beta_-$	$-0.013\,\beta_-$	$(90°)$

Cause	$\mathrm{P_b}$	$\mathrm{Out_b}$	$\mathrm{P_c}$	$\mathrm{Out_c}$	d. refl.
	Δy	δ_b	Δy	δ_c	δ_d
β_a	$4.797\,\mathrm{m} \cdot \beta_\mathrm{a}$	$-0.727\,\beta_\mathrm{a}$	$1.994\,\mathrm{m} \cdot \beta_\mathrm{a}$	$-0.701\,\beta_\mathrm{a}$	$1.43 \cdot \beta_\mathrm{a}$
β_b	$-6.720\,\mathrm{m} \cdot \beta_\mathrm{b}$	$0.000\,\beta_\mathrm{b}$	$-6.720\,\mathrm{m} \cdot \beta_\mathrm{b}$	$0.000\,\beta_\mathrm{b}$	$0 \cdot \beta_\mathrm{b}$
β_c	$4.797\,\mathrm{m} \cdot \beta_\mathrm{c}$	$-0.701\,\beta_\mathrm{c}$	$1.889\,\mathrm{m} \cdot \beta_\mathrm{c}$	$-0.727\,\beta_\mathrm{c}$	$0 \cdot \beta_\mathrm{c}$
β_+	$4.797\,\mathrm{m} \cdot \beta_+$	$-0.714\,\beta_+$	$1.942\,\mathrm{m} \cdot \beta_+$	$-0.714\,\beta_+$	$0.714 \cdot \beta_+$
β_-	$0.000\,\mathrm{m} \cdot \beta_-$	$-0.013\,\beta_-$	$0.053\,\mathrm{m} \cdot \beta_-$	$0.013\,\beta_-$	$0.714 \cdot \beta_-$

Table 2.7: Results of the ray-tracing program for vertical misalignments of the GEO mode-cleaner.

Alignment strategies: The most important alignment task is to superimpose the axis of the cavity eigenmode with the axis of the incoming beam. This requires the control of four degrees of freedom. For this purpose, in the differential wavefront sensing method, we place two quadrant detectors with different lens systems in the beam reflected from $\mathrm{M_a}$. The interference between the directly reflected incoming beam, which is phase modulated at an RF frequency, and the beam '$\mathrm{Out_a}$' leaking out of the cavity contains enough information to lock the cavity longitudinally and to obtain alignment error signals for those four degrees of freedom that determine the superposition of the incoming beam and the cavity eigenmode.

In particular, we now assume all mirrors to be slightly misoriented and compute the combined signals which are obtained by demodulating the outputs of two quadrant detectors, one (called S_I) with $\Phi = 0°$ and the other one (called S_Q) with $\Phi = 90°$ of extra phase shift. We scale parallel shifts Δy or Δz with the appropriate factor z_R and obtain for horizontal misalignments:

$$S_I = -2.542\,\alpha_\mathrm{b} - 1.000\,\alpha_- + 0.028\,\alpha_+, \tag{2.60}$$

$$S_Q = -1.218\,\alpha_-, \tag{2.61}$$

and for vertical misalignments:

$$S_I = -0.013\,\beta_- - 0.714\,\beta_+, \tag{2.62}$$
$$S_Q = -2.047\,\beta_\mathrm{b} + 0.591\,\beta_+. \tag{2.63}$$

We see that we can indeed obtain four independent error signals from the reflected light, which allow us to align the cavity eigenmode with the incoming beam. We need to control the four angles α_b, α_-, β_b and β_+ for this purpose. The necessary error signals can be obtained either as linear combinations of S_I and S_Q or else by introducing different phase shifts Φ. Since the angles θ^w are very different for the horizontal and vertical cases, the former approach may be easier, unless we want to use cylindrical lenses.

The remaining degrees of freedom (α_+ and β_-) will produce almost no signal in the quadrant detectors that look at the reflected light. Indeed, misorientations of these angles have only little influence on the cavity eigenmode at all and hence only little influence on the main output beams ($\mathrm{Out_c}$ and $\mathrm{Out_c}$). Their effect is illustrated in Figures 2.20 and 2.21.

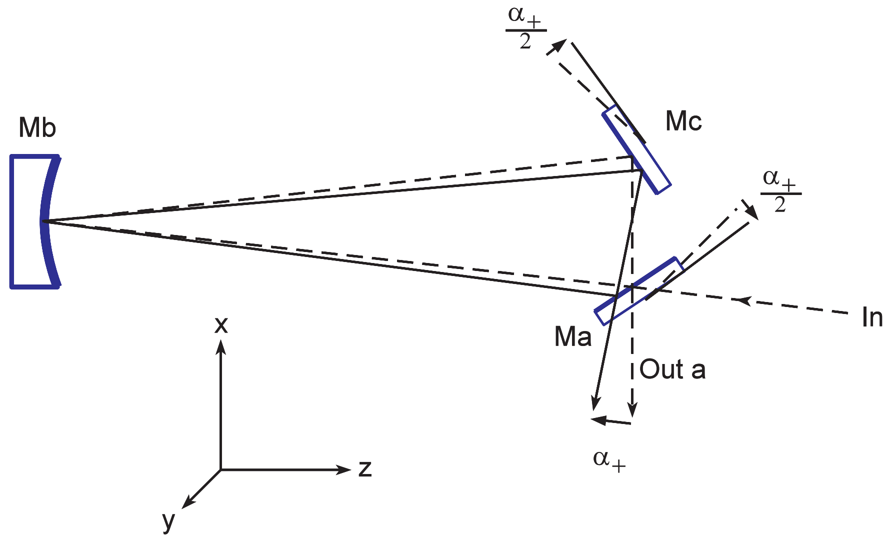

Figure 2.20: Modecleaner with misorientation of α_+. The dashed line is the well aligned reference. The main effect is a downwards motion of the outgoing beam $\mathrm{Out_a}$.

Thus it might be argued that such misorientations do not disturb and need not to be controlled. This is, however, not likely to be a practical alternative, since the effects of α_+ and β_- will be small, but finite, and because there will anyway be some involuntary feed back to them through imperfections in the α_- and β_+ feedback. At least a slow loop to prevent runaway is expected to be necessary.

Looking back at the Tables 2.6 and 2.7, we see that the main effect of α_+ and β_- is a common tilt of the two beams leaving $\mathrm{M_a}$. We find for the angles γ_a and γ_d (the latter

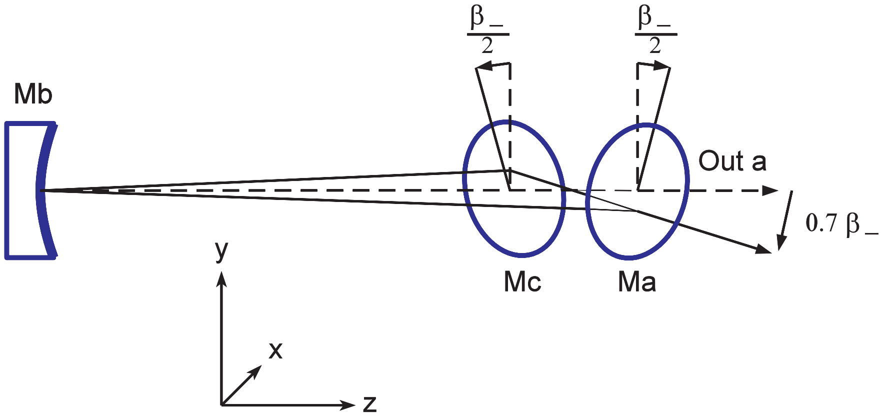

Figure 2.21: Modecleaner with misorientation of β_-. The dashed line is the well aligned reference. The main effect is a shift of the outgoing beam $\mathrm{Out_a}$.

describing the tilt of the directly reflected beam) in the horizontal case:

$$\gamma_\mathrm{a} = -2.542\,\alpha_\mathrm{b} + 1.028\,\alpha_+, \tag{2.64}$$

$$\gamma_\mathrm{d} = \alpha_- + \alpha_+, \tag{2.65}$$

and for the vertical case:

$$\delta_\mathrm{a} = 0.701\,\beta_-, \tag{2.66}$$

$$\delta_\mathrm{d} = 0.714\,\beta_- + 0.714\,\beta_+, \tag{2.67}$$

If we assume the loops described previously to be working (i.e. $\alpha_\mathrm{b} = \alpha_- = \beta_\mathrm{b} = \beta_+ = 0$), we obtain useful error signals: $\gamma_\mathrm{a} \approx \gamma_\mathrm{d} = \alpha_+$ for the horizontal case and $\delta_\mathrm{a} \approx \delta_\mathrm{d} \approx 0.7\,\beta_-$ for the vertical case.

The easiest way to detect these angles (and thus to obtain error signals for the remaining degrees of freedom) is to use the auxiliary beam-steering loops that center the beam on the RF quadrant detectors (see Section 2.6.2). These beam-steering loops need to have a wider bandwidth than the autoalignment loops for the four angles α_b, α_-, β_b and β_+, which in turn are faster than the loops for α_+ and β_-. Hence the information that we need is not contained in the *error signal* of the beam-steereing loops, but rather in their *correction signal* (i.e. the currents forced through their galvanometer coils).

In summary, we propose to use the following loops for each modecleaner (sorted by decreasing speed):

(1) Beam steerers for (2) below (four channels).

(2) Differential wavefront sensing for α_b, α_-, β_b and β_+ (four channels).

(3) α_+ and β_- via the spot positions on the quadrant detectors used for (2); error signals can be obtained from the correction signal of the loops (1) (two channels).

Appendix A

The 30 m prototype

A.1 Construction

Construction of the Garching 30 m prototype began in 1982. It is located in the basement of the Max-Planck-Institut für Astrophysik in Garching, at a distance of a few hundred meters from the Max-Planck-Institut für Quantenoptik, where the offices and other laboratories of the gravitational wave group are now located.

The central laboratory houses the laser table, the central tank, the vacuum pumps, and most of the electronic and measuring equipment. From the central laboratory, the two arms extend through the garden to the two end huts. The arms consist of stainless steel tubes approximately 40 cm in diameter, which are protected from above by a concrete hull. The tubes are approximately on ground level.

Each of the two end huts contains a vacuum tank, where the respective end mirror is suspended. The length of each arm (from the center of the central tank to the center of the end tank) can be varied by inserting smaller pieces of the stainless steel tube and moving the end tanks on rails. During this work, the length of both arms was approximately 30.6 m (the exact armlengths are discussed below).

The vacuum system consists of one roughing pump (DK100), which is used to reach a pressure of approximately 1 mbar. In addition there is a turbomolecular pump with its associated backup pump (D12) used to further reduce the pressure. The pressure achieved is usually a few times 10^{-5} mbar, after the turbomolecular pump had been running for a day or so.

Since 1983 many different experiments had been carried out by various people at the prototype. Most of the equipment used during this work remained from these earlier experiments, in particular the laser and the whole suspension system including the local controls. These items will be described only briefly here.

A.2 Laser and associated optics

The laser is an INNOVA100 Ar^+ laser running at 514 nm. It was usually operated at 35 or 40 A tube current, which yielded about 1 W of single-mode light. The laser had been modified in several ways. A fast input was added to the power supply (tube current control), which was sometimes used to apply an amplitude modulation (up to a few tens of kHz) or to suppress amplitude fluctuations.

A temperature-stabilized etalon was inserted into the cavity to ensure single-mode operation. Both end mirrors were removed from the laser case and separately mounted on the laser table. The rear (high-reflectance) mirror is mounted in an assembly consisting of a prism (to select the wavelength), a small piezo and the mirror itself. The piezo is a special construction which had been provided by the Orsay group. Its mount consists of an 'acoustical delay line' made of tungsten and designed to suppress most of the mechanical resonances. It is briefly described in [Kerr85], and a similar device is described in [Heinzel95, Section 3.4]. The frequency of the first resonance is slightly above 200 kHz. This piezo is called the 'fast PZT' (FPZT) in this work.

The front (coupling) mirror is mounted on a commercial piezo (from PI), which has a wider dynamic range than the fast piezo, at the expense of slower response (its first resonance is at 2 kHz). It is called 'slow PZT' (SPZT) in this work. One of the practical problems encountered during this work was the fact that the motion of this slow piezo was not purely longitudinal. If increasing voltages are applied to it (e.g. during long-term operation of the interferometer, when the laser frequency must follow the resonance of a slowly drifting cavity), the coupling mirror of the laser becomes tilted. This results in varying laser power and, even worse, in a misalignment of the emitted laser beam.

Most of the optical elements on the laser table were installed or changed (some of them several times) by the author during this work. These elements are described here, with references to Figure 1.29 printed in bold. Immediately after the laser there is a Faraday isolator (not shown). Next comes an electro-optic modulator (**PC1**) which is used as fast phase-corrector for the frequency stabilization. A Gsänger PM 25 cell is used for that purpose. It consists of a KD*P crystal with Brewster-angle faces mounted in a glass tube with Brewster-angle windows. It is driven by a high-voltage amplifier (built by the author) which uses two PA-85 (Apex) hybrid amplifiers in push-pull mode and which can deliver up to 800 V_{pp}, with a small-signal bandwidth of about 1 MHz. The amplifier has two equivalent inputs, one of which is permanently connected to the frequency stabilization system, whereas the other one can be used to inject test signals (for a phase modulation of the laser beam).

After another Faraday isolator (**FR1**) there are two more Pockels cells **PC2** and **PC3** which are used to apply the two modulation frequencies (12 MHz for the frequency stabilization and PR cavity lock and $\approx$ 9.7 MHz for the Schnupp modulation). The modulation index of these two modulations is approximately 0.6 rad.

These Pockels cells have been the cause of many problems. At first, PM 25 cells had also been used, however, it became apparent that they produced strong, drifting AM components in the light (at their respective modulation frequency). The AM components were mainly due to heating of the crystal and changing alignment of the laser beam (caused by slow environmental changes but also by the SPZT). Any alignment drift caused a 'polarization modulation' of the emerging beam, that was converted into AM at the next beamsplitting device (which are all polarization-sensitive).

These AM components cause offsets in all those loops which detect a beam and use a mixer to demodulate the AM component in the photocurrent (these are **Mix1**, **Mix2**, **Mix3** and **Mix4**, i.e. the most important loops of the interferometer control). The offsets were sometimes so large that the respective loops would lock at a considerably shifted operating point or, sometimes, wouldn't lock at all (see, e.g., Figure 1.57).

The situation was considerably improved by the acquisition of new Pockels cells (KDP crystals from Leysop), which have specially designed low-resistance electrical contacts (to reduce the heating) and do not have Brewster-angle surfaces. Furthermore a $\lambda/2$-plate was placed before each Pockels cell and a polarizer behind it such that the effect of any polarization modulation could also be reduced. The AM produced by each Pockels cell is monitored by two dedicated tuned photodetectors which detect the AM in a small fraction of the respective beams, split off after the polarizer that follows the Pockels cell. During the operation of the prototype (after a two-hour warm-up period), the alignment of the two Pockels cells was manually readjusted approximately once or twice per hour to minimize the residual AM.

The main laser beam is then fed into a single-mode fiber which takes the light into the vacuum tank. The end of the fiber is fixed on the 'beam injector unit', which is suspended as a pendulum such that the fiber end is decoupled from ground noise. The beam injector unit also contains another Faraday isolator and a mode-matching lens.

Between the Pockels cells **PC2** and **PC3**, a small fraction of the light is diverted to the reference cavity for the 'first loop' (frequency prestabilization). A simplified diagram of this part of the laser table is shown in Figure A.1.

The first $\lambda/2$-plate is used to adapt the polarization of the beam for the following polarizing beam splitter PBS1, such that the beam is completely transmitted. The beam then passes through the acousto-optic modulator AOM (model AA.BM.50) which is used to shift the frequency of the beam. It is driven by a 200 MHz VCO (built with a Motorola MC12148 VCO chip) via a commerical power amplifier. The frequency of the VCO can be changed by approximately ±20 MHz via a control input, which is used as an actuator for the second loop. A small mirror with a radius of curvature of 45 cm is placed 45 cm behind the AOM to select and reflect the first order diffracted beam while compensating the frequency-dependent diffraction angle. A $\lambda/4$-plate causes the reflected beam to be separated from the incoming beam at the polarizing beamsplitter PBS1, after it has passed the AOM a second time. The effective frequency shift of the light that goes to the reference cavity is thus twice the VCO frequency, and has an efficiency of 4.5 MHz/V (referred to the VCO input).

The reference cavity used in the dual recycling experiment is one of several cavities that had been built for other experiments. Its two mirrors are mounted in a cylindrical vacuum chamber. It had originally been designed as a confocal cavity with 26.1 cm

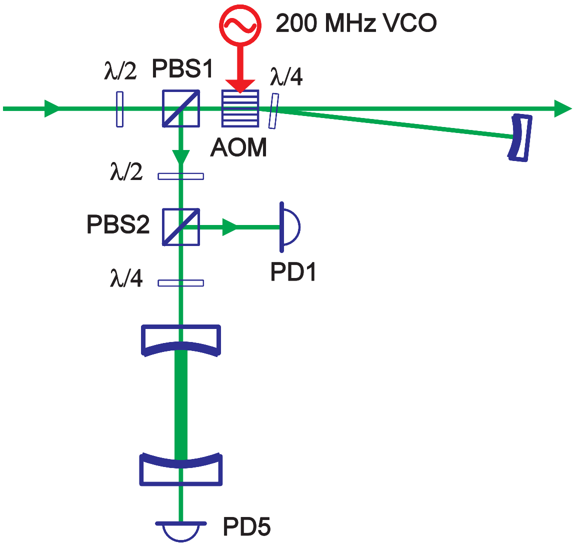

Figure A.1: Schematic diagram of the optical components for the laser prestabilization ('first loop').

separation between the mirrors. In this work it was used under non-normal incidence such that an effective length of 52.2 cm resulted. This was decided because the beam, after two passages through the AOM, was badly distorted and the (never perfect) mode degeneracy of a confocal cavity was hence undesirable. Two mode-matching lenses (not shown in Figure A.1) are also placed between the pick-off from the main beam and the reference cavity. Because of the very limited space on the laser table, the mode-matching could only be approximated, but not optimized.

The reference cavity has a measured FSR of 287 MHz[1] and a finesse of 150. One of the mirrors is mounted on a piezo, which has a rather high efficiency of 10 MHz/V and its first mechanical resonance near 9 kHz. That piezo is used to bring a resonance of the reference cavity within the range of the laser frequency. In order to avoid feeding in external noise to the laser frequency via the very sensitive piezo, a passive low-pass filter with a very low cut-off frequency (0.1 Hz) was placed between the high-voltage amplifier used for that purpose and the piezo itself. The resulting slow response was only used for manual lock acquisition (of the first loop) and subsequent periodic readjustment, but not for any electronic control loop.

Without this manual readjustment, the reference cavity is the master frequency reference for the (AOM-shifted) laser frequency. Since the average (DC) control voltage for the VCO/AOM is kept near zero via a second feedback path of the second loop to the power recycling mirror, the reference cavity is the master frequency reference of the laser at DC (with an offset of twice the VCO rest frequency, approximately 400 MHz). If one includes the slow manual feedback to the reference cavity piezo (which strives to maintain the voltage at the laser SPZT near its nominal mean value), the laser itself is

---

[1] The length of the cavity was derived from this measurement

the final frequency reference on long timescales (several minutes or more).

Another $\lambda/2$-plate, polarizing beamsplitter (PBS2) and $\lambda/4$-plate are used to separate the light reflected from the reference cavity and to direct it onto the tuned photodetector PD1. The RF output of that photodetector is mixed with the 12 MHz reference oscillator in mixer **Mix1**, to generate the error signal for the first loop.

The first loop has three actuators: the Pockels cell PC1 which acts as a phase corrector for the high-frequency signals. It needs 1620 V to achieve a phase-shift of 2π. Used as an actuator for the laser *frequency*, it behaves like a differentiator with a gain proportional to the signal frequency. At 100 kHz, its gain is 2.4 kHz/V. The second actuator is the fast piezo ('FPZT'), which has an efficiency of about 20 kHz/V. The crossover frequency between these two actuators is at about 30 kHz. Finally there is the slow piezo ('SPZT') which takes care of the slow signals with an efficiency of about 16 MHz/V. The crossover frequency between SPZT and FPZT is at about 1 kHz. The unity-gain frequency of the first loop is normally around 300 kHz.

The light transmitted through the reference cavity is also detected (by the broadband photodetector PD5) and is used for the automatic lock-acquisition circuit (see Appendix B.13).

A.3 Mirrors, suspensions and local controls

The mirror suspensions and their local controls already existed before the present work commenced and are only briefly described here.

All three tanks (central tank and the two end tanks) have a ground plate and a similar top plate, both of approximately 90 cm diameter and made out of solid aluminum with screw holes in a 5 cm raster. All three tanks rest on foundations which are separated from the foundation of the surrounding laboratory. Inside the vacuum tank, there are four legs extending upwards from the bottom plate. On top of these legs come the 'stacks', alternate layers of lead bricks and silicon-rubber cylinders, which provide the first stage of seismic isolation. A schematic picture of the central tank (drawn by P. Nelson) is shown in Figure A.2. This picture shows the setup for external modulation, which was used only during the first part of this work, but is nevertheless useful to illustrate the contents of the central tank.

The bottom plate, the top plate and the feet and stacks that hold the top plate are clearly visible. There are two types of suspensions used in the prototype, single pendulums and double pendulums. In Figure A.2, only the double pendulums are shown. In the setup for external modulation shown, both the beamsplitter and the recombination plate are suspended as double pendulums. In the present setup (with Schnupp modulation and dual recycling), only the beamsplitter is suspended as a double pendulum.

Since the type of double pendulum that is used in the prototype (and shown in Figure A.2) has meanwhile been considerably improved (by our collaborators in Glasgow), and the suspensions of GEO 600 will be different, the details of the double pendulum

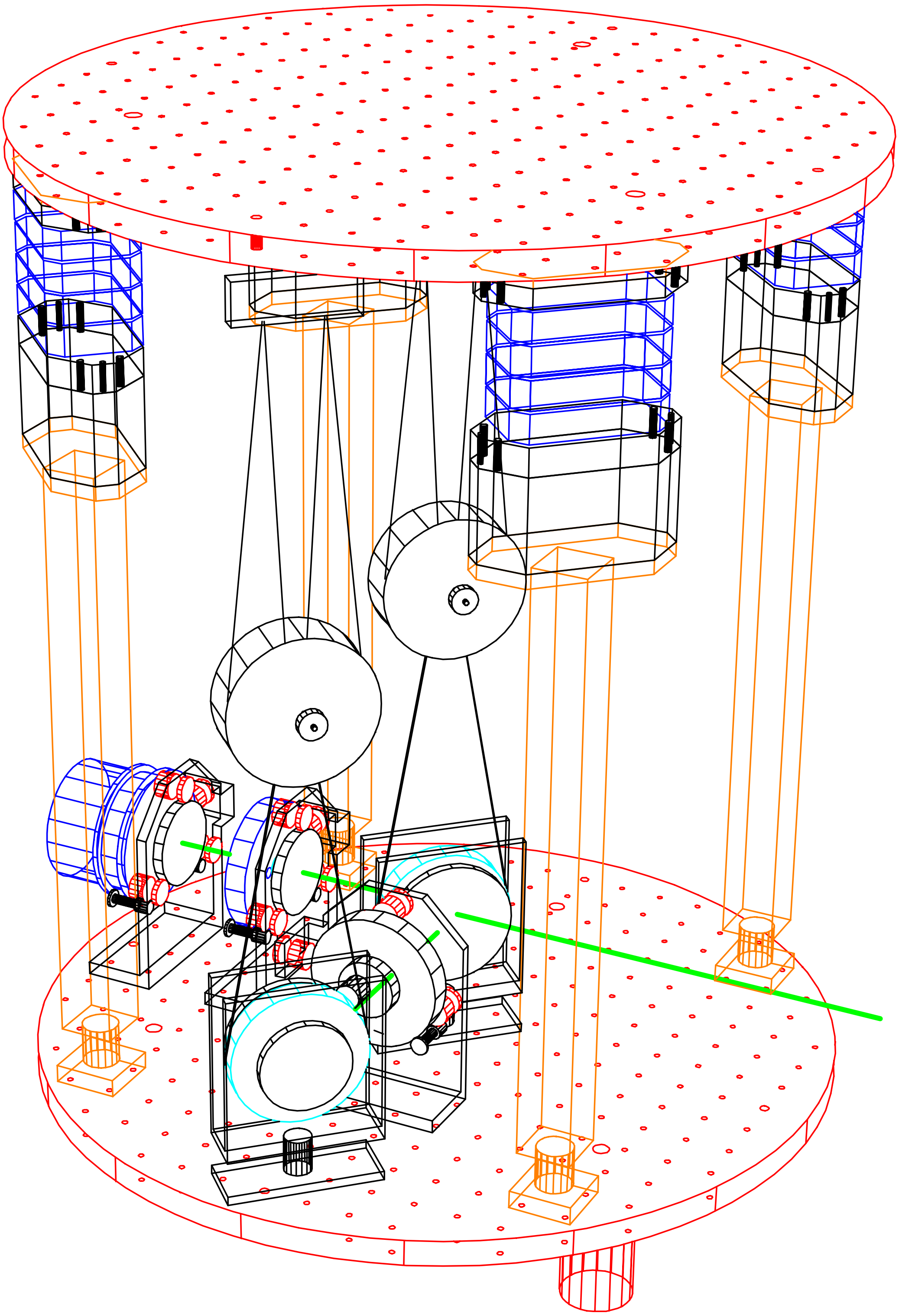

Figure A.2: Schematic picture of the central tank (in the external modulation setup).

are not discussed here. A sketch of a double pendulum used in the 30 m prototype is shown in Figure A.3.

In Figure A.2, the laser beam enters from the left side. The leftmost component is the 'beam injector', where the end of the single-mode fiber is fixed. The beam injector is suspended as a single pendulum, as are all other components apart from the beamsplitter. It is a complex unit containing several mirrors, a mode-matching lens, a Faraday isolator and a remotely controllable motor to adjust the distance between the end of the fiber and the lens.

Next comes the power recycling mirror M_{PR}. It consists of a cylindrical plate made out of fused silica (∅ 15 cm, thickness 2.5 cm) with two holes (∅ 1 cm) approximately 3 cm from each other (horizontally). Two of these plates had been prepared for a planned external modulation setup with signal recycling, where two beams need to pass the signal recycling mirror M_{SR}, one of which needs to pass straight through unaffected (see Figure 1.14).

The actual power-recycling mirror itself is a standard (∅ 2.5 cm, thickness 8 mm) flat fused-silica mirror substrate coated for 7 % power transmittance on the 'inner' side (facing the beamsplitter) and antireflection on the other side, glued on top of one of the holes in the fused-silica plate mentioned above. In our prototype it has proven to be very helpful to make such mirrors wedged, such that the spuriously reflected beam from the AR coating cannot interfere with the main beam. The presence of the two holes in the suspended fused-silica plate was used to fix two mirrors with different reflectivities on the fused-silica plate, such that switching the reflectivity of M_{PR} was slightly simplified (the part of the suspension fixed on the top plate contains a micrometer screw with sufficient range, but those parts belonging to the local control, which are fixed on the bottom plate still need to be moved and readjusted).

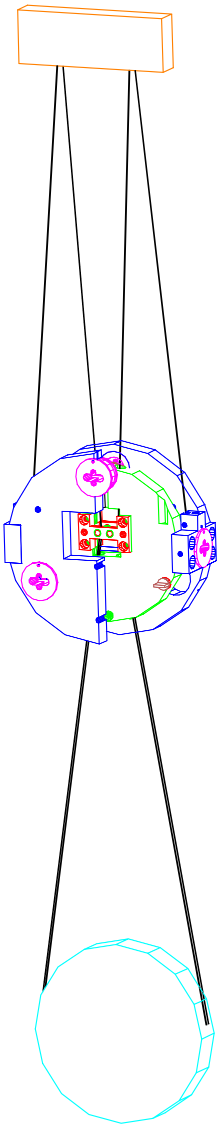

Figure A.3: Sketch of a double pendulum as it is used to suspend the beamsplitter in the prototype.

The two end mirrors in their respective end huts are also suspended as single pendulums. The fused-silica substrates are longer, having 12 cm thickness and 15 cm diameter. The mirrors themselves have a diameter of 4 cm and a thickness of 1 cm and are optically contacted on the substrates (this is different from the plan for GEO 600, where the main test mass substrates will be directly polished and coated as mirrors). The nominal radius of curvature of the 30 m prototype end mirrors is 33 m. They were manufactured and coated for maximal reflectivity by PMI (now REO). After years of use and some cleaning attempts, their surface quality is now, however, less than desirable (indicated by very clearly visible scattering and wavefront distortions that depend on the spot position on the mirror). In front of each end mirror there is a black-and-white CCD camera mounted on the ground plate (below the beam) that looks at the mirror. The light scattered from the mirror surface is strong enough to produce a clear picture of the beam spot on the mirror. The two images are displayed on monitors in the central laboratory, where they are used for initial alignment of the interferometer and also to monitor the transversal mode of the PR cavity.

The signal recyling mirror M_{SR} is suspended exactly as the power recycling mirror (replacing both the suspended Pockels cell and the recombination plate in the lower part of Figure A.2). It is also a flat dielectric mirror coated on a standard one-inch fused silica substrate, and has a power reflectivity of 3.88 % (average of three measurements, see also Section 1.8.2).

A.3.1 Local controls

All pendulum suspensions, whether they are single-, double- or multi-stage pendulums, need local controls to be useful. This is because the pendulum will have resonances (i.e. modes of proper motion) of relatively high Q. For thermal noise reasons, the Q is even made as high as possible ($Q \gtrapprox 10^6$). This means that any stimulus which contains some energy at the resonant frequency (such as seismic motion or a pulse) will induce a strong motion of the mirror, which has a long decay time. Such motions would make any component with such a suspension unusable for an interferometer. Hence it is necessary to artificially damp the resonant motion in a frequency-dependent fashion that does not spoil the performance of the detector at measurement frequencies. This is the purpose of the local control. Here the comparatively simple local controls of the single pendulums in the prototype are described, which had been developed by the Garching group around 15 years ago.

A cyclindrical test mass that is suspended as single-stage pendulum from two wires has four degrees of freedom, which are sketched in Figure A.4.

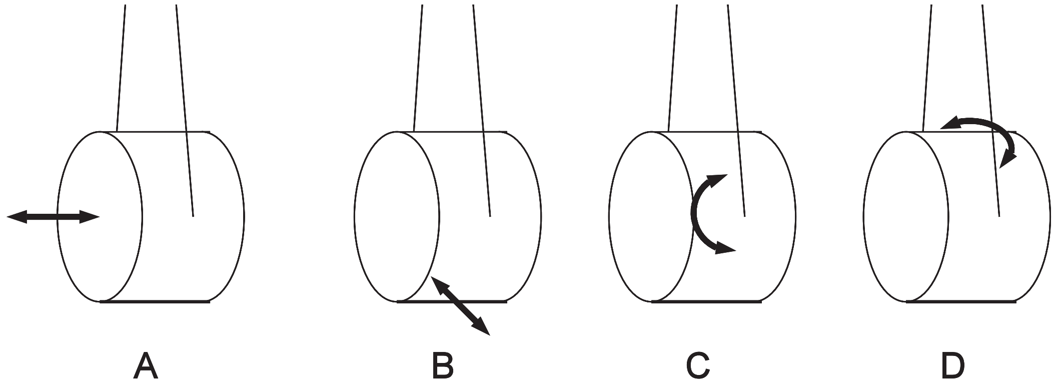

Figure A.4: The four degrees of freedom of a test mass suspended as single-stage pendulum from two wires (such as the single pendulums in the prototype).

The four degrees of freedom are (A) the longitudinal motion of the test mass as a whole in the direction of the beam axis, (B) a similar motion in the orthogonal direction, (C) a tilting motion of the test mass around a horizontal axis through its center of mass, and finally (D) a rotational motion around a vertical axis through its center of mass. These are not necessarily the eigenmodes of the system, and not all of them have necessarily a very high Q. The local control nevertheless damps these degrees of freedom and thus achieves its purpose. For multi-stage pendulums, a more detailed analysis is necessary (and indeed has been carried out by their constructors, e.g. in Glasgow).

These four degrees of freedom are damped with four channels of the local control. Each channel consists of a positional sensor for one specific direction and a coil-magnet combination that applies forces at that position in the same direction. Figure A.5 shows the approximate physical location of each channel's sensor-actuator, whereas Figure A.6 shows (in schematic form) one of the four sensor-actuator assemblies[2].

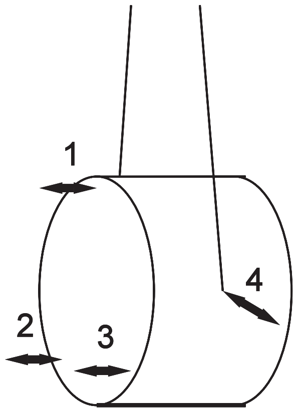

Figure A.5: The approximate physical locations of the four sensors/actuators of each local control channel. The arrows symbolize the directions in which motions are sensed and forces applied.

The suspended mirror does not touch the coil-assembly. That assembly is (in our prototype) rigidly fixed on the ground plate. Glued onto the mirror there is a small, strong, permanent magnet and a black 'flag' that protrudes into the shadow-sensor. The position of the mirror relative to this assembly is sensed with the LED lamp and the photodiode PD in Figure A.6. At the normal operating point, the flag blocks half of the light from the LED that could maximally fall onto the photodiode PD. The LED is driven from a constant-current source. Forces are applied by sending a current through the coil. If the geometry of the coil-magnet system is designed such that the gradient of the magnetic field at the permanent magnet is constant, the applied force is (to first order) *independent of the actual distance* between the mirror and the coil assembly [Rüdiger, Winterflood95]. Then ground motion is *not* coupled to the mirror (in first order[3]). This is one of several important subtleties in the design of the local

---

[2] These units are sometimes also (slightly incompletely) called 'shadow sensors'.

[3] It is even possible to design the system such that ground motion is not coupled to the mirror to *second* order [Rüdiger].

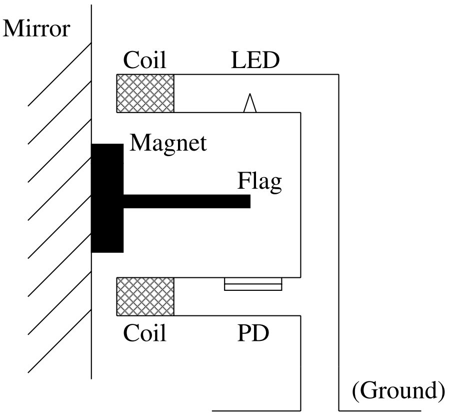

Figure A.6: Schematic picture of a 'shadow-sensor' (i.e., more precisely, a sensor-actuator assembly for one channel of a local control). The gap between the mirror and the coil is a few mm.

controls.

The next important point is the frequency response of the electronic feedback system. The loop needs to have some gain at the pendulum resonance (which is around 1 Hz). At DC, however, there must be no feedback, since the LED-photodiode combination is not a useful sensor for the absolute position and orientation of the test mass, which are determined by requirements of the whole interferometer (i.e. *not* local). At higher frequencies, in particular in the measurement band (from around 100 Hz upwards) there must be no feedback either, because for these frequencies the test-mass is supposed to be a free mass and also because with any feedback intolerable amounts of extra noise would be coupled to the mirror. Therefore the open-loop gain of the feedback loop is designed such that there is gain only in about one decade of frequency, centered around the pendulum resonance. At higher frequencies there are carefully designed filters that block all signals. It is also important that the coils are driven from current sources which have a high output impedance, such that the eddy-current damping (which would otherwise be active at all frequencies) is minimized.

Thanks to the negative feedback, each such assembly acts as a local damper which is, however, only active at frequencies near the pendulum resonance and only in one direction. The combination of four such channels, as shown in Figure A.5, damps all possible motions of the mirror. Electrically the four channels are completely independent from each other. During operation their signals are, however, coupled to each other by the motion of the test mass.

In the prototype, the three channels labelled 1, 2 and 3 in Figure A.5 are also used to apply signals for the non-local ('global') control of the interferometer. There are longitudinal control signals, which are fed equally to all three channels, and alignment control signals which are applied in the proper linear combinations. They are derived from the respective longitudinal loops (see e.g. Section 1.6) and alignment loops (Section 2.7).

Electronically, these global control signals are added to the input of the current driver in the appropriate channels. The frequency range where these channels are used is usually much wider than just around the pendulum resonance. In particular, DC signals are also applied (for example, to maintain the alignment of the interferometer). In the prototype, also faster signals are applied (up to 1 kHz for the Michelson control).

For each component there are analog circuits that convert three input voltages for the longitudinal position, rotation and tilt of the component into the proper linear combinations that control the coil currents. For the end mirrors, there are 'differential' and 'common'-mode inputs, which are added and subtracted to produce the appropriate signals for each mirror.

Fortunately the transfer function of these control inputs have a simple shape. They typically behave like two-pole low-pass filters with frequencies of around 1 Hz and pole Qs of around 0.7 to 3 (see Figure 2.8 for an example). The low effective Q results from the interaction with the local control. This approximation is valid up to around 5 kHz. At higher frequencies there are internal resonances of the test masses which make the transfer function more complicated. Since these resonances never presented a practical problem during this work, they are not treated here (but see Section 1.10.3 and Figure 1.60).

This concludes the discussion of the local controls used in the prototype. For GEO 600, more sophisticated suspensions will be used, which also include local control channels that sense and act between a suspended 'reaction mass' and another part of the multistage pendulum.

One of the end mirrors in the prototype (M_1 in Figures A.15 and 1.29) has three extra coils (also acting on the three magnets already present) that are used with separate current drivers to apply longitudinal calibration signals to the interferometer. For a long time they had been driven via a 375 Hz band-pass filter and had been used only for the 375 Hz calibration. For the detuned dual recycling experiment, however, broadband current drivers were installed and used up to 120 kHz (see Section 1.10.3).

A.4 Optical parameters of the 30 m prototype

The most important parameters of the prototype are shown in Figure A.7.

The average ('common mode') armlength is 30.66 m (measured to a precision of approximately 1 cm via the PR cavity free spectral range). The armlength difference is 6 cm, accurate to about 1 cm. Experimentally, the armlengths were first made equal by applying a strong Schnupp modulation to a simple Michelson (without recycling) locked on *mid-fringe* (see Figure A.8) and moving the end mirror in steps until no more modulation was visible at the output. (The relatively low estimated precision of that measurement comes from drifting spurious AM in the Pockels cell, which caused offsets in the output, together with other offsets caused by RF pickup.) The East mirror was then moved inwards by 6 cm.

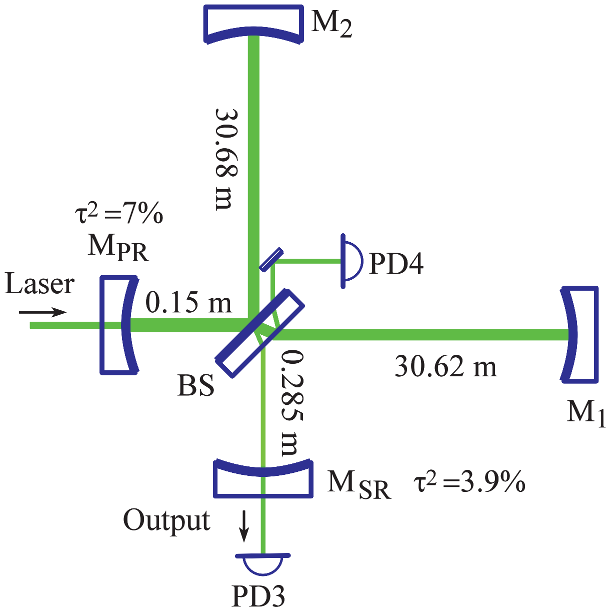

Figure A.7: Important optical parameters of the 30 m prototype in the dual recycling configuration.

The distances from beamsplitter to $\mathrm{M_{PR}}$ and $\mathrm{M_{SR}}$ were determined by direct measurement to a precision of 1 cm (estimated) and found to be 15 cm and 28.5 cm, respectively. These distances were more or less fixed by constructional constraints, although, in principle, they could be changed in the prototype with some effort (see also Section 1.11).

The PR cavity is 30.807 m long and has a FSR of 4865.6 kHz, the second harmonic being at 9731 kHz. Since this length was directly measured via the FSR (see Appendix A.6), its estimated precision is better than 1 mm.

The power transmission of the PR mirror $\mathrm{M_{PR}}$ was measured to be $T_{\mathrm{PR}} = 7\,\%$, corresponding to an amplitude reflectivity of $\rho_{\mathrm{PR}} = 0.9643$. At the proper operating point the losses of the PR cavity are dominated by this 7 % transmission, and hence the cavity can be treated as strongly overcoupled. Using the results from Appendix D, the finesse is $\mathcal{F} = 2\pi/T = 90$ and the power buildup $4/T = 57$. The FWHM bandwidth is $\mathrm{FWHM_{PR}} = 54\,\mathrm{kHz}$.

Similarly the SR cavity is 30.942 m long and has a FSR of 4844.4 kHz, the second harmonic being at 9689 kHz. The power transmission of the SR mirror $\mathrm{M_{SR}}$ was measured to be $T_{\mathrm{SR}} = 3.88\,\%$, corresponding to an amplitude reflectivity of $\rho_{\mathrm{SR}} = 0.9804$ (see also Section 1.8.2). Again, at the proper operating point the SR cavity can be treated as strongly overcoupled. Its finesse is $\mathcal{F} = 2\pi/T_{\mathrm{SR}} = 162$ and its FWHM bandwidth is $\mathrm{FWHM_{SR}} = 30\,\mathrm{kHz}$.

The Rayleigh range of the transverse eigenmode of both SR and PR cavities can easily be computed from the given data (cavity length $L \approx 30.9\,\mathrm{m}$, flat front mirror, rear curvature radius $R = 33\,\mathrm{m}$) to be

$$z_\mathrm{R} = \sqrt{L(R-L)} = 8.1\,\mathrm{m}, \tag{A.1}$$

which corresponds to a beam diameter at the waist (at $\mathrm{M_{PR}}$ and $\mathrm{M_{SR}}$) of

$$2\,w_0 = 2\sqrt{\frac{\lambda\,z_\mathrm{R}}{\pi}} = 2.3\,\mathrm{mm}, \tag{A.2}$$

and a beam diameter at the end mirrors of

$$2\,w(L) = 2w_0\sqrt{1+\frac{L^2}{z_\mathrm{R}^2}} = 9.1\,\mathrm{mm}. \tag{A.3}$$

When we first implemented Schnupp modulation, we decided on a Schnupp modulation frequency near the *second harmonic* of the free spectral ranges of the PR and SR cavity (i.e. near 9.7 MHz), because several pieces of electronics for that frequency had been available from earlier experiments. The error signals that are generated with the help of the Schnupp modulation do change when different harmonics are chosen (see Section 1.5.4).

A.5 Calibration procedures

Calibration in this section means finding the proportionality factors between measured signals (e.g. voltages at a mixer output) and the corresponding physical quantities (such as displacements, angles etc.). Various such calibrations have been carried out at the prototype at one time or another, many of them only as rough estimates. One problem is that almost all signals that are derived optically or interferometrically do depend on various parameters of the system (in particular, light levels) that are neither constant during one experiment (due to drifts in laser power, alignment etc.) nor from one day to the next.

Furthermore many interesting signals are needed and used as error signals for feedback loops, such that the signal is reduced depending on the loop gain, which again depends on light levels, etc. Some consequences of this complication are discussed below.

For brevity, this section only describes three important calibrations that have been carried out repeatedly. The first one is for the single most important signal in the whole interferometer, the Michelson phase.

A.5.1 Michelson calibration

The Michelson output signal appears at the output of mixer **Mix3** in Figure 1.29. It is used as the error signal for the dark fringe lock. In operation, that loop typically has a bandwith of a few hundred Hz (see Section 1.6.2.3). External disturbances to the Michelson phase at lower frequencies appear in the correction signal of that loop (i.e. the voltage which is fed back differentially to the end mirrors). In the prototype this low-frequency signal is monitored on an oscilloscope for curiosity, but is not really used. In GEO 600, such signals might, however, as a by-product contain interesting information for geologists or seismologists.

The useful frequency band for gravitational-wave detection starts at about 50 Hz. In the prototype, frequencies above about 500 Hz were typically looked at. In GEO, the lower limit is expected to be between 50 and 100 Hz. Signals at frequencies above the loop bandwidth appear in the Michelson error signal. If signal frequency and loop bandwidth are close to each other, the error signal is partially suppressed and additionally phase-shifted. If that happens in GEO, digital data processing facilities must analyze both the error signal and the correction signal and try to reconstruct the underlying stimulus.

In the dual-recycled prototype, only signals *above* the loop bandwidth were used for the calibration described here, such that all observed signals appeared essentially completely in the error signal.

The required calibration information generally consists of two parts: The frequency response and an overall absolute factor. In the prototype, the frequency response is essentially given by the optical response of the dual-recycled interferometer[4]. In broadband operation, this behaves like a one-pole low-pass filter with a corner frequency of 15.4 kHz (see Figure 1.19 and Section 1.5). Photodetectors, mixers etc. all have a bandwidth larger than that, and thus the frequency response can be considered flat for those frequencies that were measured (up to 5 kHz).

The absolute factor is more problematic. It depends on a multitude of factors (light levels, alignment, loop gains, etc., remember also Figure 1.40 and the problems with offsets), which cannot really be considered constant in the prototype. Hence the only way to obtain a reliable calibration for the output signal is to apply a stable and well-known test signal to the interferometer and measure its amplitude in the output signal. This was exactly what was done in the prototype (see Figures A.17, 1.51 and A.10).

The test signal was applied via the extra set of coils (described at the end of Appendix A.3.1) that are mounted behind end-mirror M_1. The three coils are driven by three dedicated wide-band current drivers that share the same input signal. A sine wave signal of constant amplitude and frequency is applied to that input. The calibration frequency used most often was 375 Hz. Later calibrations have also used a 4.9 kHz signal, which is better because it is much further above the bandwidth of the dark-fringe lock and there is less noise at that frequency. The frequency should be chosen in a range where there are no special features such as mirror resonances nearby.

For GEO 600, the tiny oscillating radiation pressure caused by a chopped low power

---

[4] Interesting things happen in a detuned interferometer that is operated in narrowband mode with a center frequency that is *below* the loop's unity-gain frequency. The information then appears in the correction signal with its own frequency response that will usually *not* have a peak at the center frequency. Signals near the center frequency hence do not appear amplified. Due to the increased optical gain, however, the effect of the shot-noise is reduced at the interferometers center frequency, and the signal-to-noise ratio is thus increased as expected.

laser beam (e.g. from a He-Ne laser) reflected off one end mirror may already produce a sufficiently strong calibration signal [Rüdiger].

Under these circumstances the amplitude of the mirror motion caused by the test signal can be considered constant. Now the only missing factor is its amplitude in physical units. It was determined by the following independent optical measurement:

Starting with a well-aligned interferometer, both recycling mirrors ($\mathrm{M_{SR}}$ and $\mathrm{M_{PR}}$) are misaligned far enough that they act as simple attenuators. Then a simple Michelson interferometer remains. Nothing is changed at the end mirrors, in particular the test signal is left untouched.

The light power at the output port (dark fringe port) is measured with a broadband photodiode (no modulation is used in this measurement). Another photodiode (PD6 in Figure 1.29) measures the injected light power, the main variable quantity during this calibration experiment. Both signals are fed to the simple circuit shown in Figure A.8.

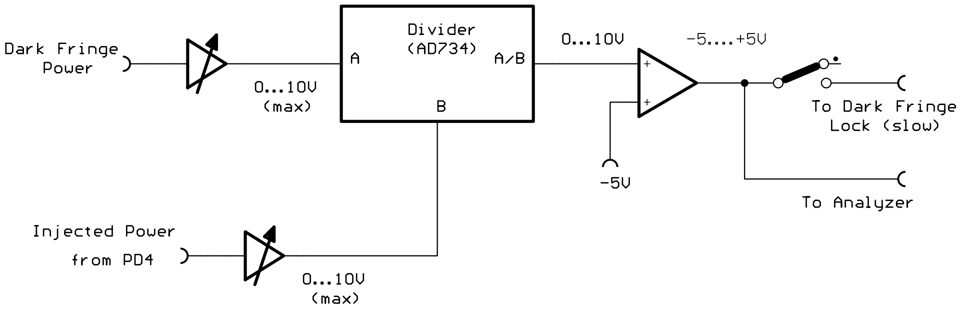

Figure A.8: Schematic of the circuit used for the Michelson calibration ('mid-fringe lock').

After appropriate scaling, the signal for the dark fringe power is divided by the injected power in an analog divider (AD734 in 'direct division mode'). The circuit can be adjusted such that the divider output swings between 0 and 10 V, independent of the injected light power. Small variations of the Michelson phase (such as the test signal) cannot directly be measured from that signal in the dark-fringe condition (see Section 1.1.3). Since complicated modulation methods are exactly what is to be avoided, the dark fringe cannot be used, and 'mid-fringe' is used instead. For that purpose, a constant voltage of 5 V is subtracted from the signal, which thus swings between −5 V and +5 V. This is used as error signal for the usual Michelson feedback, with the gain adjusted such that the interferometer stays very close to the mid-fringe condition, yet without suppressing the test signal.

Figure A.9 shows the output signal as a function of the total pathlength difference p between the two interfering beams. It is given by

$$U = 5\,\mathrm{V} \cdot \sin\left(\frac{2\pi\, p}{\lambda}\right). \tag{A.4}$$

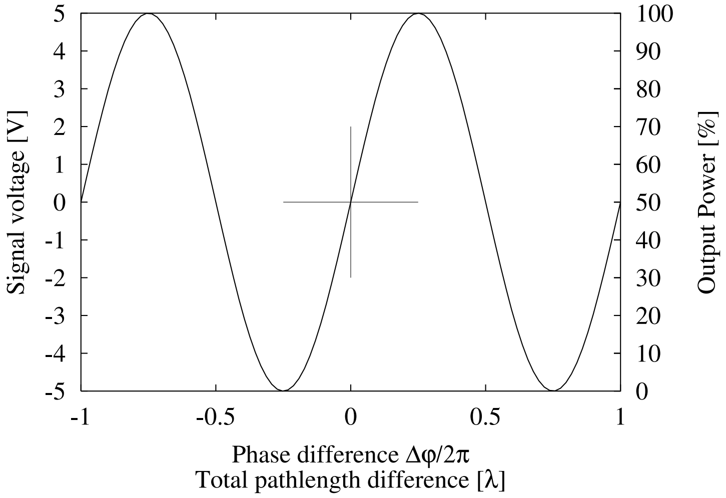

Figure A.9: Output signal of the ‘mid-fringe lock’ circuit shown in Figure A.8.

The derivative $\partial U/\partial p$ is maximal at mid-fringe and is then given by

$$\frac{\partial U}{\partial p} = 5\,\mathrm{V} \cdot \frac{2\pi}{\lambda}, \tag{A.5}$$

and a small variation δU in the output voltage can be converted into total pathlength difference by

$$\delta p = \frac{\lambda}{2\pi \cdot 5\,\mathrm{V}}\,\delta U \tag{A.6}$$

In this state, the amplitude of the test signal at the output is measured with a spectrum analyzer. A typical spectrum analyzer (in our experiment, a HP3562A was used) has some settings that become important in the calibration. The first one is the ‘window function’ [Harris78, HP]. For a measurement such as this one where we want to determine the amplitude of a sharp spectral peak, it is best to use the ‘flat top’ window. Other windows, such as Hanning, can produce an error in the amplitude (a few dB at most), if the peak happens to fall in between two frequency bins.

Other important settings concern the display units of the spectrum analyzer. First there are ‘Volts (peak)’ and ‘Volts (rms)’, which are related to each other by a factor of $\sqrt{2}$. Another, more important, distinction exists between an amplitude spectrum (with the units Volt) and a linear spectral density (with the unit Volt/$\sqrt{\mathrm{Hz}}$). The conversion factor between these is the square root of the analyzer’s effective bandwidth, which should be read from the analyzer status display. The effective bandwidth depends not only on the width of a frequency bin, but also on the window function.

The amplitude spectrum is suitable to determine the amplitude of sharp peaks, as in this experiment. The linear spectral density, on the other hand, is suitable for continuous noise spectra, such as white noise.

In an actual example, a constant 4.9 kHz calibration signal (400 $\mathrm{mV_{rms}}$ stimulus) produced an output signal of 48.6 $\mu\mathrm{V_{rms}}$. Using Equation (A.6) this can be converted into the amplitude of the oscillation in the total pathlength difference, which is found to be 795 $\mathrm{fm_{rms}}$. The actual motion of the mirror is only half that value, but this is not important for the calibration.

This concludes the measurement of the test signal, which can now be used to calibrate the output signal of the interferometer in other states, such as dual recycling. As an example, Figure A.10 shows a typical such measurement (in broadband dual recycling mode).

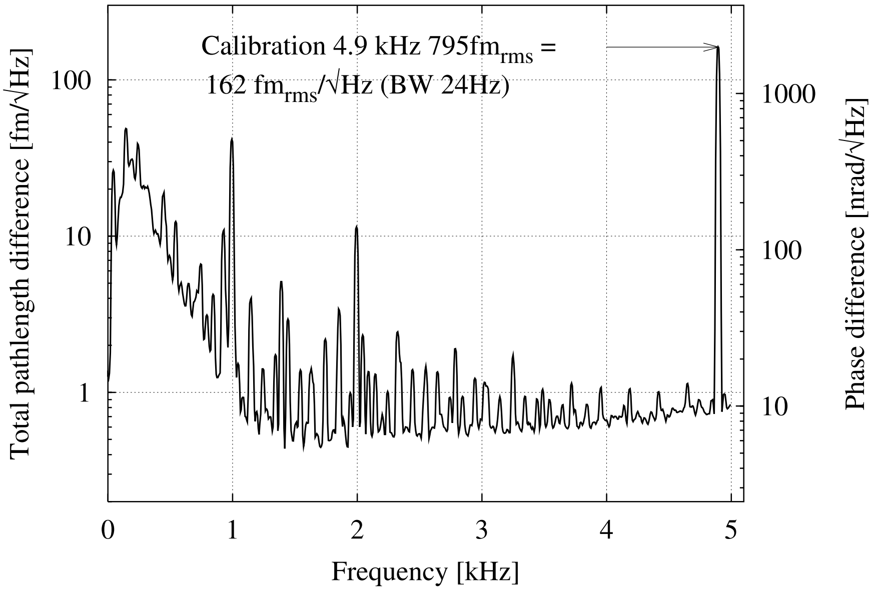

Figure A.10: A typical output spectrum of the dual recycled interferometer with the 4.9 kHz calibration signal. There are various noise peaks of technical origin visible in the spectrum, which were being investigated when this measurement was made.

Since in these measurements we are interested both in peak amplitudes (for the calibration) and in a linear noise density (for the noise floor), care must be taken concerning the display unit of the spetrum analyzer. The peak amplitude of the calibration signal can be found in a separate measurement or by setting the appropriate display unit and recording the result. The noise floor, on the other hand, must be displayed (or recorded) as linear noise density.

If only one measurement is made and recorded for later evaluation, it is essential that the effective bandwidth of the spectrum analyzer is recorded. In the example shown in Figure A.10, it was 24 Hz. (Note that due to the flat-top window, this is 3.8 times wider than the bin width, 6.25 Hz.) The known amplitude of the calibration peak (795 fm) is converted to the units of the plot by division by the square root of the bandwidth, as written in the Figure. The factor to convert from total pathlength difference to phase difference is given by $2\pi/\lambda$.

A.5.2 Frequency noise calibration

Another important calibration concerns the frequency noise of the laser with respect to the power recycling cavity (see Section 1.6.1.2 and Figure 1.34). It can be measured at the output of mixer **Mix2** in Figure 1.29. This is in fact the error signal for the PR cavity lock. Here we are not concerned with the interpretation of that signal, but only with its calibration. Figure A.11 shows the relevant parts of the loop, with an adder inserted between loop filter and the VCO's input.

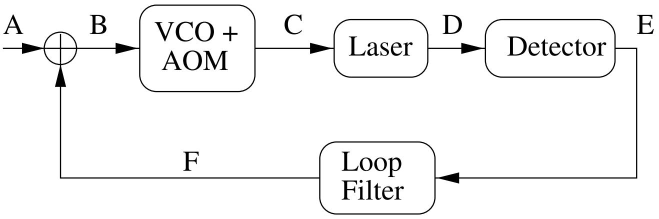

Figure A.11: Schematic of the relevant parts for the calibration of the frequency noise measurement.

Starting from the left, the VCO/AOM converts a voltage into a frequency shift. Its frequency response is known to be flat up to 10 kHz (see Figure 1.32), and the efficiency can be determined statically by measuring the VCO behaviour. Doubling this value yields the efficiency of the double-passed AOM as an actuator for the laser frequency, which was found to be 4.5 MHz/V. In other words, we know the transfer function from point **B** to point **D** in Figure A.11.

The box labelled 'Detector' comprises the PR cavity together with the resonant photodetector and mixer, which together produce the Pound-Drever-Hall error signal (see Figure 1.30). Its transfer function is also known to be flat up to at least 10 kHz, but its efficiency (in V/Hz) is still unknown. Since we can only measure at point **E** in Figure A.11, and want to refer the result to point **D**, it is just this missing efficiency that we need.

This efficiency was determined by a separate measurement, which made use of the adder in Figure A.11. If signals are added at point **A**, they are partially suppressed by the frequency-dependent loop gain. Measuring a transfer function from point **A** to any other point in the loop is therefore not useful for our present purpose. We can, however, measure the transfer function from point **B** to point **E** if the injected test signals can be separated from the noise that is added by other parts of the loop. This measurement was first done with a function generator at a few frequencies. The results were however, so badly reproducible that a full transfer function was measured from point **B** to point **E** instead, using the HP3562A spectrum analyzer. The result also showed also some variations, and only at a few frequencies were the injected signals large enough to provide sufficient coherence for the measurement. For the measurement shown below, this factor thus found was 400. Now that we know the transfer functions D/B = 4.5 MHz/V and E/B = 400, we can determine the missing factor D/E and find it to be 11 kHz/V.

Figure A.12 shows one frequency noise measurement that was calibrated with the procedure described so far. Here the noise is somewhat lower than in Figure 1.34, because for this measurement everything had just been readjusted for maximum light levels at the reference cavity, and the gain of both the first and the second loop had been increased to the limit just before oscillation occurred (the resonances of the piezo SPZT begin to show up near 10 kHz, and an oscillation of the second loop is sometimes flickering up near 50 kHz). For stability, the loop gain was somewhat reduced in normal operation.

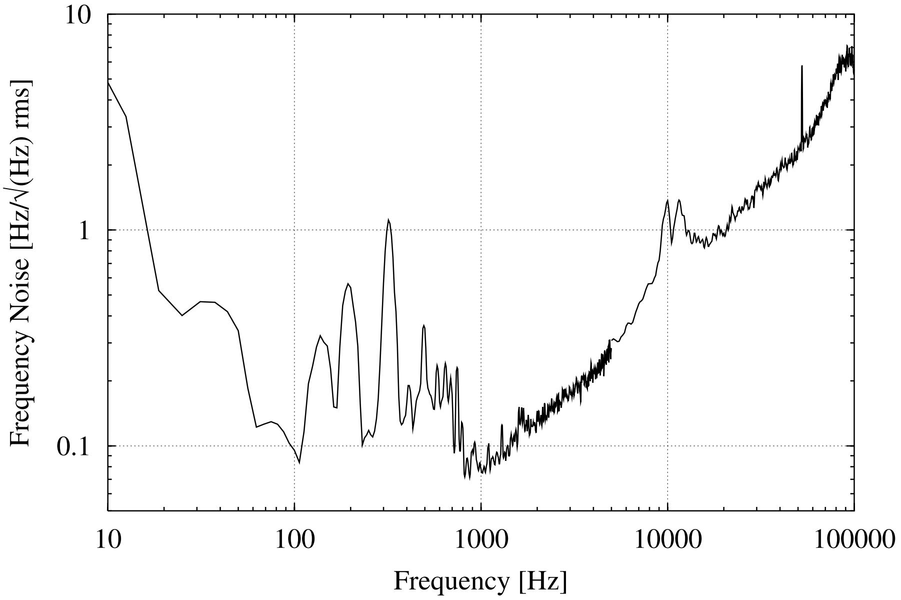

Figure A.12: Frequency noise of the laser light with respect to the power recycling cavity, with the interferometer locked in broadband dual recycling mode.

A.5.3 Calibration of the autoalignment loops

This section describes the calibration procedures that were used during the development and characterization of the autoalignment system. The simple model shown in figure A.13 was used to represent one channel of the autoalignment system.

It begins with the pendulum with the transfer function $H_{\mathrm{P}}(s)$ (Equation (2.54)), defined as the ratio of the actual movement of the respective beam to the input at the appropriate local control module. While the frequency response can be measured directly (using, e.g., the autoalignment error signals while the respective loop is disabled),

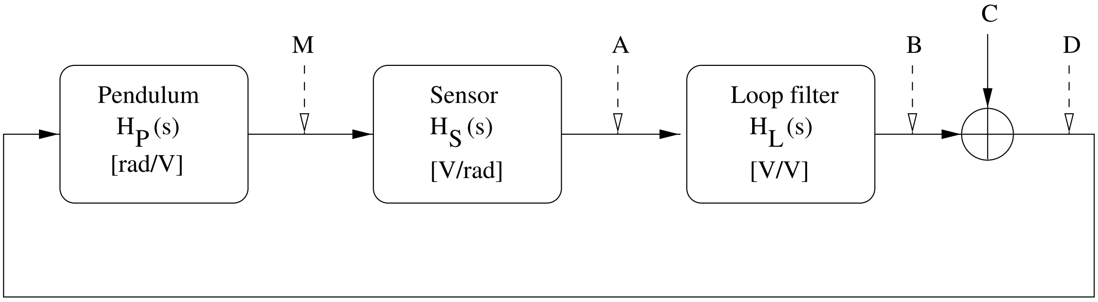

Figure A.13: Simple loop model used for the calibration of the autoalignment system.

the constant factor A_P must be determined separately. For the end mirrors, this measurement was done by misaligning $\mathrm{M_{PR}}$ such that a single-bounce Michelson remained, switching off all autoalignment loops and locking the Michelson to a dark fringe. Then a series of increasing voltages was applied to the input in question, and the deterioration of contrast (increasing light power at PD3) was measured. These data were then fitted to an appropriate model (which needs as further input the beam radius at the waist). The missing factor A_P could then be computed from the fitted parameters. These results were in reasonable accordance with an less precise earlier measurement, where the deflection was directly measured. The factor A_P for $\mathrm{M_{PR}}$ was also determined by such a direct deflection measurement.

The sensor transfer function H_S includes all optical effects, electronic gains of preamplifiers, mixers etc. such that it represents the ratio of the error signal to the angular misalignment between the respective beams. We assume this transfer function $H_\mathrm{S}(s)$ to be flat for all frequencies of interest, i.e. $H_\mathrm{S}(s) \equiv A_\mathrm{S}$.

The transfer function of the loop filter, $H_\mathrm{L}(s)$, is known by its design or can be measured directly. For the calibration measurements described here, a unity-gain adder was inserted into the loop in question. We then have the point **C** available as input, and the three points **A**, **B** and **D** as outputs, where measurements can be made. With all transfer functions known we can then compute noise spectra etc. referred to the point **M**, which is not directly accessible but which represents the most interesting quantity in the experiment (angle between wavefronts).

For the first type of measurement, which allows to determine the pendulum frequency response (f_P and Q_P) as well as the sensisivity A_S of the sensor, we add a test signal (e.g., white noise from the spectrum analyzer) at **C**, which is partially suppressed by the loop. We then measure the transfer function from point **D** to point **A**, which we call $H_2(s)$ and which is composed of H_P and H_S

$$H_2(s) = \frac{V_\mathbf{A}}{V_\mathbf{D}} = H_\mathrm{P} H_\mathrm{S} = \frac{A_\mathrm{P} A_\mathrm{S}}{1 + \dfrac{s}{\omega_\mathrm{P} Q_\mathrm{P}} + \dfrac{s^2}{\omega_\mathrm{P}^2}} \tag{A.7}$$

By fitting this transfer function to the model (2.54) we can determine the parameters $\omega_\mathrm{P} = 2\pi f_\mathrm{P}$, Q_P and A_S.

For the second type of measurement, which allows to determine the open-loop gain and unity-gain frequency, we also add a test signal at **C**. Now, however, we measure the transfer function from point **C** to either point **D** or to point **B**. Both of these alternatives usually yield similar results. If we call the open-loop gain $H_{\mathrm{OLG}}(= H_{\mathrm{P}} H_{\mathrm{S}} H_{\mathrm{L}})$, we thus measure

$$\frac{V_{\mathbf{D}}}{V_{\mathbf{C}}} = \frac{H_{\mathrm{OLG}}}{1 - H_{\mathrm{OLG}}} \quad \text{or} \quad \frac{V_{\mathbf{B}}}{V_{\mathbf{C}}} = \frac{1}{1 - H_{\mathrm{OLG}}}, \tag{A.8}$$

and we can directly compute H_{OLG} from these measurements, which are usually most reliable around the unity gain frequency of the loop, where they also are most interesting. If necessary, the measured curves can be extrapolated to other frequencies using the known transfer functions H_{P} and H_{L}. The figures 2.9 and 2.10 were produced in this way.

A.6 Measurement of the PR cavity length

The length of the PR cavity could be determined very precisely with a direct optical measurement. For this purpose, the signal recycling mirror was misaligned such that a power-recycled interferometer without signal recycling remained. It was locked (on the dark fringe of the Michelson and the resonance of the PR cavity) with the normal circuits (see Sections 1.6.2.3 and 1.6.3.2) by increasing the Michelson gain.

Then a phase modulation near 4.8 MHz was applied via Pockels cell PC1 in Figure 1.29. The light reflected from the PR cavity is detected with a wideband photodetector. The measurement is controlled by a network analyzer. The measurement frequency is swept from 4.855 to 4.875 MHz. The source drives the Pockels cell, and the detected photocurrent is coherently demodulated by the analyzer. The result of such a measurement is shown in Figure A.14.

In a perfect interferometer locked exactly on its nominal operating point, a pure phase modulation should in theory yield no AM in the reflected light. But, in practice, the modulation in the Pockels cell has some AM components, and the operating point has small offsets from its theoretical value. Any of these effects yields a signal with a minimum at the FSR. The measured data was fitted (with LISO) to a model of a band-stop filter (also shown in Figure A.14). The resulting estimated center frequency was 4.865577 MHz with an estimated standard deviation of 7 Hz.

Because the effect that leads to the signal was not exactly identified, the accuracy of 7 Hz was not fully trusted (it would correspond to a length error of 0.05 mm). But, nevertheless, the length of the PR cavity could thus be estimated as 30.8075 m with a precision of certainly better than 1 mm. Note that this is the optical pathlength, which includes the effect of passing through the beamsplitter substrate. This value formed the fundamental armlength measurement in the prototype, from which all other lengths were derived (see Appendix A.4).

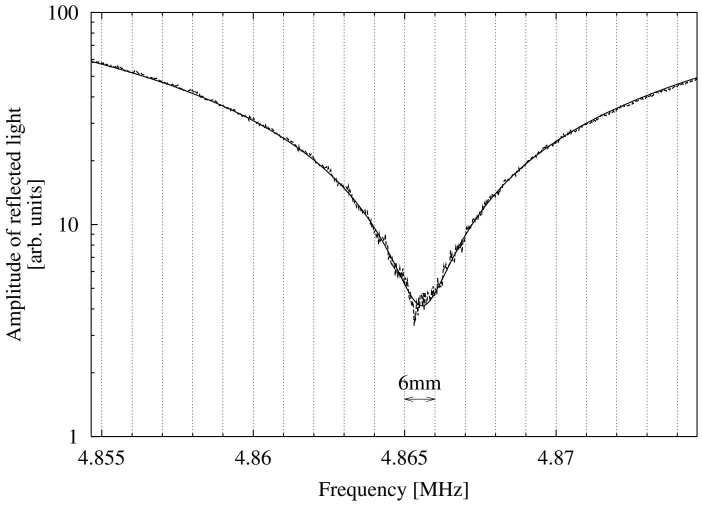

Figure A.14: Resonance of the PR cavity at its first FSR (measured data and fitted curve).

A.7 External modulation

This Section discusses experimental details and results of the experiments with external modulation at the Garching 30 m prototype, which were carried out during the first half of this work.

A.7.1 External modulation: control of the Mach-Zehnder phase ψ

As we have seen in Section 1.3.2, the Mach-Zehnder phase ψ needs to be controlled and thus an error signal must be generated.

First consider the output signal (Equation (1.37) on page 23) in the locked case, i.e. $\varphi \approx 0, \psi \approx 0$. It is proportional to

$$\sin\frac{\varphi}{2}\cos\psi. \tag{A.9}$$

This is a useful error signal for the Michelson phase φ, but not for the Mach-Zehnder phase ψ. For the latter we would like a signal proportional to ψ or $\sin\psi$ instead of $\cos\psi$. This would, however, not yet be sufficient because the $\sin\varphi$ factor would still cause the signal to vanish at the proper operating point. We hence would like to replace $\sin\varphi$ by a constant or $\cos\varphi$.

As discussed in Section 1.1.3, we can effectively obtain the derivative of a measured quantity with respect to one of its parameters by modulating the parameter at a constant frequency and then coherently demodulating the resulting signal. In order to control ψ we make use of this principle twice to obtain the mixed second derivative of the output signal (see Equation (1.37))

$$u_{\mathrm{MZ}} = \frac{\partial^2 u_1}{\partial\varphi\,\partial\psi} = \frac{1}{\sqrt{2}}\,c_1\,c_{\mathrm{LO}}\,J_1(m)\cos\frac{\varphi}{2}\sin\psi, \tag{A.10}$$

which has all the desired properties.

The signal u_1 is the demodulated photocurrent in the main detection photodiode. We now need two more modulation-demodulation procedures to obtain u_{MZ}. Both the Michelson phase φ and the Mach-Zehnder phase ψ must be modulated sinusoidally with a small modulation index.

A.7.2 Experimental realization of the Mach-Zehnder control

An overview of the 30 m prototype with external modulation is given in Figure A.15.

In the 30 m prototype the Michelson phase φ had for a long time been modulated at 375 Hz for calibration purposes. The modulation was applied via three small magnets (glued onto one end mirror) and coils nearby which were driven with the 375 Hz signal through a current driver (see also Appendix A.3.1). The amplitude of the mirror motion was a few picometers. This provided the first modulation necessary for the Mach-Zehnder control (to obtain $\partial u_1/\partial\varphi$).

The second modulation (of ψ) had traditionally been done at a lower frequency (85 Hz) by mechanically dithering the recombination plate RP. With two small magnets glued on the recombination plate and two coils driven in antiphase near the magnets, a tiny rotation of the recombination plate around an axis perpendicular to the page in Figure 1.15 could be obtained, which changed the Mach-Zehnder phase ψ. The current through the coils was both modulated at 85 Hz and used for feeding back the control signal at lower frequencies and DC.

That system worked, but not very well, the deficiencies being associated with noise and bandwidth. Since any demodulated signal is low-pass filtered shortly after the mixer, the 85 Hz demodulation must take place after the 375 Hz demodulation. As can be seen from the prototype noise spectra (see e.g. Figure A.17), the Michelson output is very noisy near 375 Hz. Thus the signal after the 375 Hz demodulation contains excessive noise, up to and including 85 Hz. The second demodulation then produces an even noisier signal, which needs heavy low-pass filtering to reduce the noise amplitude. This again limited the useful loop bandwidth for the Mach-Zehnder loop to less than 1 Hz, which was just marginally sufficient to reduce the Mach-Zehnder phase fluctuations to a level where they were small enough not to throw the interferometer out of lock. The remaining Mach-Zehnder phase flucuations were estimated to be in the order of $0.1-0.5$ rad (rms). They were dominated by differential rotational motion between beamsplitter and recombination plate, acting like a pendulum with 0.3 Hz resonance frequency and a Q of around 3. Acquisition of lock was not easy because of the slow reaction of the Mach-Zehnder loop.

Hence another modulation frequency was introduced for ψ. It was chosen to be well above 375 Hz, in a region where the interferometer output is much quieter. It was no

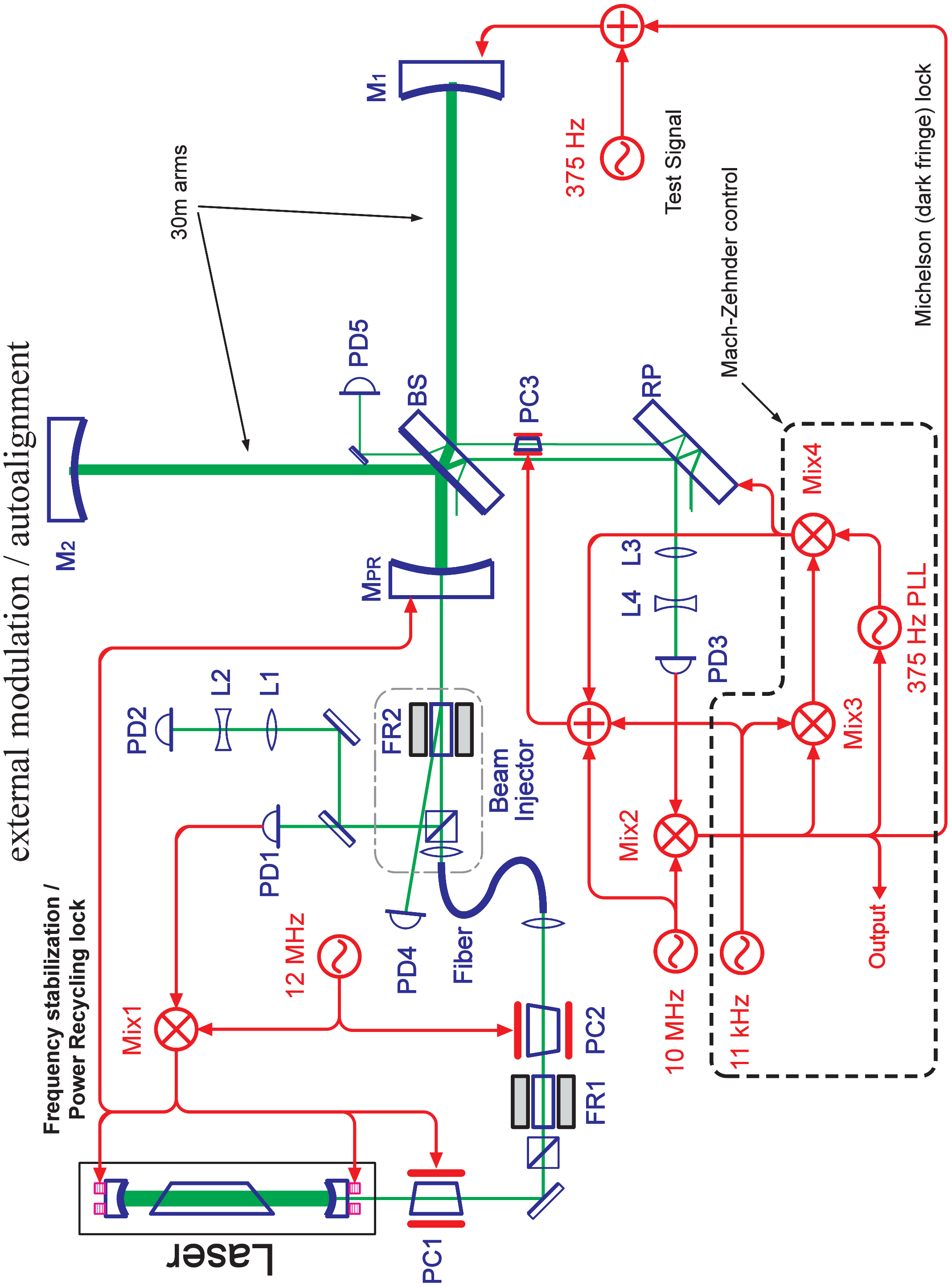

Figure A.15: Overview of the 30 m prototype with external modulation.

longer possible to apply this fast modulation mechanically to the recombination plate. Instead, it was added to the suspended Pockels cell PC3, via a ±120 V high-voltage amplifier. The frequency chosen was 11 kHz. Of course, now the order of demodulations had to be reversed. The resulting Mach-Zehnder error signal was much quieter, and a loop bandwidth of around 10 – 20 Hz was obtained, making the Mach-Zehnder lock tighter and helping lock acquisition. The fast components of the correction signal were fed back to the Pockels cell PC3, whereas the slow components were applied (as a rotational movement) to the recombination plate RP.

In this setup the unity-gain frequency of the Michelson loop could be increased up to around 1000 Hz, causing another unexpected complication. The Mach-Zehnder phase ψ is obtained by first demodulating the output signal at 11 kHz, and again demodulating the resulting signal at 375 Hz. The 375 Hz signal, however, is caused by the Michelson phase modulation, which is suppressed by the respective loop. If the unity-gain frequency of that loop approaches or passes 375 Hz, the signal is suppressed by the loop gain and, even more troublesome, phase-shifted by angles approaching 90°.

To obtain a reliable error signal for the Mach-Zehnder phase, it was thus necessary to take into account the phase shift for proper demodulation. Hence the phase of the 375 Hz signal as it appeared at the output was detected by a phase-locked loop (PLL). As input signal for the PLL the Michelson output was taken, which at the proper operating point contains a strong 375 Hz component with the same phase shift as the 375 Hz component in the 11 kHz demodulated signal. This was used to phase-lock an ICL8038 sine-wave generator, which then served as local oscillator for the final 375 Hz demodulation. A sketch of these loops is shown in Figure A.16.

A.7.3 Experimental results of external modulation

The main part of this work considers the newer system with Schnupp modulation and dual recycling. Therefore this section will briefly discuss the earlier experimental results that have been achieved with external modulation, because they have not been published anywhere else.

Most interesting is the achieved phase (or displacement) sensitivity of the interferometer. It is shown in Figure A.17. It was calibrated as discussed in Appendix A.5.1. The two measured curves shown in Figure A.17 were measured with two different loop gains for the Michelson (dark fringe) lock, such that the unity gain frequencies were below 375 Hz in one case and around (or just above) 375 Hz in the other case.

The predicted shot noise level (also shown in Figure A.17) was computed from the following formula [Winkler97] for the linear spectral density of the phase noise:

$$\tilde{\varphi} = \sqrt{\frac{2q_e}{I_0}} \, \frac{\sqrt{1 + \dfrac{2I_{\min} + 4I_{\mathrm{cam}}}{\rho^2 \, I_0}}}{J_1(m)} \tag{A.11}$$

The formula is already simplified under the assumption that both beamsplitter and the central spot of the recombination plate have an exact 50:50 coating. The meanings of the symbols are:

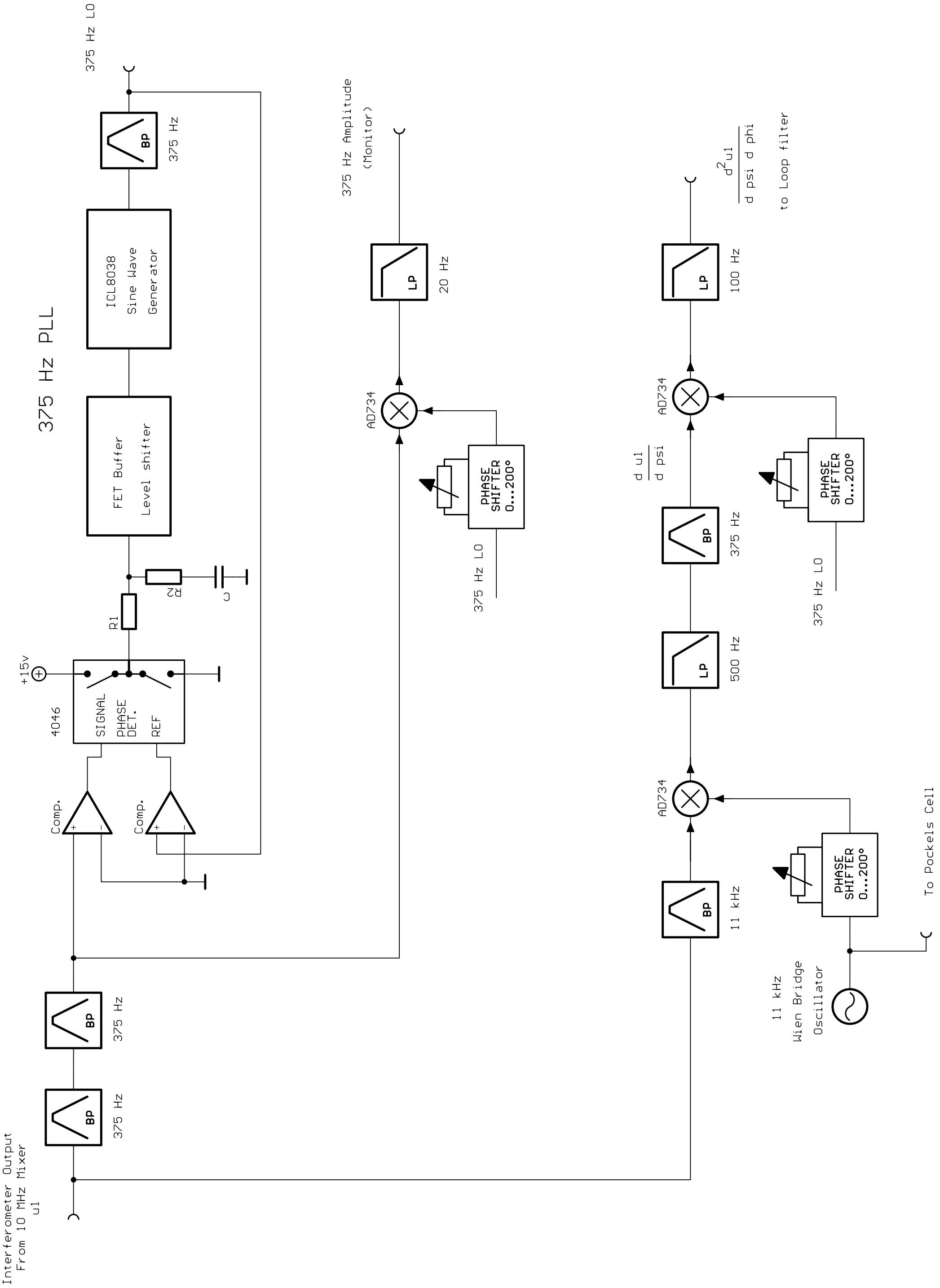

Figure A.16: Simplified diagram of the demodulators used to extract the Mach-Zehnder error signal ψ in the external modulation setup.

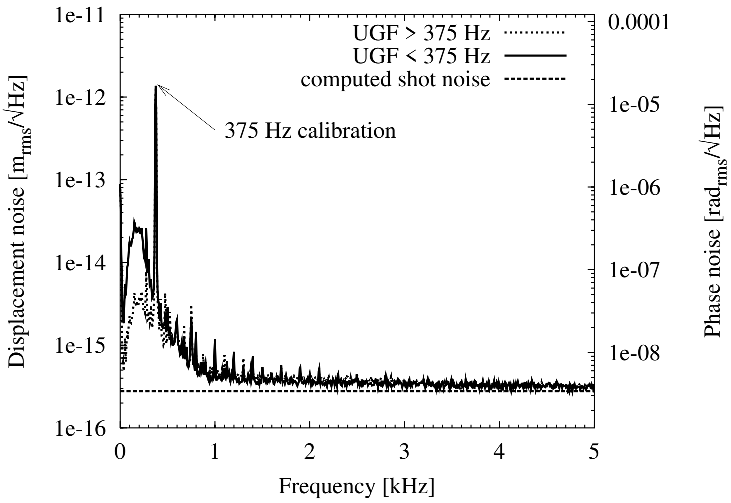

Figure A.17: Sensitivity of the Garching 30 m prototype with external modulation.

q_e is the electron charge, $1.6 \cdot 10^{-19}$ C.

I_0 is the photocurrent equivalent to the light power hitting the beamsplitter (9.74 A).

I_{min} is the photocurrent equivalent to the light power arriving at the dark finge port before the recombination plate (the 'Signal beam' in Figures 1.14 and 1.15). This expresses the contrast of the Michelson. A value of 6 mA has been used for the computation.

I_{cam} is the noise equivalent photocurrent of the photodetector. This value was 100 μA.

m is the modulation index in the Pockels cell PC3 of Figure A.15. Its estimated value was 0.25 rad.

ρ^2 is the power reflectivity of the beamsplitter's rear side (which splits off the local oscillator beam). The value used was 290 ppm.

Plugging in these numbers, formula A.11 becomes:

$$\tilde{\varphi} = 1.8 \cdot 10^{-10} \frac{\text{rad}}{\sqrt{\text{Hz}}} \cdot \frac{2.32}{0.12} = 3.4 \cdot 10^{-9} \frac{\text{rad}}{\sqrt{\text{Hz}}} \,. \tag{A.12}$$

The sensitivity could be improved by a factor of $\sqrt{2}$, if both beams (see Figure 1.15) were detected. This was not done in the prototype. Furthermore it can be seen from Equation (A.12) that the modulation index was too low (this is responsible for the factor $1/0.12 = 8.3$), and the beamplitter rear coating was not optimal for the contrast reached (yielding the factor of 2.32).

A.7.4 Conclusions about external modulation

We can summarize our experiences with external modulation as follows:

As compared to Schnupp modulation (discussed below), the system is far more complex. Two more modulations (375 Hz and 11 kHz in Figure A.15) are needed, which are unnecessary in Schnupp modulation. There is an additional degree of freedom, the Mach-Zehnder phase ψ, which needs to be controlled. This would make lock acquisition in a *dual* recycled system even more complicated than it is anyway (see Section 1.7). Furthermore, the recombination plate is another extra suspended component which requires careful alignment (or even autoalignment). Suspending the Pockels cell (PC3 in Figure A.15) *and* driving it with the high voltage, high frequency, modulation signal is a difficult technical problem with problematic side-effects such as radiation at the modulation frequency and coupling of ground noise through the electrical connections.

In order to come close to the shot-noise limited sensitivity, the level of the local oscillator beam must be carefully chosen. Since it is determined by the reflectivity of AR coating applied to the beamsplitters rear side, it cannot easily be changed (unless one changes the polarization of the injected beam, which is, however, undesirable for other reasons, such as the desire to maintain a particular ratio of transmittance to reflectance at the main beamsplitter). Finally, two beams must be detected.

On the other hand, external modulation has one important advantage: it allows the use of equal armlengths of the Michelson and hence reduces the interferometer's sensitivity to laser frequency fluctuations (see Section 1.8.3).

Appendix B

Electronics

B.1 Photodiode preamplifiers

In a complex interferometer, many light levels need to be detected and to be converted to electrical signals (typically voltages). The most common detector is a photodiode, which has three basic modes of operation: photovoltaic, photoconductive without bias and photoconductive with a reverse bias voltage. In photovoltaic mode, the photodiode is operated as a voltage source into a high impedance, yielding a voltage that is proportional to the *logarithm* of the light power. For this reason, and also for speed and noise reasons, we do not use photodiodes in photovoltaic mode.

In photoconductive mode, on the other hand, the photodiode is operated as a current source into a low impedance. The photocurrent is proportional to the light power. If very low light levels are to be measured, the lowest noise can be obtained with zero bias voltage, at the expense of slow reaction (due to the large junction capacitance). For faster reaction, the junction capacitance can be reduced by applying a reverse bias voltage. All photodiodes in the prototype are operated with a reverse bias voltage.

In the prototype we have found two basic circuit configurations to be useful, which will be briefly introduced. Both of them are based on circuits that have previously been used in Garching and elsewhere.

The *broadband* circuit has a frequency response extending from DC to some corner frequency and is typically used to monitor light levels in some part of the interferometer.

The *tuned* circuit, on the other hand, behaves like a band-pass filter tuned to a preset frequency. It is used to detect the AM component in the light power which is caused by an intentional modulation at a fixed frequency (e.g. the phase modulation applied in a Pound-Drever-Hall system, or the Schnupp modulation).

The two circuits can also be combined to yield a circuit with two output voltages from a single photodiode, the RF component at the modulation frequency, and the DC component with a frequency response from DC to a corner frequency well below the modulation frequency. This section briefly discusses the basic circuits, their frequency response and noise behaviour. For a detailed design it has proven useful to analyze the circuit numerically using Liso (see Appendix C).

B.1.1 Broadband circuit

Figure B.1 shows the basic circuit diagram for a broadband photodiode preamplifier.

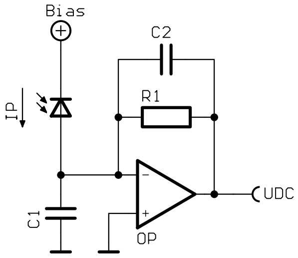

Figure B.1: Basic circuit of a broadband photodiode preamplifier.

The photodiode behaves as a current source yielding the photocurrent I_p. The op-amp is used as a current-to-voltage converter (transimpedance amplifier), with the scaling factor given by the resistor R_1, i.e. the output voltage is $-R_1 I_\mathrm{p}$. Of course, positive output voltages can be generated, if desired, by reversing the polarity of both the photodiode and the bias voltage. The op-amp keeps its inverting input at ground potential and thus keeps the voltage across the photodiode constant. The capacitor C_1 represents the parasitic capacitances (mainly of the photodiode), but can also be an intentional bigger capacitor needed for a tuned detector (see Section B.1.3). The capacitor C_2 will usually be needed to ensure stability of the circuit, and suitable values are computed below.

To analyze the frequency response of the circuit we need to know the frequency-dependent gain of the op-amp. The simplest model, which is, however, often adequate, is given by

$$A(s = \mathrm{i}\,\omega) = \frac{A_0}{1 + A_0 \frac{s}{\omega_\mathrm{T}}}\,, \tag{B.1}$$

with A_0 the DC-gain and ω_T the transit frequency. It is illustrated in Figure B.2. Typical values for a standard bipolar low-noise op-amp such as an OP-27 are $A_0 \approx 10^6$ and $\omega_\mathrm{T} \approx 2\pi \cdot 10\,\mathrm{MHz}$. Op-amps with more complicated open-loop gain structures can be treated by Liso.

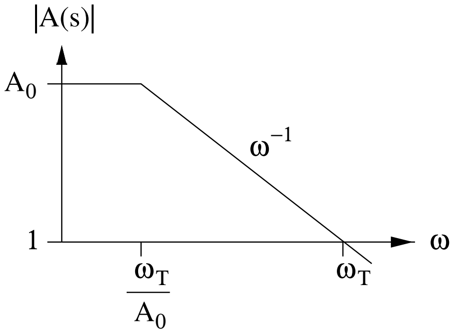

Figure B.2: Simplest model of the open-loop gain of an op-amp.

A straightforward analysis of the circuit yields the transfer function

$$U_{\mathrm{DC}} = -R_1\, I_{\mathrm{p}} \frac{1}{\left(1+\dfrac{1}{A_0}\right) + \left(R_1\, C_2 + \dfrac{1}{\omega_{\mathrm{T}}} + \dfrac{1}{A_0\omega_1}\right) s + \dfrac{s^2}{\omega_{\mathrm{T}}\omega_1}} \tag{B.2}$$

$$\approx -R_1\, I_{\mathrm{p}} \frac{1}{1 + \left(R_1\, C_2 + \dfrac{1}{\omega_{\mathrm{T}}}\right) s + \dfrac{s^2}{\omega_{\mathrm{T}}\omega_1}}, \tag{B.3}$$

where the abbreviation

$$\omega_1 = \frac{1}{R_1(C_1+C_2)} \tag{B.4}$$

has been introduced.

Apart from the expected factor $-R_1 I_{\mathrm{p}}$, we are left with a two-pole low-pass filter, the normal form of which is given by

$$H_{\mathrm{TP}}(s) = \frac{1}{1 + \dfrac{s}{\omega_{\mathrm{P}}\, Q} + \dfrac{s^2}{\omega_{\mathrm{P}}^2}}, \tag{B.5}$$

with the pole frequency ω_{P} and the quality factor Q. By comparing equations (B.3) and (B.5) we find

$$\omega_{\mathrm{P}} = \sqrt{\omega_{\mathrm{T}}\omega_1} \tag{B.6}$$

and

$$Q = \sqrt{\frac{\omega_{\mathrm{T}}}{\omega_1}} \frac{1}{1 + R_1\, C_2\, \omega_{\mathrm{T}}}. \tag{B.7}$$

If C_2 is omitted (as is mostly seen in textbook circuits[1]), the frequency response may have a distinct peak at ω_{P} and the circuit may be unstable. The peak Q can usually be

---

[1] The only exceptions known to the author are Burr-Brown's data sheet for their OPA655 op-amp and [Horowitz–Hill, Fig. 15.45] (also taken from Burr-Brown).

flattened without sacrificing bandwidth by adding an appropriately chosen capacitor C_2. This usually also ensures stability of the circuit.

Solving equations (B.7) and (B.4) for C_2 yields

$$C_2 = \frac{1 - 2Q^2 + \sqrt{1 + 4Q^2(R_1 C_1 \omega_\mathrm{T} - 1)}}{2Q^2 R_1 \omega_\mathrm{T}}. \tag{B.8}$$

For a maximally flat Butterworth transfer function ($Q = 1/\sqrt{2}$) this simplifies to

$$C_2 = \frac{\sqrt{2R_1 C_1 \omega_\mathrm{T}}}{R_1 \omega_\mathrm{T}}, \tag{B.9}$$

with a pole frequency of

$$\omega_\mathrm{P} = \frac{\omega_\mathrm{T}}{\sqrt{R_1 C_1 \omega_\mathrm{T} + \sqrt{2R_1 C_1 \omega_\mathrm{T} - 1}}}, \tag{B.10}$$

(which equals the 3 dB corner frequency for a Butterworth filter). It turns out that a flat frequency response usually corresponds to a stable circuit (if necessary, the stability can be analyzed in detail with LISO).

The output noise at low frequencies[2], expressed as linear spectral density of the output voltage, has four contributions:

- The thermal (Johnson) noise in resistor R_1, given by $\sqrt{4kTR_1}$.
- The op-amp's input current noise $\widetilde{I}_\mathrm{op}$, which appears at the output as $R_1 \widetilde{I}_\mathrm{op}$.
- The op-amp's input voltage noise $\widetilde{U}_\mathrm{op}$.
- The shot noise associated with the photocurrent I_p, given by $\sqrt{2eI_\mathrm{p}}$, which appears at the output as $R_1\sqrt{2eI_\mathrm{p}}$.

The total noise at the output is found by adding quadratically all contributions:

$$\widetilde{U}_\mathrm{out}^2 = 4kTR_1 + \left(R_1 \widetilde{I}_\mathrm{op}\right)^2 + \widetilde{U}_\mathrm{op}^2 + R_1^2 2eI_\mathrm{p}. \tag{B.11}$$

To characterize the performance of the preamplifier, it is convenient to introduce the 'noise equivalent photocurrent' I_NE which is defined by the condition that its shot noise contributes the same amount of noise at the output as the rest of the circuit [Schilling]. It is desirable to have I_NE smaller than the actual photocurrent in the typical operating condition, such that the preamplifier doesn't add significant extra noise to the inevitable shot noise. The noise equivalent photocurrent is given by

$$I_\mathrm{NE} = \frac{1}{2e}\left(\frac{4kT}{R_1} + \widetilde{I}_\mathrm{op}^2 + \frac{\widetilde{U}_\mathrm{op}^2}{R_1^2}\right). \tag{B.12}$$

It can be seen that, in order to obtain the maximal signal-to-noise ratio, the resistor R_1 should be chosen as large as possible, i.e. such that the largest anticipated photocurrent yields an output voltage near the op-amp's maximal output voltage.

---

[2] The following approximation is valid only for frequencies $\omega \ll \omega_\mathrm{P}$. In particular the op-amp's input voltage noise $\widetilde{U}_\mathrm{op}$ has a peculiar transfer function to the output, which starts to increase at frequencies well below ω_P. A detailed analysis is possible with LISO. In fact, the difficulty of this kind of analysis even for such a simple circuit was one of the reasons to write LISO in the first place.

B.1.2 Tuned circuit

The tuned preamplifier circuits are usually applied in situations where their output signal is (after mixing with an appropriate local oscillator) used as error signal for some loop (such as the Michelson dark fringe lock). Hence in normal operation no large output signal is expected and the performance should be optimized for small signals. In the typical operating condition, there is, however, a non-negligible DC photocurrent flowing through the photodiode. In the circuits used in the prototype, the best small-signal RF performance is achieved with a resonant passive LC-circuit, where the capacitance C is the inevitable parasitic capacitance of the photodiode. A simplified circuit diagram is shown in Figure B.3, together with the RF equivalent circuit.

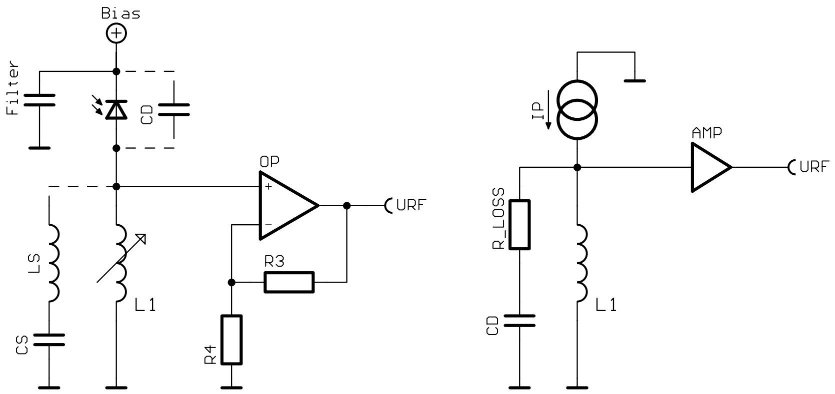

Figure B.3: Basic circuit of a tuned photodiode preamplifier, together with its RF equivalent circuit. The capacitance C_{D} represents the photodiode capacitance, whereas the optional series resonant circuit formed by C_{S} and L_{S} can be used to suppress signals at another unwanted frequency.

The capacitance C_{D} is the sum of the photodiode junction capacitance, the input capacitance of op-amp OP, and parasitic PC board capacitances. For the circuits used in the prototype (which use one quadrant of a Centronics QD50-0 quadrant diode operated with 15 V reverse bias voltage), C_{D} is typically around 30 pF. In the equivalent circuit, C_{D} forms a parallel resonant circuit together with the inductance L_1. All losses of the resonant circuit are modelled by the resistor R_{loss}. In the prototype circuits that are tuned for 12 MHz, L_1 needs to have around 6 μH and R_{loss} was found to be around 70 Ω. Sometimes it is necessary to suppress unwanted signals at another frequency that is also contained in the photocurrent (such as the second harmonic of the modulation frequency). This can be achieved with a series resonant LC-circuit, such as L_S and C_S in Figure B.3. The rest of this discussion assumes, however, no such series resonant circuit.

The frequency-dependent impedance of the parallel resonant circuit is given by

$$Z(s) = \frac{1}{\frac{1}{s\,L_1} + \frac{1}{R_{\text{loss}} + \frac{1}{s\,C_{\text{D}}}}} = \frac{s\,L_1(1 + s\,C_{\text{D}}\,R_{\text{loss}})}{1 + s\,C_{\text{D}}(R_{\text{loss}} + s\,L_1)}. \tag{B.13}$$

In the narrowband approximation, the resonance frequency is given by

$$\omega_0 = \frac{1}{\sqrt{L_1\,C_{\text{D}}}} \tag{B.14}$$

The impedance at the resonance frequency can be approximated by

$$Z_{\text{max}} \approx \frac{L_1}{C_{\text{D}} R_{\text{loss}}} = \frac{1}{\omega_0^2\,C_{\text{D}}^2\,R_{\text{loss}}} \tag{B.15}$$

For our prototype circuit, this impedance amounts to 2.8 kΩ. The quality factor Q is then approximately given by

$$Q = \frac{1}{R_{\text{loss}}}\sqrt{\frac{L}{C_{\text{D}}}}, \tag{B.16}$$

which amounts to around 6.5 for the prototype circuit. Figure B.4 shows the frequency-dependent impedance together with its real part and its phase.

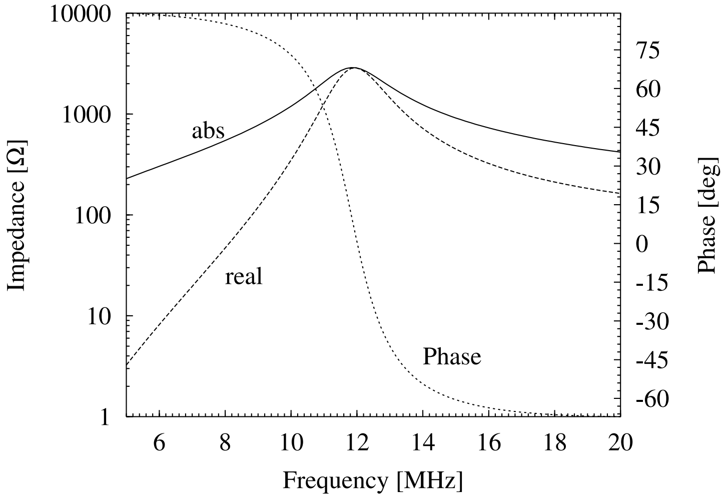

Figure B.4: Impedance of the parallel resonant circuit shown in Figure B.3 for typical values used in the prototype.

The photocurrent produces a voltage proportional to $|Z|$ across the impedance Z, which is amplified by the wideband op-amp OP. At the same time, the real part of the impedance Z produces a thermal (Johnson) noise voltage proportional to $\sqrt{\Re\{Z\}}$. Thus, for best small-signal noise performance, we will want the impedance Z to be as large as possible. This can be achieved by minimizing the capacitance C_D via increasing the reverse-bias voltage. Limits will be given by the power dissipation in the photodiode, and its reverse breakdown voltage. Furthermore it may be undesirable to reduce the bandwidth of the tuned circuit below a certain limit, if the resulting signal is to be used as error signal in a wideband loop.

Similar to the broadband circuit, we can compute a noise-equivalent photocurrent I_NE (at the resonance frequency) in order to characterize the noise performance of the preamplifier. The result is

$$I_\mathrm{NE} = \frac{1}{2e}\left(\frac{4kT\Re\{Z\}}{|Z|^2} + \widetilde{I}_\mathrm{op}^2 + \frac{\widetilde{U}_\mathrm{op}^2}{|Z|^2}\right), \tag{B.17}$$

where $\widetilde{U}_\mathrm{op}$ and $\widetilde{I}_\mathrm{op}$ are the input voltage and current noise spectral densities of op-amp OP, respectively. The contributions of the two gain-setting resistors, R_3 and R_4 in Figure B.3, are neglected here. A more complete noise analysis can be carried out with LISO. With the typical values[3] for the prototype circuit given above, the result is

$$I_\mathrm{NE} \approx 30\,\mu\mathrm{A}, \tag{B.18}$$

which is dominated by the first term of Equation (B.17), i.e. the thermal noise in the losses of the photodiode.

It is possible to measure the most important parameters of a tuned photodiode preamplifier with only two measurements, if an RF spectrum analyzer is available. First, a reference measurement of the output noise spectral density is made when no light is falling on the photodiode. Then white light from an incandescent bulb is shone on the photodiode, such that the DC photocurrent has a value of I_p, which should be approximately equal to I_NE. The ratio of these two measurements (i.e. their difference in dB) has a peak of approximately 3 dB at the resonance frequency. It can be fitted with the following model:

$$y(\omega) = 20\,\log_{10}\sqrt{1 + \frac{I_\mathrm{p}}{I_\mathrm{NE}}\,|H_\mathrm{BP}(\mathrm{i}\,\omega)|^2} = 10\,\log_{10}\left(1 + \frac{I_\mathrm{p}}{I_\mathrm{NE}}\,|H_\mathrm{BP}(\mathrm{i}\,\omega)|^2\right), \tag{B.19}$$

where the transfer function of a band-pass is used:

$$H_\mathrm{BP}(s = \mathrm{i}\,\omega) = \frac{\dfrac{s}{\omega_0 Q}}{1 + \dfrac{s}{\omega_0 Q} + \dfrac{s^2}{\omega_0^2}}\,. \tag{B.20}$$

The model results from quadratically adding the shot-noise caused by I_NE (which is proportional to $\sqrt{I_\mathrm{NE}}$) and the band-pass filtered shot-noise caused by I_p (which is

---

[3] For this computation it was assumed that the circuit is operated *on resonance*; and all tuned circuits used in the prototype were operated on resonance. As is suggested by Figure B.4, theoretically I_NE might be slightly reduced by operating off-resonance, if $4kT\Re\{Z\}$ is the dominant noise contribution. This was, however, never tested in practice.

proportional to $\sqrt{I_\mathrm{p}}$). The three parameters to be fitted are I_NE, the band-pass center frequency ω_0 and it's quality factor Q. Figure B.5 shows the result of such a measurement. In this case the actual photocurrent was $I_\mathrm{p} = 27\,\mu\mathrm{A}$ and the fitted parameters were $I_\mathrm{NE} = 34\,\mu\mathrm{A}$, $\omega_0 = 2\pi \cdot 11.27\,\mathrm{MHz}$ and $Q = 4.6$.

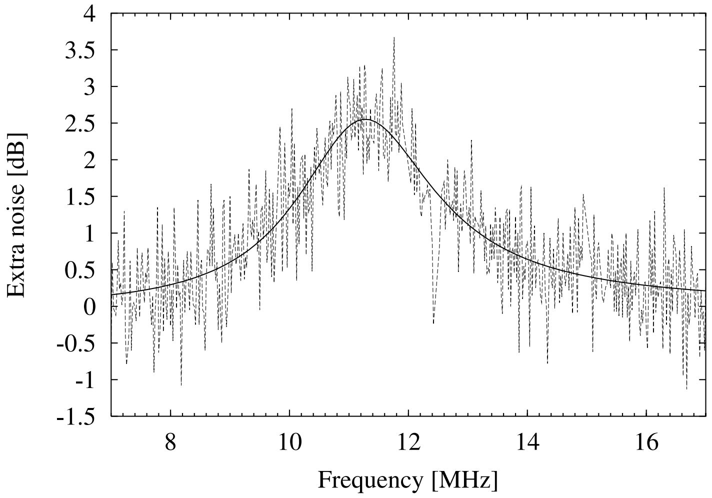

Figure B.5: Measurement of the increased output noise of a tuned photodiode preamplifier caused by a photocurrent approximately equal to I_NE. Shown are the measured data and the curve that was fitted to obtain the photodiode parameters.

If the inductance L_1 is directly measured, then the unknown photodiode parameters C_D and R_loss can be computed from such a measurement via Equations (B.14) and (B.16).

B.1.3 Combined circuit

A tuned preamplifier is usually combined with a broadband circuit that allows to monitor the DC photocurrent. A typical circuit used in the prototype is shown in Figure B.6. The op-amp OP1 keeps the DC voltage across the photodiode constant and thus helps to ensure a constant photodiode capacitance. The capacitor C_1 is necessary to provide an RF ground connection for the tuned circuit and must be taken into account in the computation of C_2 (see Equation (B.9)). The high-pass formed by C_3 and R_2 is optional. If desired, one or more series resonant circuits such as shown in Figure B.3 can be added.

B.2 Resonant transformers for Pockels cells

Pockels cells (electro-optic modulators) are often used to apply a phase modulation of a fixed frequency to a light beam. The voltage required at the crystal may need

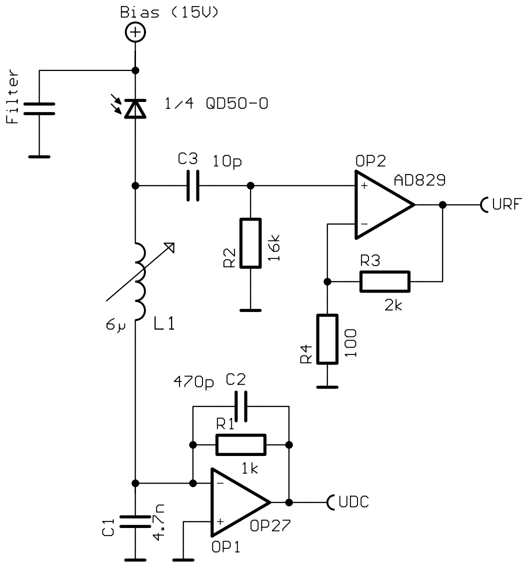

Figure B.6: Combined photodiode preamplifier with a broadband output and a tuned RF output.

to reach several hundreds of volts. This is best achieved with a resonant transformer, several types of which are discussed in this Section. Electrically a Pockels cell looks like a small capacitor. In the neighborhood of the modulation frequency, the losses of the resonant circuit can be modelled by a small series resistance. Typical values are 50 pF and 2 Ω (this last value was derived from measured 'Q' values of resonant circuits and includes wiring losses and the losses of typical coils). In the following these values, and a modulation frequency of 10 MHz, will be assumed for the examples.

Usually the modulation signal is amplified with a broadband power amplifier, which typically has 50 Ω output impedance. In the prototype, power levels of 1 or 2 Watt were used.

A coil of around 5 μH is needed to make a resonant circuit with the capacitance of the Pockels cell. The coil can be an air coil or can be wound on a core. In the prototype ring-cores are used because it was feared that air coils might radiate too strongly. Big cores are necessary to avoid magnetic saturation.

With the values given above, the impedance of that resonant circuit will be about 50 kΩ, and would be very badly matched to the source impedance. Therefore the impedance of the resonant circuit must be transformed to 50 Ω. The most straightforward way to do this would be to add a suitable primary winding such that a transformer is obtained. There is, however, a practical obstacle: The secondary typically has about 5 windings (determined by the resonance frequency and the chosen core). For an impedance ratio of about 1000, the primary would have to consist of $5/\sqrt{1000} \approx \frac{1}{6}$ windings. This is impossible to realize. The problem can, however, be solved by using two transformers in series. The second transformer has one primary winding, and the first one a winding ratio of 1:6. The resulting circuit, which in this form was successfully used in the prototype, is shown in Figure B.7.

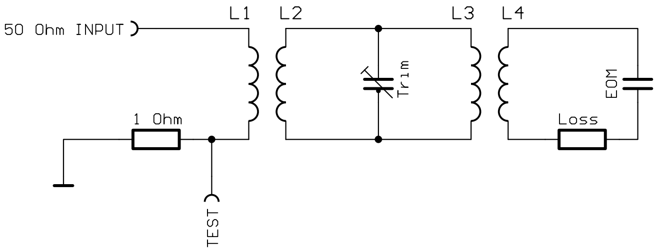

Figure B.7: Resonant transformer to drive a Pockels cell.

A 1 Ω resistor is used to monitor the current through the circuit. This is useful in the adjustment procedure described below. The resonance frequency can be trimmed with the small capacitor. It is placed in between the two transformers, because there the impedance level is such that typically a standard 5–60 pF trimmable capacitor gives a useful adjustment range, and also because at this point the voltage is not yet as high as at the Pockels cell.

A practical procedure to build such a circuit is as follows: First, find a suitable core (preferably the biggest available ring-cores made out of RF-suitable ferrite). Use the power amplifier that will finally be used, which should be able to handle short-circuit loads, at least for short times.

The coil L4 is determined by the resonance frequency, and L3 has one winding. Start with a rough estimate of the winding ratio for the first coil. Now apply a signal (from an adjustable signal generator or a network analyzer) of the right level to the power amplifier's input. Watch the voltage at the 1 Ω resistor, as the frequency is swept through the resonance. The aim of the adjustment procedure is to reach something that looks like Figure B.8.

At frequencies far away from resonance, the circuit behaves like a short circuit. The current is then limited by the amplifier's output impedance. At resonance, and when the impedances are matched, the total impedance seen by the hypothetical voltage source inside the RF amplifier is doubled, and hence the current drops to one half (i.e. by 6 dB).

Now the circuit can be adjusted. The resonance frequency is mainly determined by coil L4 and can be trimmed with the small capacitor. The impedance matching is visible from the depth of the drop in current on resonance (see Figure B.8) and can be adjusted via the winding ratio of L1/L2. These adjustments may need to be iterated a few times, because resonance frequency and impedance matching are not completely independent from each other. It is important that the measurement is done with the same amplifier and power level that is later to be used, because the coils may already start to show nonlinear behaviour due to core saturation (L4 is most strongly affected), and the amplifier's output impedance may be different from 50 Ω. With the procedure described (adjust for 6 dB drop in current), the impedance of the circuit is automatically

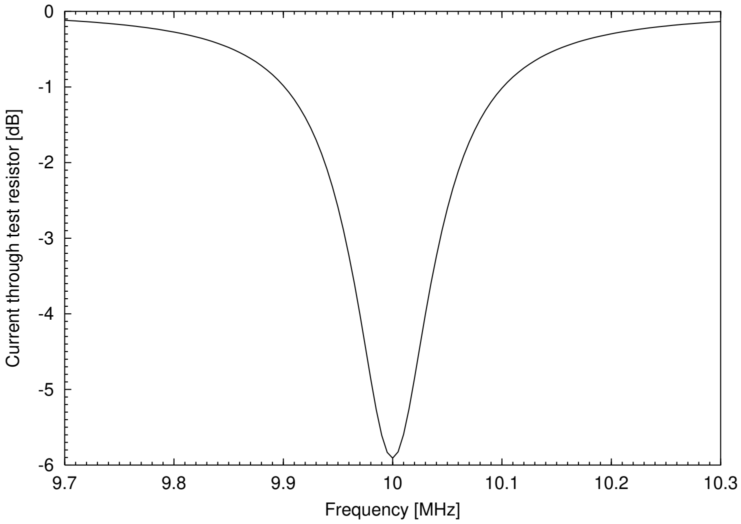

Figure B.8: Current through the 1 Ω resistor in Figure B.7.

matched to the actual output impedance of the amplifier, which is optimal in terms of power transfer.

With the amplifier connected and impedance matched, the Q of the resonant circuit drops to about one half of its previous value, because the amplifier output impedance, transformed to the secondary (L4 and Pockels cell), equals the previous impedance of the resonant circuit. With the numbers of the example, the transformed amplifier's output impedance looks like a 50 kΩ resistor in parallel to the resonant circuit. The voltage at the Pockels cell is about 31 times higher than the voltage at the circuit's input. With 1 W of RF power, corresponding to 20 $\mathrm{V_{p-p}}$ in 50 Ω, about 600 $\mathrm{V_{p-p}}$ can be reached at the Pockels cell. Having matched the impedances means that most of the available power is dissipated in the losses of the secondary resonant circuit. These are mainly located in the crystal itself, the connections to the crystal (the peak current is about 1 A), and the core of coil L4.

Figures B.9 and B.10 show two possible alternative circuits. In Figure B.9, the transformer is replaced by an 'autotransformer'. It suffers from the same problems as the circuit with the true transformers, i.e. coil saturation and impractical small winding numbers (with the numbers of the example, the lower part of the coil would need $\frac{1}{6}$ winding). Otherwise, if it can be built, it behaves completely equivalently to the circuit of Figure B.7 (but it has no galvanic isolation, and trimming is not so easy).

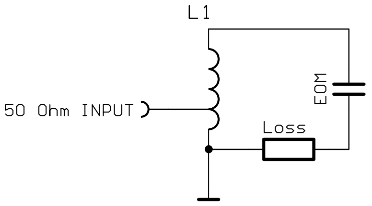

Figure B.9: Alternative resonant transformer circuit with an autotransformer.

Figure B.10 shows the use of a capacitive voltage divider as input (this circuit was proposed by R. Schilling during a discussion with the author). With the numbers of

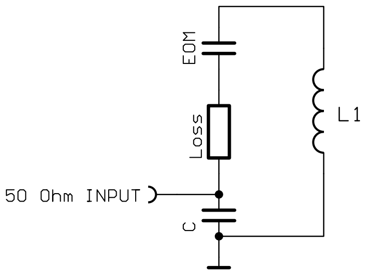

Figure B.10: Alternative resonant transformer circuit with a capacitive voltage divider.

the example, the capacitor C needs to have about 1.6 nF. It behaves differently from the previously discussed circuits in so far as there are now *two* resonances close to each other (a parallel resonance and a series resonance). Figure B.11 shows the input impedance of this circuit. The presence of the two resonances makes the adjustment more difficult. On the other hand, it may be an advantage that at low frequencies the input impedance is very high (instead of a short circuit as in Figure B.9).

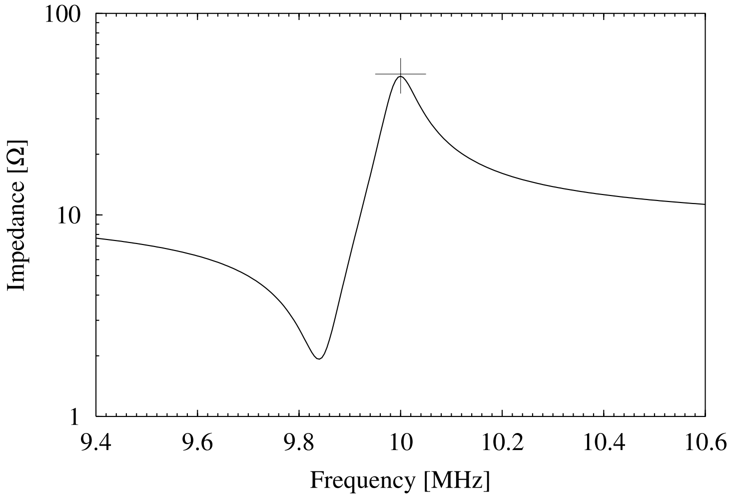

Figure B.11: Input impedance of the alternative resonant transformer circuit with a capacitive voltage divider.

B.3 The automatic lock acquisition circuit

Overview of the function: The function of the automatic lock acquisition circuit can best be explained with Figure B.12.

The topmost trace (labelled ‘PD5’) represents the light power that is transmitted through the reference cavity, which is detected by photodiode PD5 in Figure A.1.

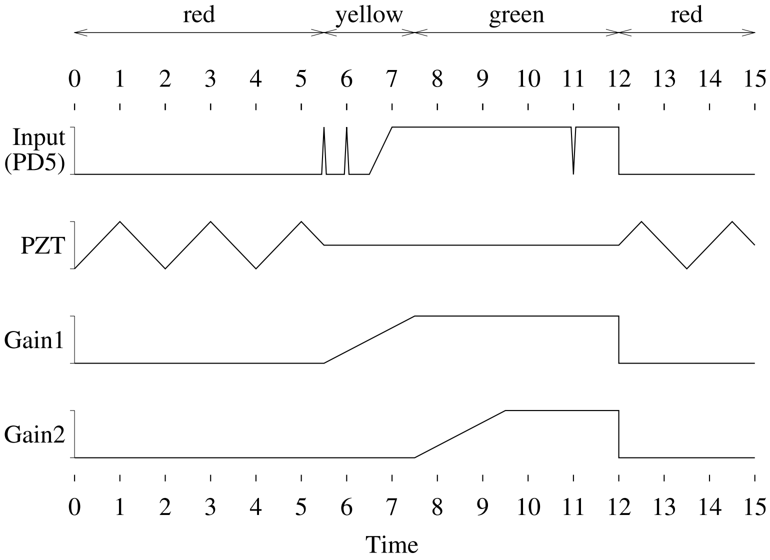

Figure B.12: Sketch of important signals in the automatic lock acquisition circuit and of the corresponding color-coded states. The time-scale is arbitrary.

It is the main input to the circuit. In the example of Figure B.12, it is very small from $t = 0$ to $t = 5$. In reality this is a typical behaviour when there is no resonance of the reference cavity in the frequency range of the laser.

During this time the circuit generates a triangle-wave that scans the laser frequency. This voltage (an output of the circuit) is shown in the second trace (labelled 'PZT') of Figure B.12. It is fed to the slow laser piezo SPZT.

The circuit has three main states, called 'red', 'yellow' and 'green' (these states are indicated with a traffic-light like arrangement of LED lamps). The first state, when the laser is scanned, is called 'red'. The circuit also controls the loop gain of the first and second loop by multiplying their error signals with a factor between zero and unity. In the 'red' state, both factors are zero. This means in particular that the first loop is disabled and does not apply any correction signal to the laser frequency.

In Figure B.12, the laser frequency is scanned through a resonance of the reference cavity at $t = 5.5$. This results in a short peak in the transmitted light (PD5). At this moment, the 'yellow' state is entered. The scanning of the piezo is stopped and the piezo voltage is held at the value where the peak was detected.

The gain of the first loop is ramped up from zero to unity (between $t = 5.5$ and $t = 7.5$). Hopefully the first loop acquires lock at a certain point during this ramp ($t = 7$ in Figure B.12). If that happens, the circuit switches into the 'green' state at the end of the ramp ($t = 7.5$). Otherwise, if at the end of the ramp the first loop is not locked (indicated by a low level at PD5), the circuit returns to the 'red' state and resumes to scan the laser piezo.

The ramp is triggered by a high level on PD5 in the ‘red’ state and is always completed for its full length, i.e. the duration of the ‘yellow’ state is fixed, independent of the light level at PD5 during the ramp.

During this ramp, the loop gain of the second loop is held at zero. At the end of the ramp (i.e. the start of the ‘green’ state at $t = 7.5$), another ramp starts which increases the loop gain of the second loop from zero to unity. The state of the second loop is, however, not monitored by the circuit.

If in the ‘green’ state the light level at PD5 drops again to zero (i.e. the lock of the first loop is lost), the circuit immediately returns to the ‘red’ state ($t = 12$), i.e. the scanning of the laser piezo is resumed and the two loop gains are reset to zero.

Since sometimes there may be very short drops in the light level at PD5 that do not justify a return to the ‘red’ state (which invariably throws the whole interferometer out of lock), very short interruptions ($< 3\,\mathrm{ms}$) in the high level at PD5 are ignored ($t = 11$ in Figure B.12).

Circuit details: Figure B.13 shows the main part of the circuit diagram. The light level from PD5 is amplified and optionally inverted with op-amps N5A and N5B. The comparator N6A compares it with an adjustable level to generate a digital signal. The monostable N9A, together with the gates IC2C and IC5A, is used to eliminate very short LOW peaks in that signal and ‘debounce’ it. Any short LOW peaks are, however, extended by the monostable N9B and indicated with the red LED lamp D9[4].

In the top part of the circuit diagram, the FET op-amp N1B and the comparator N2A form a standard triangle generator with an output signal that swings between -10 and $+10$ volts, and which is fed to SPZT. The oscillation frequency is approximately 10 Hz. The CMOS switch N3A is there to stop the oscillation and hold the output voltage. In the ‘yellow’ and ‘green’ states, when the first loop has non-zero loop gain, this ‘held’ voltage is added to the correction signal that is applied by the first loop. Hence any slow drifts in the ‘held’ voltage are compensated by the first loop. The momentary direction of the triangle wave (‘up’ or ‘down’) is indicated with two yellow LED lamps (D1 and D2 in the lower part of the diagram). This information is not really essential to the user, but the alternatingly flickering LED lamps are an easily visible indication that the first loop is not locked.

Since it was anticipated that there might be time delays between the occurrence of the resonance and its detection by the circuit, switch N4A and op-amp N1A are implemented to compensate the overshoot by taking a small step ‘back’ in the output voltage, when the hold mode is entered. However, this proved to be unnecessary in practice.

In the lower part of the diagram, op-amp N8B generates a ramp from 0 to 10 Volts (by integrating a negative voltage with an inverting integrator). The duration of the ramp

---

[4] In almost all circuits built for the prototype, it has proven very advantageous to liberally include red LED lamps for all easily detectable error conditions.

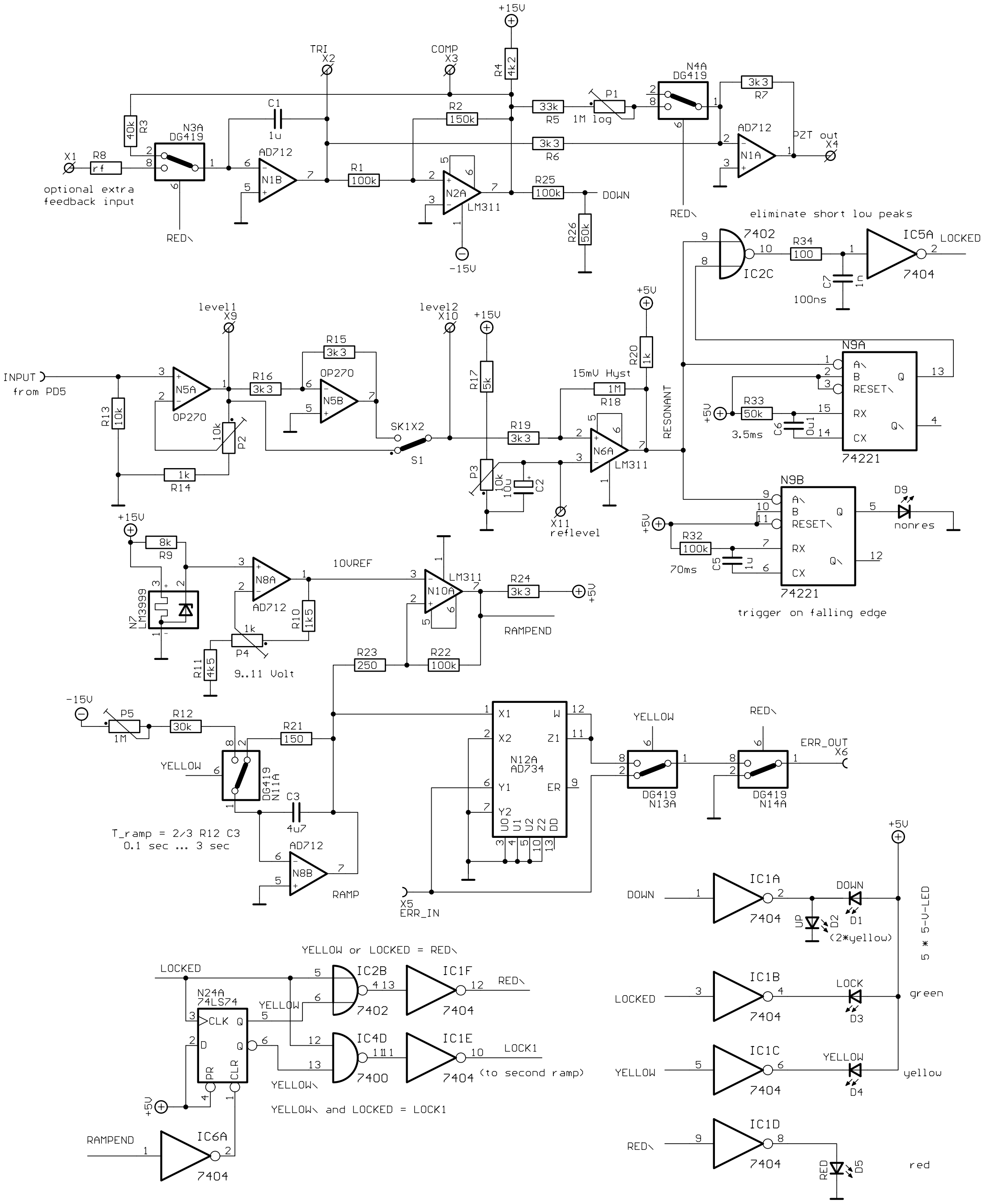

Figure B.13: The main part of the circuit diagram of the automatic lock acquisition circuit.

(which is also the duration of the ‘yellow’ state) can be adjusted with potentiometer P5. A duration of approximately one second works well in the prototype.

That ramp voltage is used to multiply the error signal of the first loop in the analog multiplier N12A. In the ‘green’ state (unity gain), switch N13A is used to connect the error signal directly to the output, without the offset and noise of the multiplier. Another reason for this arrangement is that, in the ‘green’ state, the ramp integrator N8B is reset to zero. Likewise, switch N14A sets the loop gain to a true zero in the ‘red’ state. The end of the ramp (transition from ‘yellow’ to ‘green’ state) is detected by the comparator N10A. The ramp for the loop gain of the second loop is generated by a similar circuit as for the first loop (components N12A, N13A, N14A, N8B, N11A and N10A) and is not shown.

The digital logic ICs are ‘HC’ types. The digital logic parts of the circuit are not explained here in detail, because they were changed several times during the development of the circuit, and a redesign from scratch might be preferable for a new circuit, if the control is not anyway handled by a computer. In short, flip-flop N24A controls the ‘yellow’ state. It is set by a rising edge of the signal called ‘LOCKED’ (which is high when light is transmitted through the reference cavity) and reset by the ‘end of ramp’ signal from N8B. The ‘red’ state is indicated by a low level on the line ‘RED\’ (the backslash indicates logical inversion). The signal called ‘LOCK1’ corresponds to the ‘green’ state and is used to control the second ramp (not shown in Figure B.13).

B.4 Analog filter with $f^{+1/2}$ frequency response

Introduction. The filter described in this section is useful in servo loops where one element of the feedback loop has a two-pole low-pass characteristic (such as a pendulum), and where unconditional stability is required, e.g., because the overall gain may change. The straight-line approximation of the frequency response is shown in figure B.14. All frequencies are used as angular frequencies $\omega = 2\pi f$ throughout this section.

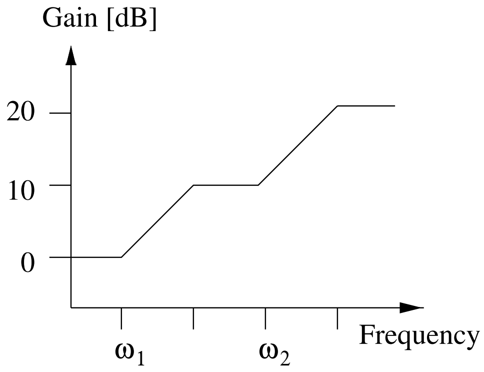

Figure B.14: Straight-line approximation of the desired frequency response for the $f^{+1/2}$ filter ($\omega_2 = 10\,\omega_1$).

The filter consists of two cascaded sections, each extending over half a decade and separated by half a decade. The idea to approximate a frequency response with an $f^{\pm 1/2}$ behaviour and ±45° phase shift by using these half-decade sections is based on circuits previously used by R. Schilling [Schilling].

The corresponding transfer function is

$$H(s)=\frac{\left(1+\frac{s}{\omega_1}\right)\left(1+\frac{s}{\omega_2}\right)}{\left(1+\frac{s}{\sqrt{10}\,\omega_1}\right)\left(1+\frac{s}{\sqrt{10}\,\omega_2}\right)}=\frac{1}{\sqrt{10}}\frac{\left(1+\frac{s}{\omega_1}\right)}{\left(1+\frac{s}{\sqrt{10}\,\omega_1}\right)}\sqrt{10}\frac{\left(1+\frac{s}{\omega_2}\right)}{\left(1+\frac{s}{\sqrt{10}\,\omega_2}\right)}. \tag{B.21}$$

The computed exact frequency reponse is shown in figure B.15. The figure can be used to select a suitable 'start' frequency ω_1 and to estimate the phase shift introduced by the filter.

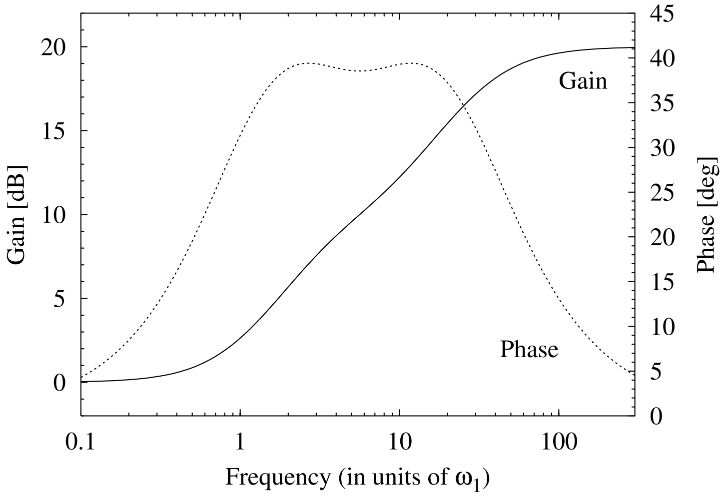

Figure B.15: Computed exact frequency response of the $f^{+1/2}$ filter.

If several such stages are cascaded (with corner frequencies differing by factors of 100), the phase shift in the 'central' frequency region oscillates around $45 \pm 2°$. A non-inverting DC-gain of 1 was chosen which makes the HF-gain 10.

Figure B.16 shows how this filter modifies the transfer function of a resonant element. The resonance frequency ω_r is taken as unity. Three different quality factors (0.7, 2, and 10) are plotted. The 'start frequency' ω_1 of the $f^{+1/2}$ filter is taken as $5\,\omega_\mathrm{r}$, $3\,\omega_\mathrm{r}$, and $2\,\omega_\mathrm{r}$ respectively, as examples of how a 135° phase delay can be approximated.

Electronic realization: The circuit diagram is shown in figure B.17.

It consists of two stages, each of which contributes one pole-zero pair. The input stage is a passive RC-highpass filter with a DC-gain of $1/\sqrt{10}$ and unity HF-gain. The

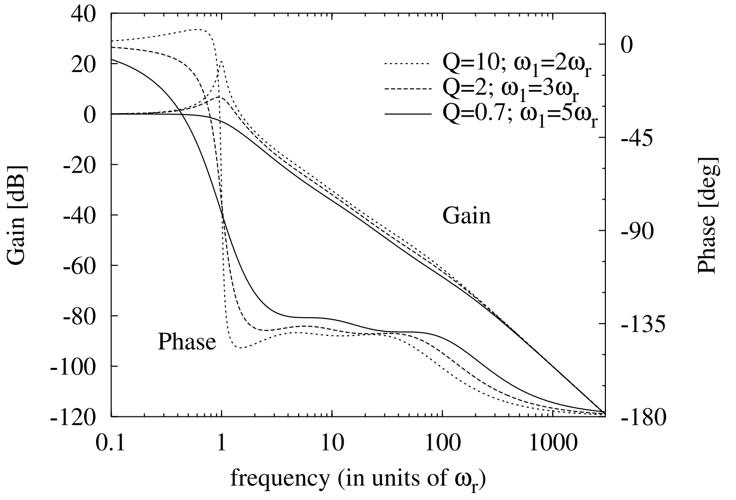

Figure B.16: Computed frequency response of resonant systems together with the $f^{+1/2}$ filter.

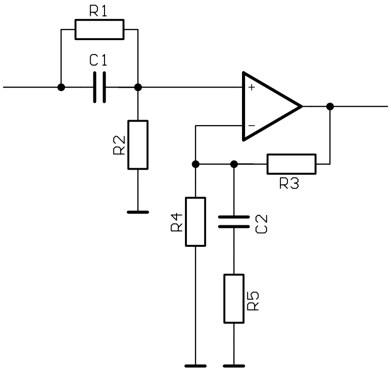

Figure B.17: Circuit diagram of the $f^{+1/2}$ filter.

feedback network provides the rest of the transfer function, with a DC-gain of $\sqrt{10}$ and a HF-gain of 10. This means that a unity-gain stable op-amp is not necessary in this application; stability for gains ≥ 10 is sufficient.

Component values: One possible set of component values can be computed from the transfer function as follows (note that ω_1 and ω_2 may be exchanged as desired).

The relevant design equations are:

$$\begin{aligned}
&\omega_1 R_1 C_1 = 1\,, \\
&R_2 = \frac{1}{\sqrt{10}-1} R_1 \approx 0.4625\, R_1\,, \\
&\omega_2 R_4 C_2 = 1\,, \\
&R_3 = R_4(\sqrt{10}-1) \approx 2.162 R_4\,, \\
&R_5 = \frac{R_4}{\sqrt{10}} \approx 0.3162\, R_4\,.
\end{aligned} \tag{B.22}$$

Other component values can also be found with LISO's `fit` function, which also allows to use a different overall gain or gain distribution.

B.5 Analog filter with $f^{-1/2}$ frequency response

Introduction. The filter described in this section is useful in servo loops where more gain at low frequencies is desired than can be obtained with the usual $1/f$ gain drop, but where unconditional stability is required, e.g., because the overall gain may change. Another possible use is to generate 'pink noise' from white noise. The straight-line approximation of the frequency response is shown in figure B.18. This filter is based on circuits previously used by R. Schilling [Schilling].

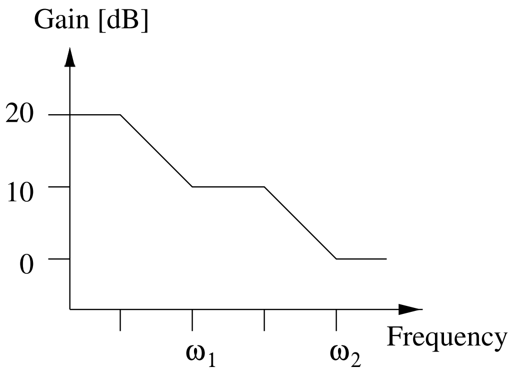

Figure B.18: Straight-line approxmation of the desired frequency response for the $f^{-1/2}$ filter ($\omega_2 = 10\,\omega_1$).

The filter consists of two cascaded $1/f$ sections, each extending over half a decade and separated by half a decade. The corresponding transfer function is

$$H(s) = 10 \frac{\left(1+\frac{s}{\omega_1}\right)\left(1+\frac{s}{\omega_2}\right)}{\left(1+\frac{s}{\omega_1/\sqrt{10}}\right)\left(1+\frac{s}{\omega_2/\sqrt{10}}\right)}\,. \tag{B.23}$$

The computed exact frequency reponse is shown in figure B.19.

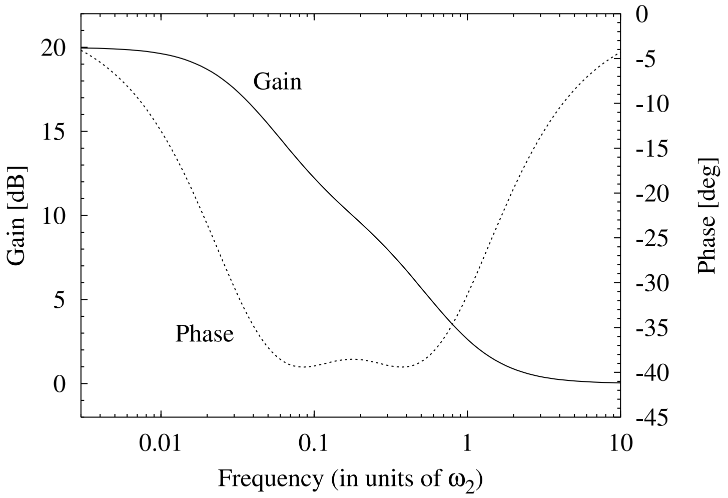

Figure B.19: Computed exact frequency response of the $f^{-1/2}$ filter

The features of the transfer function correspond to those of the $f^{+1/2}$ filter described in the previous section (but note the different definition of ω_1 and ω_2). A non-inverting DC-gain of 10 was chosen because that makes the HF-gain unity and the filter can then usually be introduced into existing servo loops without modification.

Electronic realization: The circuit diagram is shown in figure B.20.

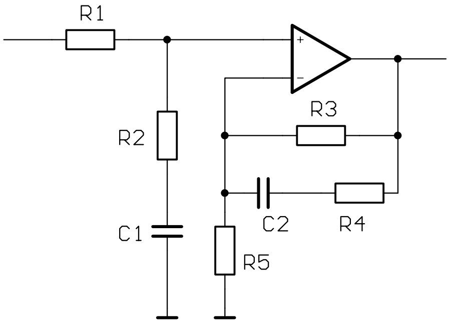

Figure B.20: Circuit diagram of the $f^{-1/2}$ filter

It consists of two stages, each of which have one pole-zero pair. The input stage is a passive RC low-pass filter with unity DC-gain and a HF-gain of $1/\sqrt{10}$. The feedback network provides the rest of the transfer function, with a DC-gain of 10 and a HF-gain of $\sqrt{10}$. That means that a unity-gain stable op-amp is not necessary in this application; stability for gains ≥ 3 is sufficient.

Component values: One possible set of component values is given here (note that ω_1 and ω_2 may be exchanged as desired). The relevant design equations are:

$$
\begin{aligned}
&\omega_1 R_2 C_1 = 1\,, \\
&R_1 = (\sqrt{10} - 1) R_2 \approx 2.162\, R_2\,, \\
&\underbrace{\frac{9}{10}\left(\sqrt{10} + 1\right)}_{\approx\, 3.746} \omega_2 R_5 C_2 = 1\,, \\
&R_3 = 9\, R_5\,, \\
&R_4 = \frac{9}{\sqrt{10}} R_5 \approx 2.846\, R_5\,.
\end{aligned}
\tag{B.24}
$$

Again, other solutions may be found with Liso.

Appendix C

LISO

C.1 Introduction

During this work it was often found necessary to simulate linear electronic circuits and transfer functions. 'Linear' here means that the circuits consist only of passive components and op-amps. Typical problems that were frequently encountered and that caused the author to write LISO include:

- To predict the frequency response of an active filter circuit with non-ideal op-amps.
- To find component values for such a circuit that yield a certain predetermined frequency response.
- To fit a transfer function of a given general type (e.g. a band-pass defined by its pole data) to measured data, with proper weighting options and taking into account a measured phase.
- To understand why op-amps in some circuits are unstable and show oscillations, and to find stable circuits instead.
- To predict the noise behaviour of a given circuit and to identify the dominant noise contributions.
- To maximize the dynamic range of a circuit, i.e., to find component values that minimize the noise of a given circuit while maintaining a given transfer function and not exceeding other given limits (in particular, maximal op-amp output currents).
- To compute the input impedance of a given circuit.

Hence the author has written the program which is now called LISO and which is briefly described in this section. A detailed manual with examples, and the program itself, are available upon request from the author[1]. The program is now used by various members of the GEO 600 project, and also by some researchers in other institutions (University of Florida, University of Tokyo), to design electronic circuits for gravitational wave detectors. Various predictions of LISO (transfer functions, input impedances and noise spectra) for some rather complicated circuits were compared with measurements, and consistently excellent agreement was found. This section can only give a very brief introduction to LISO and necessarily omits many details.

C.2 Features and limitations

The input to LISO is a fixed circuit consisting of passive components (any combination of R, C, L, and transformers) and op-amps. It can have a voltage input (grounded or floating) or a current input (such as for photodiode preamplifiers). Any node of the circuit can be designated the input. The program then computes and plots:

- The frequency response from the input to any component or node (i.e., the voltage at any node, or the current through any component, as a function of the input frequency).
- The frequency-dependent input impedance of the circuit.
- The maximal permissible input signal, taking into account the maximal op-amp output voltage, output current and slew rate.
- The stability of each op-amp in the circuit. Since op-amps are the only elements with gain, this is equivalent to computing the stability of each closed loop in the circuit and the stability of the circuit as a whole.
- The voltage noise at any node of the circuit (in particular the output), taking into account Johnson noise of resistors and voltage noise and current noise of op-amps. It can separate the individual contributions of these noise sources and identify the dominating noise source for any frequency range.
- The spectral density of the noise *current* in any component, taking into account the same noise sources as in the above item.

Some features of the program include:

- The program uses a user-expandable library of op-amp models with their main characteristics. For each op-amp in the circuit, the library parameters can be 'overridden' by individual parameters.
- A very important function of the program is its ability to **fit** the model to given data (either measured or ideal desired data) by varying specified components or parameters.

---

[1] At present (January 1999), the program and the complete manual are available by anonymous ftp from `ftp.rzg.mpg.de` in the directory `pub/grav/ghh/liso`.

- All computations are carried out with complex numbers. In particular, data measured with phase information can be properly fitted.
- Some effort has been made to incorporate state-of-the-art algorithms for the simulation and fitting parts, i.e. the author believes that the results are accurate for reasonable inputs and they are delivered fast.
- In a separate mode of operation of the program, a frequency response can be computed and fitted using the poles and zeroes of the transfer function as input instead of a circuit description (see, e.g., Figures 1.32, 1.45, A.14, and D.2).
- Extensions to the basic fitting algorithm allow the user to find circuits with a user-specified transfer function under additional constraints such as a required minimal output swing and minimum noise.
- Two additional recent fitting procedures, '*Direct Search Simulated Annealing*' and '*Controlled Random Search*', often converge to solutions even when no reasonable starting values are given.
- The combination of the last two items allows the user to almost automatically find circuits with a specified transfer function and the maximum possible dynamic range. Many of these solutions are almost impossible to find by other means.
- The results are plotted via GNUPLOT, a public domain program that is available for numerous platforms and supports a multitude of different 'output devices' (including Postscript). LISO writes an ASCII batch file for GNUPLOT that can be carried to other platforms, or modified by the user, e.g., to to change the appearance of the plot.

The program has at present several limitations. Some of them (marked with an asterisk *) could possibly be overcome if necessary, others not.

- The circuit topology is fixed and must be known and entered by the user.
- All computations are done linearly in the frequency domain. In particular, the DC operating point is not computed. No time-domain analyses are performed. No non-linear components such as discrete semiconductors can be simulated.
- Only voltage-feedback op-amps can be simulated. *
- There is no graphical user interface. Input and output are done via ASCII files in a batch-mode like operation. Plots are produced by calling GNUPLOT. Without GNUPLOT, the only output is an ASCII data file, which may be plotted by other software.
- At present the program has mainly been tested under various versions of UNIX (mainly LINUX, also SUN Solaris and IBM AIX) and MS-DOS. There should, however, be no big problem in porting it to any reasonable operating system. It is entirely written in standard C and the preferred compiler is the GNU C-compiler.

- Fitting is only possible for the 'transfer functions', not for noise. *
- There is only a very simple electrical rule check (ERC) which will not detect many kinds of errors in the circuit (e.g. outputs connected to ground etc.). Many erroneous circuit descriptions will cause the program to abort with a 'singular matrix' error without further explanation. *
- Not all useful transfer functions can be entered by the present `pole`/`zero` syntax.*

C.3 Principles of operation

C.3.1 Circuit simulation algorithm

The fundamentals of the circuit simulation are surprisingly simple. They can be stated as follows:

First Kirchhoff law: The sum of all currents flowing into a node is zero.

Impedance of passive components: For a passive component with the (complex) impedance $Z(s)$ which is connected between *node1* and *node2*, we have

$$Z(s)I = U_{node1} - U_{node2}, \tag{C.1}$$

where I is the current through that component flowing from *node1* to *node2*.
For a resistor we have $Z(s) \equiv R$,
for a capacitor $Z(s) = 1/(s\,C)$
and for an inductor $Z(s) = sL$,
with $s = \mathrm{i}\,\omega = 2\pi\,\mathrm{i}\,f$.

Op-amp open loop gain: For an op-amp with open-loop gain $H(s)$, which is connected to the nodes 'p', 'm' and 'o' with its noninverting input, inverting input and output, respectively, we have

$$U_o = H(s)(U_p - U_m). \tag{C.2}$$

Note that for finite U_o and $|H(s)| \gg 1$, it follows that $U_p \approx U_m$.

Voltage input: For a voltage input at the node *nin*, we set

$$U_{nin} = 1 \tag{C.3}$$

In the special case of a floating voltage input, the equation is

$$U_{nin} - U_{nin2} = 1, \tag{C.4}$$

where *nin* represents the input node and *nin2* the second input node of a floating voltage input.

Current input: For a current we set

$$I_{in} = 1. \tag{C.5}$$

Mutual inductances: These are not so obvious. The procedure is as follows ([Hoefer, section 2.2.4]): If two coils L_1 and L_2 are coupled with the coupling factor k_{12} ($0 \leq k_{12} \leq 1$), a mutual inductance M_{12} with the unit Henry is computed as

$$M_{12} = k_{12}\sqrt{L_1 L_2}\,. \tag{C.6}$$

In the equation for L_1, which normally states something like

$$s\,L_1\,I_{\mathrm{L1}} - U_{\mathrm{node1}} + U_{\mathtt{node2}} = 0, \tag{C.7}$$

an additional term $+s\,M_{12}\,I_{\mathrm{L2}}$ is introduced on the left-hand side. Correspondingly, in the equation for L_2, the term $+s\,M_{12}\,I_{\mathrm{L1}}$ is added. Note that in a complex transformer with more than two windings *all* windings must be coupled to each other. In other words, if there are three coils L_1, L_2 and L_3 on a common core, *three* mutual inductances M_{12}, M_{23} and M_{13} must be treated as above.

We find that for each component we get one equation and one unknown (the current through that component). For each node, we also get one equation and one unknown (the voltage at that node). Furthermore, for the input we have one extra equation and also an extra unknown (the input current I_{in} for a voltage input, or the voltage at the input node for a current input). All these equations are linear in the unknowns. This can most easily be demonstrated with an example, using the low-pass filter shown in Figure C.1. We obtain the following equations:

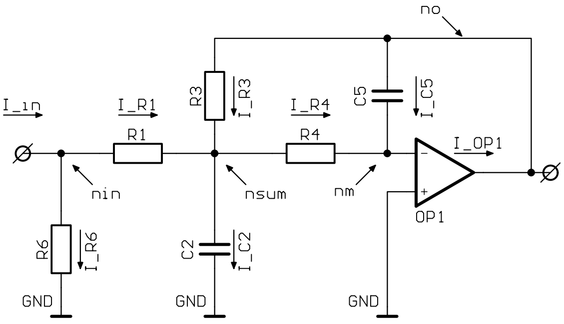

Figure C.1: Example of a low-pass filter with nodes and currents shown.

$$\begin{aligned}
\frac{1}{s\,C_2} I_{\mathtt{C2}} - U_{\mathtt{nsum}} &= 0 \quad (\mathtt{C2}) \\
\frac{1}{s\,C_5} I_{\mathtt{C5}} - U_{\mathtt{no}} + U_{\mathtt{nm}} &= 0 \quad (\mathtt{C5}) \\
\frac{1}{H_{\mathtt{OP1}}(s)} U_{\mathtt{no}} + U_{\mathtt{nm}} &= 0 \quad (\mathtt{OP1}) \\
R_1 I_{\mathtt{R1}} - U_{\mathtt{nin}} + U_{\mathtt{nsum}} &= 0 \quad (\mathtt{R1}) \\
R_3 I_{\mathtt{R3}} + U_{\mathtt{nsum}} - U_{\mathtt{no}} &= 0 \quad (\mathtt{R3}) \\
R_4 I_{\mathtt{R4}} - U_{\mathtt{nsum}} + U_{\mathtt{nm}} &= 0 \quad (\mathtt{R4}) \\
R_6 I_{\mathtt{R6}} - U_{\mathtt{nin}} &= 0 \quad (\mathtt{R6}) \\
-I_{\mathtt{R1}} - I_{\mathtt{R6}} + I_{\mathrm{in}} &= 0 \quad (\mathtt{nin}) \\
-I_{\mathtt{C2}} + I_{\mathtt{R1}} + I_{\mathtt{R3}} - I_{\mathtt{R4}} &= 0 \quad (\mathtt{nsum}) \\
-I_{\mathtt{C5}} + I_{\mathtt{OP1}} - I_{\mathtt{R3}} &= 0 \quad (\mathtt{no}) \\
I_{\mathtt{C5}} + I_{\mathtt{R4}} &= 0 \quad (\mathtt{nm}) \\
U_{\mathtt{nin}} &= 1 \quad (\mathtt{input})
\end{aligned} \tag{C.8}$$

These are 12 linear equations for the 12 unknown variables
$I_{\mathtt{C2}}$, $I_{\mathtt{C5}}$, $I_{\mathtt{OP1}}$, $I_{\mathtt{R1}}$, $I_{\mathtt{R3}}$, $I_{\mathtt{R4}}$, $I_{\mathtt{R6}}$,
$U_{\mathtt{nin}}$, $U_{\mathtt{nsum}}$, $U_{\mathtt{no}}$, $U_{\mathtt{nm}}$ and I_{in}.

Note that for a current input, the first eleven equations remain unchanged, and the last one is replaced by $I_{in} = 1$. This basic set of equations is already sufficient to compute the currents through all components and the voltages at all nodes for a given frequency. The equations are solved using a specialized algorithm for 'sparse' matrices. All transfer functions, the input impedance and the maximal permissible input signal can be obtained from the solution of these equations.

C.3.2 Noise calculations

It turns out that a set of linear equations very similar to the one above can be used to compute the noise, if we now interpret all voltages and currents as linear spectral densities. We introduce noise sources into the circuit, as described below, and compute the voltage at a certain node, interpreted as linear spectral noise density. All component characteristics and Kirchhoff's law remain valid. We must, however, take care to compute only one noise source at a time, and then quadratically add the results. Otherwise different noise sources might be added with a complex phase, or even subtracted, whereas we want to treat all noise sources as independent and uncorrelated. Furthermore we only use the absolute value of the computed noise voltage, but not its phase, and hence the sign with which we introduce the noise source becomes unimportant.

Resistor noise: The equation describing a resistor,

$$R\,I - U_{node1} + U_{node2} = 0, \tag{C.9}$$

is replaced by

$$R\,I - U_{node1} + U_{node2} = U_n, \tag{C.10}$$

where U_n is the Johnson noise expressed as voltage noise source, $U_n = \sqrt{4kTR}$. This corresponds to connecting the noise source U_n in series with the resistor:

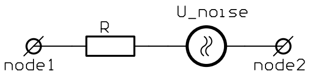

Note that as compared with the equations above, only the *right hand side* is now changed, whereas we still have the same unknowns and left-hand sides. The result is the voltage at a certain node, which is interpreted as linear spectral noise density.

Op-amp voltage noise: To compute the contribution of the voltage noise of an op-amp, we replace the equation describing the op-amp

$$U_o = H(s)(U_p - U_m) \tag{C.11}$$

by

$$U_o = H(s)(U_p - U_m + U_n). \tag{C.12}$$

This corresponds to amplifying not only the differential input voltage, but also the additional (equivalent input noise) voltage U_n (see Figure C.2).

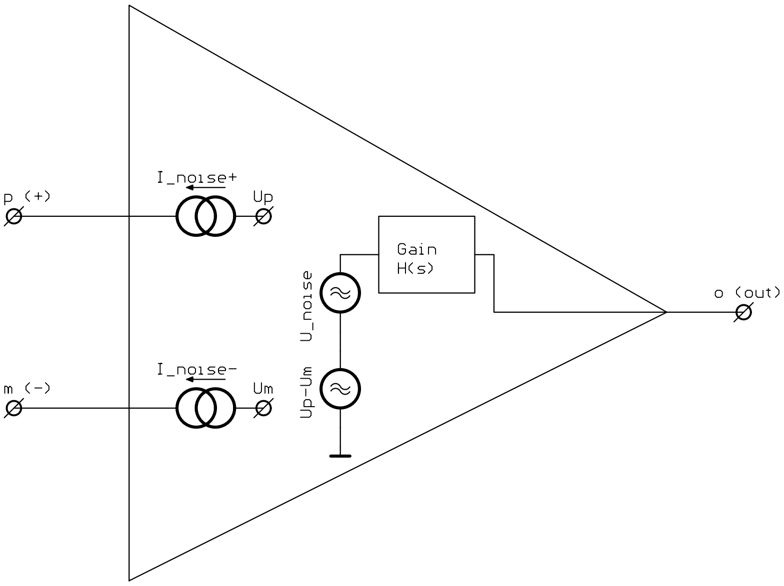

Figure C.2: Noise model of an op-amp.

Note that there is no direct action of the voltage noise source to the input nodes. Without feedback, no contribution of the voltage noise would appear at the input nodes. By rearranging the equation we get

$$\frac{1}{H(s)}U_o - U_p + U_m = U_n, \tag{C.13}$$

in other words, again only a change in the right-hand side.

Op-amp current noise: The current noise is modelled as a current source connected between the node where the op-amp input is usually connected, and its true, ideal input. Since the latter has infinite impedance, no current can flow into it. Consequently the noise current must flow into the node where the input is connected. In other words, we inject the noise current into that node (see Figure C.2).

Assuming the equation describing that node (without the noise source) had been

$$I_1 + I_2 - I_3 - I_4 = 0, \tag{C.14}$$

we replace it by

$$I_1 + I_2 - I_3 - I_4 = I_n, \tag{C.15}$$

with I_n the noise current spectral density. Again this changes only the right-hand side of our equations.

C.3.3 Op-amp stability calculations

In many circuits it is difficult to determine beforehand whether an op-amp will be stable or will oscillate. In order to understand and predict this behaviour, the 'stability function' for some or all op-amps in a given circuit can be computed. The following procedure is used to compute an op-amp stability function (see Figure C.3):

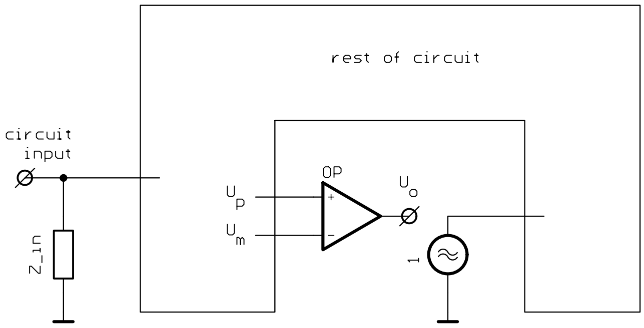

Figure C.3: How the stability function of an op-amp is computed.

- The op-amp in question is 'disconnected' from the circuit and the voltage at its former output node is set to unity. Specifically, the equation (C.2) describing the op-amp is replaced by

  $$U_o = 1. \tag{C.16}$$

  This procedure is done for one op-amp at a time, i.e. all other op-amps remain active when the stability for one particular op-amp is computed.

- The differential input voltage $U_p - U_m$ is computed. This represents the transfer function of the rest of the circuit from the op-amp's output to its input.

- That transfer function is multiplied by the op-amp's open-loop gain.

Thus, the result is the open-loop gain of the feedback loop consisting of the op-amp in question and the rest of the circuit, which could theoretically be measured in the circuit by disconnecting the op-amp's output, injecting a test signal to where the output was formerly connected and measuring the transfer function from that test signal to the op-amp's output. The usual stability conditions for control loops can be applied to this open-loop gain, e.g. the phase delay must be less than 360° at the unity-gain frequency[2]. Although it is not always easy to interpret, the author found the op-amp stability function one of the most useful features of LISO. All unexplained op-amp oscillations that had occured during the first three years of the author's work in Garching could immediately be explained by LISO.

C.4 Fitting algorithms

The fitting functions of LISO are what make the program really useful and allow to design circuits that could otherwise not be found.

Basically, a non-negative real function (called χ^2) is defined, which can be understood as a 'figure of merit'. The lower that number, the better the fit. The basic χ^2 function known from standard statistics is modified in various ways to include:

- One of several possible weighting options for the data points.
- A 'penalty function' that increases χ^2 if pre-set parameter limits are exceeded.
- More specialized 'penalty functions' which are needed to implement the dynamic range optimization (see below).

The user defines the 'parameters', which are to be varied by the fitting procedure. These parameters can be the values of individual components, characteristics of op-amps, or the numerical values of poles and zeroes (if a transfer function is to be fitted from poles and zeroes instead of from a circuit description). It is possible to define 'dependent

---

[2] This corresponds to the usual 180°, where *negative* feedback is implicitly assumed.

parameters', i.e. parameters that are always proportional (or inversely proportional) with a fixed factor to one of the freely variable parameters.

The task of the fitting algorithm is then to minimize χ^2 by varying the parameters. This is achieved by a combination of up to four algorithms.

The main fitting algorithm is a combination of two 'classical' algorithms (both with some extensions by the author), which are repeatedly looped over with tightening tolerances. The first one is the Nelder-Mead Simplex algorithm [Nelder65], a very robust geometrical algorithm which is good at approaching a minimum from far-off starting values[3]. Secondly there is the well-known Levenberg-Marquardt algorithm (see, e.g., [Press]), which is much faster once the vicinity of the (or a) minimum has been found.

The success of these fitting algorithms critically depends on good starting values for the parameters, especially if there are many ($\gtrsim 5$) parameters. In order to make LISO even more useful, two new algorithms [Ali97, Ali97b] have recently been implemented, which are related to 'simulated annealing' methods used in global optimization problems. These algorithms often succeed in finding parameters near the optimal solution (which are then refined by the above-mentioned standard algorithms) even when no starting values at all are known[4].

At the end of the fitting procedure, some statistical indicators are computed, such as estimated standard deviations for the best-fit parameters and correlation coefficients between the parameters. Although these indicators have a well-defined meaning only under special conditions that are often violated in practice, they are nevertheless useful as qualitative indicator of mutual parameter dependencies and as a debugging aid if something went wrong.

C.4.1 Optimizing the dynamic range

In designing filter circuits, there is often a multitude of possible 'solutions' (i.e. sets of component values that provide the desired transfer function). With the standard instructions, such sets can be found and the resulting circuit can be analyzed for op-amp stability, noise, maximum input signal etc.

Sometimes it is desirable to optimize the dynamic range of the circuit, i.e. the ratio of permissible input signal to the noise generated in the circuit itself. Usually the dynamic range is limited at the upper end by the op-amps' maximum output voltage and/or output current[5]. A typical specification might be that the output must be able to swing ±12 V in the frequency range of interest, i.e. the circuit is not limited by either overcurrent from op-amps' outputs or by higher voltages at internal nodes due

---

[3] Although many numerical analysists frown upon this algorithm, it is still the favourite of many practitioners, including the author.

[4] Both of these algorithms do indeed ignore any given starting values and initialize by generating random points within the given limits for each parameter.

[5] The slew-rate of each op-amp is also taken into account.

to suboptimal gain distribution. This condition sets lower limits to resistor values and may impose restrictions on the gain distribution etc.

At the lower end, the limit is noise. The noise can be reduced by reducing resistor values (thereby reducing both Johnson noise and the effect of op-amp current noise), but also by redistributing the gain between the stages of a multi-stage filter or by other modifications, which are sometimes rather unintuitive.

Optimizing the dynamic range hence involves changing component values without overloading any op-amp, while always maintaining the desired transfer function. Since in many circuits transfer function, noise and op-amp load are connected in a very complicated way, this optimization rarely finds the true optimum, if done 'manually'.

Hence two extra instructions have recently been added to LISO which allow (at least partially) to automate the procedure. They work by modifying the 'figure-of-merit' function χ^2 with additional penalty functions. A lower limit can be given for the permissible input signal (thus guaranteeing that the resistors do not become so small as to over-demand the op-amps) and at the same time the noise at the output can be minimized in a defined frequency range.

By minimizing χ^2, the fitting algorithm then finds the (often unique) circuit that meets all constraints and has the lowest possible noise. In particular in conjunction with the 'global optimization' algorithms, these instructions have led to astonishing improvements in circuits which before had been believed to be optimal.

Appendix D

Two–mirror cavities

In our experiment there are various cavities consisting of two mirrors (Fabry–Perot interferometers). First there is the reference cavity used for the pre-stabilization of the laser frequency. More importantly, at the proper operating point (dark fringe) of the interferometer both power recycling cavity and signal recycling cavity can be considered two–mirror cavities for the carrier and the signal sidebands, respectively. Therefore, we consider here a general two–mirror cavity and note down some useful relationships for the light amplitudes and powers at a fixed light frequency ω, which is considered to be an offset from an integer multiple of the cavity FSR.

Consider the cavity shown in Figure D.1 with *amplitude* reflectivities and transmittances $\rho_1, \rho_2, \tau_1, \tau_2$. The length of the cavity is L, and thus the one–way phase shift from traversing the length of the cavity is given by $\exp(-ikL)$ with $k = \omega/c$. We consider two inputs i_1 and i_2, the latter of which is particularily useful for the case of the SR cavity. We call these two cases 'external' and 'internal' input, respectively.

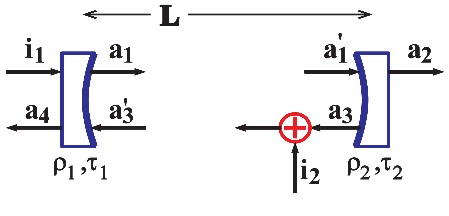

Figure D.1: Model of a two–mirrror cavity.

The relationships between the amplitudes are given by the linear equations

$$\begin{pmatrix} a_1 \\ a_4 \end{pmatrix} = \begin{pmatrix} \mathrm{i}\,\tau_1 & \rho_1 \\ \rho_1 & \mathrm{i}\,\tau_1 \end{pmatrix} \begin{pmatrix} i_1 \\ a_3' \end{pmatrix}, \tag{D.1}$$

$$\begin{pmatrix} a_2 \\ a_3 \end{pmatrix} = \begin{pmatrix} \mathrm{i}\,\tau_2 & \rho_2 \\ \rho_2 & \mathrm{i}\,\tau_2 \end{pmatrix} \begin{pmatrix} a_1' \\ 0 \end{pmatrix}, \tag{D.2}$$

$$a_1' = \exp(-\mathrm{i}\,kL)a_1 \,, \tag{D.3}$$

$$a_3' = \exp(-\mathrm{i}\,kL)\,(a_3 + i_2)\,. \tag{D.4}$$

We now separately consider the two input cases and compute in each case the most interesting amplitudes a_1 (internal light), a_2 and a_4 (emerging light). We use the abbreviation

$$d = \frac{1}{1 - \rho_1\rho_2\exp(-2\,\mathrm{i}\,kL)} \tag{D.5}$$

(the ‘resonance factor’) and find:

- ‘external’ input (unity input i_1 and no input at i_2):

$$a_1 = \mathrm{i}\,\tau_1\, d, \tag{D.6}$$

$$a_2 = -\tau_1\tau_2\exp(-\mathrm{i}\,kL)\,d, \tag{D.7}$$

$$a_4 = \rho_1 - \rho_2\tau_1^2\exp(-2\,\mathrm{i}\,kL)\,d. \tag{D.8}$$

- ‘internal’ input (unity input i_2 and no input at i_1):

$$a_1 = \rho_1\exp(-\mathrm{i}\,kL)\,d, \tag{D.9}$$

$$a_2 = \mathrm{i}\,\rho_1\tau_2\exp(-2\,\mathrm{i}\,kL)\,d, \tag{D.10}$$

$$a_4 = \mathrm{i}\,\tau_1\exp(-\mathrm{i}\,kL)\,d. \tag{D.11}$$

The ‘resonance factor’ d reaches its extreme values

$$d \approx \frac{1}{2} \quad \text{at anti–resonance} \quad (2\,\mathrm{i}\,kL = \pi \mod 2\pi) \tag{D.12}$$

and

$$d \approx \frac{1}{1-\rho_1\rho_2} \gg 1 \quad \text{at resonance} \quad (2\,\mathrm{i}\,kL = 0 \mod 2\pi). \tag{D.13}$$

The *finesse* $\mathcal{F}$ of a cavity is defined as ratio of the *Free Spectral Range* FSR, which is given by

$$\mathrm{FSR} = \frac{c}{2L}, \tag{D.14}$$

to its *Full Width at Half Maximum* bandwidth FWHM (the latter refers to power, not amplitudes) and is given by

$$\mathcal{F} = \frac{\pi}{2\arcsin\left(\frac{1-\rho_1\rho_2}{2\sqrt{\rho_1\rho_2}}\right)} \approx \frac{\pi\sqrt{\rho_1\rho_2}}{1-\rho_1\rho_2} \approx \frac{\pi}{1-\rho_1\rho_2}. \tag{D.15}$$

Note that both FSR and FWHM are expressed as frequencies f, not angular frequencies $\omega = 2\pi\, f$.

The results obtained so far are valid for arbitrary reflectivities and transmittances. We now consider two common special cases with simplifying assumptions:

D.1 Impedance–matched cavity

We assume no losses other than transmission and have

$$\tau_1 = \tau_2 = \tau = \sqrt{T} \tag{D.16}$$

with $T \ll 1$ the (identical) power transmittance of both mirrors and hence

$$\rho_1 = \rho_2 = \rho = \sqrt{1-T}\,. \tag{D.17}$$

The maximum value of d is then

$$d_{\max} = \frac{1}{\tau^2} = \frac{1}{T}, \tag{D.18}$$

and the finesse is given by

$$\mathcal{F} \approx \frac{\pi\sqrt{1-T}}{T} \approx \frac{\pi}{T}. \tag{D.19}$$

For the amplitudes and powers in the three interesting beams we obtain:

		internal		transmitted		reflected	
Input	resonance	a_1	$\lvert a_1\rvert^2$	a_2	$\lvert a_2\rvert^2$	a_4	$\lvert a_4\rvert^2$
external	resonant	$\frac{\mathrm{i}}{\tau}$	$\frac{1}{T}$	-1	1	0	0
external	antiresonant	$\frac{\mathrm{i}\,\tau}{2}$	$\frac{T}{4}$	$\frac{\mathrm{i}\,\tau^2}{2}$	$\frac{T^2}{4}$	≈ 1	≈ 1
internal	resonant	$\frac{1}{\tau^2}$	$\frac{1}{T^2}$	$\frac{\mathrm{i}}{\tau}$	$\frac{1}{T}$	$\frac{\mathrm{i}}{\tau}$	$\frac{1}{T}$
internal	antiresonant	$-\frac{\mathrm{i}}{2}$	$\frac{1}{4}$	$-\frac{\mathrm{i}\,\tau}{2}$	$\frac{T}{4}$	$\frac{\tau}{2}$	$\frac{T}{4}$

D.2 Overcoupled cavity

In an overcoupled cavity, we have $\tau_1 > \tau_2$. We consider the extreme case $\tau_1 \gg \tau_2$ and set

$$\tau_1 = \tau = \sqrt{T}, \tag{D.20}$$
$$\tau_2 = 0, \tag{D.21}$$

with $T \ll 1$ the power transmittance of the input mirror and hence

$$\rho_1 = \rho = \sqrt{1-T}, \tag{D.22}$$
$$\rho_2 = 1. \tag{D.23}$$

The maximum value of d is then

$$d_{\max} = \frac{2}{\tau^2} = \frac{2}{T}, \tag{D.24}$$

and the finesse is given by

$$\mathcal{F} \approx \frac{2\pi}{T}. \tag{D.25}$$

For the amplitudes and powers in the two interesting beams (now $a_2 \equiv 0$) we obtain:

		internal		reflected	
Input	resonance	a_1	$\lvert a_1\rvert^2$	a_4	$\lvert a_4\rvert^2$
external	resonant	$\frac{2\,\mathrm{i}}{\tau}$	$\frac{4}{T}$ *	-1	1
external	antiresonant	$\frac{\mathrm{i}\,\tau}{2}$	$\frac{T}{4}$	1	1
internal	resonant	$\frac{2}{\tau^2}$	$\frac{4}{T^2}$	$\frac{2\,\mathrm{i}}{\tau}$ **	$\frac{4}{T}$
internal	antiresonant	$\frac{\mathrm{i}}{2}$	$\frac{1}{4}$	$\frac{\tau}{2}$	$\frac{T}{4}$

In the prototype, the both PR- and SR-cavity can be considered overcoupled. The two important 'gain factors' are marked in the table. The PR gain is marked with an asterisk (∗). With the 7 % mirror, a power buildup in the cavity of 57 is expected.

The formula for the SR gain is marked with two asterisks (∗∗). Because of the detection scheme, the amplitude $|a_4|$ is important instead of the power $|a_4|^2$. For the 3.88 % SR mirror, a gain of 10.1 is computed.

D.3 Approximations of the frequency response

If we are interested in the frequency response of the amplitudes computed above (i.e. their dependence on the light frequency ω), the most important term is the 'resonance factor' d (Equation (D.5)). Here approximate expressions for two common cases are derived.

D.3.1 Resonant case

If the frequency of interest is identical to the light frequency ω (this occurs in computing the frequency response of broadband signal recycling), the 'resonance factor' d can be approximated by the transfer function of a one-pole low-pass as follows. We write Equation (D.5) as

$$d = \frac{1}{1 - \rho_1 \rho_2 \exp(-2\,\mathrm{i}\,kL)} = \frac{1}{1 - r\,\exp\left(-\frac{s}{\mathrm{FSR}}\right)}, \tag{D.26}$$

where for brevity $r = \rho_1 \rho_2$ has been introduced and the frequency is expressed by the Laplace variable $s = \mathrm{i}\,\omega$, as is usual in describing electrical transfer functions. The free spectral range is defined in Equation (D.14). Note that FSR is defined as frequency, whereas the ω in $s = \mathrm{i}\,\omega$ is an angular frequency, i.e. there is an implicit factor 2π in Equation (D.26).

For small frequencies ω (i.e. $|s| \ll \mathrm{FSR}$) the exponential function can be approximated by the first two terms of its Taylor series, and we get

$$d \approx \frac{1}{1 - r\left(1 - \frac{s}{\mathrm{FSR}}\right)} = \frac{1}{1 - r + \frac{r\,s}{\mathrm{FSR}}} = \frac{1/(1-r)}{1 + s\frac{r}{(1-r)\mathrm{FSR}}}. \tag{D.27}$$

This last expression has the form of the transfer function of a one-pole low-pass with an angular corner frequency

$$\omega_{\mathrm{c}} = \frac{1-r}{r}\,\mathrm{FSR} \approx (1-r)\,\mathrm{FSR}. \tag{D.28}$$

By substituting

$$\mathcal{F} = \frac{\mathrm{FSR}}{\mathrm{FWHM}} = \frac{\pi}{1-r} \tag{D.29}$$

(see Equation (D.15)) and converting to the corner frequency $f_{\mathrm{c}} = \omega_{\mathrm{c}}/2\pi$ we finally find

$$f_{\mathrm{c}} = \frac{\mathrm{FWHM}}{2}\,. \tag{D.30}$$

Thus the resonance factor d has a frequency response similar to that of a one-pole low-pass filter with the corner frequency FWHM/2, for frequencies small compared to the cavity's free spectral range.

D.3.2 Detuned case

In approximating the frequency response of detuned signal recycling, the signal frequency of interest ω is referred to the carrier frequency, whereas the cavity's resonance is at another frequency $\omega_{\mathrm{det}} = 2\pi\, f_{\mathrm{det}}$. Thus we consider the function

$$d = \frac{-\,\mathrm{i}}{1 - r\,\exp\left(-\dfrac{s}{\mathrm{FSR}}\right)}, \tag{D.31}$$

where

$$s = \mathrm{i}\,(\omega - \omega_{\mathrm{det}}), \tag{D.32}$$

and the factor '$-\,\mathrm{i}$' has been introduced for later convenience. Looking at, for example, Figure 1.56, one might be tempted to conclude that the transfer function can be approximated by that of a two-pole low-pass filter. Unfortunately this is only true in a rather limited frequency range around the peak frequency, and only for $\mathrm{FWHM} \ll f_{\mathrm{det}} \ll \mathrm{FSR}$. Since these conditions are, however, realistic for many applications, it is worthwhile to study a possible approximation by a two-pole low-pass filter.

Some attempts to find an algebraic similarity were not successful, and hence a numerical comparison was done using LISO's fitting function. The parameters used were those of the prototype ($\mathrm{FSR} = 4844\,\mathrm{kHz}$, $r = \sqrt{1 - 3.88\,\%}$) and a detuning frequency of $f_{\mathrm{det}} = 400\,\mathrm{kHz}$ was chosen (approximately the geometric average of the FSR and the FWHM, which is 30 kHz).

Figure D.2 shows that the low-pass filter is a reasonable approximation around the peak frequency, even for the phase (if the rather arbitrary, but unimportant factor '$-\,\mathrm{i}$' is included in Equation (D.26)). The pole frequency found by the fit was 400 kHz, and the pole Q was 13, corresponding to a bandwidth of 30.7 kHz, which is very close to the cavity's FWHM.

Figure D.3 was produced using the low-pass parameters which were fitted near the peak and shows that at frequencies considerably far away from the peak the approximation is not very useful. Thus in general Equation (D.31), or, even better, Jun's program (which takes into account the other sideband) should be preferred to any approximation.

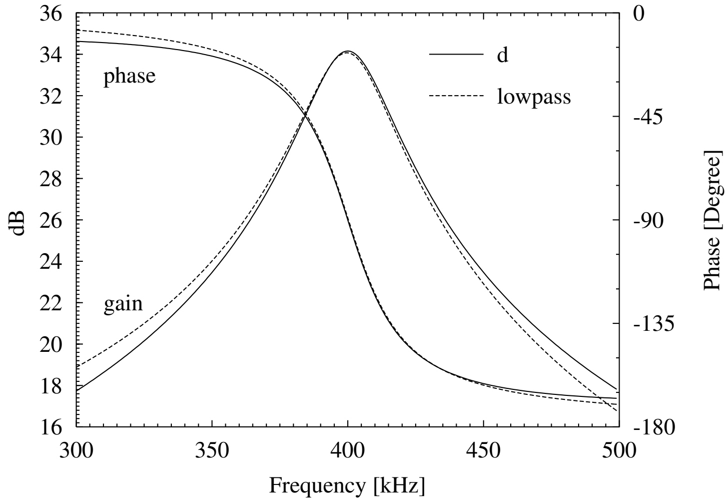

Figure D.2: Approximation of the resonance factor d by a the transfer function of a two-pole low-pass filter around the resonance.

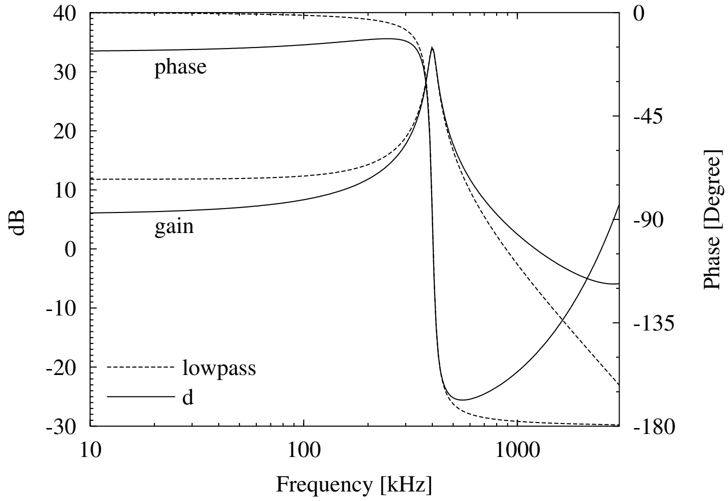

Figure D.3: The approximation of Figure D.2 in a wider frequency range.

Appendix E

Mathematica programs

E.1 Simplified interferometer models

E.1.1 Auxiliary functions

The following short modules contain a few auxiliary functions that are repeatedly used by the programs in the next sections.

The first module, called `clear.m` resets MATHEMATICA by deleting all previouisly defined symbols.

```
(* clear.m *)
Unprotect[In,Out]
Clear["a*", "b*", "c*", "d*", "e*", "f*", "g*", "h*", "i*", "j*", "k*",
"l*", "m*", "n*", "o*", "p*", "q*", "r*", "s*", "t*", "u*", "v*", "w*",
"x*", "y*", "z*", In, Out]
Protect[In,Out]
Off[Remove::rmnsm]
Remove["Global‘*"]
On[Remove::rmnsm]
$Line=0
Null
```

The second module is somewhat more interesting. The functions defined in it are used to extract the components swinging at $n\,\sin(\omega_\mathrm{m}t)$ and $n\,\cos(\omega_\mathrm{m}t)$ separately for $n = 1, 2, \ldots$.

```
(* demod.m: Auxiliary functions to describe demodulation
   The modulation frequency must be called ’wm’,
   and the time ’t’. *)

(* The Power in a beam with amplitude x, i.e. |x|^2 *)
power[x_]:=ComplexExpand[x Conjugate[x],TargetFunctions->{Re,Im}];

(* Extract only terms swinging at the mod. frequency *)
sinrule[1]:={
Sin[a_.+(m_/;(Abs[m]!=1))t wm]->0,
```

```
Cos[a_.+(m_/;(Abs[m]!=1))t wm]->0
};

(* Rules to extract terms at a multiple of the modulation frequency *)
sinrule[n_]:={
Sin[a_.+(m_/;(Abs[m]!=n))t wm]->0,
Cos[a_.+(m_/;(Abs[m]!=n))t wm]->0,
Sin[a_.+t wm]->0,
Cos[a_.+t wm]->0,
Sin[a_.-t wm]->0,
Cos[a_.-t wm]->0
\renewcommand{\baselinestretch}{1.0}
};

(* Compute components of 'a' at 'n' times the mod. frequency *)
s[a_,n_] := Select[ExpandAll[TrigReduce[a]],!FreeQ[#,t]&]/.sinrule[n];

(* Compute DC component of 'a' *)
s[a_,0] := Select[ExpandAll[TrigReduce[a]],FreeQ[#,t]&];
```

The function `power` takes an expression (typically a complex amplitude) and computes its squared magnitude, such that exponential functions are converted into trigonometric functions. As a (somewhat artificial) example, consider the amplitude a of a phase modulated beam (see Equation (1.10)), where the upper sideband has an additional phaseshift ψ:

$$a = J_0(m) + J_1(m)\exp(\,\mathrm{i}\,\omega_\mathrm{m} t) + J_1(m)\exp(-\,\mathrm{i}\,[\omega_\mathrm{m} t + \psi]). \tag{E.1}$$

The application of the `power` function to this amplitude yields the result

$$\begin{aligned}|a|^2 = {} & J_0(m)^2 + 2J_1(m)^2 + \\ & 2J_1(m)\,(J_0(m)\,[\cos(\omega_\mathrm{m} t) + \cos(\omega_\mathrm{m} t + \psi)] + J_1(m)\cos(2\omega_\mathrm{m} t + \psi))\end{aligned} \tag{E.2}$$

The work of extracting the components at a certain frequency is done by the function `s[]`. It takes an expression and first expands[1] all terms such as $\sin^n(\omega_\mathrm{m} t)$ into terms of the form $\sin(n\,\omega_\mathrm{m} t)$ and $\cos(n\,\omega_\mathrm{m} t)$. Then the terms swinging with the desired multiple of $\omega_\mathrm{m} t$ are extracted with the `Select[]` function and `sinrule` rules.

Applying the function `s[]` to the expression (E.2) in order to extract the ω_m components yields

$$2J_0(m)J_1(m)[\cos(\omega_\mathrm{m} t) + \cos(\omega_\mathrm{m} t + \psi)]. \tag{E.3}$$

E.1.2 Internal modulation

The following program computes the demodulated output signal of a simple Michelson interferometer with internal modulation. It is described in Section 1.3.1.

---

[1] The program relies heavliy on the function `TrigReduce` which performs conversions such as $\cos^2 x \rightarrow (1 + \cos(2x))/2$. This function is available in MATHEMATICA versions 3.0 and above. In earlier versions or other programs that function must be directly implemented by the appropriate rules.

```
<<clear.m
<<demod.m

(* Simplifications *)
rho=tau=1/Sqrt[2];
l3=l1;
l4=l2;

(* amplitudes *)
a1=I tau;
a2=a1 (j0 + 2 I j1 Cos[wm t - km l1]);
a3=a2;
a4=a3 (j0 + 2 I j1 Cos[wm t - km l1 - 2 km l2])
b1=rho;
b2=b1 (j0 - 2 I j1 Cos[wm t - km l3]);
b3=b2;
b4=b3 (j0 - 2 I j1 Cos[wm t - km l1 - 2 km l4]);
a5=I tau b4 - rho a4 Exp[I phi];

(* power in output beam *)
i5=power[a5];

(* compute 1*fmod component in output power *)
Simplify[s[i5,1]]
```

E.1.3 External modulation

The following program computes the output signal from a simple Michelson interferometer with external modulation. It is described in Section 1.3.2.

```
<<clear.m
<<demod.m

(* external modulation *)

a1e=c1 Exp[I phi/2];
a2e=-c2 Exp[-I phi/2];
as=(a1e+a2e)/Sqrt[2];
alo=clo Exp[I psi] (j0 +2 I j1 Cos[t wm]);
o1=(as+alo)/Sqrt[2];
o2=(as-alo)/Sqrt[2];

u1=Simplify[s[power[o1],1]];
u2=Simplify[s[power[o2],1]];

Print[u1];

(* Now simplify for c2=c1 *)

Print[Simplify[u1/.c2->c1]];
```

E.1.4 Schnupp modulation

The following program computes the output signal in a simple Michelson interferometer with Schnupp modulation (see Section 1.3.3).

```
<<clear.m
<<demod.m

(* Simplifications *)
rho=tau=1/Sqrt[2];

(* wave vectors *)
k0=0
kp=wm/c
km=-wm/c

(* amplitudes *)
a3=I tau (j0+I j1 Exp[I (wm t + kp 2 (l1-dl/2))] +
 I j1 Exp[ I (-wm t + km 2 (l1-dl/2))])
a5=rho(j0+I j1 Exp[I (wm t + kp 2 (l1+dl/2))] +
 I j1 Exp[I (-wm t + km 2 (l1+dl/2))])
a6=rho a3 - I tau a5 Exp[I phi]

(* power in output beam *)
i6=power[a6]

(* and its fmod component *)
Simplify[s[i6,1]]
```

E.1.5 Autoalignment error signals

The following program computes all autoalignment error signals given in Scetion 2.3.

```
<<clear.m
<<demod.m

(* Integrals over transverse modal functions *)
vrule={u0^2->1, u0 u1->0, u1^2->1}
wrule={u0^2->0, u0 u1->Sqrt[2/Pi], u1^2->0}
v[x_] := Simplify[ExpandAll[x]/.vrule];
w[x_] := Simplify[ExpandAll[x]/.wrule];

Print["Fabry-Perot :"];
a1f = c1 u0 Exp[I phi] (j0 +2 I j1 Cos[t wm]);
a2f = -c2 (u0 + k Exp[I theta] u1);
sf=Simplify[s[power[a1f+a2f],1]];
Print[v[sf]];
Print[w[sf]];

Print["Schnupp :"];
mod1=(j0+2 I j1 Cos[wm t + eps]);
mod2=(j0+2 I j1 Cos[wm t - eps]);
a1s=c1 Exp[-I phi/2] (u0 + k/2 Exp[I theta] u1) mod1;
a2s=-c2 Exp[I phi/2] (u0 - k/2 Exp[I theta] u1) mod2;
ss=Simplify[s[power[a1s+a2s],1]];
```

```
Print[FullSimplify[v[ss]]];
Print[FullSimplify[w[ss]]];

Print["External Modulation :"];
a1e=c1 u0;
a2e=-c2 (u0+k Exp[I theta] u1) Exp[I phi];
a3e=c3 u0 Exp[I psi] (j0 +2 I j1 Cos[t wm]);
se=Simplify[s[power[a1e+a2e+a3e],1]];
Print[vse=FullSimplify[v[se]]];
Print[wse=FullSimplify[w[se]]];

Print["Mach-Zehnder :"];
a1mz=c1 u0;
a2mz=-c1 u0 Exp[I phi];
a3mz=c3 Exp[I psi] (j0 +2 I j1 Cos[t wm]) (u0+k Exp[I theta] u1);
smz=Simplify[s[power[a1mz+a2mz+a3mz],1]];
Print[vmz=FullSimplify[v[smz]]];
Print[wmz=FullSimplify[w[smz]]];
(* For the form given in the text, TrigReduce[] must be applied
   to the result after removing the (wm t) term *)
```

E.2 Full interferometer simulation

Jun's program is not printed here. It can be obtained from the author upon request.

E.2.1 Static response example

The following example shows how the plots shown in Figure 1.18 were produced. The MATHEMATICA code is printed in `typewriter`, with comments in between.

`<<"clear.m"` *This resets* MATHEMATICA.

`<<"Drint.m"` *This loads Jun's program.*

`clight = 299792458.;` *The speed of light, c in m/s.*

`rBS = Sqrt[0.515];` *The beamsplitter's amplitude reflectivity* ρ_{BS}.

`rlist = {0.9995, 0.9995, 0.9643, 0};` *Amplitude reflectivities of the four mirrors. Signal recycling is disabled by setting* $\rho_{\mathrm{S}} = 0$. *The order of the four parameters is always North, East, West and finally South.*

`llist = {30.6873, 30.6273, 0.15, 0.285} / clight;`
One-way light travel times in each arm, computed as armlength divided by c.

`tlist = {-phi/2, phi/2, 0, 0};` *The tunings. Zeroes represent the nominal operating point. The Michelson tuning* φ_{MI}, *is introduced as differential detuning of both long arms (North and East). It is to be used as independent variable in the plot and is hence the only variable which is not yet given a numerical value.*

`wmod = 2 * Pi * 9.686 * 10^6 ;` *The modulation frequency is 9.686 MHz.*

`midx = 0.6;` *The modulation index is 0.6.*

```
errsig = 100 *Simplify[SigTM[South, wmod, midx,
   tlist, llist, rlist, rBS][[2]]];
```

This computes the static response at the **South** *port for the given parameters. A list of five elements is returned. They are, in this order,* H_0, H_{1i}, H_{1q}, H_{2i} *and* H_{2q}. *The second element, selected by '*`[[2]]`*' is* H_{1i}, *which is multiplied with the arbitrary scaling factor 100. It represents the Michelson error signal.*

```
outpow = Simplify[SigTM[South, wmod, midx,
   tlist, llist, rlist, rBS] [[1]]];
```

The DC power (H_0*) at the South port.*

```
prpow = Simplify[SigTM[East, wmod, midx, tlist, llist,
   rlist,rBS][[1]]/(1-rlist[[2]]^2) +
   SigTM[North, wmod, midx, tlist, llist,
   rlist, rBS][[1]]/(1-rlist[[1]]^2) ];
```

The power in the PR cavity. `SigTM[East, ...]   [[1]]` *is actually the DC power leaving through the East mirror. The power in the East arm is found by dividing it by* $\tau^2_{\rm East} = 1 - \rho^2_{\rm East}$. *The same is computed for the North arm, and their sum is the total power in the PR cavity.*

```
Plot[errsig,{phi,-2,2},PlotRange->All];
   Plot[outpow,{phi,-2,2},PlotRange->All];
   Plot[prpow,{phi,-2,2},PlotRange->All];
```

The three results are plotted as a function of $\varphi_{\rm MI}$. *Figure 1.18 was produced by exporting the data as a table and plotting it with* GNUPLOT.

E.2.2 Frequency response

The following code was used to produce Figure 1.19. Comments are given only for those lines which differ from the previous example.

```
<<"clear.m"

<<"DRint.m"

clight = 299792458.;

rBS = Sqrt[0.515];

rlist = {0.9995, 0.9995, 0.9643, 0.9804};
```

Signal recycling is active.

```
llist = {30.6873, 30.6273, 0.15, 0.285} / clight;

tlist = {0, 0, 0, 0};
```

The nominal operating point.

```
wmod = 2 * Pi * 9.686 * 10^6 ;

midx = 0.6;

source={-.5,.5,0,0};
```

This defines where the dithering is applied (differentially to the end mirrors).

```
sig1 = SigFQ[2*Pi*fsig, South, source, wmod, midx, tlist,
     llist, rlist, rBS] [[2]];
```

This computes the frequency response for one signal frequency $\omega_{\mathrm{sig}} = 2\pi f_{\mathrm{sig}}$*, measured at the South port. The result is a list of five (complex) elements,* G_0*,* G_{1i}*,* G_{1q}*,* G_{2i} *and* G_{2q}*. The second element, the in-phase component at 9.686 MHz, is selected as result. As compared to* `SigTM` *there are two more parameters,* `2*Pi*fsig` *and* `source`*.*

E.2.3 Resonance of the PR cavity

As explained in Section 1.6.1.3, for a realistic simulation of error signals in the 30 m prototype it is necessary to compute the PR mirror tuning φ_{PR} that makes the PR cavity resonant for arbitrary conditions of the Michelson and SR mirror.

In Jun's program this can be done by the following code:

```
r0list={rlist[[1]],rlist[[2]],0,rlist[[4]]};
```

If `rlist` *is the list of mirror reflectivities,* `r0list` *is the same list with the PR mirror left out.*

```
zz[pmi_,psr_] := TMresponse[0,tlist+{-pmi/2,pmi/2,0,psr},
     llist,r0list,rBS][[3]];
```

This computes the amplitude of carrier light that is injected through the West port upon its return to the West port. `pmi` *and* `psr` *are the Michelson and SR mirror tuning, respectively. For the other parameters, see Appendix E.2.1.*

```
z[pmi_,psr_] := z[pmi,psr] = (Arg[-zz[pmi,psr]])/2;
```

This is the PR tuning necessary to keep the PR cavity resonant.

The amplitude of the light returning towards the power recycling mirror (M_W) results as

$$a_{\to\mathrm{W}} = \frac{\exp(2\,\mathrm{i}\,\varphi_{\mathrm{SR}})\big(\rho_{\mathrm{N}}\exp(2\,\mathrm{i}\,\varphi_{\mathrm{MI}}) + \rho_{\mathrm{E}})\big) - 2\rho_{\mathrm{N}}\rho_{\mathrm{E}}\rho_{\mathrm{S}}\exp(\mathrm{i}\,\varphi_{\mathrm{MI}})}{\rho_{\mathrm{E}}\rho_{\mathrm{S}} + \rho_{\mathrm{N}}\rho_{\mathrm{S}}\exp(2\,\mathrm{i}\,\varphi_{\mathrm{MI}}) - 2\exp\big(\mathrm{i}\,(\varphi_{\mathrm{MI}} + 2\varphi_{\mathrm{SR}})\big)}\,. \tag{E.4}$$

The PR tuning necessary to keep the PR cavity resonant is then given by

$$\varphi_{\mathrm{PR,res}} = \frac{\angle(-a_{\to\mathrm{W}})}{2}. \tag{E.5}$$

E.2.4 Optimal demodulation phase

The following short function computes the optimal demodulation phase χ_{opt} according to Equation 1.74, if all parameters of the interferometer are given numerical values:

```
chiopt := Module[{h, a, b, c, d, w, chi},
   h = SigFQ[2*Pi*fsig, South, source, 2 * Pi * fmod * 10^6, midx,
           {0,0,0,phisr}, llist, rlist, rBS];
```

```
a = Re[h[[2]]]; b = Im[h[[2]]]; c = Re[h[[3]]]; d = Im[h[[3]]];
w = Sqrt[(b + c)^2 + (a - d)^2]*Sqrt[(b - c)^2 + (a + d)^2];
chi = ArcCos[(a^2 + b^2 - c^2 - d^2)/w]/2;
chi *= Sign[a*c - b*d];
chi]
```

E.3 Ray-tracing program

The following program uses geometrical optics to find the axis of the eigenmode for a given combination of reflecting and/or refracting plane and spherical surfaces. Its application is described in Section 2.10. An outline of the procedure is as follows: For each surface, the following parameters must be given:

- The ‘center’ of the surface, i.e. the point where the well aligned beam is supposed to hit the surface.
- The radius of the mirror (substrate) which is only used for some drawing routines, but not for the calculations.
- The curvature of the surface, given as the reciprocal of the radius of curvature (such as to avoid infinity for flat surfaces).
- The normal vector of the surface at its center.

The term ‘beam’ in this Appendix refers to the geometrical axis of a beam, without taking into account the transverse shape or optical phase. A beam is described by six coordinates: A point of origin (measured in meters) and a direction (given as a unity vector). Although not all of them are independent, the full set is used without problems. There are functions for reflecting and refracting a beam at a given surface, which, using vector algebra, return the reflected or refracted new beam.

The program starts with a well-aligned interferometer and traces the beam through it. The beams thus found (including the beams transmitted through each mirror and the beam directly reflected from the input coupler) are saved and will be used as reference. The simplest procedure to find this well-aligned interferometer is to arbitrarily fix the spot positions on each mirror and then construct the normal vector of each mirror accordingly. This can be done in the same program.

Then one mirror at a time is misoriented by a small angle ε (good values are $10^{-6} \lesssim \varepsilon \lesssim 10^{-4}$ rad). The beam is again traced through one roundtrip in the interferometer. A set of six equations is set up, which demand that the beam after the roundtrip equals the original beam, with the 6 parameters of the starting beam as variables. These equations are then numerically solved by the Newton-Raphson method (see, e.g., [Press]), yielding a new starting beam that reproduces itself. The solution thus represents the axis of the new cavity eigenmode. This new starting beam is once more traced through the interferometer, now with full output. The results of the program are the differences in beam origins and directions at each mirror between the well-aligned case and the misaligned case, divided by ε. In other words, we compute the numerical partial derivatives of spot positions and beam angles with respect to the mirror misorientations.

The program printed below computes the results for vertical misalignments in the GEO 600 modecleaner (shown in Table 2.7). To obtain the corresponding results for horizontal misalignments (Table 2.6), the functions `vrot` and `vangle` must be replaced by `hrot` and `hangle`, respectively.

```
<<clear.m
pi = N[Pi];

(* Parameters of the GEO modecleaner:
   mdist = length of cavity (4 m)
   roc = radius of curvature (6.72 m)
   d = distance of near mirrors (15 cm)
   eps = amount of misalignment for numerical differentiation *)

mdist = 4.;
roc = 6.72;
d = .15;
eps = N[10^-5];

(* There are 2 modes of operation:
 "plot = True" draws some graphics with exaggerated parameters
               (for an overview), whereas
 "plot = False" performs the calculations *)

plot = False;

If [plot, (* Other parameters for plotting *)
 {mdist = 0.3;
  roc = 0.5;
  N[4 Degree]; }];

(* length of a vector *)
len[a_] := Sqrt[a.a];

(* unity vector in the direction of 'a' *)
normvec[a_] := a/len[a];

(* distance between two points *)
dist[a_, b_] := len[a-b];

(* Vector cross product *)
cross[a_, b_] := {-(a[[3]]*b[[2]]) + a[[2]]*b[[3]],
 a[[3]]*b[[1]] - a[[1]]*b[[3]], -(a[[2]]*b[[1]]) + a[[1]]*b[[2]]};

(* Convert spherical coordinates into rectangular coordinates *)
s2r[x_] := {x[[1]]*Cos[x[[3]]]*Sin[x[[2]]],
 x[[1]]*Sin[x[[2]]]*Sin[x[[3]]], x[[1]]*Cos[x[[2]]]};

(* Convert rectangular coordinates into spherical coordinates *)
r2s[x_] := {Sqrt[x[[1]]^2 + x[[2]]^2 + x[[3]]^2],
 ArcCos[x[[3]]/Sqrt[x[[1]]^2 + x[[2]]^2 + x[[3]]^2]],
 ArcTan[x[[1]], x[[2]]]};
```

```
(* rotate vector 'x' horizontally by angle 'a' *)
hrot[x_, a_] := Module[{r, theta, phi, xx, yy, zz},
 {r, theta, phi} = r2s[{x[[1]], x[[3]], x[[2]]}];
 {xx, zz, yy} = s2r[{r, theta, phi+a}];
 N[{xx, yy, zz}] ];

(* rotate vector 'x' vertically by angle 'a' *)
vrot[x_, a_] := Module[{r, theta, phi, xx, yy, zz},
 {r, theta, phi} = r2s[{x[[1]], x[[3]], x[[2]]}];
 {xx, zz, yy} = s2r[{r, theta+a, phi}];
 N[{xx, yy, zz}] ];

(* find horizontal angle between vectors 'v0' and 'v1' *)
hangle[v0_, v1_] := Module[{a},
 a = r2s[{v1[[1]], v1[[3]], v1[[2]]}] [[3]]
   - r2s[{v0[[1]], v0[[3]], v0[[2]]}][[3]];
 Mod[N[a+pi], 2 pi]-pi ];

(* find vertical angle between vectors 'v0' and 'v1' *)
vangle[v0_, v1_] := Module[{a},
 a = r2s[{v1[[1]], v1[[3]], v1[[2]]}] [[2]]
   - r2s[{v0[[1]], v0[[3]], v0[[2]]}][[2]];
 Mod[N[a+pi], 2 pi]-pi ];

(* find 2 orthonormal vectors which are orthogonal to 'v' *)
onvec[v_] := Module[
 {ev = IdentityMatrix[3], ctab, e, max, maxpos, i, e1, e2},
 ctab = Table[len[cross[ev[[i]], v]], {i, 3}];
 max = -1.;
 maxpos = -1;
 For[i = 1, i<=3, i++,
   If[ctab[[i]]>max, max = ctab[[i]];
      maxpos = i;]];
 e = ev[[maxpos]];
 e1 = normvec[cross[e, v]];
 e2 = normvec[cross[e1, v]];
 {e1, e2} ];

(* plotting function: make a circle representing a mirror 'm' *)
disk[m_] := Module[{zen, rs, k, nvec, e1, e2, phi},
 {zen, rs, k, nvec} = m;
 (* Center, Substrate Radius, Curvature, Normal *)
 {e1, e2} = onvec[nvec];
 Table[zen+e1 rs N[Cos[phi]]+e2  rs N[Sin[phi]],
    {phi, 0, 2 pi, pi/12}]];

(* plotting functions *)
mplot[m_] := Graphics3D[Line[disk[m]]] (* Plot mirror *)
splot[x_] := Graphics3D[Line[x]]
  (* Plot segment (Line between two points) *)

(* plotting function for a 'beam' *)
bplot[x_] := Graphics3D[
  Line[{Take[x, 3], Take[x, 3] + plotlen*normvec[Take[x, -3]]}]];

(* compute the point where beam 'b' intersects surface 'm' *)
isect[m_, b_] := Module[{zen, rs, k, nvec, orig, dir, pis},
```

```
 {zen, rs, k, nvec} = m;
    (* Center, Substrate Radius, Curvature, Normal *)
 orig = Take[b, 3]; dir = Take[b, -3];
    (* origin, direction *)
 pis = orig-dir*((orig-zen).nvec)/(nvec.dir); (* plane intersection *)
 If[k==0, (* Flat mirror *)
   pis,
  Module[{cc, p1, p2, x, y, z, lam, gl1, gl2, sol}, (* curved mirror *)
   cc = zen+(1/k)*normvec[nvec];
   gl1 = (x-cc[[1]])^2+(y-cc[[2]])^2+(z-cc[[3]])^2==1/k^2;
   gl2 = {x, y, z}==orig+lam*dir;
   sol = NSolve[{gl1, gl2}, {x, y, z, lam}];
   p1 = {x, y, z}/.sol[[1]];
   p2 = {x, y, z}/.sol[[2]];
   If[(Im[p1[[1]]]!=0 || Im[p1[[2]]]!=0 || Im[p1[[3]]]!=0),
      Print["Error: no real intersection"]; Abort[];, Null];
   If[(Im[p2[[1]]]!=0 || Im[p2[[2]]]!=0 || Im[p2[[3]]]!=0),
      Print["Error: no real intersection"]; Abort[];, Null];
   If[dist[p1, pis]<dist[p2, pis], p1, p2]]
 ] (* End If *)
] (* End Module *)

(* compute the reflected beam, when beam 'b' hits mirror 'm' *)
refl[m_, b_] := Module[{zen, rs, k, nvec, dir, is, u, k1, k2},
 {zen, rs, k, nvec} = m;
   (* Center, Substrate Radius, Curvature, Normal *)
 dir = Take[b, -3];  (* direction *)
 is = isect[m, b]; (* intersection *)
 u = normvec[If[k==0, nvec, zen+(1/k)*normvec[nvec]-is]];
 k1 = normvec[dir];
 u = Sign[k1.u]*u;
 k2 = normvec[k1-2*(k1.u)*u];
 Join[is, k2]];

(* compute the refracted beam, when beam 'b' hits mirror 'm',
  where index of refraction changes from 'n1' to 'n2' at 'm'. *)
refr[m_, b_, n1_, n2_] :=
Module[{zen, rs, k, nvec, dir, is, u, k1, ct1},
 {zen, rs, k, nvec} = m;
     (* Center, Substrate Radius, Curvature, Normal *)
 dir = Take[b, -3];  (* direction *)
 is = isect[m, b]; (* intersection *)
 u = normvec[If[k==0, nvec, zen+(1/k)*normvec[nvec]-is]];
 k1 = normvec[dir];
 u = Sign[k1.u] u;
 ct1 = k1.u;
 Join[is, ((-(ct1*n1) + Sqrt[(-1 + ct1^2)*n1^2 + n2^2]) u+n1 k1)/n2] ];

h = 10^-6; (* Stepwidth for Newton-Raphson *)
hh = N[h IdentityMatrix[6]];

(* One iteration of the Newton-Raphson method to find
 the solution of   f[x]=0
 x is a 6-dim. vector (beam starting from first mirror),
 and f[x] (defined below) is the difference between the
 beam after one roundtrip and the original beam *)
```

```
raphson[x_] := Module[{jac, i, dx},
jac = Transpose[Table[(f[x+hh[[i]]]-f[x-hh[[i]]])/(2*h), {i, 1, 6}]];
f0 = -f[x]; dx = LinearSolve[jac, f0];
If[len[f[x+dx]]>10^-9, Print["Residual = ", len[f[x+dx]]]];
x+dx];

(* Definition of mirrors etc. Here: GEO modecleaner *)

(* pa, pb, pc = center of mirror a,b,c *)
pa0 = {-d/2, 0, 0};
pb0 = {0, 0, -mdist};
pc0 = {d/2, 0, 0};

(* na, nb, nc = normal vector of mirror a,b,c *)
na0 = normvec[0.5 (normvec[pb0-pa0]+normvec[pc0-pa0])];
nb0 = normvec[0.5 (normvec[pa0-pb0]+normvec[pc0-pb0])];
nc0 = normvec[0.5 (normvec[pa0-pc0]+normvec[pb0-pc0])];

(* ma, mb, mc = mirror a,b,c *)
ma = ma0 = {pa0, .05, 0, na0};
mb = mb0 = {pb0, .05, 1./roc, nb0}
mc = mc0 = {pc0, .05, 0, nc0};

(* Now the beams are computed for non-rotated mirrors (as reference):

 b00 = incoming beam (starting at mirror 'a' travelling to mirror 'b')
 bdref = directly reflected input beam
 b10 = beam after reflection at mirror b
 b20 = beam after reflection at mirror c
 b30 = beam after reflection at mirror a, should be = b00
 sin, s1, s2, s3 = 'distance' vectors (for plotting only)
 bouta, boutb, boutc = output beams leaving through mirrors a,b,c
*)

b00 = Join[pa0, normvec[pb0-pa0]];
 sin = {Take[b00, 3] - 0.1*Take[b00, -3], Take[b00, 3]};
bdref = refl[ma0, b00];
b10 = refl[mb0, b00]; s1 = {pa0, pb0};
 boutb = Join[Take[b10, 3], Take[b00, -3]];
b20 = refl[mc0, b10]; s2 = {pb0, pc0};
 boutc = Join[Take[b20, 3], Take[b10, -3]];
b30 = refl[ma0, b20]; s3 = {pc0, pa0};
 bouta = Join[Take[b30, 3], Take[b20, -3]];

(* This is the function f[x], which should be zero for the
 cavity eigenmode. The beam 'b0' makes one roundtrip,
 resulting in b3. For the eigenmode, b3=b0 *)

f[b0_]:=Module[{b1, b2, b3},
 b1 = refl[mb, b0];
 b2 = refl[mc, b1];
 b3 = refl[ma, b2];
 b0-b3];

(* r[x] = round to 3 digits after decimal point *)
r[x_] := 10.^-3 Round[N[10.^3 x]];
```

```
(* rp[x] = prints r[x] nicely *)
rp[x_] := PaddedForm[r[x], {7, 4}];

(* the function 'compute' does the main job for misaligned mirrors.
It computes the cavity eigenmode in the misaligned case and compares
it to the previously calculated eigenmode in the well aligned case
(b00 etc.). Mirrors are misaligned by an angle 'eps'. *)

compute:=(
(* b0n is the beam b0 (from mirror a to mirror b) of the eigenmode
   of the misaligned cavity *)
b0n = raphson[b00]; (* 1st iteration *)
b0n = raphson[b0n]; (* 2nd iteration *)
If[plot, b0n = raphson[b0n]]; (* 3rd iteration *)

(* bdrefn, ... have the same meaning as bdref0, ... above.
   They describe the misaligned cavity *)

bdrefn = refl[ma, b00];
b1n = refl[mb, b0n]; s1n = {Take[b0n, 3], Take[b1n, 3]};
       boutbn = Join[Take[b1n, 3], Take[b0n, -3]];
b2n = refl[mc, b1n]; s2n = {Take[b1n, 3], Take[b2n, 3]};
       boutcn = Join[Take[b2n, 3], Take[b1n, -3]];
b3n = refl[ma, b2n]; s3n = {Take[b2n, 3], Take[b3n, 3]};
       boutan = Join[Take[b3n, 3], Take[b2n, -3]];
If[len[b3n-b0n]>10^-10, Print["test=", len[b3n-b0n]]];

(* now the beams '...n' (misaligned eigenmode) are compared to
the beams '...0' (well aligned reference eigenmode), and divided
by the small misalignment angle 'eps'.
dpa, dpb, dpc are differences in the beam position on mirrors a, b, c
ama, gamb, gamc are the differences in angle of the output beams.
gamd is the difference in angle of the directly reflected beam.
gamas is the angle between output beam a and direct reflection. *)

dpa = Take[(boutan-bouta), 3]/eps;
dpb = Take[(boutbn-boutb), 3]/eps;
dpc = Take[(boutcn-boutc), 3]/eps;
gama = vangle[Take[bouta, -3], Take[boutan, -3]]/eps;
gamd = vangle[Take[bdref, -3], Take[bdrefn, -3]]/eps;
gamas = vangle[Take[bdrefn, -3], Take[boutan, -3]]/eps;
gamb = vangle[Take[boutb, -3], Take[boutbn, -3]]/eps;
gamc = vangle[Take[boutc, -3], Take[boutcn, -3]]/eps;

(* rt2 is half the cavity round-trip length *)
rt2 = Sqrt[mdist^2+d^2/4]+d/2;

(* zr is the rayleigh range of the cavity eigenmode *)
zr = Sqrt[rt2(roc-rt2)];

(* dzwaist is the shift of the eigenmode at the waist *)
dzwaist = (dpc[[2]]+dpa[[2]])/2.;

(* theta describes the 'character' of misalignment *)
theta = N[ArcTan[gamas zr/dzwaist]];

(* this is only for plotting *)
```

```
plotlen = 0.1;
If[plot,
Show[mplot[ma0], mplot[mb0], mplot[mc0], splot[sin],
 splot[s1], splot[s2], splot[s3],
 bplot[bdref], bplot[bouta], bplot[boutb], bplot[boutc],
Graphics3D[Dashing[{0.05, 0.05}]],
 mplot[ma], mplot[mb], mplot[mc],
 splot[s1n], splot[s2n], splot[s3n],
 bplot[bdrefn], bplot[boutan], bplot[boutbn], bplot[boutcn],
ViewPoint->{0, 0, -100}] ];

(* the results are printed *)
Print[text];
Print[" pady=", rp[dpa[[2]]], " wdy=", rp[dzwaist],
" gama=", rp[gama], " gamas=", rp[gamas], " theta=", rp[theta/Degree]];
Print[" pbdy=", rp[dpb[[2]]], " gamb=", rp[gamb],
" pcdy=", rp[dpc[[2]]], " gamc=", rp[gamc]];
Print[];
)
(********* end of function 'compute' ***********)


(* Now the function 'compute' is called several times, each time with
   one mirror misaligned. The common mode and differential mode
   misalignments of mirrors a and c are also computed separately.

   The signal detected by a camera in the reflected light
   consists of "repart" and "impart" for parallel shifts and angular
   rotations, respectively, between the directly reflected beam and
   output beam 'a'. These are added up in 'repart' and 'impart'
   'ala', 'alb' and 'alc' is the misalignment of mirror a, b, c,
   respectively.

   Furthermore the angular shift of output beams a and d (directly
   reflected) are also added up.
*)

repart = impart = sumgama = sumgamd = 0;

ma = ma0; mb = mb0; mc = mc0;
text = "vrot ma"; ma[[4]] = vrot[ma0[[4]], -eps]; compute;
repart += dzwaist/zr ala;
impart += gamas ala;
sumgama += gama ala;
sumgamd += gamd ala;

ma = ma0; mb = mb0; mc = mc0;
text = "vrot mb"; mb[[4]] = vrot[mb0[[4]], eps]; compute;
repart += dzwaist/zr alb;
impart += gamas alb;
sumgama += gama alb;
sumgamd += gamd alb;

ma = ma0; mb = mb0; mc = mc0;
text = "vrot mc"; mc[[4]] = vrot[mc0[[4]], -eps]; compute;
repart += dzwaist/zr alc;
impart += gamas alc;
```

```
sumgama += gama alc;
sumgamd += gamd alc;

ma = ma0; mb = mb0; mc = mc0;
text = "vrot ma+mc";
ma[[4]] = vrot[ma0[[4]], -eps];
mc[[4]] = vrot[mc0[[4]], -eps];
compute;

ma = ma0; mb = mb0; mc = mc0;
text = "vrot ma-mc";
ma[[4]] = vrot[ma0[[4]], -eps];
mc[[4]] = vrot[mc0[[4]], eps];
compute;

(* Now we have all contributions to repart, impart, sumgama, sumgamd.
 We introduce the common mode angles 'amc' and 'apc' (minus and plus)
 which satisfy
 amc == ala - alc,
 apc == ala + alc,
 and express the results with these common mode angles. *)

acrule = {ala -> (amc - apc)/2 + apc, alc -> (-amc + apc)/2};

repart = repart/.acrule;
impart = impart/.acrule;
sumgama = sumgama/.acrule;
sumgamd = sumgamd/.acrule;

Print["repart = ", Simplify[repart]];
Print["impart = ", Simplify[impart]];
Print["sumgama = ", Simplify[sumgama]];
Print["sumgamd = ", Simplify[sumgamd]];
```

Bibliography

[Ali97] M. Ali, A. Törn, S. Viitanen: 'A Direct Search Simulated Annealing algorithm for optimization involving continuous variables', Turku Center for Computer Science, TUCS Technical Report No. 97 (1997). 206

[Ali97b] M. Ali, A. Törn, S. Viitanen: 'A numerical comparison of some modified Controlled Random Search algorithms', Turku Center for Computer Science, TUCS Technical Report No. 98 (1997). 206

[Anderson84] D.Z. Anderson: 'Alignment of resonant optical cavities', Appl. Opt. **23** (1984) 2944–2949. 109, 111

[Babusci97] D. Babusci, H. Fang, G. Giordano, G. Matone, L. Matone, V. Sannibale: Phys. Lett. A **226** (1997) 31–40. 110

[Barthel97] A. Barthel: 'Abstimmbares Signal-Recycling mit externer Modulation', Diploma thesis, University of Hannover, 1997 (in German). 73

[Blair] D.G. Blair [ed.]: 'The Detection of Gravitational Waves', Cambridge University Press 1991. v, 237

[Drever83a] R.W.P. Drever, talk at '10th Int. Conf. on General Relativity and Gravitation', Padua 1983. 19

[Drever83b] R.W.P. Drever, J.L. Hall, F.V. Kowalski, J. Hough, G.M. Ford, A.J. Munley, H. Ward: 'Laser Phase and Frequency Stabilization Using an Optical Resonator', Appl. Phys. **B 31** (1983) 97–105. 2, 53, 114

[Drever83c] R.W.P. Drever et al., in: 'Quantum Optics, Experimental Gravitation, and Measurement Theory', eds. P. Meystre and M.O. Scully (Plenum Press, New York, 1983) 503. 3

[Drever83d] R.W.P. Drever, in 'Gravitational Radiation', eds. N. Deruelle and T. Piran (North-Holland, Amsterdam, 1983) 321. 3

[Forward78] R.L. Forward: 'Wideband laser-interferometer gravitational-radiation experiment', Phys. Rev. **D 17**, (1978) 379–390. 33

[Freise98] A. Freise: 'Ein neues Konzept für Signal-Recycling', Diploma thesis, University of Hannover, March 1998 (in German). 73, 73

[Gradstein-Ryshik] I.S. Gradstein; I.M. Ryshik: 'Tables of Series, Products and Integrals', Harri Deutsch 1981 10, 116

[Harris78] F.J. Harris: 'On the Use of Windows for Harmonic Analysis with the discrete Fourier transform', Proc. IEEE **66** (1978) 51–83. 162

[Hefetz97] Y. Hefetz, N. Mavalvala, D. Sigg: 'Principles of calculating alignment signals in complex resonant optical interferometers', J. Opt. Soc. Am. B **14**, (1997) 1597–1605. 111

[Heinzel95] G. Heinzel: 'Resonant Sideband Extraction – Neuartige Interferometrie für Gravitationswellendetektoren', Diploma thesis, University of Hannover, 1995 (in German). 5, 33, 148

[Heinzel96] G. Heinzel, J. Mizuno, R. Schilling, W. Winkler, A. Rüdiger, K. Danzmann: 'An experimental demonstration of resonant sideband extraction for laser–interferometric gravitational wave detectors', Phys. Lett. **A 217** (1996) 305–314. 5

[Heinzel98] G. Heinzel, K.A. Strain, J.Mizuno, K.D. Skeldon, B. Willke, W. Winkler, R. Schilling, A. Rüdiger, and K. Danzmann: 'Experimental demonstration of a suspended Dual Recycling interferometer for gravitational wave detection', Phys. Rev. Lett. **81** (1998) 5493–5496. vi, 73

[Heinzel99] G. Heinzel, A. Rüdiger, R. Schilling, K. Strain, W. Winkler, J. Mizuno, K. Danzmann: 'Automatic beam alignment in the Garching 30-m prototype of a laser-interferometric gravitational wave detector', in press, Opt. Comm. 1999. v, 109

[Hoefer] E.E.E. Hoefer, H. Nielinger: 'SPICE – Analyseprogramm für elektronische Schaltungen', Springer Verlag 1985 (in German). 201

[Horowitz–Hill] P. Horowitz, W. Hill: 'The Art of Electronics', 2. ed., Cambridge University Press 1989. 9, 177

[HP] Manual for the HP3562A spectrum analyzer. 162

[Kawabe94] K. Kawabe, N. Mio, K. Tsubono: Appl. Opt. **33** (1994) 5498–5505. 110

[Kerr85] G.A. Kerr, N.A. Robertson, J. Hough, C.N. Man: 'The Fast Frequency Stabilisation of an Argon Laser to an Optical Resonator Using an Extra–Cavity Electro–Optic Modulator', Appl. Phys. **B 37** (1985) 11–16. 148

[Lobo92] J.A. Lobo: 'Effect of a weak plane GW on a light beam', Class. Quantum Grav. **9** (1992) 1385–1394. 33

[Maass95] D. Maaß: 'Signal-Recycling mit Schnupp-Modulation', Diploma thesis, University of Hannover, 1995 (in German). 73

[Man90] C.N. Man, D. Shoemaker, T.M. Pham, D. Dewey: 'External modulation technique for sensitive interferometric detection of displacements', Phys. Lett. **A 148** (1990) 8–16. 19

[Mavaddat95] R. Mavaddat, D.E. McClelland, P. Hello, J.-Y. Vinet: 'Dual Recycling Laser Interferometric Gravitational Wave Detectors: Simulating the performance with imperfect mirrors', J. Optics (Paris) **26** (1995) 145–149. 87, 90

[McClelland93] D.E. McClelland, C.M. Savage, A.J. Tridgell, R. Mavaddat: Phys. Rev. **D 48** (1993) 5475. 87

[McMahon64] G.W. McMahon: 'Experimental Study of the Vibrations of Solid, Isotropic, Elastic Cylinders', Journ. Acoust. Soc. Am. **36** (1964) 85–92. 100

[Meers88] B.J. Meers: 'Recycling in laser-interferometric gravitational-wave detectors', Phys. Rev. **D 38** (1988) 2317–2326. 5

[Meers89] B.J. Meers: 'The frequency response of interferometric gravitational wave detectors', Phys. Lett. A **142** (1989) 465–470. 5, 33

[Meers91] B.J. Meers, K.A. Strain: 'Modulation, signal and quantum noise in interferometers', Phys. Rev. **A 44** (1991) 4693–4703. 38

[Meers91b] B.J. Meers, K.A. Strain: 'Wave-front distortion in laser-interferometric gravitational-wave detectors' Phys. Rev. **D 43** (1991) 3117-3130. 87, 90

[Mizuno93] J. Mizuno, K. Strain, P.G. Nelson, J.M. Chen, R. Schilling, A. Rüdiger, W. Winkler, K. Danzmann: ' Resonant sideband extraction: A new configuration for interferometric gravitational wave detectors', Physics Letters A **175** (1993) 273–276. 5

[Mizuno99] J. Mizuno, I. Yamaguchi: 'Analysis of multiple–mirror optical systems using matrices', to be published. 14, 19, 27, 35

[Morrison94] E. Morrison, B.J. Meers, D.I. Robertson, H. Ward: Appl. Opt. **33**, (1994) 5037–5040 and 5041–5049. v, 109, 115

[MPQ203] J. Mizuno: 'Comparison of optical configurations for laser–interferometric gravitational wave detectors', Ph.D. Thesis, University of Hannover, 1995. Also available as MPQ Report 203 (July 1995). 5, 12, 14, 47, 88

[Nelder65] J.A. Nelder, R. Mead: 'A simplex method for function minimization', Computer Journal **7** (1965) 308–313. 206

[Nelson] P. Nelson, unpublished personal communication, communicated by Ken Strain (1998). 20

[Niebauer91] T.M. Niebauer, R. Schilling, K. Danzmann, A. Rüdiger, W. Winkler: 'Nonstationary shot noise and its effect on the sensitivity of interferometers', Phys. Rev. **A 43** (1991) 5022–5029. 38

[Press] W.H. Press, S.A. Teukolsky, W.T. Vetterling, B.P. Flannery: 'Numerical Recipes in C, The Art of Scientific Computing', Cambridge University Press, 2nd ed., 1992. 206, 224

[Razavi] B. Razavi, ‘RF Microelectronics’, Prentice-Hall 1998. 13

[Regehr95] M.W. Regehr: ‘Signal extraction and control for an interferometric gravitational wave detector’, Ph.D. Thesis, California Institute of Technology, Pasadena (1995). 29

[Rüdiger] A. Rüdiger, personal communication (1997). 155, 155, 161

[Rüdiger78] A. Rüdiger: ‘Phasenbeziehungen an einem symmetrischen Strahlteiler’, internal note (1978, in German). 14

[Rüdiger81] A. Rüdiger, R. Schilling, L. Schnupp, W. Winkler, H. Billing, K. Maischberger: ‘A mode selector to suppress fluctuations in laser beam geometry’, Optica Acta **28** (1981) 641–658. 110, 111

[Sampas90] N. M. Sampas, D. Z. Anderson: ‘Stabilization of laser beam alignment to an optical resonator by heterodyne detection of off-axis modes’, Appl. Opt. **29**, (1990) 394–403. 109

[Saulson] P. R. Saulson: ‘Fundamentals of Interferometric Gravitational Wave Detectors’, World Scientific, Singapore 1994. v

[Schilling] R. Schilling, personal communication. 18, 20, 178, 191, 193

[Schilling:PR] The control scheme required for ‘power recycling’ was introduced to the Garching prototype by R. Schilling (1981, unpublished). 3

[Schilling97] R. Schilling: ‘Angular and frequency response of LISA’, Class. Quantum Grav. **14** (1997) 1513–1519. 33

[Schnier97] D. Schnier, J. Mizuno, G. Heinzel, H. Lück, A. Rüdiger, R. Schilling, M. Schrempel, W. Winkler, K. Danzmann: ‘Power Recycling in the Garching 30 m prototype interferometer for gravitational–wave detection’, Phys. Lett. **A 225** (1997) 210–216. 3, 57

[Schutz87] B.F. Schutz, M. Tinto: ‘Antenna patterns of interferometric detectors of gravitational waves – I. Linearly polarized waves’, Mon. Not. R. astr. Soc. **224** (1987) 131–154. 33

[Siegman] A.E. Siegman: ‘Lasers’, University Science Books, Mill Valley 1986. 14, 88, 122

[STAIC] ‘Workshop on Software Tools for Advanced Interferometer Configurations (STAIC)’ held at MPQ, Garching, April 22–25, 1998. 26, 95, 237

[Strain] K. Strain, personal communication. 18

[Strain91] K.A. Strain, B.J. Meers: ‘Experimental Demonstration of Dual Recycling for Interferometric Gravitational-Wave Detectors’, Phys. Rev. Lett., **66** (1991) 1391–1394. 5, 6, 72

[Tietze–Schenk] U. Tietze, Ch. Schenk: ‘Halbleiter–Schaltungstechnik’, 10. Aufl. Springer 1993.

[Thorne87] K.S. Thorne: ‘Gravitational Radiation’, in ‘300 Years of Gravitation’, S.W. Hawking and W. Isreal, eds. (Cambridge University Press, 1987) 330–458. v

[Vinet88] J.-Y. Vinet, B.J. Meers, C.N. Man, A. Brillet: ‘Optimisation of Long-Baseline Optical Interferometers for Gravitational-wave Detection’, Phys. Rev. **D 38** (1988) 433.

[Wangenheim] L. v. Wangenheim: ‘Aktive Filter in RC– und SC–Technik’, Hüthig–Verlag Heidelberg 1991. 72

[White] D.R.J. White: ‘Electrical Filters: Synthesis, Design and Applications’, published by D. White Consultants, Gainesville, Virginia, USA, 1980.

[Winkler] W. Winkler, personal communication. 4, 85

[Winkler91] W. Winkler: ‘A Michelson interferometer using delay lines’, Chapter 11 of [Blair].

[Winkler97] W. Winkler: ‘Shot noise and external modulation’, internal note, 1997. 171

[Winterflood95] J. Winterflood, D.G. Blair, R. Schilling, M. Notcutt: Rev. Sci. Instrum. **66** (1995) 2763–2776. 155

[Yamamoto] H. Yamamoto: Talk given at [STAIC]. 23, 26

[Yariv] A. Yariv: ‘Quantum Electronics’, Wiley, 3rd ed. 1988. xx, xx, 112, 122

List of publications

Heinzel G., Mizuno J., Schilling R., Winkler W., Rüdiger A., Danzmann K.:

'An experimental demonstration of resonant sideband extraction for laser-interferometric gravitational wave detectors',

Physics Letters A **217** (1996) 305–314.

Schnier D., Mizuno J., Heinzel G., Lück H., Rüdiger A., Schilling R., Schrempel M., Winkler W., Danzmann K.:

'Power recycling in the Garching 30 m prototype interferometer for gravitational-wave detection',

Physics Letters A **225** (1997) 210–216.

Heinzel G., Mizuno J., Schilling R., Winkler W., Rüdiger A., Danzmann K.:

'Resonant Sideband Extraction for Detectors with Fabry–Perot Arms',

in: 'Gravitational Wave Detection', Proceedings of TAMA Workshop in Saitama, Japan, November 12–14, 1996, edited by K. Tsubono, M.-K. Fujimoto, K. Kuroda, 271–279, Universal Academy Press, Tokyo, Japan.

Heinzel G., Mizuno J., Winkler W., Rüdiger A., Schilling R., Danzmann K.:

'Automatic beam alignment at the Garching 30 m prototype',

to appear in the proceedings of the Second Edoardo Amaldi Conference on Gravitational Waves, held at CERN, Geneva (Switzerland) 1-4 July 1997.

Heinzel G., Strain K.A., Mizuno J., Skeldon K.D., Willke B., Winkler W., Schilling R., Rüdiger A., Danzmann K.:

'Experimental Demonstration of a Suspended Dual Recycling Interferometer',

Phys. Rev. Lett. **81** (1998) 5493–5496.

Heinzel G., Rüdiger A., Schilling R., Strain K., Winkler W., Mizuno J., Danzmann K.:

'Automatic beam alignment in the Garching 30-m prototype of a laser-interferometric gravitational wave detector',

accepted for publication in Opt. Comm.